# Nuclei Production and Azimuthal Anisotropy of Charged Particles in Heavy-ion Collisions at RHIC

*By*

**Md. Rihan Haque**

**Enrolment No.: PHYS07201004014**

**National Institute of Science Education and Research**

**Bhubaneswar - 751005, India**

A thesis submitted to the

Board of Studies in Physical Sciences

In partial fulfillment of requirements

for the Degree of

**DOCTOR OF PHILOSOPHY**

*of*

**HOMI BHABHA NATIONAL INSTITUTE**

**August, 2015**

# STATEMENT BY AUTHOR

This dissertation has been submitted in partial fulfillment of requirements for an advanced degree at Homi Bhabha National Institute (HBNI) and is deposited in the Library to be made available to borrowers under rules of the HBNI.

Brief quotations from this dissertation are allowable without special permission, provided that accurate acknowledgement of source is made. Requests for permission for extended quotation from or reproduction of this manuscript in whole or in part may be granted by the Competent Authority of HBNI when in his or her judgement the proposed use of the material is in the interests of scholarship. In all other instances, however, permission must be obtained from the author.

Md. Rihan Haque

# DECLARATION

I, Md. Rihan Haque, hereby declare that the investigation presented in the thesis has been carried out by me. The work is original and has not been submitted earlier as a whole or in part for a degree/diploma at this or any other Institution/University.

Md. Rihan Haque

*Dedicated*
*to*
*My Family and Friends*

# Acknowledgements

# SYNOPSIS

Quantum chromodynamics (QCD) predicts that at very high temperature and/or high density quarks and gluons will be no longer confined within the hadrons [1]. This deconfined state is known as Quark-Gluon-Plasma (QGP). It is believed that the universe was once in such a state of free quarks and gluons just after the Big-Bang. The main goal of the Relativistic Heavy Ion Collider (RHIC) at Brookhaven National Laboratory (BNL) is to create such deconfined state in the laboratory and find its properties.

Light nuclei (anti-nuclei) can be produced in such heavy-ion collisions by the recombination of produced nucleons (anti-nucleons) or stopped nucleons [2, 3, 4, 5, 6]. This formation process is called final-state coalescence. Since the binding energy of light nuclei are very small ($\sim$2.2 MeV for $d$, $\overline{d}$), they cannot survive when the interactions between nucleons and other particles are strong. Therefore, light nuclei can only form at a later stage of the evolution, when the interactions between the nucleons and others particles are weak. The advantage of studying light nuclei is that space momentum distribution of both light nuclei and their constituents (proton and antiproton) are measurable quantities in a given experiment. Therefore, by studying the yield and azimuthal anisotropy of light nuclei and comparing them with that of proton (anti-proton) we can gain insight in the particle production mechanism via coalescence.

This thesis includes the study of the yield and the $2^{nd}$ order azimuthal anisotropy ($v_2$) of light nuclei ($d$, $\overline{d}$, $t$, $^3He$, $^3\overline{He}$) produced in Au+Au collisions at RHIC beam energies $\sqrt{s_{NN}}$= 7.7, 11.5, 19.6, 27, 39, 62.4 and 200 GeV. The data presented in this thesis are those collected by the STAR detector at RHIC.

Invariant yield of light nuclei ($d$, $\overline{d}$) has been measured as a function transverse momentum ($p_T$) for Au+Au collisions at RHIC beam energies $\sqrt{s_{NN}}$= 7.7, 11.5, 19.6, 27 and 39 GeV. The $p_T$ spectra has been fitted with hydrodynamic inspired Blast-wave model to extract kinetic freeze-out temperature and collective flow velocity. $p_T$-integrated yield of $d$, $\overline{d}$ and their average transverse momentum ($\langle p_T \rangle$) has also been extracted.

A systematic measurement of energy and centrality dependence of $v_2$ of light nuclei has also been presented. Comparison of nuclei and anti-nuclei $v_2$ has been carried out for the measured energy range. Similarly the comparison of $v_2$ for $t$ and $^3He$, which have same mass but different nuclear composition, has been presented. The atomic mass number ($A$) scaling of light nuclei $v_2$, as expected from the coalescence mechanism, has been also studied. The light nuclei $v_2$ is found to show atomic mass number scaling for $p_T/A$ up to 1.3 GeV/c. Light nuclei $v_2$ has also been calculated using coalescence + transport model. Light nuclei $v_2$ from coalescence model is found to reproduce the $v_2$ measurements from data. Therefore, one important finding in this thesis work is that in heavy-ion collisions, light nuclei are most probably formed via coalescence of nucleons.

This thesis also includes the study of azimuthal anisotropy of charged particles using transport and hydrodynamic models. The study of the $2^{nd}$ and $3^{rd}$ order azimuthal anisotropy ($v_2$, $v_3$), corresponding eccentricity ($\varepsilon_2$, $\varepsilon_3$) and eccentricity fluctuations has been presented for asymmetric (Au+Ag, Au+Cu, and Au+Si) and compared with symmetric (Au+Au and Cu+Cu) collisions at $\sqrt{s_{NN}}=$ 200 GeV using transport (AMPT) model. $\varepsilon_2$, fluctuation in $\varepsilon_2$ and $v_2$ are found to be strongly dependent of system size whereas, $\varepsilon_3$, fluctuation in $\varepsilon_3$ and $v_3$ and are found to be independent of the system size. Using the same transport model, azimuthal anisotropy ($v_2$, $v_3$), eccentricity ($\varepsilon_2$, $\varepsilon_3$), eccentricity fluctuations, charged particle multiplicity ($N_{ch}$), transverse energy ($E_T$), and $\langle p_T \rangle$ has been measured in deformed U+U collisions. In this study, it was found that $v_2$, $v_3$ and $N_{ch}$ are higher in the U+U collisions compared to that in Au+Au for similar collision energy. It is also found that $v_2$ and $\varepsilon_2$ are strongly dependent on the different collision configurations in U+U, whereas $v_3$ and $\varepsilon_3$ are almost independent of the different configurations.

Azimuthal anisotropy of produced charged particles and their correlation with initial eccentricity has also been studied using a hydrodynamic model. The effect of smoothing of Glauber Monte Carlo initial conditions on charged particle $v_2$, $v_3$ has been estimated. It was found that integrated as well as differential flows remain largely unaltered, irrespective of functional form of the smoothing function, or the

smoothing parameter. It was also found in hydrodynamic calculations that for all the higher flow coefficients ($v_n$, n = 3, 4, 5), correlation with initial eccentricity is reduced with collision centrality. Elliptic flow $v_2$, however, was found to be strongly correlated with the initial eccentricity in all the collision centralities.

# Bibliography

[1] G. Baym, Nucl. Phys. A **698** (2002) XXIII.

[2] S.T. Butler and C.A. Pearson, Phys. Rev. **129**, 836 (1963).

[3] H. H. Gutbrod et al., Phys. Rev. Lett. **37**, 667 (1976).

[4] H. Sato and K. Yazaki, Phys. Lett. B **98**, 153 (1981).

[5] W. J. Llope et al., Phys. Rev. C **52**, 2004 (1995).

[6] R. Scheibl and U. Heinz, Phys. Rev. C **59**, 1585 (1999).

# Publications

## List of publication as primary author:

(*) indicate papers on which this thesis is based.

1. **Elliptic and Triangular flow in asymmetric heavy-ion collisions** *
   Md.Rihan Haque, Md. Nasim and Bedangadas Mohanty,
   Phys. Rev. C **84**, 067901 (2011); arXiv:1111.5095.

2. **Multiplicity, average transverse momentum and azimuthal anisotropy in U+U collisions at $\sqrt{s_{\mathrm{NN}}} = $ 200 GeV using AMPT model** *
   Md.Rihan Haque, Zi-Wei Lin and Bedangadas Mohanty,
   Phys. Rev. C **85**, 034905 (2012); arXiv:1112.2340.

3. **Fluctuating initial condition and smoothening effect on elliptic and triangular flow** *
   Md. Rihan Haque, Victor Roy and A. K. Chaudhuri,
   Phys. Rev. C **86**, 037901 (2012); arXiv:1204.2986.

4. **Even-by-event hydrodynamical simulations for $\sqrt{s_{\mathrm{NN}}} = $ 200 GeV Au+Au collisions and the correlation between flow coefficients and initial asymmetry measures** *
   A.K. Chaudhuri, Md. Rihan Haque, Victor Roy and Bedangadas Mohanty,
   Phys. Rev. C **87**, 034907, (2013); arXiv:1211.2040.

5. **Selecting specific initial configurations using spectator neutrons in U + U collisions**
   Vipul Bairathi, Md. Rihan Haque and Bedangadas Mohanty,
   Phys. Rev. C **91**, 054903 (2015); arXiv:1504.04719.

## Paper under review in collaboration (as a primary author)

1. **Measurement of elliptic flow of light nuclei at $\sqrt{s_{\mathrm{NN}}} = 200, 62.4, 39, 27, 19.6, 11.5$ and 7.7 GeV at RHIC** *

   to be submitted in Physical Review C.

## List of conference proceedings:

1. **Study of flow in asymmetric heavy-ion collisions** *

   Md Rihan Haque, Md Nasim and Bedangadas Mohanty,

   Proceedings of the DAE Symp. on Nucl. Phys. **56**, 930−931, (2011).

2. **Elliptic flow of [anti-]deuteron in Au+Au collisions at sNN = 39 GeV in STAR** *

   Md. Rihan Haque (for STAR Collaboration)

   Proceedings of the DAE Symp. on Nucl. Phys. **57**, 834−835, (2012).

3. **Elliptic flow of light nuclei in Au+Au collisions at sNN = 39, 27, 19.6, 11.5, 7.7 GeV in STAR** *

   Md. Rihan Haque (for STAR Collaboration)

   Proceedings of the DAE Symp. on Nucl. Phys. **58**, 760−761, (2013).

4. **Elliptic flow of light nuclei and identified hadrons, their energy and centrality dependence in STAR** *

   Md. Rihan Haque (for STAR Collaboration)

   Nuclear Physics A, **931**, 915−919, (2014).

## List of STAR collaboration papers as an author:

1. **Freeze-out Dynamics via Charged kaon femtoscopy in $\sqrt{s_{\mathrm{NN}}} = 200$ GeV Central Au+Au Collisions**

   STAR Collaboration (L Adamczyk *et al.*),

   Phys. Rev. C **88**, 034906 (2013); arXiv:1302.3168.

2. **Fluctuations of charge separation perpendicular to the event plane and local parity violation in $\sqrt{s_{\mathrm{NN}}} = 200$ GeV Au+Au collisions at RHIC**
STAR Collaboration (L Adamczyk *et al.*),
Phys. Rev. C 88, 064911 (2013); arXiv:1302.3802.

3. **Neutral pion cross section and spin asymmetries at intermediate pseudorapidity in polarized proton collisions at $\sqrt{s_{\mathrm{NN}}} = 200$ GeV**
STAR Collaboration (L Adamczyk *et al.*),
Phys. Rev. D 89, 012001 (2014); arXiv:1309.1800.

4. **Energy Dependence of Moments of Net-proton Multiplicity Distributions at RHIC**
STAR Collaboration (L Adamczyk *et al.*),
Phys. Rev. Lett. 112, 032302 (2014); arXiv:1309.5681.

5. **Jet-Hadron Correlations in $\sqrt{s_{\mathrm{NN}}} = 200$ GeV p+p and Central Au+Au Collisions**
STAR Collaboration (L Adamczyk *et al.*),
Phys. Rev. Lett. 112, 122301 (2014); arXiv:1302.6184.

6. **Beam-Energy Dependence of the Directed Flow of Protons, Antiprotons, and Pions in Au+Au Collisions**
STAR Collaboration (L Adamczyk *et al.*),
Phys. Rev. Lett. 112, 162301 (2014); arXiv:1401.3043.

7. **Dielectron Mass Spectra from Au+Au Collisions at $\sqrt{s_{\mathrm{NN}}} = 200$ GeV**
STAR Collaboration (L Adamczyk *et al.*),
Phys. Rev. Lett. 113, 022301 (2014); arXiv:1312.7397.

8. **Beam-energy dependence of charge separation along the magnetic field in Au+Au collisions at RHIC**

STAR Collaboration (L Adamczyk *et al.*),

Phys. Rev. Lett. 113, 052302 (2014); arXiv:1404.1433.

9. **J/Ψ production at low $p_\text{T}$ in Au+Au and Cu+Cu collisions at $\sqrt{s_\text{NN}}$ = 200 GeV at STAR**

STAR Collaboration (L Adamczyk *et al.*),

Phys. Rev. C 90, 024906 (2014); arXiv:1310.3563.

10. **Measurement of longitudinal spin asymmetries for weak boson production in polarized proton-proton collisions at RHIC**

STAR Collaboration (L Adamczyk *et al.*),

Phys. Rev. Lett. 113, 072301 (2014); arXiv:1404.6880.

11. **Beam Energy Dependence of Moments of the Net-Charge Multiplicity Distributions in Au+Au Collisions at RHIC**

STAR Collaboration (L Adamczyk *et al.*),

Phys. Rev. Lett. 113, 092301 (2014); arXiv:1402.1558.

12. **Observation of $D_0$ meson nuclear modifications in Au+Au collisions at $\sqrt{s_\text{NN}}$ = 200 GeV**

STAR Collaboration (L Adamczyk *et al.*),

Phys. Rev. Lett. 113, 142301 (2014); arXiv:1404.6185.

13. **J/Ψ Polarization in p+p collisions at $\sqrt{s_\text{NN}}$ = 200 GeV at STAR**

STAR Collaboration (L Adamczyk *et al.*),

e-Print: arXiv:1311.1621.

14. **Suppression of Upsilon Production in d+Au and Au+Au Collisions at $\sqrt{s_\text{NN}}$ = 200 GeV**

STAR Collaboration (L Adamczyk *et al.*),

e-Print: arXiv:1312.3675.

15. **Beam energy dependent two-pion interferometry and the freeze-out eccentricity of pions in heavy ion collisions at STAR**

STAR Collaboration (L Adamczyk *et al.*),

e-Print: arXiv:1403.4972.

16. **Precision Measurement of the Longitudinal Double-spin Asymmetry for Inclusive Jet Production in Polarized Proton Collisions at $\sqrt{s_{\mathrm{NN}}}$ = 200 GeV**

STAR Collaboration (L Adamczyk *et al.*),

e-Print: arXiv:1405.5134.

17. **Elliptic flow of non-photonic electrons in Au+Au collisions at $\sqrt{s_{\mathrm{NN}}}$ = 200, 62.4 and 39 GeV**

STAR Collaboration (L Adamczyk *et al.*),

e-Print: arXiv:1405.6348.

18. **Charged-to-neutral correlation at forward rapidity in Au+Au collisions at $\sqrt{s_{\mathrm{NN}}}$ = 200 GeV**

STAR Collaboration (L Adamczyk *et al.*),

e-Print: arXiv:1408.5017.

19. **Isolation of Flow and Nonflow Correlations by Two and Four Particle Cumulant Measurements of Azimuthal Harmonics in $\sqrt{s_{\mathrm{NN}}}$ = 200 GeV Au+Au Collisions**

STAR Collaboration (L Adamczyk *et al.*),

e-Print: arXiv:1409.2043.

20. **Di-Hadron Correlations with Identified Leading Hadrons in 200 GeV Au+Au and d+Au Collisions at STAR**

STAR Collaboration (L Adamczyk *et al.*),

e-Print: arXiv:1410.3524.

# Contents

# List of Figures

# List of Tables

# Chapter 1

# Introduction

## 1.1 The Standard Model

The goal of elementary particle physics is to identify the basic constituents of matter and to understand their properties and interactions. From the past studies we know that protons and neutrons are not fundamental particles as electrons, since they consist of point like particles namely quarks. These constituent quarks are held together by the exchange of gluons. Collectively these quarks and gluons are called partons. The Standard Model (SM) was proposed by Glashow, Salam and Weinberg to explain the fundamental structure of matter as well as the fundamental interactions [1]. The gravitational interaction, however, has not yet been incorporated in this model. According to this model, all the elementary particles are divided into three groups namely, Quarks, Leptons and Gauge Bosons [2]. All the quarks and leptons are spin half particles, i.e., fermions and the gauge bosons are the mediator of the interaction between quarks and leptons. All together they represent three of the four fundamental forces in nature: the strong force, the weak force, the electromagnetic force and the gravitational force. The six different gauge bosons are: The massless photons ($\gamma$) and gluons ($g$), the massive $W^{\pm}$ and $Z^0$ bosons and gravitons. The SM also predicts the existence of Higgs boson ($H$) which has been discovered very recently [3, 6]. The

leptons are divided into three generations: The electron and electron neutrino, the muon and muon neutrino and the tau and tau neutrino. The leptons interact among each other via the electromagnetic and the weak interaction. There are also three generations of quarks in the SM, namely, the up (u) and down (d) quarks, the charm (c) and strange (s) quarks and the top (t) and bottom (b) quarks. Figure 1.1 shows all the fundamental particles in the SM.
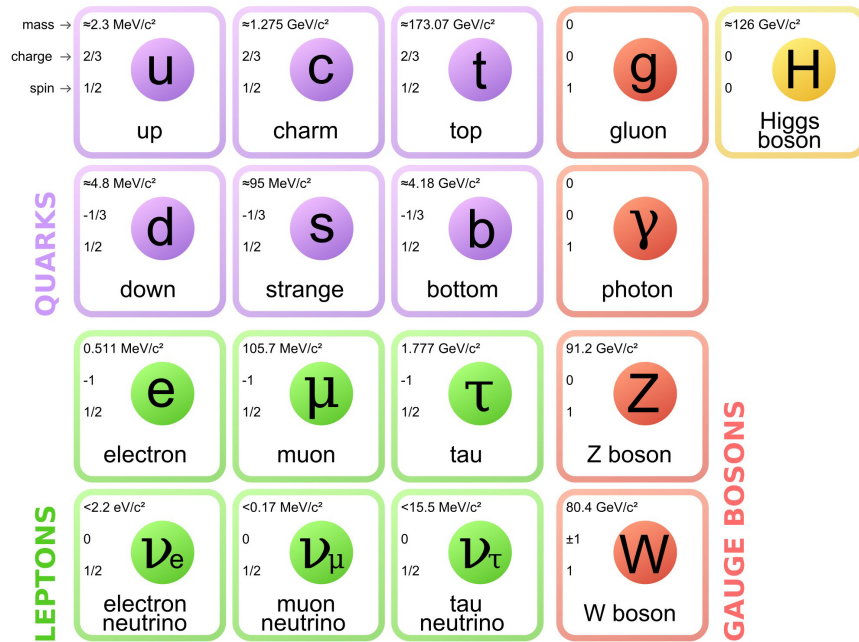


Figure 1.1: The fundamental particles of the standard model and the force mediating gauge bosons.

## 1.2 Quantum Chromodynamics

Quantum Chromodynamics (QCD) is the theory of the strong interaction, one of the four fundamental forces in nature [7]. It describes the interactions between quarks and gluons in the standard model similar to Quantum electrodynamics (QED) for electrons. In QCD, the quarks and gluons are said to have color charge, similar to electric charge of an electron. It explains the chromo component of the theory's name.

There are two key features of QCD, which are: confinement and asymptotic freedom. The QCD theory of strong interaction is characterized by a coupling constant, $\alpha_S$, given by:

$$\alpha_S \approx \frac{12\pi}{(11n - 2f)\ln(|Q^2|/\Lambda^2)},$$

(1.1)

where $Q^2$ is the amount of momentum transfer, $n$ is the number of colors and $f$ is the number of flavors. The value of the scale parameter $\Lambda$ appears to be lie in between the range 100 MeV to 500 MeV. It is very difficult to determine value of $\Lambda$ very precisely from experimental data. The values of $\alpha_S$ has been extracted from different experimental results and compared with perturbative QCD (pQCD) predictions [8]. The value of $\alpha_S$ from pQCD calculation for various experiments are shown in Figure 1.2. At large distances or for small momentum transfers, the value of $\alpha_S$ is large and increases as the distance between two quarks is increased. This property is called Confinement and this is the reason that quarks are never found free but are always bound together in groups of three in the form of baryons or as quark-antiquark pairs in the form of mesons. On the other hand when the amount of momentum transfers is large $i.e.$, distances between quarks are very small, the coupling between quarks becomes very small and therefore, quarks behaves like free particles. As a consequence, QCD medium at very high temperatures behaves like a gas of free quarks and gluons. This property, where the interactions between the quarks becomes arbitrarily weak at length scales that asymptotically goes to zero, is known as Asymptotic Freedom and was discovered in 1973 by David Gross, Frank Wilczek, and David Politzer. They received nobel prize in 2004 for their discovery [4, 5].

## 1.3 Deconfinement and Quark-Gluon Plasma

In the year 1974, T.D. Lee suggested that by having high nucleon density over a relatively large volume, it might be possible to create very high dense states of nuclear
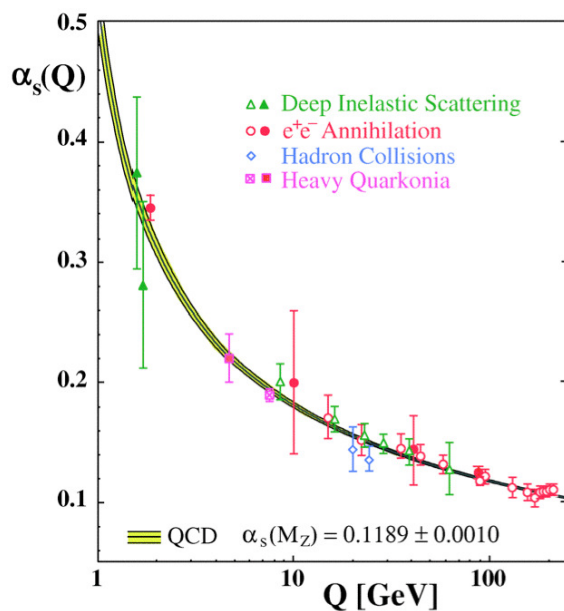
Figure 1.2: Various measurements on the strong coupling constant $\alpha_S$ as function of energy scale Q. The curves are the QCD predictions. Figure has been taken from Ref. [8].

matter which would contain asymptotically free quarks. Such dense nuclear matter of free quarks is known as the Quark-Gluon Plasma (QGP) [9], and it is believed to have existed a few microseconds after the Big Bang. This plasma also exhibits the so-called Chiral Symmetry which, in normal nuclear matter is spontaneously broken, results in effective quark mass which are much larger than their actual mass. The lattice QCD calculations also show that there are two phases in the high temperature QCD calculations, predicting a phase transition from a confined hadronic matter to a deconfined state of quarks and gluons at a critical temperature ($T_c$) of ~154 MeV [10] and an energy density of $\varepsilon \sim 1$ GeV/fm$^3$ [11]. Figure 1.3 shows the temperature dependence of pressure ($p$) and energy density ($\varepsilon$) as obtained from lattice QCD calculations [11]. These calculations are performed with non-zero temperatures and non-zero chemical potentials. The $\varepsilon/T^4$ is proportional to the number of degrees of freedom in a thermodynamic system. The sharp increase of $\varepsilon/T^4$ around $T_c$ indicates a transition in the system to a state where the quarks and gluons have become relevant degrees of freedom rather than nucleons. A schematic phase diagram of strongly

4
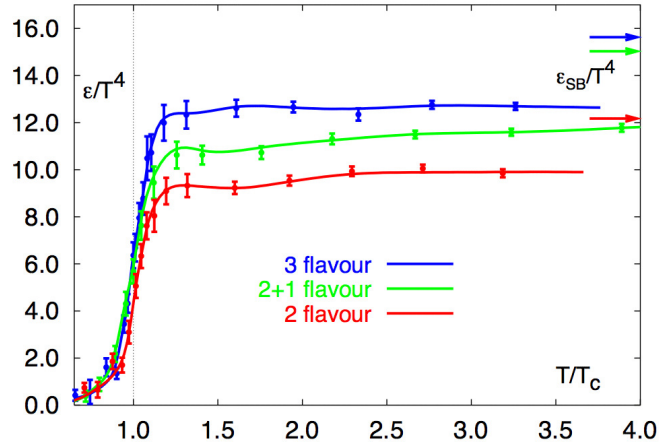
Figure 1.3: Lattice QCD calculations for energy density as a function of temperature [11]. Stefan-Boltzmann ideal gas limits are also shown by arrows.

interacting matter, has been shown in the Fig. 1.4 which depicts possible phases of nuclear matter depending on its temperature $(T)$ and the baryon chemical potential $(\mu_B)$. At a larger $T$ and smaller $\mu_B$, lattice QCD predicts a smooth crossover between phases [14] while theoretical calculations show that at smaller $T$ and larger $\mu_B$ a first order phase transition may take place between hadron gas and QGP [15]. QCD calculations also suggest that at low $T$ and very high $\mu_B$, quarks form a colour super-conducting phase [16].

## 1.4 Relativistic Heavy Ion Collisions

The primary motivation for heavy-ion collisions at ultra-relativistic energies is to study nuclear matter at such extreme conditions which is believed to be existed a few microsecond after the Big Bang. At such extreme conditions of temperature and energy density it is expected that a phase transition will occur from a confined hadronic matter to a plasma of deconfined quarks and gluons. The first heavy-ion collision was done at Lawrence Berkeley National Laboratory in the 1970s. Projectile of energy upto $1A$ GeV/c energy were made to collide with the target nuclei to yield compressed nuclear matter with density few times higher than the normal nuclear
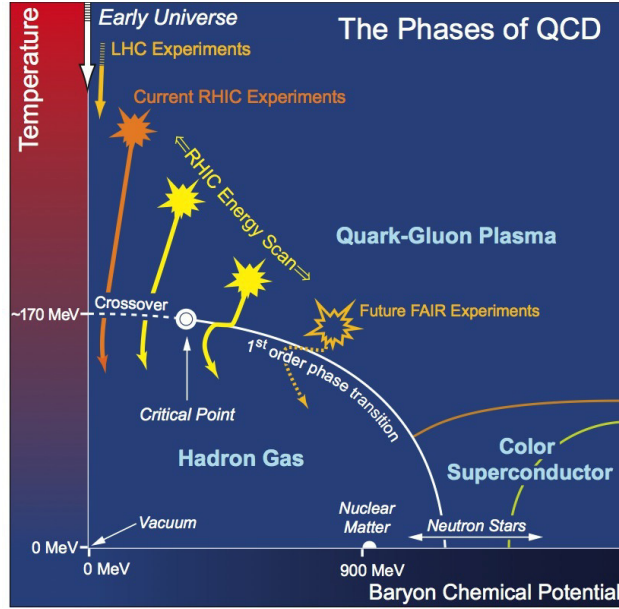
Figure 1.4: Schematic QCD phase diagram for nuclear matter [12]. The solid lines show the phase boundaries for the indicated phases. The solid circle depicts the critical point [13].

matter. The success of these early experiments lead to the possibility of study of compressed matter in the experiments at Brookhaven National Laboratory (BNL) and at European Organisation for Nuclear Research (CERN) with more projectile energy as well as with different projectiles and targets. The Alternating Gradient Synchrotron (AGS) at BNL and the Super Proton Synchrotron (SPS) at CERN were such moderately relativistic heavy-ion collision experiments with maximum projectile energy of $\sqrt{s_{\mathrm{NN}}} = 4.86$ GeV and 17.3 GeV respectively. The Relativistic Heavy Ion Collider (RHIC) at BNL is one of a kind of machine in the world to be able to collide polarized protons as well as heavy ions such as Cu, Au and U. RHIC can accelerate heavy ions for various beam energies starting from $\sqrt{s_{\mathrm{NN}}} = 7.7$ GeV upto 200 GeV. However, the top energy for p+p collisions can be extended up to $\sqrt{s} = 500$ GeV. Till date, the Large Hadron Collider (LHC) at CERN is the largest and most energetic heavy-ion collider which collides Pb ions at $\sqrt{s_{\mathrm{NN}}} = 2.76$ TeV.

## 1.4.1  Space-time Evolution of Heavy-ion Collision

In relativistic heavy-ion collisions, two bare nuclei are accelerated in opposite directions with velocities nearly to the speed of light. The bare nuclei traveling at relativistic velocities appear like pancakes due the Lorentz contraction along the beam direction ($z$-axis). Figure 1.5 shows theoretically motivated space-time evolution of a heavy-ion collision at relativistic energy.
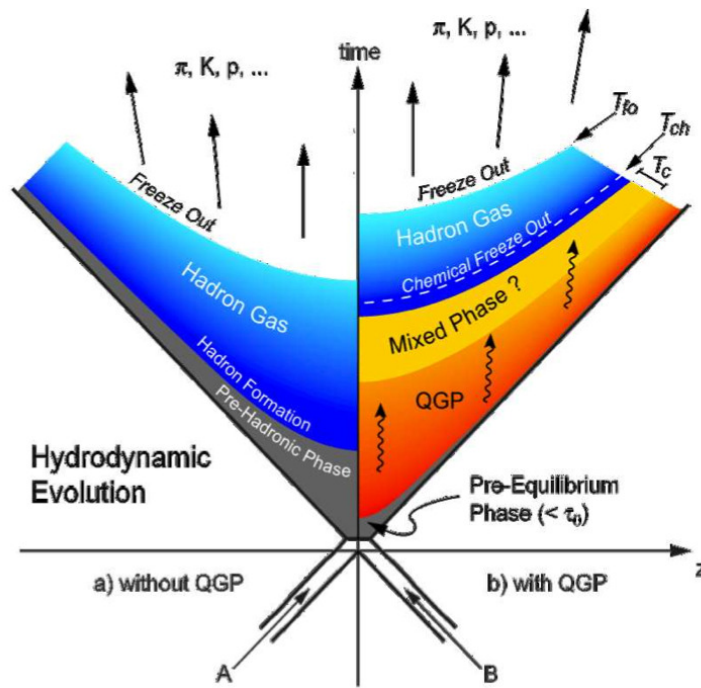


Figure 1.5: Space-time diagram and different types of evolution stages of a relativistic heavy-ion collision.

In such a heavy-ion collision, large amount of the energy is deposited in the overlap region of the two nuclei. If the energy density created in the collision does not reach the critical value necessary for QGP formation, then the system will be composed of a gas of interacting hadrons as shown on the left-hand side of Fig. 1.5. However, if the initial energy density is large enough and the temperature of the created system exceeds $T_c$, then phase transition from hadrons to deconfined quarks and gluons is

expected to occur. This scenario is shown on the right-hand side of Fig. 1.5. The hot and dense medium formed in such heavy ion collision is often called *fireball*. The fireball may take some time to thermalize via subsequent interactions among quarks and gluons. This thermalized phase of quarks and gluons are often called the Quark Gluon Plasma (QGP). The subsequent expansion of the medium is governed by the relativistic hydrodynamics. As the system expands and cools and reaches $T_c$, hadronization process starts and the quarks and gluons become confined inside hadrons. As the system of hadrons continues to expand, "chemical freeze-out" occurs at a temperature $T_{ch}$, where the inelastic interactions between the hadrons cease and the relative abundances for hadron species do not change any more. The expansion continues until a temperature $T_{kin}$, where the mean free path of hadrons becomes larger than the system size and the elastic interactions between the hadrons cease. This phenomena is called "thermal freeze-out" or "kinetic freeze-out". At this stage, the particles come out of the system freely and stream towards the detectors.

## 1.5 Kinematic Variables in Heavy-ion Collision

At the RHIC, the coordinate system is chosen such that the $z$-axis is parallel to the beam axis (details will be shown in chapter 2). The nominal interaction point (IP) is at the $(x, y, z)$ : $(0, 0, 0)$ co-ordinate. The beams are focused in such a way so that most of the collisions take place around this point. However, collisions do not always happen exactly at the IP. Thus the collision point, called the primary vertex, has to be measured for each interaction. The main kinematic variables which are widely used in heavy-ion collision analysis are detailed in the following subsections.

### 1.5.1 Transverse Momentum

In heavy-ion collisions, the total momentum of each produced particle is divided into two parts, namely transverse momentum ($p_T$) and longitudinal momentum ($p_z$). The transverse momentum is defined as,

$$p_{\mathrm{T}} = \sqrt{p_x^2 + p_y^2} \qquad (1.2)$$

where $p_x$ and $p_y$ are the $x$ and $y$ components of total momentum ($p$) measured in the laboratory (detector frame) of reference. The transverse momentum ($p_{\mathrm{T}}$) is Lorentz invariant. Therefore $p_{\mathrm{T}}$ is a very useful quantity in heavy-ion collisions.

## 1.5.2 Rapidity

In heavy-ion collisions, $p_z$ is seldom used in the analysis. Instead another variable, namely rapidity, is used in place of $p_z$. The rapidity $y$ of a particle is defined as,

$$y = \frac{1}{2} \ln \Big( \frac{E + p_z}{E - p_z} \Big) \qquad (1.3)$$

where $E$ is the energy of the particle. Rapidity has the advantage of being additive under Lorentz transformations, while $p_z$ is not. In the non-relativistic limits (i.e. $p << m$), rapidity is equivalent to the velocity of the particle. Here $m$ is the rest mass of the particle.

## 1.5.3 Pseudo-rapidity

In heavy-ion collisions, it is not always possible to measure the total momentum ($p$) and Energy ($E$) simultaneously. Therefore, another variable namely pseudo-rapidity is used for kinematic calculations. The pseudo-rapidity ($\eta$) of a particle is defined as,

$$\eta = \frac{1}{2} \ln \Big( \frac{p + p_z}{p - p_z} \Big) \qquad (1.4)$$

Looking at the definition of $\eta$ it could be easily noticed that this variable is Lorentz invariant. Therefore, $\eta$ is a better variable than $y$ when we need to migrate our observables from center-of-mass frame to laboratory frame and vice versa. For relativistic limits (*i.e.* $p >> m$), $\eta \approx y$ in the mid-rapidity ($y \approx 0$) region.

### 1.5.4 Particle Multiplicity

The multiplicity of an event is defined as the number of particles produced in a single collision. Since most of the tracking and particle identification detectors only measure charged particles, therefore the multiplicity generally refers to the number of charged particles produced in an event.

### 1.5.5 Invariant Yield

The quantity $Ed^3\sigma/dp^3$, is invariant under Lorentz transformations, and it is called invariant cross section. In experiments, the invariant cross section is measured using the equation,

$$E\frac{d^3\sigma}{dp^3} = \frac{1}{L_{\text{int.}}}E\frac{d^3N}{dp^3} \tag{1.5}$$

where $\sigma$ is the cross section, $E$ is the energy and $L_{\text{int.}}$ is the integrated luminosity. The quantity, $E\frac{d^3N}{dp^3}$ can be further decomposed as,

$$E\frac{d^3\sigma}{dp^3} = \frac{1}{L_{\text{int.}}}\frac{1}{2\pi}\frac{d^2N}{p_T dp_T dy}. \tag{1.6}$$

The right hand side of equation 1.6 is measured experimentally and called differential cross section.

### 1.5.6 Centrality

Figure 1.6 shows the geometrical view of a typical heavy-ion collision. The perpendicular distance $b$, going from the centre of one nucleus to the centre of the other, is called impact parameter. It is a measurement of the overlap between the two colliding nuclei. The nucleons inside the overlap region is known as participant nucleons. A central collision is defined as having a very small impact parameter resulting in large number of participating nucleons, whereas, peripheral collisions are defined when im-

pact parameter is large with a small number of participating nucleons. The impact parameter cannot be measured experimentally, so the multiplicity (or charged particle multiplicity) is often used to characterize centrality. The multiplicity is used to
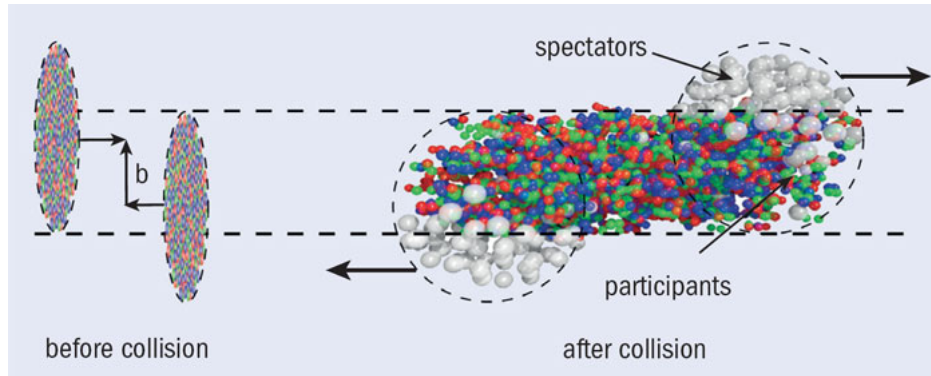


Figure 1.6: A geometrical view of the heavy ion collision. See text for details.

define centrality assuming its monotonic variation with impact parameter. Higher values of multiplicity correspond to central event and lower values of multiplicity corresponds to peripheral events. The details of centrality determination technique using charged particle multiplicity will be discussed in chapter 2.

## 1.5.7   Units in Heavy-ion Collisions

In heavy-ion collisions, all quantities are expressed in natural units *i.e.*, velocity of light $c = 1$ and Plank's constant $\hbar = 1$. Therefore, regular physical units can be converted into natural units using the conversion formula, $\hbar c = 197$ MeV-fm. Therefore, the natural units of mass is GeV, that of length and time is GeV$^{-1}$. The use of natural units simplifies the expressions and kinematic calculations of experimental observables in heavy-ion collision.

## 1.6 Experimental Observables of QGP

The hot and dense medium created in the heavy-ion collision has a very short lifetime ($\sim$5$-$10 fm/c). In heavy-ion experiments we only detect the freely streaming particles from the final state of the evolution of the hot and dense medium. By performing measurements on these produced particles we try to understand the properties of the medium created in heavy-ion collisions. Many signatures of QGP formation and associated characteristics of the medium have been proposed in [17, 18]. In the following sub-sections, we briefly discuss some of the proposed signatures of QGP formation.

### 1.6.1 Jet Quenching

A jet is a high $p_\mathrm{T}$ quark or gluon, which fragments into a number of highly correlated hadrons. Dihadron azimuthal correlations can be used to observe jets in high energy collisions.
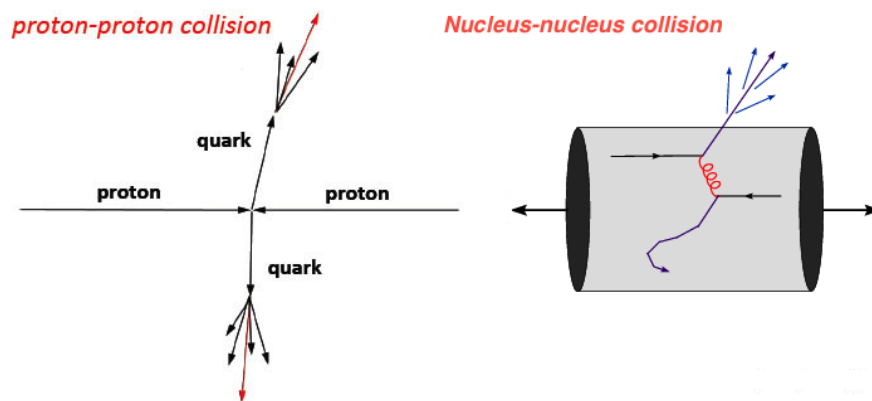


Figure 1.7: Formation of jets in p+p and Au+Au collisions. See text for details.

The idea is that if two jets are created near the fireball edge, one is emitted away from the fireball, while the other traverses the medium and appear on the other side. This is true in both p+p and d+Au collisions, but not in Au+Au collisions as illustrated

in the Fig. 1.7. An example of a dihadron azimuthal correlation analysis is shown in Fig. 1.8 [19].
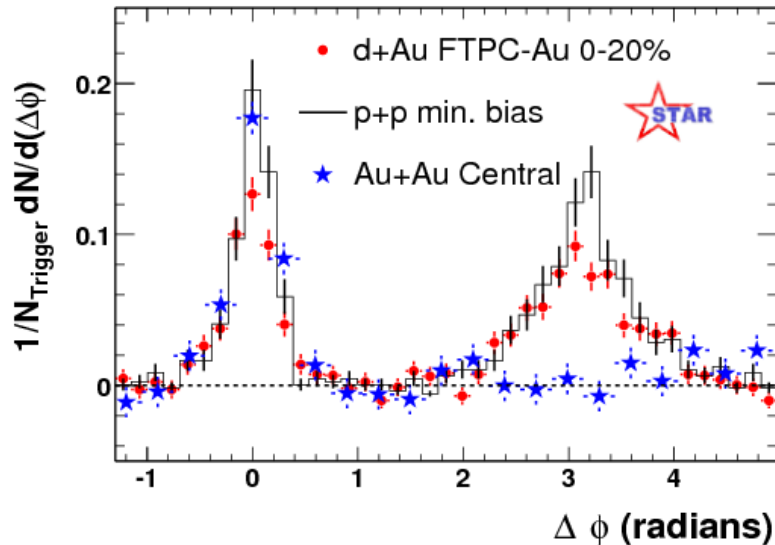


Figure 1.8: Di-hadron azimuthal correlations as observed in Au+Au, d+Au and p+p collisions [19].

The red points are from d+Au collisions, the black line is from p+p collisions and the blue points are from Au+Au collisions show a peak at $\Delta\phi = 0$, this is the near side jet, which is emitted away from the fireball. At $\Delta\phi = \pi$, only d+Au and p+p data shows a peak. This means the away side jet does not appear in Au+Au collisions. The theory is that the jet is completely quenched, i.e. it looses all its energy while traversing in the dense medium. This has been considered as a signature of QGP at RHIC [19].

## 1.6.2  High $p_\mathrm{T}$ Probes

Bjorken first suggested that the QGP state should manifest itself by the suppression of the high momentum partons as they interact elastically with the medium [20]. It was then proposed that inelastic collisions would also lead to energy loss via gluon radiation [21]. In relativistic nucleus-nucleus collisions, the main source of high mo-

mentum particle production is from scattered partons which fragment into hadron jets. In order to compare jet production rates in Au+Au and p+p (or d+Au) collisions, the $R_{AA}$ is measured which is defined as,

$$R_{AA} = \frac{1}{\langle N_{coll} \rangle} \frac{\text{Yield}_{AA}}{\text{Yield}_{pp}}, \tag{1.7}$$

where $\langle N_{coll} \rangle$ is the average number of binary collisions. $R_{AA}$ is known as a Nuclear Modification Factor. Another observable $R_{CP}$ is also used to quantify the differences between the systems created in collisions with different centralities. The $R_{CP}$ is defined as,

$$R_{CP} = \frac{\langle N_{coll} \rangle_{periferal}}{\langle N_{coll} \rangle_{central}} \times \frac{\text{Yield}_{central}}{\text{Yield}_{periferal}} \tag{1.8}$$

The $R_{AA}$ and $R_{CP}$ measured at top RHIC energy is shown in Fig. 1.9 and Fig. 1.10 respectively [9, 19].
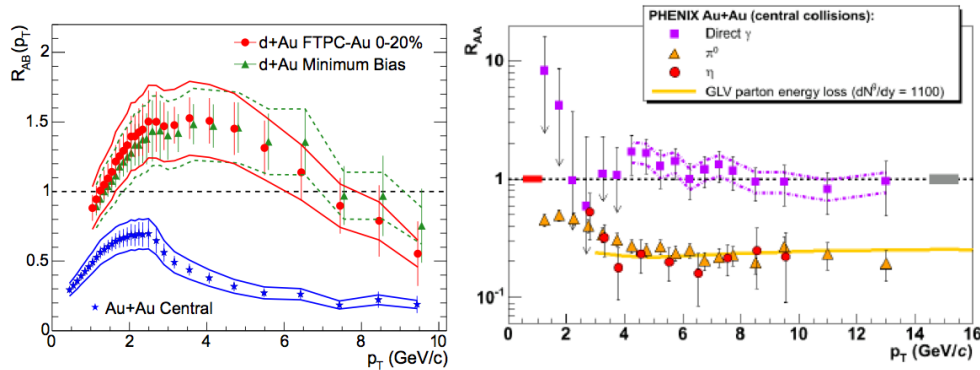


Figure 1.9: Left panel: $R_{AA}$ (also known as $R_{AB}$) measured in central Au+Au and d+Au collisions with $\sqrt{s_{NN}} = 200$ GeV for charged hadrons. Right panel: $R_{AA}$ measured in central Au+Au at $\sqrt{s_{NN}} = 200$ GeV for $\eta$, $\pi^0$ and photons. The grey error band reflects the uncertainty in the number of binary collisions for central Au+Au collisions [19].

For nucleus-nucleus collisions, the hadrons produced from hard processes are expected to scale with the number of binary collisions if there is no medium effects. In this case nucleus-nucleus collisions is just simple superposition of nucleon nucleon colli-
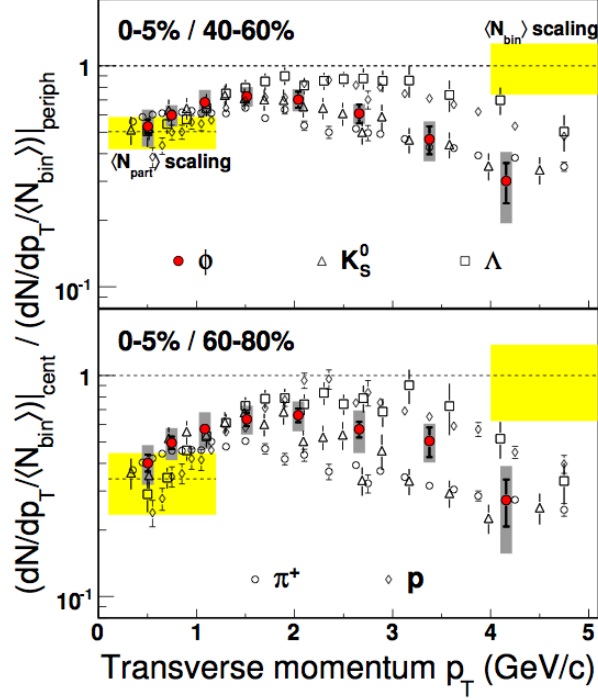
Figure 1.10: The $R_{CP}$ of identified hadrons at mid-rapidity in Au+Au collisions at $\sqrt{s_{NN}}$ = 200 GeV. The shaded bands represents the uncertainty in the number of binary collisions in Au+Au collisions [9].

sions and $R_{AA}$ will be equal to unity. The RHIC experiments report values for the nuclear modification factor below 1 for charged and identified hadrons for Au+Au collisions. This means that for intermediate to high $p_T$ there is a suppression of particle production in central and mid-central Au+Au collisions compared to d+Au (or p+p) collisions and in central Au+Au compared to peripheral Au+Au collisions. This suppression has been attributed to energy loss of high-$p_T$ partons in the dense medium created in central collisions. Moreover, for d+Au collisions where the QGP is not expected to form, an enhancement is observed. The enhancement is commonly attributed to the Cronin effect. The right panel of Fig 1.9 shows the $R_{AA}$ of $\eta$, $\pi^0$ and photons in Au+Au central collisions. One can see that high $p_T$ hadron ($\eta$ and $\pi^0$) production are suppressed but production of photons, which do not participate in strong interactions, is not suppressed. This again indicates the effect of strong

interactions in the hot and dense medium on the hadrons production in Au+Au collisions. From Fig. 1.10 one can see that at intermediate $p_{\mathrm{T}}$, $R_{\mathrm{CP}}$ shows particle-type dependence. The mesons and baryons seem to follow different trends from each other as a function of $p_{\mathrm{T}}$ . This can be explained by considering particle production via recombination or coalescence of quarks [22, 23].

### 1.6.3 Strangeness Enhancement

Strange particle production is one of the observables expected to deliver detailed information on the reaction dynamics of relativistic nucleus-nucleus collisions [24]. In experiments at the CERN SPS accelerator it was found that the ratio of the number of produced kaons to that of pions is higher by a factor of about two compared to that in proton-proton reactions at the same energy  [25, 26, 27, 28]. In the past, several possible reasons for this strangeness enhancement have been discussed. Firstly, if nucleus-nucleus reactions proceed through a deconfined stage, then strange-quark production should be abundant [29]. Alternative ideas of canonical suppression of strangeness have been proposed to be a source of strangeness enhancement in small systems (proton-proton) [30]. Figure 1.11 shows the ratio of strange hadron yields normalized to $\langle N_{\mathrm{part}} \rangle$ in nucleus-nucleus collisions relative to yields from proton-proton collisions as a function of $\langle N_{\mathrm{part}} \rangle$ at 62.4 and 200 GeV [31]. Enhancement of $\varphi$ production in Cu+Cu and Au+Au relative to p+p collisions clearly indicate the formation of a QGP medium in these collisions.

### 1.6.4 Collective Phenomena: Elliptic Flow

In non-central heavy ion collisions, the overlap region of two colliding nuclei is spatially asymmetric with an almond-like shape as shown in the 1.12. The interactions among constituents of the system generate a pressure gradient, which is larger along the short axis than along the long axis of the almond-shaped collision region. There-
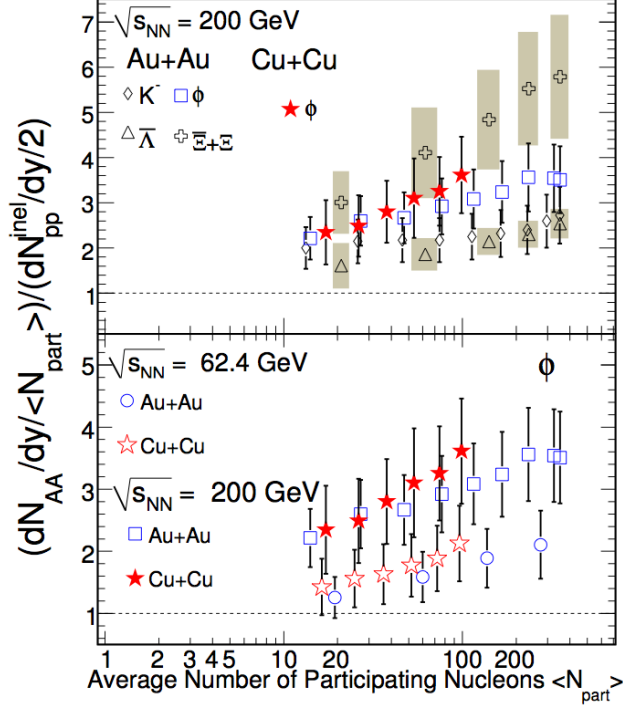
Figure 1.11: The ratio of the yields of $K^-$, $\phi$, $\overline{\Lambda}$, and $\Xi$, $\overline{\Xi}$ normalized to $\langle N_{\text{part}} \rangle$ nucleus-nucleus collisions to corresponding yields in inelastic proton-proton collisions as a function of $\langle N_{\text{part}} \rangle$ at 62.4 and 200 [31].

fore, the initial spatial anisotropy causes the nuclear matter to have a final momentum space anisotropy. Consequently, the azimuthal distribution of produced particles may carry information about the pressure of the nuclear matter produced in the early stage of the heavy ion collisions [32].

The azimuthal anisotropy can be quantified by studying the Fourier expansion of azimuthal angle distribution of produced particles with respect to the reaction plane (the plane spanned by the beam direction and impact parameter vector) [33]:

$$E\frac{d^3N}{dp^3} = \frac{d^2N}{2\pi p_{\mathrm{T}} dp_{\mathrm{T}} dy}\Big(1 + \sum_{n=1}^{\infty} 2v_n \cos[n(\phi - \Psi_{\mathrm{r}})]\Big), \qquad (1.9)$$

where $\phi$ is the azimuthal angle of the particle, $\Psi_{\mathrm{r}}$ is the reaction plane angle and $v_n$ is the $n^{\text{th}}$ harmonic coefficient. The first harmonic coefficient, $v_1$, is called the directed flow and the second harmonic coefficient, $v_2$, is called the elliptic flow. The elliptic
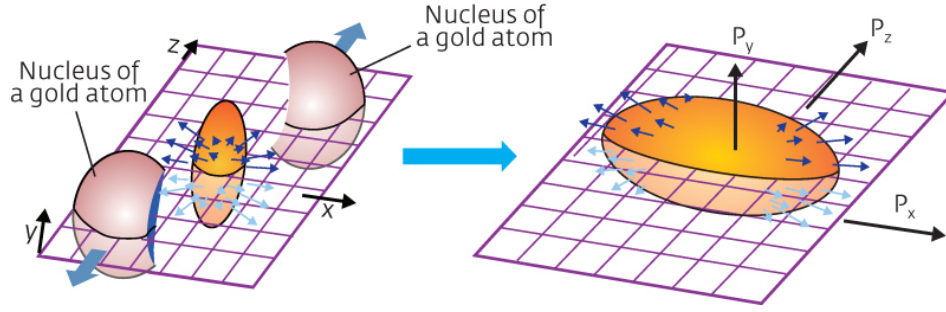
Figure 1.12: Schematic views of a non-central nucleus-nucleus collision.

flow has been measured in heavy ion collisions for a long time and results for identified particles from Au+Au collisions at $\sqrt{s_{NN}} = 200$ GeV measured by RHIC experiments are presented in Fig. 1.13 [34]. At low $p_T$ ($\leq 2$ GeV/c), the differential elliptic flow $v_2(p_T)$ for different hadrons has been observed to scale with particle mass. The
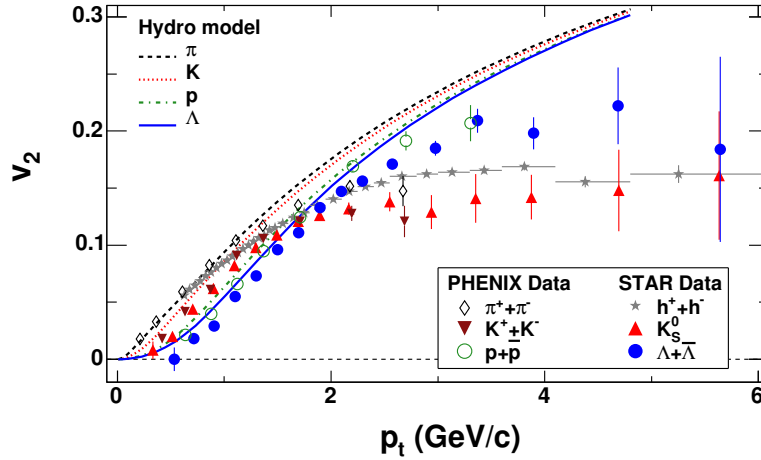


Figure 1.13: Measurements of $v_2(p_T)$ for identified particles for 080% centrality at RHIC. The lines are the results from hydrodynamic model calculation [34].

hadron mass ordering of $v_2$ is seen in the low $p_T$ region, where at a given $p_T$, the higher is the hadron mass the lower is the value of $v_2$. This mass dependence, as well as the absolute magnitude of $v_2$, is well reproduced by the hydrodynamic calculations [35]. The agreement with the hydrodynamic calculation, which assume early thermalization and ideal relativistic fluid expansion, is one of the centerpieces of the discovery of

18
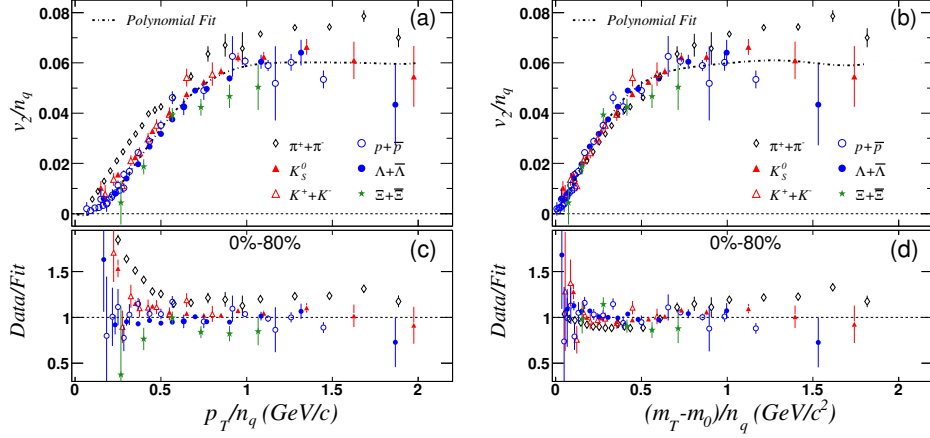
Figure 1.14: The $v_2(p_T)$ scaled by number-of-constituent quarks ($n_q$) as a function of $p_T/n_q$ and $(m_T - m_0)/n_q$ for identified hadrons in Au+Au collisions at $\sqrt{s_{NN}} = 200$ GeV [36].

QGP, as claimed at RHIC. The hydrodynamic calculations over predict the data for $p_T > 2$ GeV/c. If we divide the $v_2$ values with the number of constituent quarks, $n$ (i.e. $n = 2$ for mesons and $n = 3$ for baryons), we observe a scaling of $v_2$ of all hadrons, which is called the Number of Constituent Quark (NCQ) scaling. The upper panel in Fig. 1.14(a) shows the STAR results on $v_2/n$ as a function of $p_T/n$ for identified hadrons in minimum bias Au+Au collisions at $\sqrt{s_{NN}} = 200$ GeV. The dashed-dotted line denotes a polynomial fit to the data. To investigate the quality of agreement between particle species, the data from the left panel are scaled by the fitted polynomial function and plotted in the bottom panel (Fig. 1.14(c)). This shows that in the intermediate $p_T$ range ($0.6 < p_T/n < 2$ GeV/c), the $v_2$ of the identified hadrons (except pion) scales with the number of constituent quarks. The large resonance decay contribution to pion production has been suggested as a possible explanation for the apparent deviation from this scaling [37]. This observation of NCQ scaling, is of particular interest and importance, as it indicates that the system is in a deconfined stage. In a more general sense, it appears that high energy nuclear collisions provide an opportunity to prove that hadron production indeed happens via coalescence of the constituent quarks [38]. The constituent quarks carry their own substantial azimuthal anisotropy which is later summed up to give the hadronic

19

flow. Figure 1.14(b) shows the plotting of $v_2$ as a function of transverse kinetic energy $m_T$-$m_0$ ($= KE_\mathrm{T}$) where $m_T = \sqrt{p_\mathrm{T}^2 + m^2}$. If we scale both $x$ and $y$ observables with the number of constituent quarks $n_q$ then the scaling behavior is reproduced. The re-plotting the data as a function of transverse kinetic energy is done to compensate for the effect of radial flow to some extent [39].

## 1.7 Thesis Motivation

### 1.7.1 Light Nuclei Production

In relativistic heavy-ion collisions, a very high energy and high baryon dense medium is formed in the reaction zone. In heavy-ion collisions light nuclei and anti-nuclei can be produced by the recombination of created nucleons (anti-nucleons) or stopped nucleons [40, 41, 42, 43]. This process is called final-state coalescence. As the binding energy of light nuclei are small ($\sim$2.2 MeV for d ($\overline{d}$) and $\sim$7.7 MeV for $^3$He), they can not survive when the interactions between nucleons and other particles are strong and temperature is high. Therefore, the light nuclei formation can only happen at the later stage of the evolution when the interactions between nucleons and other particles are weak. Hence, the production of nucleus provides a tool to measure baryon distribution at the thermal freeze-out where the interactions between particles are weakening. Since the probability of coalescence of a particular nuclear system ($d$, $\overline{d}$, $^3$He, etc.) depends on the properties of the hadronic system formed at later stage. Therefore, study of light nuclei production will help us to gain knowledge about the evolution and hadronization process as well as understanding of nuclei formation in heavy-ion collision. Together with the measurements of other particle yields, integrated nuclei yields can be used in the statistical model to understand the chemical freeze-out properties of the system. According to the coalescence formalism, the momentum distribution of the light nuclei (anti-nuclei) is related to the nucleon (anti-nucleon)

20

momentum distribution as,

$$E_A \frac{d^3 N_A}{dp_A^3} = B_A (E_p \frac{d^3 N_p}{dp_p^3})^Z (E_n \frac{d^3 N_n}{dp_n^3})^N \qquad (1.10)$$

where $E \frac{d^3 N}{dp^3}$ is the invariant yield of nucleons or nuclei, $A$ is the nuclear number of the produced nucleus and $Z$, $N$ are the numbers of proton and neutron inside the nucleus, respectively. The quantity $B_A$ is called coalescence parameter and its magnitude depends on the correlation volume of the system [44].

At RHIC energy, STAR experiment has measured the $\overline{d}$ and $^3$He spectra at low $p_T$ [45]. The particle identification was done using the ionization energy loss, as measured by the TPC detector (described in details in chapter 3) of STAR.

The STAR experiment has also measured the heaviest anti-particle ever produced in the history of heavy-ion collision. In 2011, the STAR experiment at RHIC measured 18 $^4\overline{He}$ (or anti-$\alpha$) candidates in Au+Au collisions at $\sqrt{s_{NN}} = 200$GeV [46]. The antimatter yield is found to be consistent with expectations from thermodynamic [47] and coalescence nucleosynthesis models [48] providing an indication of the production rate of even heavier antimatter nuclei and a benchmark for possible future observations of in cosmic radiation.

Very recently, the ALICE experiment at the LHC has measured production of $d$ and $\overline{d}$ in Pb+Pb collisions at $\sqrt{s_{NN}} = 2.76$ TeV, in which the observation of 31 anti-tritons is also reported [49]. The spectra is found to exhibit a significant hardening with increasing centrality which is interpreted as caused by an increase of radial flow [49]. PHENIX experiment has measured the $d$ and $\overline{d}$ spectra at intermediate $p_T$ by using the Time-of-Flight (TOF) detector [50]. The light nuclei production has also been measured at lower energy heavy-ion and p+p colliders such as SPS, AGS and Bevelac [51]. Figure 1.15 shows the summary of the coalescence parameter $B_2$ measured in those previous experiments. Clearly, there is no experimental measurements of the coalescence parameter $B_2$ in the STAR beam energy range $\sqrt{s_{NN}} = 7.7$, 11.5, 19.6, 27, 39 GeV. Therefore, it will be interesting to see the behavior of $B_2$ in
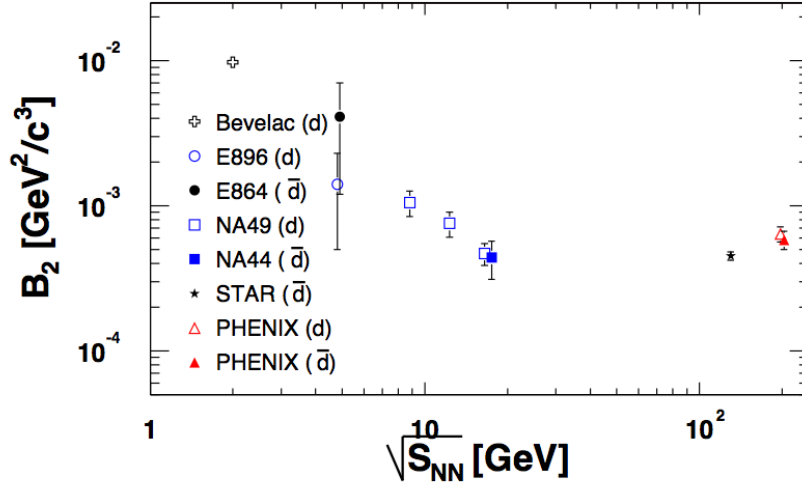
Figure 1.15: Comparison of the coalescence parameter for deuterons and anti-deuterons with other experiments at different values of $\sqrt{s_{\mathrm{NN}}}$. See text for details.

the aforesaid beam energy range. In this thesis, we have extended the study of light nuclei production for STAR beam energies $\sqrt{s_{\mathrm{NN}}} = 39, 27, 19.6, 11.5$ and $7.7$ GeV. The results in this thesis, combined with the previous experimental results, will be discussed in chapter 3.

## 1.7.2   Elliptic Flow of Light Nuclei

Hadrons at intermediate $p_{\mathrm{T}}$ mainly come from the coalescence of quarks. It directly results in the NCQ scaling of the baryon and meson elliptic flow ($v_2$) [36], which is shown in Fig. 1.14. The light nuclei are mostly formed by the final-state coalescence, which happens at the moment of thermal freeze-out. Therefore, like the NCQ scaling of the hadrons, one would predict the light nuclei $v_2$ follow the atomic mass number ($A$) scaling. In this case, both the nuclei and their constituent nucleons are directly observable in experiments. So, it is important to study the elliptic flow of light nuclei and compare the same with their constituents. Thus, the light nuclei $v_2$ study, will provide valuable information for studying the freeze-out dynamics and coalescence mechanism. Earlier measurements of $v_2$ of light nuclei were carried out at the top

RHIC energy ($\sqrt{s_{NN}} = 200$ GeV) by the PHENIX [52] and the STAR [53, 54] experiment. The PHENIX collaboration has measured the $v_2$ of $d$ and $\bar{d}$ in the intermediate transverse momentum ($1.1 < p_T < 4.5$ GeV/$c$). The scaling behavior of these light nuclei $v_2$ with that of proton (anti-proton) were also reported [52]. The STAR collaboration has measured the $v_2$ of $d, \bar{d}$, $^3He$, $^3\overline{He}$ in Au+Au collisions at $\sqrt{s_{NN}} = 200$ GeV using the data taken in the year 2004 [53] and 2007 [54]. Negative $v_2$ of $\bar{d}$ at low transverse momentum was reported [53]. In this thesis work, we have expanded previous studies with a detailed investigation on the energy and centrality dependence of $v_2$ of light nuclei, with more statistics. During the BES program, the STAR detector has recorded data in Au+Au collisions in a wide range of beam energy starting from top RHIC energy of $\sqrt{s_{NN}} = 200$ GeV down to 7.7 GeV. The measurement of elliptic flow $v_2$ of light nuclei at mid-rapidity ($|y| < 1.0$) for Au+Au collisions at $\sqrt{s_{NN}} = 200, 62, 39, 27, 19.6, 11.5$ and 7.7 GeV are discussed in chapter 4. Light nuclei $v_2$ has also been studied using coalescence + transport model and presented in chapter 4.

In addition, study of azimuthal anisotropy of charged particles and their correlation with initial eccentricity has also been presented in this thesis using a transport and a hydrodynamic model. These studies provide a better understanding about generation of second order ($v_2$) and other higher order ($v_n$, $n = 3, 4, 5$) flow coefficients. The results of these model studies are discussed in detail in chapters 5 and 6.

# Bibliography

[1] S. L. Glashow, Nucl. Phys. 22, 579 (1961); A. Salam and J. C. Ward, Phys. Lett. 13, 168 (1964); S. Weinberg, Phys. Rev. Lett. 19, 1264 (1967).

[2] Introduction to elementary particles - by David Griffiths.

[3] P. W. Higgs, Phys. Lett. 12, 132 (1964); P. W. Higgs, Phys. Rev. Lett. 13, 508 (1964); F. Englert and R. Brout, Phys. Rev. Lett. 13, 321 (1964).

[4] D. Gross and F. Wilczek, Phys. Rev. Lett. 30, 1343 (1973); Phys. Rev D 8, 3633 (1973).

[5] H. D. Politzer, Phys. Rev. Lett. 30, 1346 (1973).

[6] G. Aad *et al.* (ATLAS Collaboration), Phys. Lett B 716, 1 (2012); W. Adam *et al.* (CMS Collaboration), Phys. Lett B 716, 30 (2012).

[7] H. Kastrup, P. Zerwas, eds., QCD 20 yrs later World Scientific, Singapore (1993). D. J. Gross and F. Wilczek, Phys. Rev. Lett. 30, 1343 (1973); H. Politzer, Phys. Rev. Lett. 30, 1346 (1973).

[8] S. Bethke, Prog. Part. Nucl. Phys. 58, 351 (2007).

[9] G. Baym, Nucl. Phys. A 698, XXIII (2002).

[10] F. Karsch and K. Redlich, Phys. Rev. D 84, 051504(R) (2011)

[11] F. Karsch, Nucl. Phys. A 698, 199 (2002).

[12] B. Mohanty, New Journal of Physics 13, 065031 (2011).

[13] R. V. Gavai and S. Gupta Phys. Rev. D 71, 114014 (2005).

[14] F. R. Brown *et al.*, Phys. Rev. Lett. 65, 2491 (1990).

[15] Y. Hatta and T. Ikeda, Phys. Rev. D 67, 014028 (2003) and references therein.

[16] Z. Fodor, Nucl. Phys. A 715, 319 (2003).

[17] J. W. Harris and B. Muller, Ann. Rev. Nucl. Part. Sci. 46, 71 (1996).

[18] S. A. Bass *et al.*, J. Phys. G 25 R1 (1999).

[19] J. Adams *et al.* (STAR Collaboration), Nucl. Phys. A 757,102 (2005).

[20] J. D. Bjorken. Energy loss of energetic partons in quark-gluon plasma: Possible extinction of high momentum jets in hadron - hadron collisions. FERMILAB-PUB-82-059-THY.

[21] M. Gyulassy and M. Plumer, Phys. Lett. B 243, 432 (1990); R. Baier *et al.*, Nucl. Phys. B 483, 291 (1997).

[22] D. Molnar and S. A. Voloshin, Phys. Rev. Lett. 91, 092301 (2003).

[23] R. J. Fries *et al.*, Phys. Rev. Lett. 90, 202303 (2003).

[24] P. Koch *et al.* Phys. Rep. 142, 167 (1986).

[25] T. Alber *et al.* (NA49 Collaboration), Z. Phys. C 64, 195 (1994).

[26] P. G. Jones (for the NA49 Collaboration), Nucl. Phys. A 610, 188c (1996).

[27] F. Sikler (for the NA49 Collaboration), Nucl. Phys. A 611, 45c (1996).

[28] C. Hohne (for the NA49 Collaboration), Nucl. Phys. A 611, 485c (1996).

[29] J. Rafelski and B. Muller, Phys. Rev. Lett. 48, 1066 (1982).

[30] K. Redlich and A. Tounsi, Eur. Phys. J. C 24, 589 (2002).

[31] B. I. Abelev *et al.* (STAR Collaboration), Physics Letters B 673, 183 (2009).

[32] J.-Y. Ollitrault, Phys. Rev. D 46, 229 (1992).

[33] S. Voloshin and Y. Zhang, Z. Phys. C 70, 665 (1996).

[34] J. Adams *et al.* (STAR Collaboration), Phys. Rev. C 72, 014904 (2005).

[35] P. Huovinen *et al.*, Phys. Lett. B 503, 58 (2001).

[36] B. I. Abelev *et al.* (STAR Collaboration), Phys. Rev. C 75, 054906 (2007).

[37] X. Dong *et al.*, Phys. Lett. B 597, 328 (2004).

[38] D. Molnar and S. A. Voloshin, Phys. Rev. Lett. 91, 092301 (2003); S. A. Voloshin, Nucl. Phys. A 715, 379 (2003).

[39] S. A. Voloshin, A. M. Poskanzer, and R. Snellings, arXiv:nucl-ex/0809.2949 (2008).

[40] J. L. Nagle *et al.*, Phys. Rev. C 53, 367 (1996).

[41] R. Scheibl, U. Heinz, Phys. Rev. C 59, 1585 (1999).

[42] W. J. Llope *et al.*, Phys. Rev. C 52, 2004 (1995).

[43] R. Bond *et al.*, Phys. Lett. B 71, 43 (1977); A. Baltz *et al.*, Phys. Lett. B 325, 7 (1994); R. Mattiello *et al.*, Phys. Rev. C 55, 1443 (1997); P. Braun-Munzinger *et al.*, Phys. Lett. B 334, 43 (1995); A. Z. Mekjian, Phys. Rev. C 17, 1051 (1978); H. Sato and K. Yazaki, Phys. Lett. B 98, 153 (1981); J. I. Kapusta, Phys. Rev. C 21, 1301 (1980).

[44] R. Bond, P. J. Johnansen, S. E. Koonin, and S. Garpman, Phys. Lett. **71B**, 43 (1977).

[45] C. Adler *et al.*, Phys. Rev. Lett. 87, 262301 (2001).

[46] H. Agakishiev *et al.*, Nature 473, 353356 (2011)

[47] P. Braun-Munzinger and J. Stachel, Nature 448, 302309 (2007).

[48] H. Sato and K. Yazaki, Phys. Lett. B 98, 153157 (1981).

[49] ALICE Collaboration, arXiv:1506.08951 [nucl-ex] (2015).

[50] .S. S. Adler *et al.*, Phys. Rev. Lett. 94, 122302 (2005).

[51] S. Wang *et al.*, Phys. Rev. Lett. 74, 2646 (1995); S. Albergo *et al.*, Phys. Rev. C 65, 034907 (2002); T.A. Armstrong *et al.*, Phys. Rev. Lett. 85, 2685 (2000); T. Anticic *et al.*, Phys. Rev. C 69, 024902 (2004); I.G. Bearden *et al.*, Phys. Rev. Lett. 85, 2681 (2000).

[52] S. Afanasiev *et al.*, Phys. Rev. Lett. **99**, 052301 (2007).

[53] B. I. Abelev *et al.*, arXiv:0909.0566v1 [nucl-ex].

[54] C. Jena *et al.*, arXiv:1101.4196 [nucl-ex].

# Chapter 2

# Experimental Setup at RHIC

This chapter briefly describes the accelerator and the detector systems used for this analysis. The focus is mainly on the detectors which were primarily used to record the data whose analysis and the physics results are presented in this thesis.

## 2.1  Introduction

The Bevatron-Bevalac at Lawrence Berkley National Laboratory (LBNL) was the first facility to exploit relativistic nucleus-nucleus collisions at fixed target energies. The first beams of carbon and oxygen nuclei were accelerated up to 2 GeV per projectile nucleon [2]. The theoretical work on QCD with the goal of locating and characterizing the hadron-parton de-confinement phase transformation led to experiments with higher energy beams of heavier nuclei directed at fixed targets. The AGS at BNL provided oxygen, silicon, and gold ion beams at collision energies per nucleon pair, $\sqrt{s_{\mathrm{NN}}} = 4.86$ GeV, and the SPS at CERN accelerated oxygen, sulphur, lead, and indium ion beams up to $\sqrt{s_{\mathrm{NN}}} = 17.3$ GeV. At AGS energies, the phenomenon of nuclear stopping created a baryon rich collision region [3]. In the year 2000, RHIC at BNL became the first machine in the world, capable of colliding heavy ions at relativistic energies. It is a flexible accelerator and provides data on collisions of different

species of nuclei such as deuteron, copper, gold, uranium at center-of-mass energies from $\sqrt{s_{\mathrm{NN}}} = 7.7$ up to 200 GeV. The highest energy reached at RHIC is about 10 times more than that was achieved at previous fixed target experiments. It can also accelerate polarized protons up to $\sqrt{s} = 500$ GeV [4, 5].
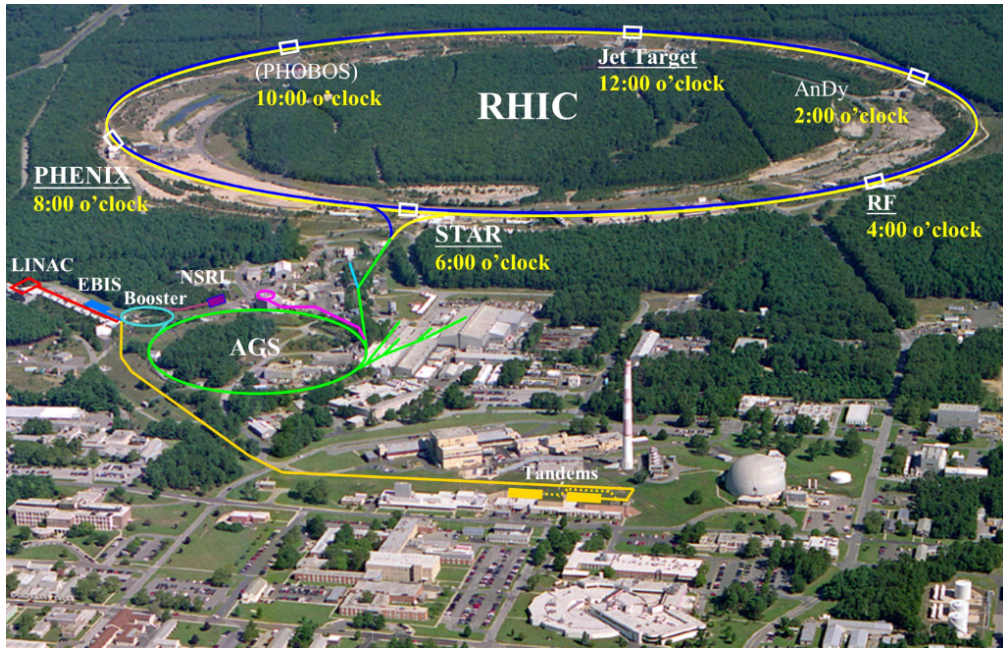


Figure 2.1: Overview of the RHIC accelerator complex at Brookhaven National Laboratory, Upton, New York [1].

A layout of RHIC is shown in Fig. 2.1. A brief description how the accelerator operates is described as follows [6]. For heavy-ion collision, at first negatively charged ions are used as source in the Tandem Van de Graaff accelerator [7]. Then the negative ions are passed through carbon stripping foil (areal density of 2 $\mu$g/cm$^2$) which partially strips electrons from the ions. After that the ions are accelerated to an energy of 1 MeV per nucleon, and then travel towards the Booster. For collision of proton beams at RHIC, the energetic protons are supplied by the 200 MeV Linac. Protons from the Linac are then transfered to the booster synchrotron. The booster is a powerful circular accelerator that provides the ions more energy by having them surf ride on the downhill slope of radio frequency electromagnetic waves. To confine

the charged beam a series of bending magnets around the ring is used. An electric field is used to accelerate particles. Inside the booster, the ions are put into six bunches, accelerated to about 37% of the speed of light and put through another electron stripper. So, for Au+Au collisions, the booster synchrotron accelerates the ions to 95 MeV per nucleon and the ions are stripped again to reach a charge state of $Au^{77+}$ at the moment of exit from the booster. The $Au^{77+}$ ions from the booster are transferred by the Booster-to-AGS line into a larger synchrotron, with four-time the radius of the booster, called the Alternating Gradient Synchrotron (AGS). To fill one AGS cycle of 24 ion bunches, it takes 4 batches of ions from the booster. Inside the AGS, the $Au^{77+}$ ions are de-bunched and re-bunched into four final bunches and further accelerated to 99.7% of the speed of light. The $Au^{77+}$ ions are here accelerated to 10.8 GeV per nucleon. After passing through a final stripping foil, the ions are fully stripped off electrons and reach a charge state of $Au^{79+}$ at the exit of the AGS. The $Au^{79+}$ ion bunches are then injected into the RHIC collider via AGS-to-RHIC transfer line. A switching magnet sends the ion bunches down one of two beam lines of RHIC. Bunches are directed either left to travel clockwise in the RHIC ring or right to travel anticlockwise in the second RHIC ring. The RHIC is an intersecting storage ring particle accelerator. It consists of two quasi circular, underground counter-rotating rings of circumference 3.8 Km, named Blue Ring, where the beam moves in a clockwise direction and Yellow Ring, where the beam moves in an anticlockwise direction. These independent rings have their sets of superconducting magnets which bend and focus the ions [8] as well as radio frequency acceleration cavities. This allows independent tuning of the magnetic fields in each ring which is required to achieve equal rotation frequencies of the different particle/ion species in each ring. The ion beams are accelerated to the desired collision energy inside the RHIC rings and stored for data taking. When the luminosity drops below a certain level, the beams are removed from the rings (dumped). Then the cycle restarts inside the Tandem for ions (or in LINAC for proton).

RHIC now provides beams of very high luminosities as shown in Fig. 2.2, which
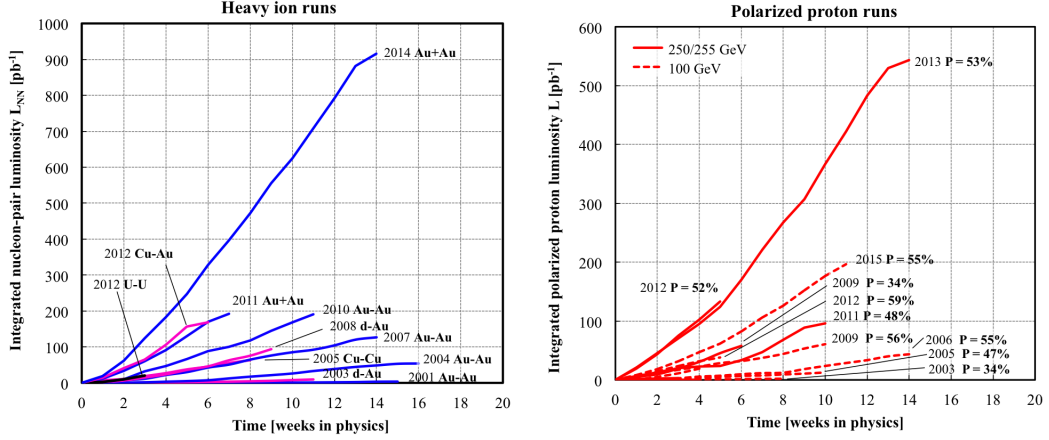
Figure 2.2: The nucleon-pair luminosity of the RHIC collider for different year and collision system [10].

makes possible to measure rare processes having small cross sections. The interaction rate $(R)$ between two colliding beams depend on Luminosity $(L)$ and cross section $(\sigma)$, which is given by $R = L \times \sigma$. In experiment, luminosity can be controlled and optimised. If Blue beam has $N_B$ particles per bunch, Yellow beam has $N_Y$ particles per bunch, each beam with $n$ bunches per revolution, circling in the machine at revolution frequency $f$, then the luminosity is given by [9],

$$ L = fn\frac{N_B N_Y}{A} \tag{2.1} $$

where, $A$ is cross-sectional area of the overlap between the two colliding beams of particles. To date, different particle combinations explored at RHIC are p+p, d+Au, $^3$He+Au, Cu+Cu, Cu+Au, Au+Au, and U+U. During the start of RHIC, an average luminosity of $2 \times 10^{26}$ cm$^{-2}$s$^{-1}$ was targeted which has been increased and the current average Au+Au luminosity of the collider is $50 \times 10^{26}$ cm$^{-2}$s$^{-1}$ which is 25 times higher than the designed value. The heavy-ion luminosity is substantially increased through stochastic cooling. A list of luminosities for different year and colliding ions can be found in [10]. In the next major upgrades with the eRHIC [11], new and exciting physics possibilities are planned to start in the year 2020. The

31

RHIC rings have six interaction points, and four of these interaction points have been occupied by heavy ion experiments: BRAHMS [33], located at 2 o′clock position, STAR [34] located at 6 o′clock position, PHENIX [35] located at 8 o′clock position and PHOBOS [36] located at 10 o′clock position. Currently only STAR and PHENIX detectors are in an operational mode.
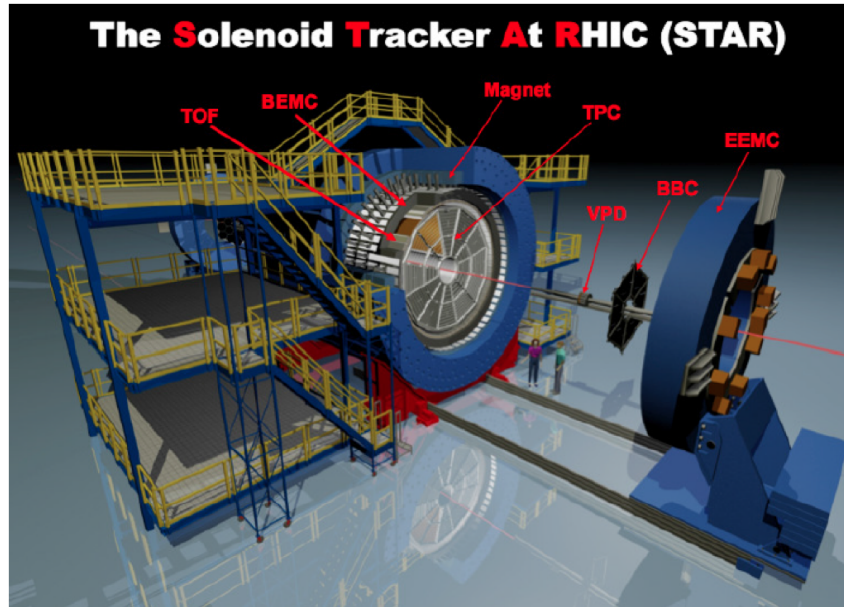


Figure 2.3: Three dimensional view of STAR detector system. Figure is taken from [38].

## 2.2 The STAR (Solenoid Tracker At RHIC)

All the results presented in this thesis are based on data collected using the STAR detector. STAR consist of a several detector subsystems, as shown in Fig. 2.3 and Fig. 2.4. In the STAR coordinate system [12], $z$-axis is along the beam direction, whereas $x$ points parallel to the ground and $y$ axis points normal to the ground. The magnetic field of the STAR magnet is applied in the $z$ direction, which bends the trajectories of charged particles allowing measurement of the corresponding momentum. The STAR magnet can be maintained at magnetic fields of $\pm 0.25$ or $\pm 0.5$ Tesla. The data which are presented in this thesis were recorded with $\pm 0.5$ Tesla

magnetic field. The STAR experiment consists of different types of detectors, each specializing in detecting certain types of particles or characterizing their motion. The Time Projection Chamber (TPC) [13] is the heart of the STAR detector, which is used for the charged particle tracking and particle identification within $|\eta| < 1.8$, with full azimuthal coverage in the $xy$ plane. In 2010, a barrel Time-of-Flight (TOF) detector based on Multi-gap Resistive Plate Chamber (MRPC) technique was fully installed in STAR [14] . The TOF consists of a total of 120 trays covering a pseudo-rapidity range of $|\eta| < 0.9$ and full azimuth. A Barrel Electromagnetic Calorimeters (BEMC) [18] and an Endcap Electromagnetic calorimeter (EEMC) [18] are used to measure the transverse energy deposited by electrons and photons. The full Barrel Electromagnetic Calorimeter (BEMC) covers $|\eta| < 1.0$ and Endcap Electromagnetic Calorimeter
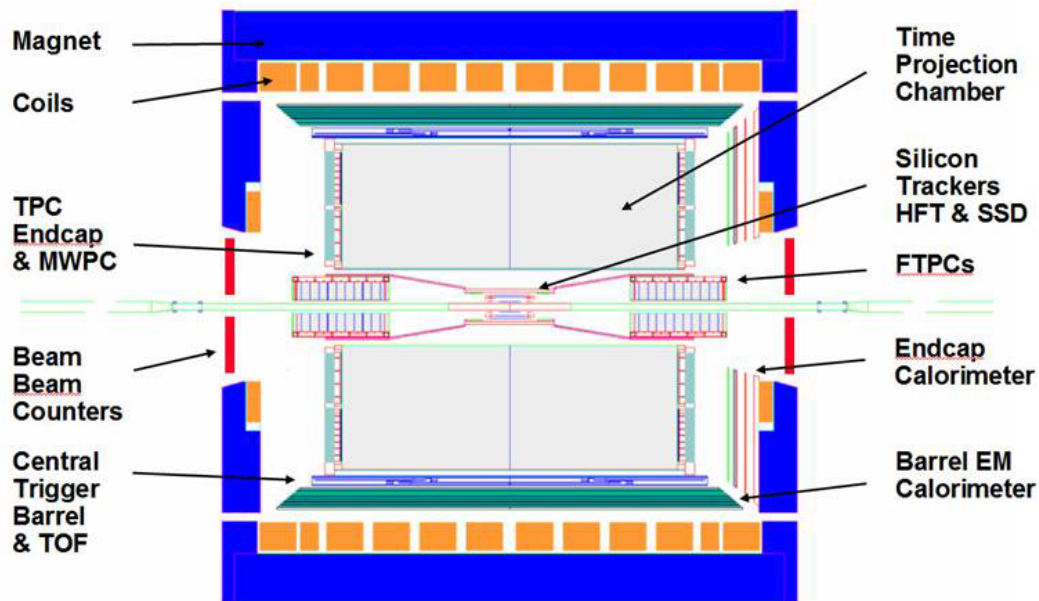


Figure 2.4: A cut-away side view of the STAR detector [23].

(EEMC) covers $1 < \eta < 2$. Both BEMC and EEMC are azimuthally symmetric. There are two Forward Time Projection Chamber detectors (FTPCs) [20] with $2.5 < \eta < 4.0$ and complete azimuthal coverage in the $xy$ plane. The FTPCs extend STAR's

tracking capabilities in the forward and backward $\eta$ direction. Two Zero Degree Calorimeters (ZDCs) [15], two Beam Beam Counters (BBCs) [16] and two upgraded Pseudo Vertex Position Detectors (VPDs) [17] are used for event triggering [21]. Photon Multiplicity Detector (PMD) [22] is used to measure photon multiplicity at forward rapidity. The PMD covers a pseudo-rapidity range -3.7 < $\eta$ < -2.3 and full azimuth in the $xy$-plane.

Since the TPC, TOF and Trigger detectors are the main detectors used in this analysis, therefore these detector systems are discussed in detail in the following sub-sections.

## 2.2.1  The Time Projection Chamber (TPC)

In STAR experiment, the TPC [13] is the primary tracking device. It covers a pseudo-rapidity region $|\eta| < 1.8$ and full azimuth ($0 < \phi < 2\pi$). Using the TPC, charged particles momenta can be measured from 100 MeV/c to 30 GeV/c. The TPC can also identify charged particle over a momentum range from 100 MeV/c to greater than 1.0 GeV/c.

### 2.2.1.1  The Technical Design of TPC

The TPC is a 4.2 m long cylinder having external diameter of 4 m. The whole detector is enclosed in a solenoidal magnet that provides a uniform magnetic field of maximum 0.5 Tesla parallel to the beam direction ($z$-axis). Due to this applied magnetic field, the tracks of the charged particles coming from a collision point bends while passing though the detector volume. The track curvature is used to determine momenta and the charge of the particle. Figure 2.5 shows the three dimensional schematic diagram of the TPC in the STAR experiment. The TPC consists of one outer field cage (OFC), one inner field cage (IFC) and two end caps. The OFC and IFC are used to provide a nearly perfect electric field in which the electrons drift to the anode plane. It avoids the distortions of the recorded tracks and also designed in such a way to

contain the TPC gas and prevent it from being contaminated with outside air. The end caps providing the readout system are at ground potential and act as anodes. A thin conductive central membrane (CM) made of 70 $\mu$m thick carbon coated kapton is located in the $xy$ plane, which bisects the cylinder in the middle, forming an east
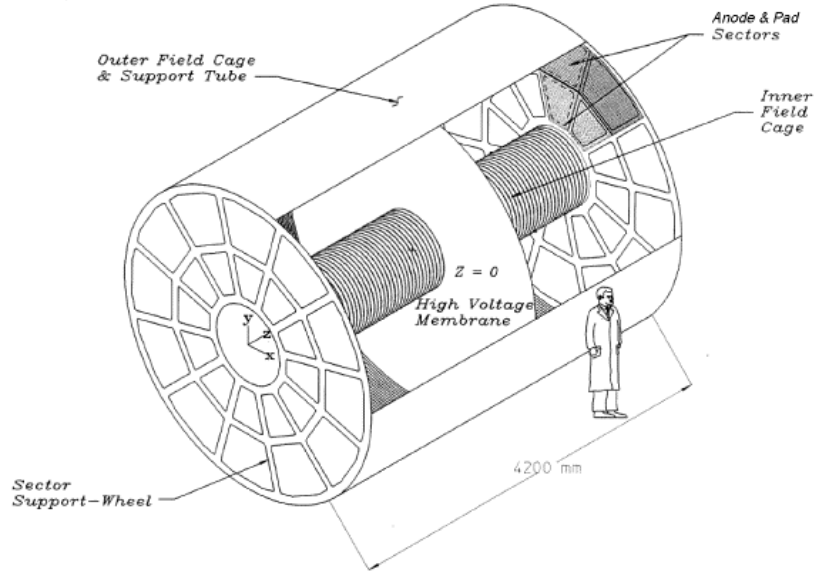


Figure 2.5: The three dimensional schematic diagram of the STAR TPC [13].

and west end of the TPC as shown in the Fig. 2.5. The CM is maintained at a voltage of -28 kV with respect to the detection planes and acts as cathode. A uniform electric field of ~135 V/cm, pointing $\pm z$ directions is maintained between the CM, concentric field-cage rings, and the readout end caps. A chain of 183 resistors and equipotential rings along the concentric field cage cylinders help to maintain this uniformity of the electric field which is critical for uniform electron drift [13]. An outer support hoop mounted on the outer field cage keeps the CM taut and secured under tension. There are 36 Aluminium stripes which act as targets emitting electrons for the TPC Laser Calibration System and attached on each side of the CM. TPC is filled with P10 gas, a mixture of Argon and Methane (90% Ar + 10% $CH_4$) and regulated at a pressure of 2 mbar above the atmospheric pressure. The P10 gas is chosen due to

its fast drift velocity which peaks at a low electric field. Operating on the peak of the velocity curve makes the drift velocity stable and insensitive to small variations in temperature and pressure. The design of the detector becomes simpler because of lower field strengths which require lower voltages. The drift velocity of electron through P10 gas is relatively fast, $\sim$5.5 cm/$\mu$s at 130 V/cm drift field [13]. The
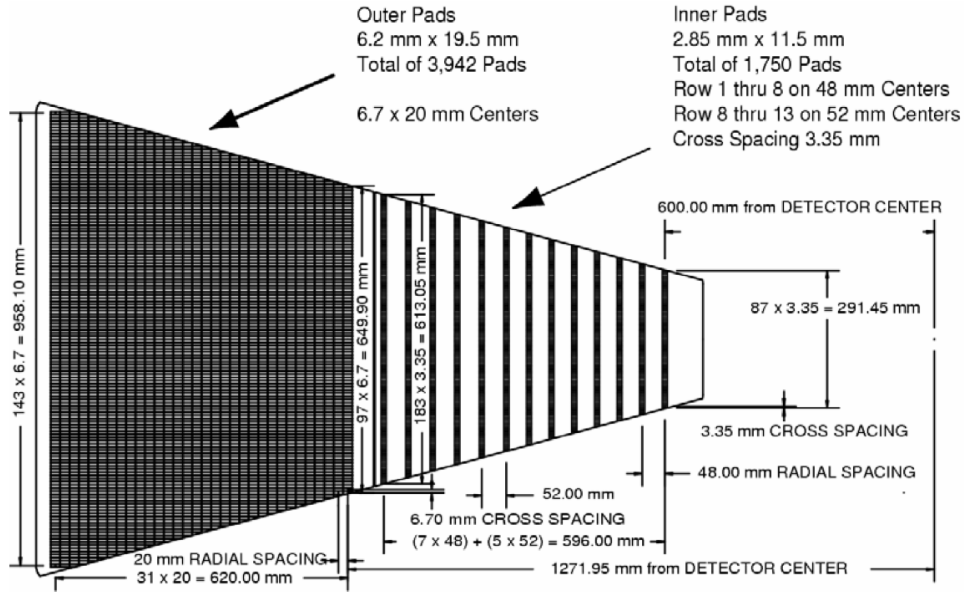


Figure 2.6: One sector of the TPC anode plane with the inner and outer subsectors and their respective padrows [13].

TPC readout system is based on the Multi-Wire Proportional Chamber (MWPC) [13]. The MWPC, located at the readout endcaps, consists of the pad plane and three wire planes. The complete readout system is divided into 24 sectors, having 12 readout sectors for each endcap. Each sector is further divided into inner and outer subsectors characterized by a change in the readout padrow geometry. Each inner sector contains a large number of small pads, distributed in 13 pad rows, to maximize the position and two-track resolution in a region with high particle density. The pads of the outer sectors are densely packed in 32 rows per sector to optimize the measure of energy loss by the ionisation in a region with lower particle densities [13]. Therefore, a track in the TPC can have a maximum of 45 hits if it crosses all 45 pad rows. Figure 2.6

36

represents one full sector of the anode pad plane.

### 2.2.1.2 Track Reconstruction Inside TPC

The TPC track can be reconstructed by identifying the three dimensional space coordinate points $(x, y, z)$. When a charged particle traverses through the TPC volume, it ionizes the gas atoms and molecules along its path leaving behind trail of ionized atoms and electrons. This electron then moves towards the anodes due the strong electric field in between CM and anode plane. The axial magnetic field of the STAR Magnet constrains the electron to move in a straight path towards the anode. When the electrons reach the anode plane, the signal in adjacent pads (along a single pad row) provides the information of $xy$ position. The z-position of the cluster is determined by multiplying the drift time, measured from the point of origin of the cluster to the anode, by the average drift velocity. After finding the positions of the clusters, a Time Projection Chamber Tracker (TPT) algorithm is used to reconstruct the tracks by a helical trajectory fit. Each track is a helix to first order, but there can be deviations from the helical shape due to energy loss in the gas and multiple Coulomb scattering. To find a global track, the resulting track information collected from the TPC together with additional tracking information from other inner detectors are then refit by application of the Kalman Fit Method [27]. Extrapolating the trajectories of the reconstructed global tracks back to the origin, the $z$-position of the primary collision vertex is determined. If a global track has a distance of closest approach (DCA) (with respect to the primary vertex) less than 3 cm, then the track is refitted to include the primary vertex as an additional space point and those tracks are called primary tracks. The reconstruction efficiency for primary tracks depends on the track quality cuts, particle type, and track multiplicity.

### 2.2.1.3 Particle identification by TPC

Charged particles can be identified using TPC through their energy loss (dE/dx) due to interactions in the gas atoms inside the TPC. If a particle travels through the

entire volume of the TPC, it will provide a maximum of 45 dE/dx points on the 45 pad rows. However, due to the large ionisation fluctuations and the short length over which the particle energy loss is measured, we use the most probable dE/dx instead of the average dE/dx. This is done by calculating the truncated mean of the 70% of the clusters and removing the remaining 30% of the largest ionisation clusters. The ionisation energy loss can be described by the Bichsel functions [28], which is an improved version of the Bethe-Bloch formula [29]. The Bethe-Bloch equation shows that dE/dx is mass dependent and hence useful in particle identification.
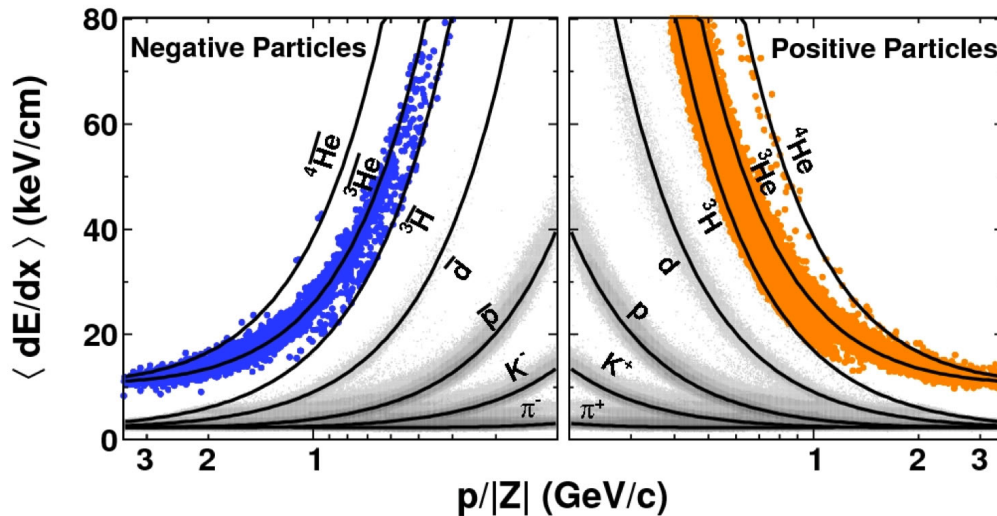


Figure 2.7: The energy loss as a function of momentum/charge for charged particles in the STAR TPC [39].

The energy loss for measured by the TPC as a function of particle rigidity (momentum/charge) is shown in Fig. 2.7. The lines represent the theoretical predictions from Bichsel functions for different particle species and the dots represent the measured values of dE/dx in the experiment. The TPC dE/dx resolution of around $6-9\%$ for Au+Au collisions allows identification of charged pions and kaons up to a transverse momentum of about 0.75 GeV/c. Protons, anti-protons, deuterons and anti-deuterons can be identified up to about 1.1 GeV/c using the TPC detector. However, the separation of dE/dx of particles at relativistic rising region also allows to identify particles

38

at high momentum (p > 3 GeV/c) statistically [24].

Quantitatively, the particle identification can be described by the variable namely $n\sigma$ define by,

$$n\sigma_i = \frac{1}{R} \log \left( \frac{\langle dE/dx \rangle_{\text{Expt.}}}{\langle dE/dx \rangle_{\text{Theory}}} \right), \tag{2.2}$$

where $i$ is the particle type (e.g., $\pi$, $K$, $p$), $\langle dE/dx \rangle_{\text{Expt.}}$ is the measured energy loss of a charged particle track, $\langle dE/dx \rangle_{\text{Theory}}$ is the expected mean energy loss of particle calculated using Bichsel functions [28]. $R$ is the dE/dx resolution of the TPC detector which is found to range between 6−9%. Therefore, $n\sigma_i$ corresponds to the standard deviation of a Gaussian between the measured track and its expected value.

There is another method to identify charged particle by defining a variable $Z$ such that,

$$Z = \ln \left( \frac{\langle dE/dx \rangle_{\text{Expt.}}}{\langle dE/dx \rangle_{\text{Theory}}} \right). \tag{2.3}$$

This $Z$ variable has been used in this analysis to identify light nuclei. Details of light nuclei identification technique using $Z$ variable is explained in detailed in chapter 3 and 4.

## 2.2.2 Time of Flight (TOF) Detector

The main goal of the STAR Time-of-Flight (TOF) [14] system is to extend particle identification capabilities of the experiment, mainly at high $p_{\text{T}}$ (>1.0 GeV/c) . It consists of a highly segmented cylindrical detector immediately surrounding the TPC and arranged in 120 trays covering pseudorapidity range of $|\eta| < 0.9$ and full azimuth. Each individual tray is 2.4 m long, 21.3 cm wide and 8.5 cm deep. Each tray covers 6 degree in azimuthal direction around the TPC. There are 32 Multigap Resistive Plate Chamber (MRPC) [25] modules in each tray, placed along beam ($z$) direction. The MRPC is basically a stack of resistive plates arranged in parallel. The intermediate plates create a series of gas gaps. Electrodes are applied to the outer surfaces of the
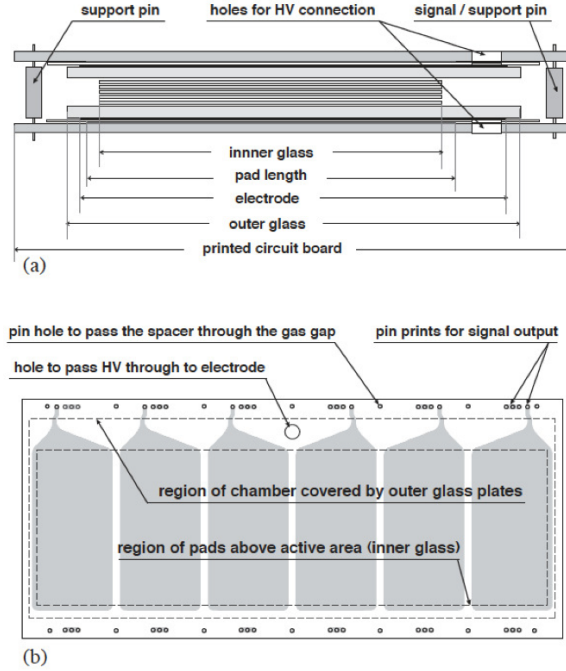
Figure 2.8: (a) Cross section of the MRPC module for TOF. (b) Top view of the printed circuit board (PCB) with a 1 × 6 readout pads array. The projection of the glass layers on the readout pads is also shown [14] .

two outer plates. A strong electric field is generated in each subgap by applying a high voltage across these external electrode. A charged particle going through the chamber generates avalanches in the gas gaps. Since plates are resistive they are transparent to signal induced by avalanches, thus a signal induced in the pickup pad is the sum of signals from all the gas gaps. A cross-section view of the MRPC module is shown in Fig. 2.8(a). The dimensions of the current modules are 94 mm × 212 mm × 12 mm and the active area is 61 mm × 200 mm. The electrodes are made of graphite tape with a surface resistivity of 400 kΩ/square which covers the entire active area. The outer and inner glass plates are 1.8 and 0.55 mm thick, respectively. They are kept parallel by using 220 $\mu$m diameter nylon fishing-line. The signal is read out with a 1 × 6 array of copper pickup pads, each pad with an area of 63 mm × 31.5 mm, and the distance between pads is 3 mm. The pickup pad layers are separated from the outer electrodes by 0.35 mm of Mylar. Figure 2.8(b) shows the readout pad
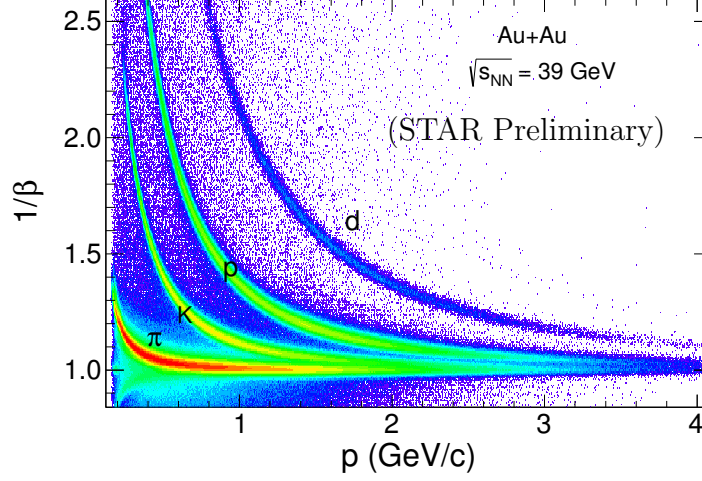
Figure 2.9: $1/\beta$ as a function of momentum in Au+Au collisions at $\sqrt{s_{\text{NN}}} = 39$ GeV.

array. TOF system consists of TOF trays and Vertex Position Detectors (VPDs) [17]. The TOF trays provide the stop time of each track. The VPD provides the common start time of the event. The difference of these two is the time of flight ($\tau$) of the associated track. Time resolution of TOF is ~80 to 100 ps. Now measuring this time $\tau$ in TOF and corresponding path length $L$ travelled by the track, we can calculate the velocity of that particle as, $\beta$ ($=Lc/\tau$), where $c$ is velocity of light. Figure 2.9 shows the $1/\beta$ as function of particle momentum for few selected particles. Using information from TOF we can separate midrapidity $\pi$, $K$ up to $p_{\text{T}}$ ~1.6 GeV/c, midrapidity $K$, $p$ up to $p_{\text{T}}$ ~3.0 GeV/c and midrapidity $d$, $p$ up to $p_{\text{T}}$ ~4.0 GeV/c, respectively. Using the velocity $\beta$ from TOF and momentum $p$ from TPC we can calculate the mass of each individual charged track using the relativistic formula,

$$ m \;=\; p/(\beta\gamma c), \tag{2.4} $$

where, $\gamma = 1/\sqrt{1 - \beta^2}$. The details about light nuclei identification using TOF is discussed in the later chapter in the thesis.

## 2.2.3 Trigger Detectors

The STAR is designed to detect charged and neutral particles produced at RHIC. The trigger system looks at every RHIC crossing and decide whether or not to accept that event and initiate recording the data. The STAR data acquisition system (DAQ) [30] is fast, flexible, and receives data from multiple detectors which have a wide range of readout rates. The interaction rates at RHIC for the beams of highest luminosity can approach ∼10 MHz. The major part of the STAR data is provided by the slow detectors such as TPC, FTPC, and EMC (Electro Magnetic Calorimeters), which can operate at rates of ∼100 Hz and not all events can be recorded by the DAQ.
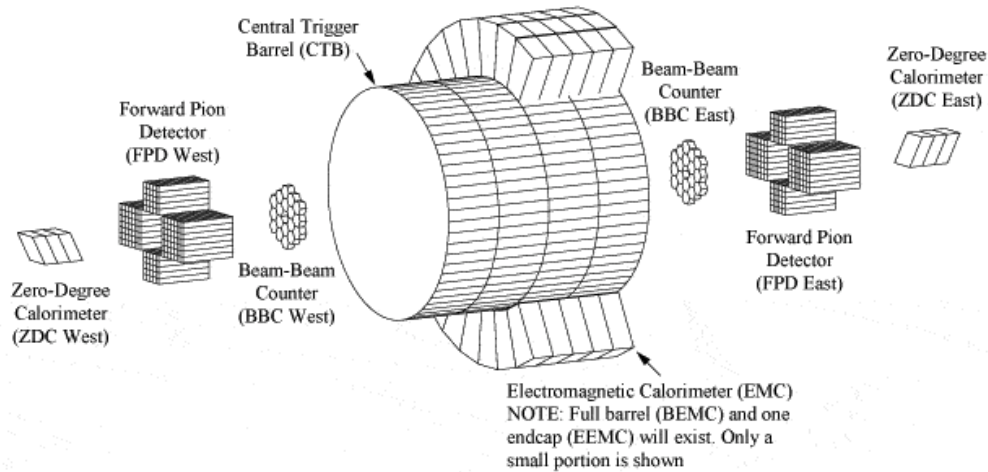


Figure 2.10: The schematic diagram of all the trigger detectors fit together in the STAR system [21]. Now Central Trigger Barrel (CTB) is replaced by the barrel TOF system and Forward Pion Detector (FPD) is preceded by Forward Meson Spectrometer (FMS) at STAR.

Therefore, the STAR trigger system [31] is based on input from fast detectors to control the selection of events for the much slower tracking detectors in order to record data. In addition, the trigger is used to select events with rare or specific signals of interest to increase the recorded statistics of these events. The main trigger detectors are the Zero Degree Calorimeters (ZDCs) [15], Beam Beam Counters (BBCs) [16], the

Vertex Position Detectors (VPDs) [17], and the Electromagnetic Calorimeter (EMC). A schematic diagram of a STAR trigger system are shown in Fig. 2.10 [21]. The ZDCs are hadronic calorimeters and are placed at $\pm 18$ m from the center $z = 0$ of the STAR detector and are at zero degrees ($\theta < 2$ mrad) with respect to the beam direction ($z$-axis). Since the charged particles are deflected by the dipole magnets from the zero degree region, they are not measured in the ZDCs. Therefore, the ZDC detectors measures the energy deposited by the spectator neutrons only. The real collisions are distinguished from the background events by selecting events with ZDC coincidence from the two beam directions. This makes ZDC as a useful event trigger and a luminosity monitor in steering the beams to the collision point. In addition to the beam monitoring and triggering, ZDCs are also very useful locating interaction vertices by using the time delay between the coincidences. A shower maximum detector was installed between the first and second modules of each existing STAR ZDC to study the spatial distribution of the neutron hits on the transverse plane of the ZDCs. The addition of ZDC-SMD to the STAR experiment enhances its capability in different areas of physics such as anisotropic flow, ultra-peripheral collisions, and spin physics [32].

The BBC consists of a hexagonal scintillator array structure, located on each side of the interaction region covering the full azimuth and $2.1 < |\eta| < 5.0$ [16]. It is mounted around the beam pipe at a distance of 3.7 m from the interaction point. For a minimum bias trigger, a coincidence of signals is required between two BBC. The timing difference between the two counters is used to get information of the primary vertex position. BBC coincidences are also used to reject beam gas events. In addition, the small tiles of BBC are used to reconstruct the first order event plane for flow analysis [26].

Since 2009, a pair of Vertex Position Detectors (VPD) [17] is also used to select events. Each VPD consists of 19 lead converters plus plastic scintillators with photo-multiplier tube readout that are positioned very close to the beam pipe on each side of STAR. Each VPD is approximately 5.7 m from the interaction point and covers the

pseudo-rapidity range $4.24 < |\eta| < 5.1$. Trigger for the minimum-bias (MB) events using VPD is defined as a coincidence signal in the east and west VPD detectors. The VPD can also provide the information about the $Z$ component of the primary vertex. The VPD has much better timing resolution than the BBC detector.

The main STAR calorimeters comprise a full Barrel Electromagnetic Calorimeter (BEMC) [18], single Endcap Electromagnetic Calorimeter (EEMC) [19], plus a Forward Meson Spectrometer (FMS) [40]. The electromagnetic calorimeters allow STAR to trigger on and study rare and high $p_T$ processes such as jets, leading hadrons, direct photons, and heavy quarks. They provide large acceptance for photons, electrons along with neutral pions, and $\eta$ mesons in all collision systems from polarized p+p to Au+Au collisions. These are also used for event characterization in heavy-ion collisions including ultra-peripheral collisions.

# Bibliography

[1] RHIC Accelerators, `https://www.bnl.gov/rhic/complex.asp`.

[2] D. A. Bromley, in Treatise on Heavy-Ion Science, vol. 1, 3 (1984).

[3] R. Lacasse (E877 Collaboration), Nucl. Phys. A 610, 153c (1996).

[4] G. Bunce, N. Saito, J. Soffer, and W. Vogelsang, Ann. Rev. Nucl. Part. Sci. 50, 525 (2000); W. Vogelsang, Pramana 63, 1251 (2004).

[5] L. C. Bland, AIP Conf. Proc. 675, 98 (2003); M. Stratmann, arXiv:0211317.

[6] M. Harrison *et al.*, Nucl. Instr. and Meth. A 499, 235 (2003).

[7] J. Benjamin *et al.*, IEEE Particle Accelerator Conference (PAC99).

[8] M. Anerella *et al.*, Nucl. Instr. Meth. A 499, 280 (2003).

[9] R. Fernow, Introduction to Experimental Particle Physics (Cambridge University Press, Cambridge, 1986).

[10] `http://www.agsrhichome.bnl.gov/RHIC/Runs/`.

[11] E. C. Aschenauer *et al.*, arXiv:1409.1633; R. G. Milner, AIP Conf. Proc. 698, 806 (2004).

[12] `https://drupal.star.bnl.gov/STAR/starnotes/public/csn0121` (1996).

[13] M. Anderson *et al.*, Nucl. Instr. Meth. A 499, 659 (2003); H. Wieman *et al.*, IEEE Trans. Nuc. Sci. 44, 671 (1997); J. Thomas *et al.*, Nucl. Instr. Meth. A 478, 166 (2002).

[14] B. Bonner *et al.*, Nucl. Inst. and Meth. A 508, 181 (2003).

[15] C. Adler *et al.*, Nucl. Instr. Meth. A 470, 488 (2001).

[16] J. Kiryluk, Local polarimetry for proton beams with the STAR beam beam counters, 718 (2005).

[17] M. Shao *et al.*, Nucl. Instr. Meth. A **492** (2002) 344; W. J. Llope *et al.*, Nucl. Instr. Meth. A **522** (2004) 252.

[18] M. Beddo *et al.*, Nucl. Inst. and Meth. A 499, 725 (2003).

[19] C. E. Allgower *et al.*, Nucl. Inst. and Meth. A 499, 740 (2003).

[20] K. H. Ackermann *et al.*, Nucl. Inst. and Meth. A 499, 713 (2003).

[21] C. Adler *et al.*, Nucl. Inst. and Meth. A 499, 778 (2003).

[22] M. M. Aggarwal *et al.*, Nucl. Inst. and Meth. A 499, 751 (2003).

[23] Nucl. Inst. and Meth. A 499, 624632, (2003).

[24] Y. Xu *et al.*, Nucl. Inst. and Meth. A 614, 28 (2010).

[25] E. C. Zeballos *et al.*, Nucl. Inst. and Meth. A 374, 132 (1996).

[26] L. Adamczyk *et al.* (STAR Collaboration), Phys. Rev. C 86, 054908 (2012).

[27] D. Liko, STAR Note 00087, 1 (1992).

[28] H. Bichsel, Nucl. Instr. Meth. A 562, 154 (2006).

[29] W. M. Yao *et al.*, J. Phys. G: Nucl. Part. Phys. 33, 1 (2006).

[30] A. Ljubicic *et al.*, IEEE Trans. Nucl. Sci., 99, NS-47 (2000); J. M. Landgraf *et al.*, Nucl. Instr. and Meth. A, 499, 758 (2003).

[31] F. S. Beiser *et al.*, Nucl. Instr. and Meth. A, 499, 762 (2003).

[32] B. I. Abelev *et al.* (STAR Collaboration), Phys. Rev. Lett. 101, 252301 (2008); STAR ZDC-SMD proposal, STAR Note SN-0448 (2003).

[33] M. Adamczyk *et al.* (BRAHMS Collaboration), Nucl. Inst. and Meth. A 499, 437 (2003).

[34] K. H. Ackermann *et al.* (STAR Collaboration), Nucl. Inst. and Meth. A 499, 624 (2003).

[35] K. Adcox *et al.* (PHENIX Collaboration), Nucl. Inst. and Meth. A 499, 469 (2003).

[36] B. B. Back *et al.* (PHOBOS Collaboration), Nucl. Inst. and Meth. A 499, 603 (2003).

[37] http://www.star.bnl.gov/public/trg/trouble/operating-trigger/.

[38] 3D picture of STAR detector by Alex Schmah (STAR Collaboration) and Maria.

[39] STAR Collaboration, Nature, 473, 353356, (2011).

[40] W. W. Jacobs (for the STAR Collaboration), J. Phys., Conf. Ser. **160**, 012008, (2009).

# Chapter 3

# Light Nuclei Production in Heavy-ion Collisions

## 3.1  Introduction

In relativistic heavy-ion collisions, production of light nuclei (anti-nuclei) is possible via two mechanisms. The first mechanism is the direct production of nucleus and anti-nucleus pairs in elementary NN or parton-parton interactions. Since the binding energies of light nuclei (anti-nuclei) are small, the directly produced nuclei or anti-nuclei are likely to be dissociated in the medium before escaping. The second and presumably the dominant mechanism for nucleus and anti-nucleus production is via final state coalescence of produced nucleons and anti-nucleons or participant nucleons [1, 2, 3]. In this process, nucleons (anti-nucleons) merge to form light nuclear (anti-nuclear) clusters during the final stages of kinetic freeze-out [1, 4]. The formation probability is proportional to the product of the phase space densities of its constituent nucleons [5]. Therefore, the production of light nuclei provides information about the size of the emitting system and its space-time evolution. The invariant yields of light nuclei can be related to the primordial invariant yields of nucleons as

$$E_A \frac{d^3 N_A}{dp_A^3} = B_A (E_p \frac{d^3 N_p}{dp_p^3})^Z (E_n \frac{d^3 N_n}{dp_n^3})^{A-Z} \approx B_A (E_p \frac{d^3 N_p}{dp_p^3})^A, \qquad (3.1)$$

where $N_A$, $N_p$, and $N_n$ denote the yields of the particular nucleus (anti-nucleus), and of its constituent protons and neutrons, respectively. A and Z being the atomic mass number and atomic number, respectively. Here, it is assumed that protons and neutrons are produced with identical momentum spectra and $p_A = A \times p_p$. $B_A$ is the coalescence parameter, which is related to the freeze-out correlation volume [1]: $B_A \propto 1/V_f^{A-1}$. The coalescence parameter, $B_A$, can be used to infer the space-time geometry of the system [6].

## 3.2 Dataset, Trigger and Analysis Cuts

The results presented in this chapter are from the data collected by the STAR experiment at RHIC for Au+Au collisions at $\sqrt{s_{NN}}$ = 7.7, 11.5, 19.6, 27 and 39 GeV in the years 2010 and 2011. The data with the minimum bias trigger have been used for this analysis. The minimum bias (0-80%) trigger condition for all seven energies was based on a coincidence of the signals from the zero-degree calorimeters (ZDC) [7], vertex position detectors (VPD) [8], and/or beam-beam counters (BBC) [9]. For this analysis, we have used Time Projection Chamber (TPC) and Time of Flight (TOF) detector system of the STAR experiment for tracking and identification of light nuclei. The detailed analysis procedure using these detectors are explained in the following subsections.

### 3.2.1 Event Selection for Analysis

Different cuts on primary vertex position have been used for different collision energies for selection of good events. The cuts on longitudinal component ($V_z$) of primary vertex is $\pm 40$ cm for 39 GeV and $\pm 50$ cm for 27, 19.6, 11.5 and 7.7 GeV data set. The quality assurance (QA) study was performed based on the mean transverse momenta,

the mean vertex position, the mean interaction rate, and the mean multiplicity in the detector [10]. Events were not analyzed if one of those quantities was several $\sigma$ away from the run-period averaged value. An additional cut on transverse vertex position $V_R < 1$ cm has been used to minimise the Au-plus-beam-pipe events. $V_R$ is defined as $V_R = \sqrt{V_x^2 + V_y^2}$, where $V_x$ and $V_y$ are the $x$ and $y$ components of primary vertex position. To remove pileup events, it was required that at least two tracks from the primary vertex were matched to the cells of the TOF detector. After applying all events selection cuts, the number of minimum bias events for each collision energy are listed in Table 3.1.

Table 3.1: The Z-vertex acceptance and total number of minimum-bias (MB) events.

| Energy ($\sqrt{s_{NN}}$) | $V_Z$ (cm) | MB events ($10^6$) |
|---|---|---|
| 39 GeV | $|V_z| < 40$ | 119 |
| 27 GeV | $|V_z| < 50$ | 49 |
| 19.6 GeV | $|V_z| < 50$ | 24 |
| 11.5 GeV | $|V_z| < 50$ | 11 |
| 7.7 GeV | $|V_z| < 50$ | 3 |

### 3.2.2   Track Selection for Analysis

The optimal particle identification and momentum resolution depends on the quality of the individual track measured by the TPC detector. For the study of light nuclei production, we have selected the tracks which originated from the primary vertex. The distance of the closest point of each track from the vertex is called the Distance of Closest Approach (DCA). For this analysis we have selected primary tracks with DCA $\leq 1.0$ cm. This ensures that the tracks comes from the triggered event vertex and not from any secondary vertex. We have also used rapidity cut of $|y| < 0.3$ for all the tracks. Moreover we selected tracks with pseudorapidity cut $|\eta| < 1.0$ to select tracks from maximum efficient region of the TPC. The number of fit points (nHitsFit) for each track has been selected to be equal or more than 25. We can also get the maximum number of possible fit points (nHitsPos) for each track in TPC.

To avoid the split tracks, we have selected the tracks for which the ratio of nHitsFit to nHitsPos is greater than 0.52. In addition to cuts on fit points, we have also chosen tracks which have at least 10 hits points (nHitsdEdx) to calculate the specific ionisation energy loss (dE/dx). This cut increases the purity of the selected tracks as more nHitsdEdx corresponds to more accurate measurement of dE/dx which is then used to identify tracks. We have also selected tracks with $p_T > 0.15$ GeV as it is the minimum momentum a track should have to be detected in TPC. Table 3.2 lists the cuts applied on individual tracks for the analysis.

Table 3.2: Track cuts used for light nuclei identification

| variable | condition |
|---|---|
| Number of fit points (nHitsFit) | $\geq 25$ |
| Fit points for $\langle dE/dx \rangle$ (nHitsdEdx) | $\geq 10$ |
| nHitsFit / nHitsPos | $\geq 0.52$ |
| Distance from primary vertex (DCA) | $\leq 1.0$ cm |
| Transverse momentum ($p_T$) | $\geq 0.15$ GeV/$c$ |
| rapidity ($y$) | $\leq 0.3$ |
| pseudo-rapidity ($\eta$) | $\leq 1.0$ |

## 3.2.3 Centrality Selection

The centrality of an event depends on the impact parameter which is defined as the perpendicular distance between the centers of the two colliding nuclei. Low impact parameter corresponds to central event and high impact parameter corresponds to peripheral events. In real experiment, however, impact parameter can not be measured. Therefore, an experimental observable is chosen to correlate with impact parameter and determine the centrality. In this analysis, the uncorrected charged particle multiplicity ($dN_{\text{ch}}^{\text{raw}}/d\eta$) at midrapidity ($|\eta| < 0.5$) is used to determine the centrality of an event. The measured $dN_{\text{ch}}^{\text{raw}}/d\eta$ is compared with simulated $dN_{\text{ch}}^{\text{raw}}/d\eta$ where the simulation is done using a two-component model [15]. In two-component model, the multiplicity distribution is given by,

$$\frac{dN_{\text{ch}}}{d\eta} = n_{pp}[(1-x)\frac{N_{\text{part}}}{2} + xN_{\text{coll}}], \tag{3.2}$$

where $N_{\text{part}}$ is the number of participant nucleons and $N_{\text{coll}}$ is the number of binary nucleon-nucleon collisions in the Glauber Monte-Carlo simulations. The fitting parameter $n_{pp}$ is the average multiplicity per unit pseudo-rapidity $(dN_{\text{ch}}/d\eta)$ in minimum-bias $p+p$ collisions and $x$ is the fraction of production of charged particles from the hard component. The $x$ value is kept fixed at $0.12 \pm 0.02$ based on the linear interpolation of the PHOBOS results at $\sqrt{s_{NN}} = 19.6$ and $200$ GeV [17]. Systematic errors on $n_{pp}$ are evaluated by varying both $n_{pp}$ and $x$ within the quoted uncertainty of $x$ to determine the minimum $\chi^2$ to describe the measured multiplicity distribution of data. The inelastic nucleon-nucleon cross-section $\sigma_{NN}^{\text{inel}}$ is extracted from fitting the results of available $NN$ data for total and elastic $p+p$ cross-sections from the Particle Data Group [14]. The parameters in the two-component model and $\sigma_{nn}^{inel}$ in the MC Glauber simulations are summarized in Table 3.3.

Table 3.3: Parameters $\sigma_{NN}^{\text{inel}}$ and $n_{pp}$ for different collision energies.

| Energy ($\sqrt{s_{\text{NN}}}$) | $n_{pp}$ | $\sigma_{NN}^{\text{inel}}$ (mb) |
|---|---|---|
| 200 GeV | $2.43 \pm 0.12$ | $42.0 \pm 1.00$ |
| 62.4 GeV | $1.60 \pm 0.09$ | $36.0 \pm 1.00$ |
| 39 GeV | $1.52 \pm 0.08$ | $34.0 \pm 1.10$ |
| 27 GeV | $1.39 \pm 0.06$ | $33.0 \pm 1.10$ |
| 19.6 GeV | $1.29 \pm 0.05$ | $32.0 \pm 1.11$ |
| 11.5 GeV | $1.07 \pm 0.05$ | $31.2 \pm 1.13$ |
| 7.7 GeV | $0.89 \pm 0.04$ | $30.8 \pm 1.20$ |

Figure 3.1 shows $N_{\text{ch}}^{\text{raw}}$ distribution for minimum-bias events. The values of $N_{\text{ch}}^{\text{raw}}$ for different centrality classes and energies are listed in the appendix.

In a Monte Carlo Glauber model, two colliding nuclei are independently generated and their nucleon positions are distributed according to the Wood-Saxon density profile,

$$\rho(r) = \frac{\rho_0}{1 + \exp \frac{r-r_0}{a}} \tag{3.3}$$
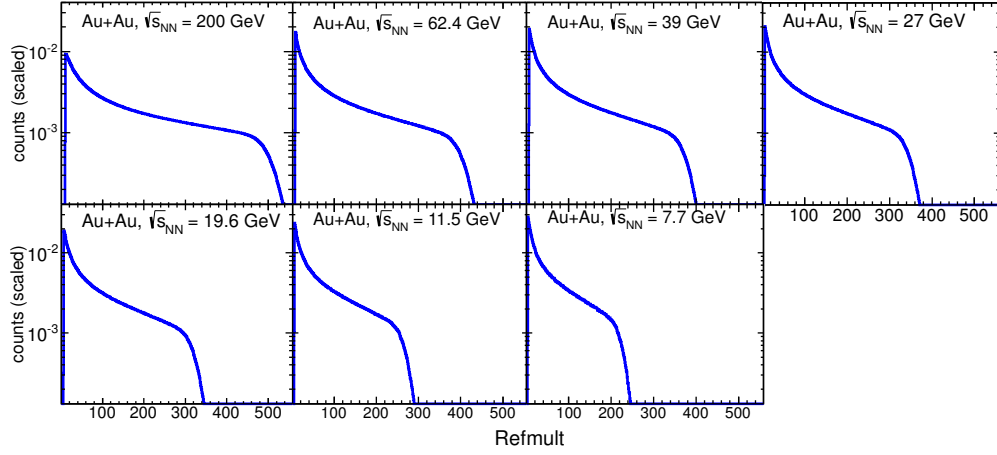
Figure 3.1: $dN_{\text{event}}/(dN_{\text{ch}}^{\text{raw}}/d\eta)$, namely, Refmult distribution for minimum-bias Au+Au collisions.

where, $\rho_0$ is the nucleon density, $r_0$ is the nuclear radius, and $a$ is the skin depth. Each nucleon in the nucleus is separated by a distance larger than the minimum inter-nucleon separation. The nuclei generation and the nucleon-nucleon pair selection is repeated with random selection of impact parameter $b$, The extracted quantities can be studied as function of total cross section ($\sigma$). The distribution of $d\sigma/db$, $d\sigma/dN_{\text{part}}$, and $d\sigma/dN_{\text{coll}}$, are determined. Each distribution is divided into bins corresponding to the fractions of the measured total cross section of the required centrality bins, and the average values of $N_{\text{part}}$ and $N_{\text{coll}}$ are extracted for each centrality. Systematic uncertainties on $N_{\text{part}}$ and $N_{\text{coll}}$ have been estimated by varying $n_{\text{pp}}$ and $x$ in the two component model as well as varying the input parameter in the Glauber Monte Carlo simulation. The final errors are the quadrature sum of these individual systematic errors. In order to introduce event by event variation in the multiplicity, the Negative Binomial Distribution (NBD) for multiplicities in p+p collisions have been convoluted with those of $N_{\text{part}}$ and $N_{\text{coll}}$. The NBD distribution in multiplicity $N$ has two parameters, $n_{\text{pp}}$ and $k$ and is defined as,

$$P_{\text{NBD}}(n_{\text{pp}}, k, N) \;=\; \frac{\Gamma(n+k)}{\Gamma(n+k)\Gamma(k)} \frac{(n_{\text{pp}}/k)^N}{(n_{\text{pp}}/k+1)^N} \tag{3.4}$$

where, $\Gamma$ is the Gamma function. The values $k$ and $n_{\text{pp}}$ are obtained by fitting the

measured multiplicities with those from the simulations. The simulated multiplicity is found to be independent of the $k$ parameter. The centrality class is defined by calculating the fraction of the total cross-section obtained from the simulated multiplicity.

In this analysis, the events are divided into 8 centrality bins from central to peripheral, namely, 0-5%, 5-10%, 10-20%, 20-30%, 30-40%, 40-50%, 50-60% and 60-80%. The values of $N_{part}$ and $N_{coll}$ are higher in central collision than the peripheral collisions. The centrality 80-100% is not used for significant trigger bias due to vertex inefficiency at low multiplicity and the contamination from the electromagnetic interactions. The average number of $N_{part}$ and $N_{coll}$ for different centralities for each beam energies are listed in the appendix.

## 3.3    Particle Identification Techniques

In this section we discuss the light nuclei identification method. We have used TPC and TOF detector to identify light nuclei. We discuss the particle identification methods in TPC and TOF in the following subsections.
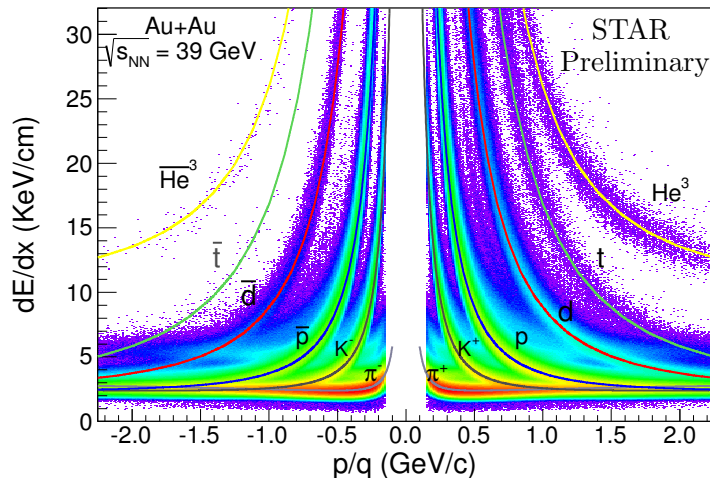


Figure 3.2: dE/dx as a function of rigidity (momentum/charge) for mid-rapidity charged particles. Solid lines corresponds to the theoretical dE/dx values. See text for details.

### 3.3.1 Particle Identification Using TPC

The TPC is the main tracking detector in the STAR experiment. The TPC can track charge particles and measure its momentum from the curvature of the track in the fixed magnetic field which is applied along the longitudinal (beam) direction [11]. The TPC also measures the specific ionization energy loss as a function of momentum. The mean specific energy loss as a function of rigidity (momentum/charge) as measured in the TPC is shown in Fig. 3.2. The different bands in this figure corresponds to different particles. The solid lines in Fig. 3.2 corresponds to the theoretical $dE/dx$ values evaluated from the modified Bethe-Bloch formula, namely the Bichsel function [12]. To identify individual particles, we define a variable $n\sigma$ such that,

$$n\sigma = \frac{1}{R} \times \frac{(dE/dx)_{\text{expt.}}}{(dE/dx)_{\text{theory}}}, \tag{3.5}$$

where $dE/dx_{\text{expt.}}$ is the measured specific ionization energy loss per unit path length and $dE/dx_{\text{theory}}$ is theoretical value obtained from Bichsel function. The quantity $R$ is the dE/dx resolution of the TPC detector. This $n\sigma$ variable is then used to identify individual hadrons. However, to identify light nuclei, we define a variable $Z$ such as,

$$Z = \ln\left[\frac{(dE/dx)_{\text{expt.}}}{(dE/dx)_{\text{theory}}}\right]. \tag{3.6}$$

We then use this $Z$ distribution to identify and select light nuclei.

### 3.3.2 Particle Identification Using TOF

The Time-of-Flight (TOF) detector covers the full azimuth and pseudo-rapidity range of -0.9 $< \eta <$ 0.9 [13]. The TOF detector has an excellent timing resolution of $\sim$85 ps. The TOF detector measures the time ($\tau$) taken by a particle to traverse the distance ($L$) from the primary vertex position to the TOF and hence it can measure the particle velocity ($\beta$). Using $\beta$ from the TOF and corresponding momentum ($p$) from the TPC, we can calculate the mass ($m$) of the charged tracks using the relativistic

equation,

$$m^2 = p^2(1/\beta^2 - 1). \tag{3.7}$$

TOF detector is able to enhance the particle identification of the tracks with high transverse momenta ($p_T > 1.0$ GeV/$c$) where the dE/dx bands of different particles starts to merge. A representative plot of $m^2$ as a function of particle momentum is shown for $\sqrt{s_{\mathrm{NN}}} = 39$ GeV in Fig. 3.3. The different bands corresponds to the square of mass of different particles.
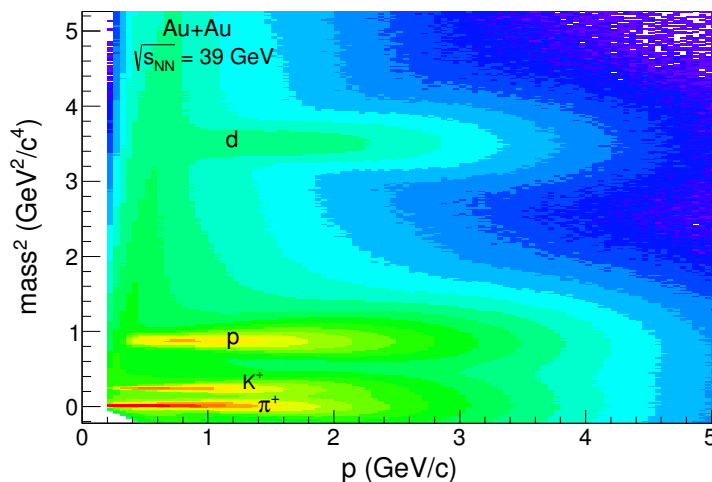


Figure 3.3: mass$^2$ as a function of momentum (p) for mid-rapidity charged particles. Different bands corresponds to the different particle m$^2$. See text for details.

## 3.4  Raw yield extraction

As mentioned earlier, we have used TPC and TOF detector to extract yield of light nuclei. The following subsections describes the procedure of yield extraction for nuclei.

### 3.4.1  Raw Yield Using the TPC Detector

As mentioned in previous subsection, we define a variable $Z$ for each track using the $dE/dx$ information from the TPC detector. Figure 3.4 shows the $Z$ distribution of $\bar{d}$
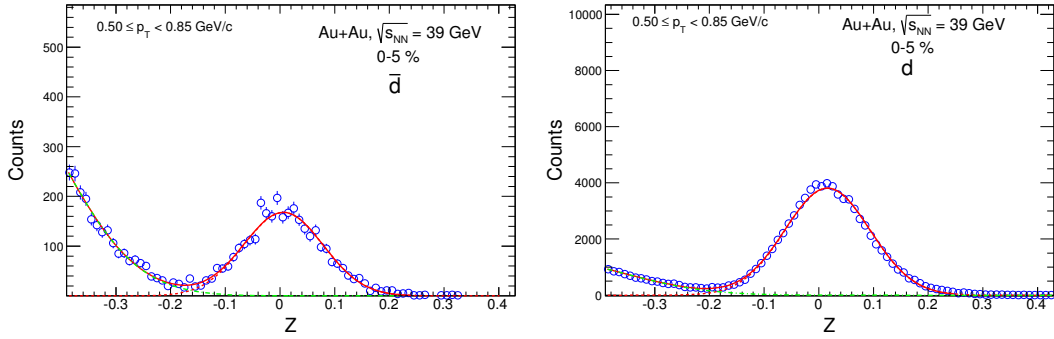
Figure 3.4: $Z$ distribution for mid-rapidity $\overline{d}$ (left) and $d$ (right), for 0-5% central collisions in Au+Au at $\sqrt{s_{NN}} = 39$ GeV. Z distribution of each nuclei is fitted with two Gaussian function (red continuous line). One Gaussian describes the Z distribution of nuclei (red dashed line) and another Gaussian is used to describe the background (green dot-dashed line).

and $d$ for central (0-5%) events of Au+Au collisions at $\sqrt{s_{NN}} = 39$ GeV. The $Z$ distribution of the selected nuclei is fitted with two Gaussian function. The Gaussian, peaked around zero as shown in Fig. 3.4, corresponds to the nuclei and the broader distribution on the left corresponds to the background. We then calculate yield of the nuclei by integrating the Gaussian function corresponding to the signal. The $\overline{d}$ and $d$ yield are calculated from this $Z$ distributions for $p_T < 1.0$ GeV/c. For $p_T > 1.0$ GeV/c, we have used the $m^2$ distribution of light nuclei to calculate the corresponding yields. This process is described in the following sub-section.

### 3.4.2   Raw Yield Using the TOF Detector

We have also used the TOF detector to calculate the yield of light nuclei at higher transverse momenta ($p_T > 1.0$ GeV/$c$) where the TPC is unable to identify particles due merging of different dE/dx bands (Fig. 3.2). Figure 3.5 shows the $m^2$ distribution of $d$ and $\overline{d}$ for Au+Au collisions at $\sqrt{s_{NN}} = 39$ GeV. This $m^2$ distribution is fitted with a Gaussian + exponential function. The Gaussian function (red dotted line) corresponds to the nuclei of interest and the exponential function (green dot-dashed line) corresponds to the background. The yield of the nuclei is then calculated by integrating the Gaussian function. Using this $m^2$ distribution we can extract light
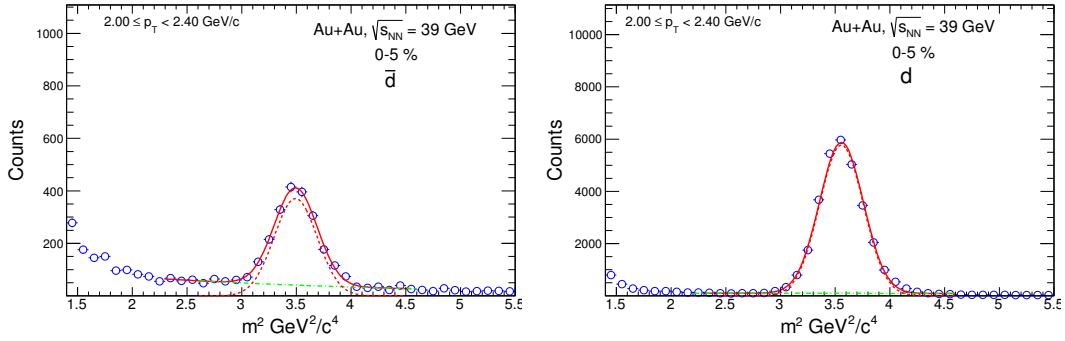
Figure 3.5: $m^2$ distribution for mid-rapidity $\overline{d}$ (left) and $d$ (right), for 0-5% central collisions in Au+Au at $\sqrt{s_{NN}} = 39$ GeV. $m^2$ distribution of each nuclei is fitted with a Gaussian + exponential function (red continuous line). The Gaussian function describes the $m^2$ distribution of nuclei (red dashed line) and the exponential function is used to describe the background (green dot-dashed line).

nuclei yield with high transverse momentum ($p_T \sim 4$ GeV/c). After calculating the raw yields from the $Z$ and $m^2$ distribution, we correct the raw $p_T$-spectra for different detector effects (matching efficiency, detector acceptance etc.) which are described in the following sections in detail.

## 3.5 Corrections for Efficiency and Acceptance

The raw spectra is obtained by calculating $\frac{d^2N}{2\pi p_T dp_T dy}$ for each $p_T$ bin. In the TPC detector, some particles may not be detected due to the finite geometry of the detector. Some of the particles may also hit at the dead region of the detector and some of the charged tracks may not be well reconstructed due to low number of hits. Some of the particles (specially light nuclei) may also arise from Au ions hitting the beam-pipe, which we do not count as primary particles. Therefore, the raw spectra has to be corrected for the aforesaid effects (detector acceptance, reconstruction inefficiency, hadronic interactions, beam-pipe fragments). The correction factors (mostly as a function of $p_T$) are determined by a simulation procedure which is termed as embedding technique. In this procedure the charged particles generated using Monte-Carlo (MC) simulations and embedded in real events. The input $p_T$ and rapidity $y$
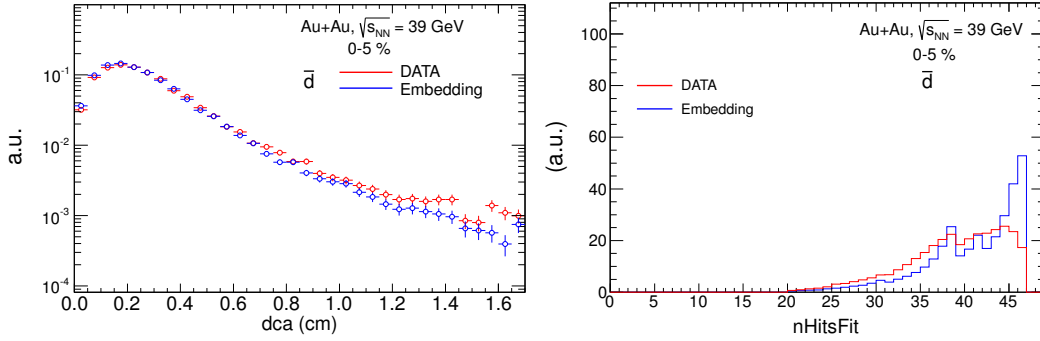
Figure 3.6: DCA distribution (left) and nHitsFit distribution (right) for mid-rapidity $\overline{d}$ in 0-5% central collisions in Au+Au at $\sqrt{s_{NN}} = 39$ GeV, compared with the corresponding results from the embedded Monte-Carlo events.

distributions are kept uniform to keep equal statistics in each $p_{\mathrm{T}}$ bins. These tracks are then passed through reconstruction processes named GSTAR [18] and TRS [18] respectively. GSTAR is the software package to run the STAR detector simulation using GEANT [19, 20] and the TRS is the TPC Response Simulator. The number of embedded MC tracks is kept low ($\sim$5%) to avoid distorting the track density of the event. The events containing these simulated charged particles tracks are referred to as mixed events. These mixed events are then passed through the standard STAR reconstruction chain and those events after reconstruction are called as reconstructed event. The reconstructed information of those simulated particles in the reconstructed event is then associated with the MC information in the mixed events. Then we get the total number of reconstructed MC tracks from mixed events in a certain $p_{\mathrm{T}}$ bin. The reconstructed tracks also need to be identified which are matched to the input MC tracks, defined as matched tracks in the reconstructed events. All the track cuts and event cuts for real tracks and MC tracks are kept same. This procedure is called embedding, which provides nearly realistic simulation of the collision and detector environment. To ensure realistic embedding procedure, all the track level properties have been checked between embedded events and the real events from the data. Figure 3.6 shows the comparison of the distributions of DCA and nHitsFit for $\overline{d}$ obtained from embedding and real data at mid-rapidity for central Au+Au collisions at $\sqrt{s_{NN}} = 39$ GeV. The overall agreement of the embedding and real data

ensures that corrections extracted from embedding reflect realistic calculations. Since detector parameters (gas pressure in TPC, temperature) can change over the run, a minimum uncertainty (∼5%) is also associated as the embedding procedure to the obtained corrected spectra. In addition to the corrections related to embedding, there are some other corrections like energy loss, TOF matching inefficiency, beam-pipe contaminations, absorption of tracks in detector material. The following subsections discusses these corrections in detail.

### 3.5.1 Energy Loss Correction

When a charged particle moves through the detector volume, it loses some energy due to multiple interactions (mainly coulomb interactions). Low momentum particles lose a significant amount of energy in this process compared to high momentum particles [21].
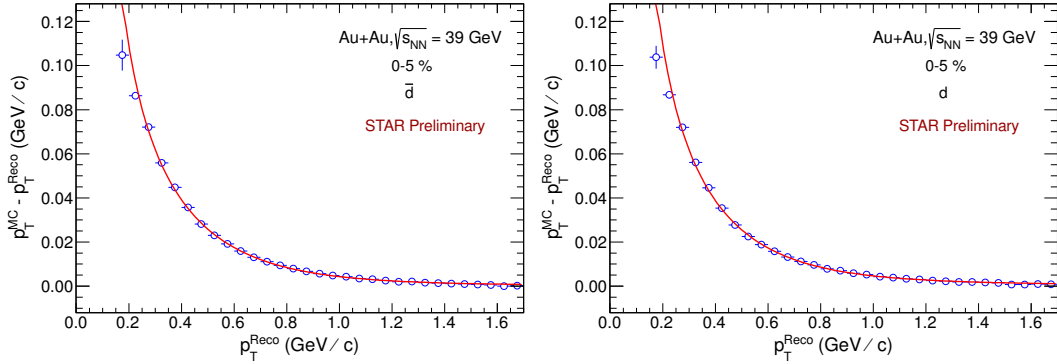


Figure 3.7: Energy loss ($p_T^{MC}$-$p_T^{Reco}$) as a function $p_T^{Reco}$ of for mid-rapidity $\bar{d}$ and $d$ as calculated using the embedded events.

Due to this effect, the momentum recorded by the detectors is less than the initial momentum when the particle freezes out. The track reconstruction algorithm takes into account the Coulomb scattering and energy loss assuming the pion mass for each particle. Therefore, a correction is needed for the energy loss by heavier particles. This correction is obtained from embedding Monte Carlo simulations (described earlier). The energy loss correction factor is obtained from the difference between the

reconstructed momentum ($p_T^{\text{Reco}}$) and the initial momentum ($p_T^{\text{MC}}$) as a function of $p_T^{\text{Reco}}$. Figure 3.7 shows the difference ($p_T^{\text{MC}}$-$p_T^{\text{Reco}}$) as a function of $p_T$ for $d$ and $\bar{d}$ respectively in Au+Au collisions at $\sqrt{s_{\text{NN}}}$ = 39 GeV for 0-5% centrality. The energy loss correction was found to have negligible dependence on centrality in Au+Au collisions. The energy loss correction for $d$ and $\bar{d}$ can be parametrised as,

$$p_T^{\text{MC}} - p_T^{\text{Reco}} \;=\; P_0 \exp(-P_1 x) + P_2 x^{P_3},\qquad(3.8)$$

where $P_0$, $P_1$, $P_2$, and $P_3$ are the fit parameters. The values of these parameters are given in Table 3.4.

Table 3.4: Parameters of energy loss function (Eq. 3.8) of $d$ for Au+Au collisions at $\sqrt{s_{\text{NN}}}$ = 39, 27, 19.6, 11.5 and 7.7 GeV. Parameters of $\bar{d}$ are shown inside the parenthesis

| $\sqrt{s_{\text{NN}}}$ | 39 GeV | 27 GeV | 19.6 GeV | 11.5 GeV | 7.7 GeV |
|---|---|---|---|---|---|
| $P_0$ (GeV/c) | 0.126 (0.134) | 0.147 (0.127) | 0.155 (0.132) | 0.116 (0.095) | 0.115 |
| $P_1$ (GeV$^{-1}$c) | 4.178 (0.397) | 4.275 (3.661) | 4.229 (3.809) | 4.334 (3.700) | 4.016 |
| $P_2$ (GeV/c) | 0.003 (0.002) | 0.003 (0.002) | 0.003 (0.002) | 0.004 (0.003) | 0.005 |
| $P_3$ (Dimensionless) | -1.87 (-2.04) | -1.68 (-2.19) | -1.60 (-2.04) | -1.75 (-1.94) | -1.56 |

The energy loss correction, as a function of $p_T$, was applied to the each individual tracks during data analysis. This correction shifts the position of $p_T$ in the low $p_T$ part of the spectra.

## 3.5.2 TOF Matching Efficiency Correction

After energy loss correction, other efficiency corrections have to be applied to the obtained raw spectra. One of these include track reconstruction efficiency, as every primary track cannot be reconstructed in the TPC and the other one is the TOF matching efficiency, as every reconstructed track in TPC can not be matched with a corresponding hit in the TOF. As TPC and TOF are two separate detectors, the final spectra obtained using these two detectors need to be matched properly to provide correct invariant yield. Only a fraction of the reconstructed primary tracks in TPC are matched with hits on the TOF detector. The matching efficiency depends on the
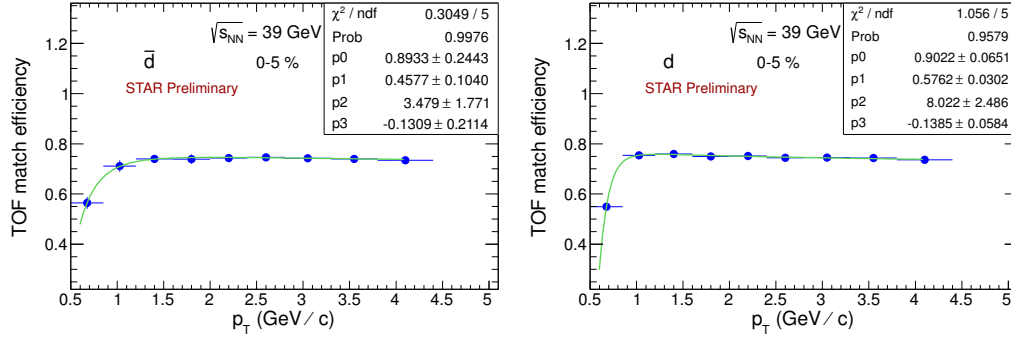
Figure 3.8: TOF matching efficiency of mid-rapidity $\bar{d}$ (left) and $d$ (right) as a function $p_T$ for 0-5% central collisions in Au+Au at $\sqrt{s_{NN}} = 39$ GeV.

fraction of tracks that are missing during the propagation from TPC to TOF. It could be due to the TOF detectors geometrical acceptance, detector inefficiency, some dead region in the TOF detector or the decays and the interactions with the material. So to quantify the matching of the tracks between TPC and TOF, a matching efficiency ($\varepsilon_{TOF}$) is calculated using the real data and is defined as,

$$\varepsilon_{TOF} = \frac{\text{Number of TOF matched track}}{\text{Number of TPC track}}. \qquad (3.9)$$

Figure 3.8 shows the TOF matching efficiency of $\bar{d}$ and $d$ as a function of $p_T$ for 0-5% centrality in Au+Au collisions at $\sqrt{s_{NN}} = 39$ GeV. Lines in Fig. 3.8 corresponds to parametrization of the data points by the function,

$$\varepsilon_{TOF}(p_T) = P_0 \exp\left[(P_1/x)^{P_2}\right] + P_3 x^{p_4}, \qquad (3.10)$$

where, $P_0$, $P_1$, $P_2$, $P_3$, $P_4$ are fit parameters. The parametrization by Eq. 3.10 is used to derive efficiency values which has smooth variation as a function of $p_T$. The TOF matching efficiency of $d$ and $\bar{d}$ for all centrality and all beam energies are shown in the Appendix at the end of this chapter. The raw spectra is corrected for matching efficiency as the following,

$$\text{Raw spectra}(p_T)_{\text{TOF match corrected}} = \frac{\text{Raw spectra}(p_T)}{\varepsilon_{TOF}}. \qquad (3.11)$$

62

### 3.5.3 TPC Efficiency and Acceptance Correction

Once the TOF matching efficiency correction is applied to the raw spectra, we then apply correction for track reconstruction efficiency ($\varepsilon_{\mathrm{TPC}}$), which is obtained using embedding method as described earlier in this chapter. The track reconstruction efficiency in the mid-rapidity range is defined as,

$$\varepsilon_{\mathrm{TPC}} = \frac{\text{Number of matched MC track}}{\text{Number of input MC track}}. \tag{3.12}$$

Figure 3.9 shows the TPC tracking efficiency of $d$ and $\overline{d}$ as a function of $p_{\mathrm{T}}$ for 0-5% centrality in Au+Au collisions at $\sqrt{s_{\mathrm{NN}}}$= 39 GeV.
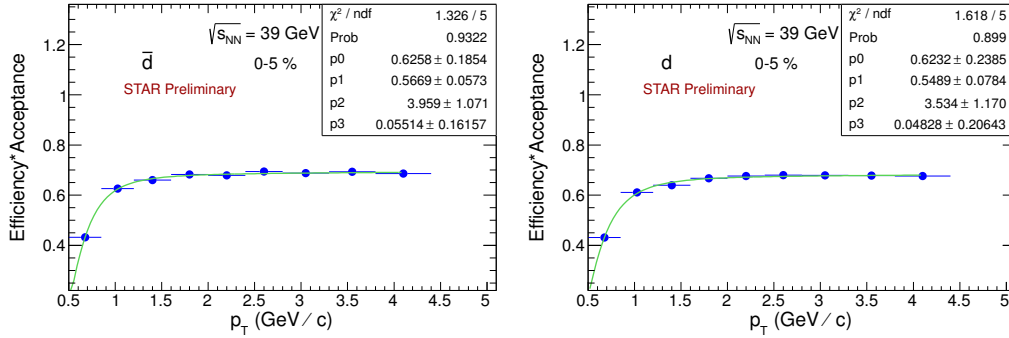


Figure 3.9: Efficiency×acceptance of TPC for mid-rapidity $\overline{d}$ (left) and $d$ (right) as a function $p_{\mathrm{T}}$ for 0-5% central collisions in Au+Au at $\sqrt{s_{\mathrm{NN}}} = 39$ GeV.

Lines in Fig. 3.9 corresponds to parametrization of the data points using the fit function,

$$\varepsilon_{\mathrm{TPC}}(p_{\mathrm{T}}) = P_0 \exp[-(P_1/x)^{P_2}] + P_3 x^{P_4}, \tag{3.13}$$

where $P_0$, $P_1$, $P_2$, $P_3$ and $P_4$ are fit parameters. The efficiency values depend on the $p_{\mathrm{T}}$ as well as on the centrality of the event. The efficiency for $d$ and $\overline{d}$ is flat for $p_{\mathrm{T}} > 1.4$ GeV/$c$. At lower $p_{\mathrm{T}}$, the efficiency drops because of the multiple scattering effect due to the higher mass of $d$ and $\overline{d}$. For more central events, the efficiency decreases due to the large number of tracks. The TPC efficiency plots for $d$ and $\overline{d}$

in all centrality and all beam energies are shown in the appendix at the end of this chapter. After obtaining the tracking efficiency of $d$ and $\bar{d}$ from these parametrized functions, the corrected $p_T$ spectra is given as,

$$\text{Raw spectra}(p_T)_{\text{Track Efficiency Corrected}} = \frac{\text{Raw spectra}(p_T)}{\varepsilon_{\text{TPC}}}. \qquad (3.14)$$

This spectra is then further corrected for beam-pipe contamination and absorption corrections. The following subsections discuss about them in detail.

### 3.5.4 Beam-pipe Contamination Removal

Each particle produced in a collision has to travel through the beam-pipe and other detector material before entering into the TPC working volume. High energetic particles, while traversing through the beam-pipe and detector materials can create secondary particles or knock out the beam-pipe material as fragmented nucleus ($d$, $t$, $^3He$, $^4He$). Due to the geometry of the beam-pipe and the detector, the secondary particles are produced far from the primary vertex (mainly on the beam-pipe) and they appear as a long, nearly flat tail in the DCA distribution of primary particles. This effect is $p_T$ dependent, which is highest at low $p_T$ and rapidly decreases at higher $p_T$. Anti-particles, however do not suffer such backgrounds from beam-pipe. Therefore, long DCA tail is absent from their DCA distribution. Hence the DCA distribution of anti-particle should be the same as that of any primary particle. To correct for the knock out deuterons from the beam-pipe, we use the DCA distributions of both deuteron and anti-deuteron from real data and compare them. This method has also been used in earlier STAR measurements [22, 23]. Figure 3.10(a) shows the DCA distribution of $d$ and $\bar{d}$ for 0-5% central collision in Au+Au at $\sqrt{s_{\text{NN}}} = 39$ GeV. Since the background shape of the DCA distribution at small DCA is not known, a Monte Carlo simulation (GEANT) was used and can be described by an exponential function,
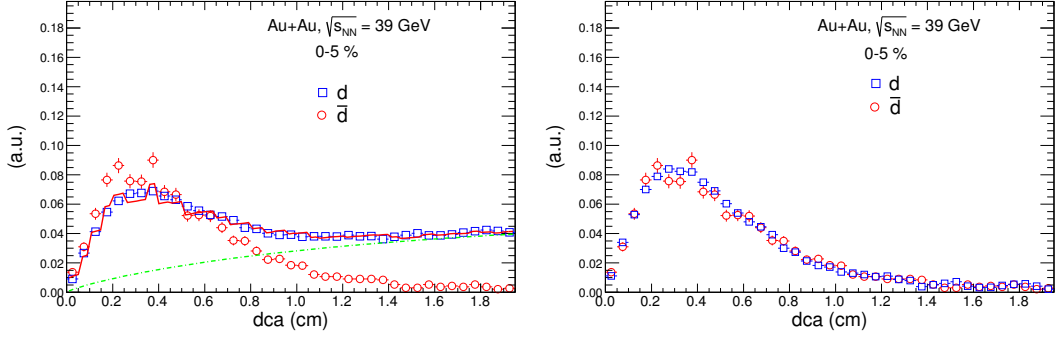
Figure 3.10: (a) DCA distribution of mid-rapidity $\bar{d}$ and $d$ at $0.5 < p_\mathrm{T} < 0.85$ GeV/c for 0-5% central collisions in Au+Au at $\sqrt{s_\mathrm{NN}} = 39$ GeV. (b) Comparison of DCA of $\bar{d}$ and $d$ after removing of beam pipe contamination. See text for details.

$$d(DCA)_\mathrm{bkg} = A[1 - exp(-DCA/B)]^C. \qquad (3.15)$$

Then assuming the identical shape of the DCA distribution of primary $d$ and $\bar{d}$, we can express the total DCA distribution of the $d$ as,

$$d(DCA) = \bar{d}(DCA)/r_{\bar{d}/d} + d(DCA)_\mathrm{bkg}, \qquad (3.16)$$

where A, B, C, and the ratio $r_{\bar{d}/d}$ are free parameters. The red solid line in Fig. 3.10(a) corresponds to the fit of DCA of $d$ using equation 3.16. The green dotted line in Fig. 3.10(a) corresponds to the DCA distribution of the beam pipe fragments. The beam-pipe contamination is then subtracted from the DCA of $d$. DCA of $d$, after subtraction of beam-pipe contamination, follows the DCA distribution of $\bar{d}$ as shown in Fig. 3.10(b). Following this method we have removed this beam-pipe deuterons from the inclusive $d$ yields for $p_\mathrm{T} < 1.0$ GeV/c.

### 3.5.5 Absorption Correction

Apart from the corrections discussed above, we also have to correct light nuclei $p_\mathrm{T}$ spectra for absorption in the detector material. Both nuclei and anti-nuclei, while travelling from primary vertex to the detectors, might get absorbed (or annihilated

65
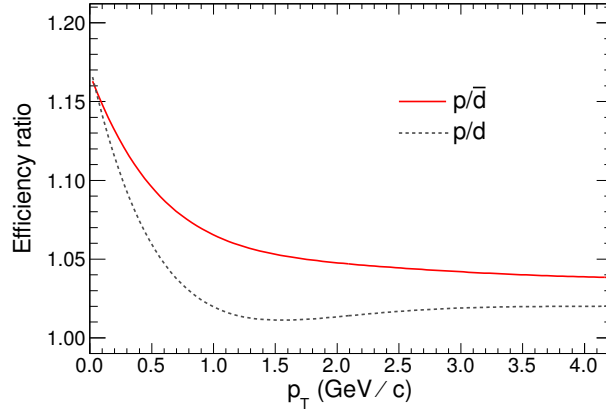
Figure 3.11: Ratio of tracking efficiencies of $p/\overline{d}$ and $p/d$ as calculated using GEANT4 + STAR TPC simulation [24].

in case of anti-nuclei) in the detector material. This effect is not included in the previously mentioned embedding events. Therefore, we have separately calculated the correction factors for absorption of light nuclei using GEANT4 model + STAR detector geometry [24]. The fraction of Un-absorbed/observed nuclei as a function of $p_T$ was calculated and applied to the raw spectra. Figure 3.11 shows the ratio of tracking efficiencies of $p/\overline{d}$ and $p/d$ as a function of $p_T$. Since $p$ efficiencies includes the corrections due to absorption effect, the ratios $p/\overline{d}$ and $p/d$ would corresponds to the unabsorbed/observed ratio. This absorption is independent of the beam energy and collision centrality which are presented in this thesis [24]. The fractions as a function of $p_T$ as shown Fig. 3.11 are used to correct the raw $\overline{d}$ and $d$ spectra.

## 3.5.6   Systematic Uncertainties

There are multiple sources of systematical errors such as tracking efficiency, PID efficiency, and fit to the spectra, which must be taken into account for the final results. For the $p_T$ spectra of $d$ and $\overline{d}$, the average systematic errors were estimated by varying the analysis track cuts, fitting range, backgrounds, and matching efficiencies. Table 3.5 represents the variation of cuts for the systematic error study. The default cuts used in this analysis are also shown in Table 3.5 for comparison. The Gaussian fit ranges are varied to estimate the systematic uncertainty on the extracted raw spectra.

The estimated uncertainties due to fit range variation are less than 4% for $d$ and $\bar{d}$.

Table 3.5: List of all systematic variations of track selection cuts used in this analysis.

| variable name | Default value | variation 1 | variation 2 | variation 3 | variation 4 |
|---|---|---|---|---|---|
| $|y| \leq$ | 0.30 | 0.20 | 0.25 | 0.35 | 0.40 |
| $|\eta| \leq$ | 1.0 | 0.8 | 0.9 | 1.1 | 1.2 |
| nHitsFit $\geq$ | 25 | 11 | 15 | 20 | 30 |
| ratio $\geq$ | 0.52 | 0.40 | 0.45 | 0.55 | 0.60 |
| nHitsdEdx $\geq$ | 10 | 5 | 8 | 12 | 15 |
| DCA $\leq$ | 1.0 | 0.6 | 0.8 | 1.2 | 1.4 |
| $|Z| \leq$ | 0.20 | 0.16 | 0.18 | 0.22 | 0.24 |

Along with the systematic cuts mentioned in the Table 3.5, the track cut for calculating TOF matching efficiency has also been varied once to include the systematic effect due to TOF match efficiency. The overall systematic error on each $p_T$ point is then obtained by calculating R.M.S. deviation, with respect to the values corresponding to the default cuts.

## 3.6    Results and Discussion

Here we present the transverse momentum spectra of light nuclei $d$ and $\bar{d}$ in Au+Au collisions at $\sqrt{s_{NN}}$ = 7.7, 11.5, 19.6, 27 and 39 GeV. The energy and centrality dependence of particle yields per unit rapidity (dN/dy), mean $p_T$ (denoted as $\langle p_T \rangle$), $B_2$ ($\overline{B_2}$), $d/p$ ($\bar{d}/\bar{p}$) ratios are also presented. The sources of systematic errors has been discussed later on.

### 3.6.1    Invariant Yield as a Function of Transverse Momentum

The shape of transverse momentum ($p_T$) spectra and centrality dependence of the spectra are sensitive to the collision dynamics. In heavy-ion collisions, high density of particles are produced. The particles collide frequently and act as a collective fluid, instead of free particles. The pressure generated during the collision process boosts the produced particle away from the center of the collision. This leads to an expanding

source, which might be thermalized. The scattering and collective expansion which is driven by internal pressure gradients introduce a blast velocity. This blast (hydro-like) velocity combined with the (thermal or kinetic) freeze-out temperature, describes the shape of the transverse momentum spectra, which depends on the mass of the measured identified particle [27]. The corrected invariant spectra presented in this chapter can be written as,

$$\frac{1}{N_{\text{event}}}\frac{d^2N}{2\pi p_{\text{T}}dp_{\text{T}}dy} = \frac{1}{N_{\text{event}}} \times \frac{1}{2\pi p_{\text{T}}} \times \frac{1}{\delta p_{\text{T}}\delta y} \times \frac{1}{C(p_{\text{T}})} \times Y(p_{\text{T}}) \qquad (3.17)$$

where $Y(p_{\text{T}})$ and $C(p_{\text{T}})$ are, respectively, raw spectra and correction factors.

Figure 3.12 and 3.13 show the $p_{\text{T}}$ spectra of $d$ and $\bar{d}$, respectively, for Au+Au collisions at $\sqrt{s_{\text{NN}}} = 39, 27, 19.6, 11.5$ and $7.7$ GeV. $p_{\text{T}}$ spectra are measured at mid-rapidity ($|y| < 0.3$) and for eight centrality bins. In Fig. 3.12 and Fig. 3.13, spectra of centrality bins are scaled by powers of 10 for better visibility. Curves shown on the spectra represent Blast-wave (defined later in Eq. 3.20) fit to the spectra. The Blast-wave fit is used to extract yield at unmeasured $p_{\text{T}}$ ranges where there is no data points. Blast-wave function is also used to calculate $\langle p_{\text{T}} \rangle$. Other functional forms were also used to fit the $p_{\text{T}}$-spectra are given in Eq. 3.21. The fit functions in Eq. 3.21, were used to calculate systematic error on the integrated yield and $\langle p_{\text{T}} \rangle$. The shape of both $d$ and $\bar{d}$ spectra seems to be hardening for increasing centrality. As central collisions produce more particles, collective effects should be stronger and therefore, heavier particles should be boosted to higher transverse momenta. The spectra can be further studied by looking at $\langle p_{\text{T}} \rangle$ which is presented in the following subsection.

### 3.6.2   Average Transverse Momentum $\langle p_{\text{T}} \rangle$

The change in the measured spectral shapes can be quantitatively characterized by the average transverse momentum ($\langle p_{\text{T}} \rangle$) in terms of energy and centrality. In general, it provides the information on the transverse dynamics of different types of particles.
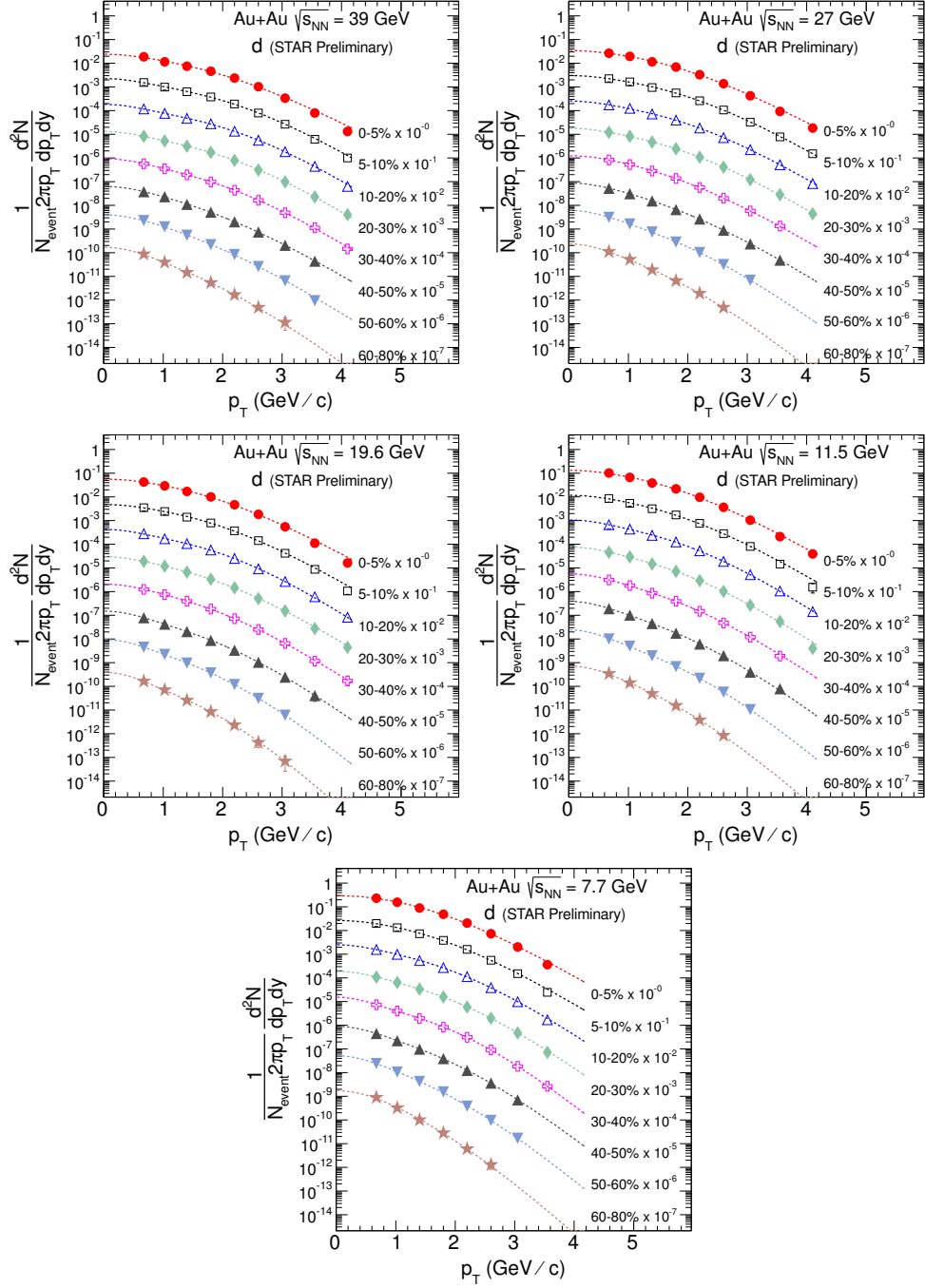
Figure 3.12: Centrality dependence of *d*-spectra measured in mid-rapidity ($|y| < 0.3$) in Au+Au collisions at $\sqrt{s_{\mathrm{NN}}}$ = 39, 27, 19.6, 11.5, 7.7 GeV. Spectra are shown in eight centrality bins and are scaled for different collision centrality for clarity. Curves represent Blast-wave fit to the data points. Error bars corresponds to quadrature sum of statistical and systematic error.
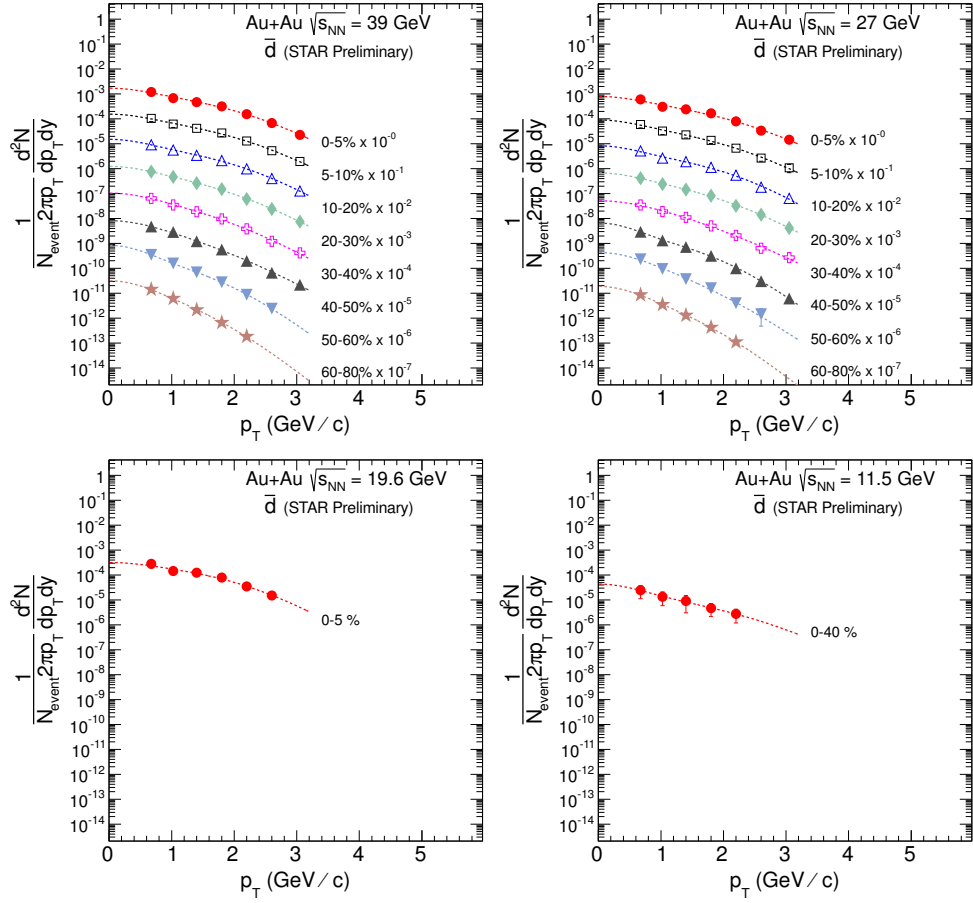
Figure 3.13: Centrality dependence of $\bar{d}$-spectra measured in mid-rapidity ($|y| < 0.3$) in Au+Au collisions at $\sqrt{s_{NN}} = 39, 27, 19.6$ and $11.5$ GeV. Spectra for $\sqrt{s_{NN}} = 39, 27$ GeV are scaled for different collision centrality for clarity. Due to low particle statistics, $\bar{d}$ spectra is shown for only one centrality in $\sqrt{s_{NN}} = 19.6$ and $11.5$ GeV. Curves represent Blast-wave fit to the data points. Error bars corresponds to quadrature sum of statistical and systematic error.

We calculate $\langle p_T \rangle$ using the following formula,

$$\langle p_T \rangle = \frac{\int p_T 2\pi p_T f(p_T) dp_T}{\int 2\pi p_T f(p_T) dp_T}, \tag{3.18}$$

where $f(p_T)$ are the fit functions used for $d$ and $\bar{d}$ as mentioned earlier and the integration is over 0-10 GeV/c.
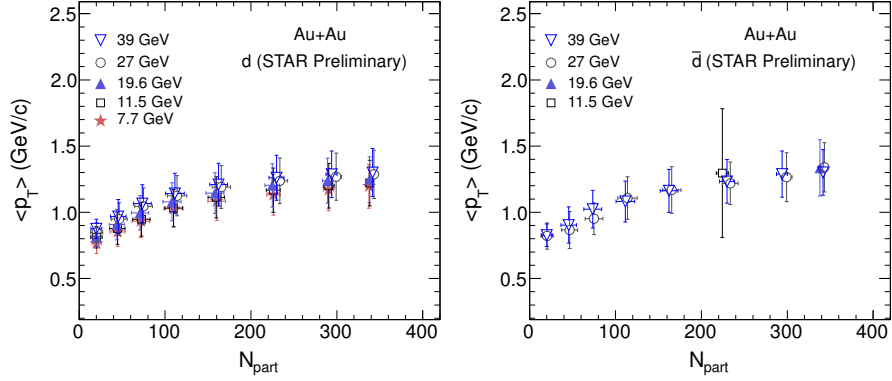
Figure 3.14: $\langle p_T \rangle$ of $d$ and $\overline{d}$ as a function of centrality ($N_{\mathrm{part}}$) for $\sqrt{s_{\mathrm{NN}}} = 39$, 27, 19.6, 11.5 and 7.7 GeV. the $\overline{d}$ $\langle p_T \rangle$ at $\sqrt{s_{\mathrm{NN}}} = 11.5$ GeV corresponds to centrality 0-40%.

**Systematic Uncertainties on $\langle p_T \rangle$**

Systematic uncertainties on $\langle p_T \rangle$ depend on the extrapolation of spectra. It is estimated by using the various functional forms used for extrapolation of the $p_T$ spectra (Eq. 3.20, Eq. 3.21.). For deuteron, an additional systematic uncertainty on $\langle p_T \rangle$ due to the $p_T$-dependent $d$ background from the beam pipe. The systematic error due to these sources estimated and included in quadrature to the total systematic uncertainties. The total uncertainties on $\langle p_T \rangle$ are $\sim$14%, and $\sim$19% for $d$ and $\overline{d}$ respectively. Figure 3.14 shows the mid-rapidity $\langle p_T \rangle$ of $d$ and $\overline{d}$ as a function of $\langle N_{\mathrm{part}} \rangle$ for Au+Au collisions at $\sqrt{s_{\mathrm{NN}}} = 39$, 27, 19.6, 11.5 and 7.7 GeV.
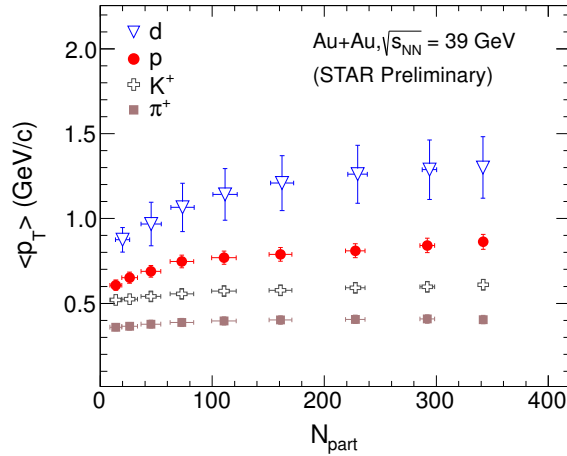


Figure 3.15: $\langle p_T \rangle$ of $d$, $p$, $K^+$ and $\pi^+$ as a function of centrality ($N_{\mathrm{part}}$) for $\sqrt{s_{\mathrm{NN}}} = 39$ GeV. $\langle p_T \rangle$ of $p$, $K^+$ and $\pi^+$ is taken from [49].

The trends of $\langle p_T \rangle$ of $d$ and $\bar{d}$ are similar in beam energies studied. $\langle p_T \rangle$ of both $d$ and $\bar{d}$ increases monotonically with increasing centrality. The $\langle p_T \rangle$ of $d$ and $\bar{d}$ shows almost no energy dependence, The increases of $\langle p_T \rangle$ with centrality implies large radial flow in central collisions. In Au+Au collisions, the increase is dominantly driven by the collective expansion of the system. These dependences are consistent with radial flow observations that it affects the heavier particles more than the lighter ones, and the strength of radial flow is larger in central collisions than in peripheral collisions. Figure 3.15 shows the comparison of $\langle p_T \rangle$ of $d$ with that of $p$, $K^+$ and $\pi^+$ at $\sqrt{s_{\mathrm{NN}}} = 39$ GeV. From Fig. 3.15, we observer that $\langle p_T \rangle$ of $d$ for each centrality is higher than that of identified hadrons. This increases in $\langle p_T \rangle$ with increasing mass is consistent with hydrodynamic model expectations. Table 3.6 and Table 3.7 lists the $\langle p_T \rangle$ values for $d$ and $\bar{d}$ respectively.

Table 3.6: $\langle p_T \rangle$ (GeV/c) of $d$ for $\sqrt{s_{\mathrm{NN}}} = 39$, 27, 19.6, 11.5 and 7.7 GeV.

| $\sqrt{s_{\mathrm{NN}}}$ | 39 GeV | 27 GeV | 19.6 GeV | 11.5 GeV | 7.7 GeV |
|---|---|---|---|---|---|
| 0-5% | $1.30 \pm 0.18$ | $1.29 \pm 0.18$ | $1.25 \pm 0.17$ | $1.22 \pm 0.17$ | $1.20 \pm 0.16$ |
| 5-10% | $1.29 \pm 0.18$ | $1.27 \pm 0.18$ | $1.24 \pm 0.17$ | $1.20 \pm 0.17$ | $1.17 \pm 0.16$ |
| 10-20% | $1.26 \pm 0.17$ | $1.24 \pm 0.17$ | $1.20 \pm 0.16$ | $1.17 \pm 0.17$ | $1.13 \pm 0.15$ |
| 20-30% | $1.21 \pm 0.16$ | $1.19 \pm 0.16$ | $1.15 \pm 0.15$ | $1.11 \pm 0.16$ | $1.08 \pm 0.14$ |
| 30-40% | $1.14 \pm 0.15$ | $1.12 \pm 0.15$ | $1.08 \pm 0.14$ | $1.03 \pm 0.14$ | $1.03 \pm 0.13$ |
| 40-50% | $1.07 \pm 0.14$ | $1.05 \pm 0.14$ | $1.00 \pm 0.13$ | $0.95 \pm 0.13$ | $0.93 \pm 0.12$ |
| 50-60% | $0.97 \pm 0.13$ | $0.95 \pm 0.12$ | $0.91 \pm 0.12$ | $0.88 \pm 0.12$ | $0.85 \pm 0.11$ |
| 60-80% | $0.87 \pm 0.07$ | $0.85 \pm 0.07$ | $0.81 \pm 0.07$ | $0.81 \pm 0.08$ | $0.76 \pm 0.08$ |

Table 3.7: $\langle p_T \rangle$ (GeV/c) of $\bar{d}$ for $\sqrt{s_{\mathrm{NN}}} = 39$, 27, 19.6, 11.5. $\langle p_T \rangle$ of $\bar{d}$ at $\sqrt{s_{\mathrm{NN}}} = 11.5$ GeV corresponds to 0-40% centrality

| $\sqrt{s_{\mathrm{NN}}}$ | 39 GeV | 27 GeV | 19.6 GeV | 11.5 GeV |
|---|---|---|---|---|
| 0-5% | $1.30 \pm 0.17$ | $1.34 \pm 0.19$ | $1.34 \pm 0.21$ | $1.30 \pm 0.49$ |
| 5-10% | $1.29 \pm 0.17$ | $1.27 \pm 0.18$ | $-$ | $-$ |
| 10-20% | $1.23 \pm 0.17$ | $1.22 \pm 0.16$ | $-$ | $-$ |
| 20-30% | $1.16 \pm 0.16$ | $1.17 \pm 0.18$ | $-$ | $-$ |
| 30-40% | $1.08 \pm 0.15$ | $1.11 \pm 0.16$ | $-$ | $-$ |
| 40-50% | $1.02 \pm 0.14$ | $0.95 \pm 0.12$ | $-$ | $-$ |
| 50-60% | $0.90 \pm 0.14$ | $0.87 \pm 0.14$ | $-$ | $-$ |
| 60-80% | $0.83 \pm 0.09$ | $0.82 \pm 0.10$ | $-$ | $-$ |

### 3.6.3  Light Nuclei Yield

The total particle multiplicity reflects the total entropy generated in the heavy-ion collision system. $p_T$ spectra provides the information of transverse dynamics of collisions whereas integrated particle yields $(dN/dy)$ versus $y$ provides the information on longitudinal dynamics of collisions. The invariant yield integrated over $p_T$ gives the total integrated particle yield at mid-rapidity. The integrated yield is calculated from spectra as,

$$\frac{dN}{dy} = \int 2\pi p_T f(p_T) dp_T \tag{3.19}$$

where $f(p_T) = \frac{1}{2\pi p_T}\frac{d^2 N}{dp_T dy}$ for the measured $p_T$ range and $f(p_T) = $ the fit function used to best fit the $p_T$ spectra. The dN/dy for $d$ and $\bar{d}$ are extracted at mid-rapidity $(|y| < 0.3)$ from the measured $p_T$ spectra up to $p_T \approx 4.0$ GeV/c and 3.0 GeV/c respectively. The yield is extrapolated to the unmeasured region (up to $p_T = 10$ GeV/c). Extrapolation is done by fitting the $p_T$ spectra by Blast-wave function which is given by,

$$\frac{dN}{p_T dp_T} = \int_0^R r\ dr\ m_T\ I_0(\frac{p_T \sinh \rho(r)}{T_{kin}})K_1(\frac{m_T \cosh \rho(r)}{T_{kin}}) \tag{3.20}$$

where $T_{kin}$ kinetic freeze-out temperature, $m_T$ is transverse mass, $\rho(r) = \tanh^{-1}\beta$ and $I_0$ and $K_1$ are the modified Bessel functions. $\beta$ is the transverse radial flow velocity. We use the flow velocity profile of the form $\beta = \beta_S(r/R)^n$, where $\beta_S$ is the surface velocity, $r/R$ is the relative radial position in the thermal source, and $n$ is the exponent of flow velocity profile. The extrapolated yields are also estimated using different fit functions. The functions used in this analysis other than Blast-wave (Eg. 3.20) are as follows,

$$f_{\text{Bose-Einstein}} = \frac{A}{\exp(m_{\text{T}}/T_{\text{BE}}) - 1}$$

$$f_{\text{Boltzmann}} = A m_{\text{T}} \exp(-m_{\text{T}}/T_{\text{BE}}) \tag{3.21}$$

$$f_{\text{m}_{\text{T}}-\text{exponential}} = A \exp(-m_{\text{T}}/T_{\text{BE}})$$

The yield from these fit functions (Eq. 3.21) is used to determine systematic error on yield due to extrapolation.

Table 3.8: $dN/dy$ of $d$ at midrapidity ($|y| <$0.3) for Au+Au collisions at $\sqrt{s_{\text{NN}}} = 39, 27,$ 19.6, 11.5 and 7.7 GeV.

| $\sqrt{s_{\text{NN}}}$ | 39 GeV | 27 GeV | 19.6 GeV | 11.5 GeV | 7.7 GeV |
|---|---|---|---|---|---|
| 0-5% | 0.161 ± 0.025 | 0.243 ± 0.038 | 0.369 ± 0.056 | 0.861 ± 0.126 | 1.944 ± 0.284 |
| 5-10% | 0.126 ± 0.021 | 0.190 ± 0.031 | 0.282 ± 0.045 | 0.651 ± 0.102 | 1.510 ± 0.234 |
| 10-20% | 0.094 ± 0.015 | 0.142 ± 0.023 | 0.208 ± 0.033 | 0.496 ± 0.077 | 1.140 ± 0.173 |
| 20-30% | 0.063 ± 0.010 | 0.094 ± 0.015 | 0.138 ± 0.021 | 0.325 ± 0.049 | 0.738 ± 0.110 |
| 30-40% | 0.041 ± 0.006 | 0.060 ± 0.009 | 0.085 ± 0.013 | 0.200 ± 0.029 | 0.460 ± 0.066 |
| 40-50% | 0.026 ± 0.004 | 0.035 ± 0.005 | 0.048 ± 0.007 | 0.113 ± 0.016 | 0.256 ± 0.036 |
| 50-60% | 0.014 ± 0.002 | 0.018 ± 0.003 | 0.025 ± 0.004 | 0.056 ± 0.008 | 0.128 ± 0.017 |
| 60-80% | $(46\pm0.38)\times10^{-4}$ | $(59\pm0.59)\times10^{-4}$ | $(81\pm1.1)\times10^{-4}$ | $(171\pm2.4)\times10^{-4}$ | $(402\pm6.6)\times10^{-4}$ |

Table 3.9: $dN/dy$ of $\overline{d}$ at midrapidity ($|y| <$0.3) for Au+Au collisions at $\sqrt{s_{\text{NN}}} = 39, 27,$ 19.6 and 11.5 GeV. $dN/dy$ of $\overline{d}$ at $\sqrt{s_{\text{NN}}} = 11.5$ GeV corresponds to 0-40% centrality

| $\sqrt{s_{\text{NN}}}$ | 39 GeV | 27 GeV | 19.6 GeV | 11.5 GeV |
|---|---|---|---|---|
| 0-5% | $(101.2\pm15)\times10^{-4}$ | $(51.7\pm7.9)\times10^{-4}$ | $(24\pm3.7)\times10^{-4}$ | $(2.36\pm0.27)\times10^{-4}$ |
| 5-10% | $(82.4\pm13)\times10^{-4}$ | $(44.8\pm7.3)\times10^{-4}$ | – | – |
| 10-20% | $(69.0\pm11)\times10^{-4}$ | $(36.4\pm6.1)\times10^{-4}$ | – | – |
| 20-30% | $(55.3\pm8.6)\times10^{-4}$ | $(29.7\pm4.7)\times10^{-4}$ | – | – |
| 30-40% | $(42.6\pm6.3)\times10^{-4}$ | $(27.1\pm3.5)\times10^{-4}$ | – | – |
| 40-50% | $(34.6\pm4.4)\times10^{-4}$ | $(16.1\pm2.4)\times10^{-4}$ | – | – |
| 50-60% | $(18.5\pm2.6)\times10^{-4}$ | $(11.2\pm1.5)\times10^{-4}$ | – | – |
| 60-80% | $(7.1\pm0.14)\times10^{-4}$ | $(4.0\pm0.16)\times10^{-4}$ | – | – |

**Systematic Uncertainties on $dN/dy$**

The systematic uncertainties on the particle yields are obtained by using different fit functions and changing the fit ranges of $p_{\text{T}}$ spectra for the obtained yields. The systematic uncertainties on total particle yields are dominated by the uncertainties in the extrapolation, which are estimated to be of the order of 18% for $\overline{d}$, and 15% for $d$. The 5% overall MC uncertainty is added in quadrature. In addition to this, the

uncertainty due to different corrections like background, TOF matching efficiency, and tracking efficiency are added in quadrature. Particle identification (PID) represents varying the dE/dx cuts and varying the Gaussian fit ranges. The total systematic errors are $\sim 25\%$ for $\bar{d}$ and $\sim 20\%$ for $d$ respectively. Table 3.8 and Table 3.9 lists the $dN/dy$ values at mid-rapidity for $d$ and $\bar{d}$ in Au+Au collisions at $\sqrt{s_{\mathrm{NN}}} = 39, 27,$ 19.6, 11.5 and 7.7 GeV.

### 3.6.3.1 Centrality Dependence of $dN/dy$

The $dN/dy$ is expected to be scaled with the average number of participants $\langle N_{\mathrm{part}} \rangle$, since the low $p_{\mathrm{T}}$ part of the spectra is dominant in particle abundance and it is
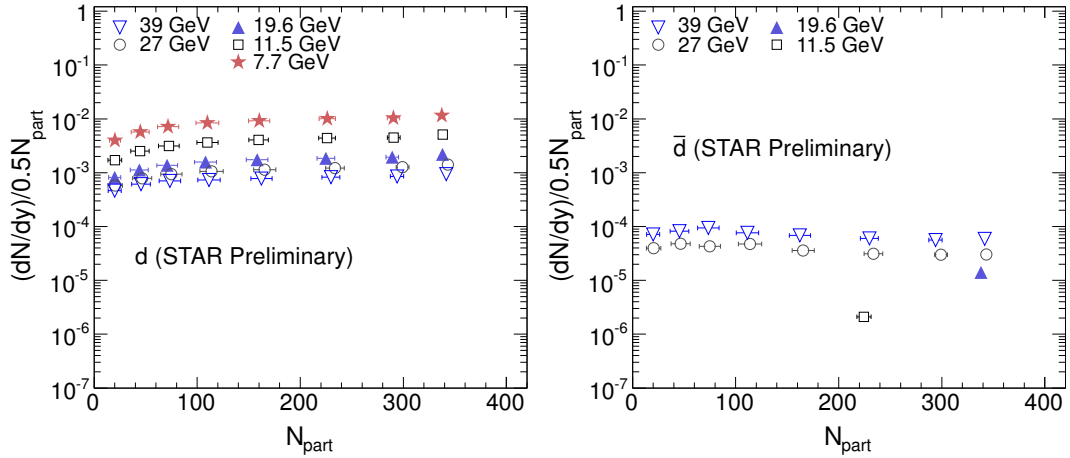


Figure 3.16: $(dN/dy)/\langle 0.5 N_{\mathrm{part}} \rangle$ of $d$ and $\bar{d}$ as a function of centrality ($N_{\mathrm{part}}$) for Au+Au collisions at $\sqrt{s_{\mathrm{NN}}} = 39, 27, 19.6, 11.5$ and 7.7 GeV. The $\bar{d}$ data point at = 11.5 GeV corresponds to centrality 0-40%.

produced by soft hadron production process. The $\langle N_{\mathrm{part}} \rangle$ values are estimated using a Glauber Monte Carlo simulation calculation as described earlier. Figure 3.16 shows the $dN/dy$ normalized to the average number of participated nucleons, $(dN/dy/\langle 0.5 N_{\mathrm{part}} \rangle)$ vs. $\langle N_{\mathrm{part}} \rangle$, for $d$ and $\bar{d}$ in Au+Au collisions at $\sqrt{s_{\mathrm{NN}}} = 39, 27, 19.6, 11.5, 7.7$ GeV. The errors on the points corresponds to quadrature sum of statistical and systematic errors. Nuclei yields per participant pair increases with average participant number, which suggests that the yield could depend on the number of nucleon-nucleon binary

collisions. The increase in $d$ yield per participating nucleon with the increasing collision centrality is due to large baryon stopping in the lower energies. However, the $N_{\text{part}}$-scaled $\overline{d}$ yields shows weak centrality dependence.

### 3.6.3.2  Energy Dependence of $dN/dy$
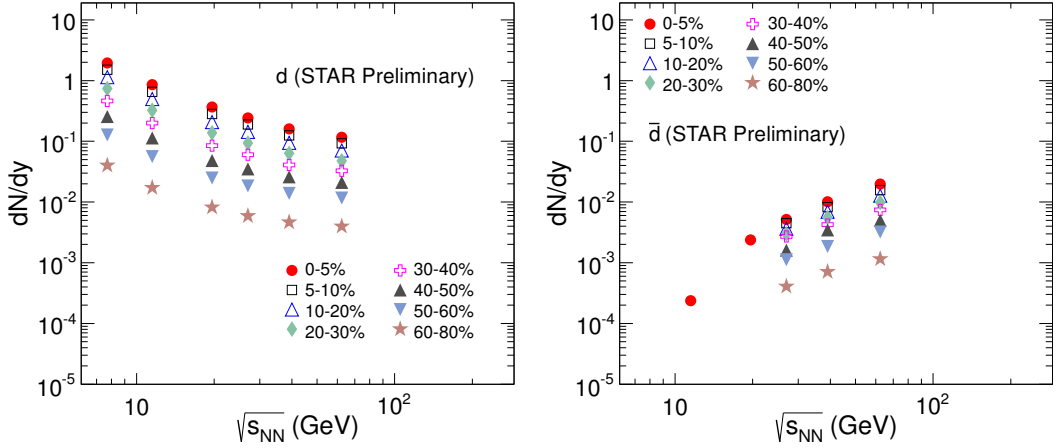


Figure 3.17: $(dN/dy)$ of $d$ and $\overline{d}$ as a function of $\sqrt{s_{\text{NN}}}$. The $\overline{d}$ data point at $= 11.5$ GeV corresponds to centrality 0-40%.

Figure 3.17 shows the $dN/dy$ of $d$ and $\overline{d}$ as a function of $\sqrt{s_{\text{NN}}}$ for different centrality classes in Au+Au collisions at $\sqrt{s_{\text{NN}}} = 39$, 27, 19.6, 11.5, 7.7 GeV. The errors on the points corresponds to quadrature sum of statistical and systematic errors. The yields of $\overline{d}$ increases with increasing collision energy whereas $d$ yields decreases with increase of collision energy. The increase in $d$ yield with the decreasing beam energy is due to large baryon stopping in the lower energies.

## 3.6.4  Coalescence Parameter

The coalescence parameter $B_2$ $(\overline{B}_2)$ is a useful tool to study the freeze-out dynamics of the system at hadronic phase as it is inversely proportional to the correlation volume of the system [33, 34]. To measure the coalescence parameter $B_2$ $(\overline{B}_2)$ and $d/p$ $(\overline{d}/\overline{p})$, shown later, we have used $p_{\text{T}}$-spectra of $p$ and $\overline{p}$ from [49]. However, the

$p$ and $\bar{p}$ spectra in [49] is not feed-down corrected for weak decay protons. Therefore, we have calculated fractions of weak decay $p$ and $\bar{p}$ from all possible particles (e.g. $\Lambda$, $\Xi$) produced in experiment and removed the contribution from the inclusive $p$ and $\bar{p}$ spectra in [49]. The procedure is explained in detail in the Appendix at the end of this chapter. We have used weak decay corrected $p$ and $\bar{p}$ spectra for the observables presented in this chapter. The following subsections shows the measurements of $B_2$ $(\overline{B}_2)$ and the corresponding physics discussion.
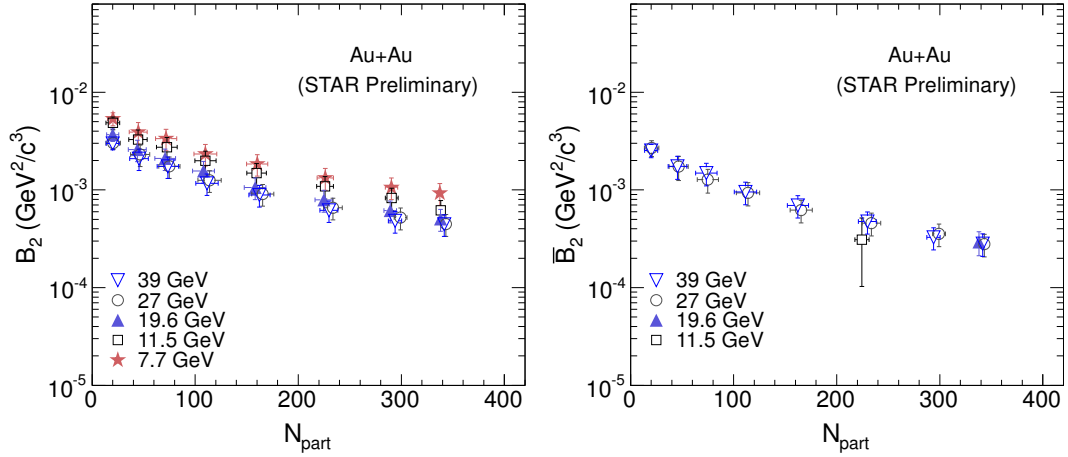


Figure 3.18: $B_2$ and $\overline{B}_2$ as a function of centrality ($N_{\mathrm{part}}$) for Au+Au collisions at $\sqrt{s_{\mathrm{NN}}}$ = 39, 27, 19.6, 11.5 and 7.7 GeV.

### 3.6.4.1 Centrality Dependence of $B_2$ and $\overline{B}_2$

Figure 3.18 shows the centrality dependence of $B_2$ and $\overline{B}_2$ for Au+Au collisions at $\sqrt{s_{\mathrm{NN}}}$ = 39, 27, 19.6, 11.5 and 7.7 GeV. As seen from Fig. 3.18, both $B_2$ and $\overline{B}_2$ decreases with increasing centrality for all beam energies. The correlation volume ($V_f$) is inversely proportional to $B_2(\overline{B}_2)$. Therefore, from Fig. 3.18, we can see that the correlation volume ($V_f$) increases with increasing centrality. The correlation volume ($V_f$) of $d$ also shows a slight energy dependence, it increases with increasing beam energy studied. Although $B_2$ shows energy dependence, $\overline{B}_2$ one the other hand is independent of energy. The centrality dependence of $\overline{B}_2$ is similar as $B_2$. Therefore,

the correlation volume ($V_f$) for $\bar{d}$ increases with increasing centrality similar to that of $d$.

### 3.6.4.2 Energy Dependence of $B_2$

Figure 3.19 shows the energy dependence of $B_2$ and $\overline{B}_2$ for central Au+Au collisions.
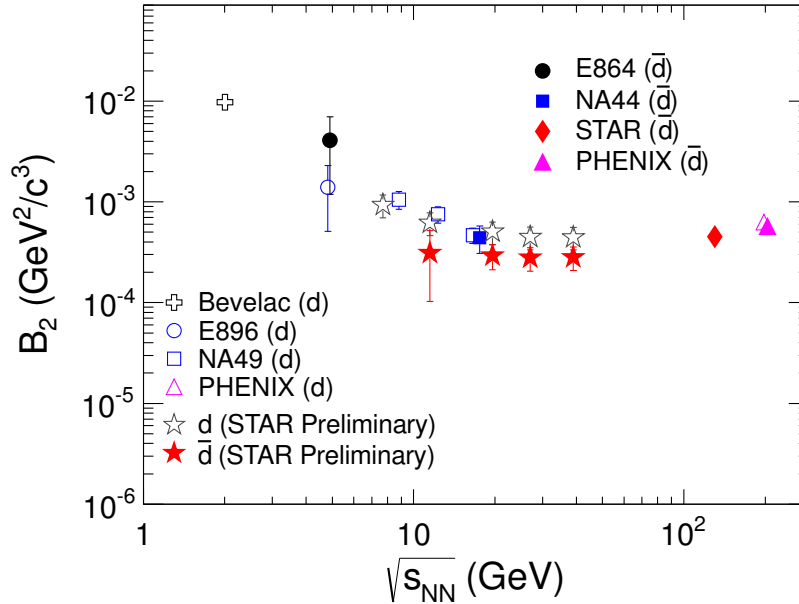


Figure 3.19: $B_2$ of $d$ and $\bar{d}$ as a function of $\sqrt{s_{\mathrm{NN}}}$ for Au+Au collisions at $\sqrt{s_{\mathrm{NN}}} = 39, 27, 19.6, 11.5$ and $7.7$ GeV. Data from other published results are also shown.

The result are also compared with other published results from Bevalac [28], SPS [30], AGS [29], and RHIC [31]. The measurement of $B_2$ of $d$ and $\bar{d}$ performed in this analysis are shown by open and filled star symbol in Fig. 3.19. The $B_2$ measurements in this thesis work are consistent with other previous measurements in similar energies. As seen in Fig. 3.19, $B_2$ decreases with increasing beam energy then reaches a plateau. $B_2$ of $\bar{d}$ on the other hand decreases rapidly from the AGS energies and then becomes almost constant with respect to $\sqrt{s_{\mathrm{NN}}}$. This indicates that the source volume does not change appreciably with center-of-mass energy (with the caveat that $B_2$ varies as a function of centrality). This observation is consistent with what has been observed in Bose-Einstein correlation Hanbury Brown Twiss analysis at RHIC [32] for identified

particles. The beam energy dependence of $B_2$ for $d$ and $\bar{d}$ in the measured beam energy ($\sqrt{s_{NN}} = 39, 27, 19.6, 11.5, 7.7$ GeV) is almost equal within the error, indicating that nuclei and anti-nuclei might have similar temperature, flow, and freeze-out density distributions.

## 3.6.5 Nuclei to Nucleon Ratio

The coalescence measurement is sensitive to the phase space of baryon and anti-baryon [35, 36] [18, 73]. $\bar{d}/\bar{p}$ (ratio of the differential cross section) can be taken as a measure of the anti-baryon phase space density at kinetic freeze-out where coalescence happens. The following subsections presents the measurements of $d/p$ and $\bar{d}/\bar{p}$ ratio and corresponding physics discussion.

### 3.6.5.1 Centrality Dependence of Nuclei to Nucleon ratio
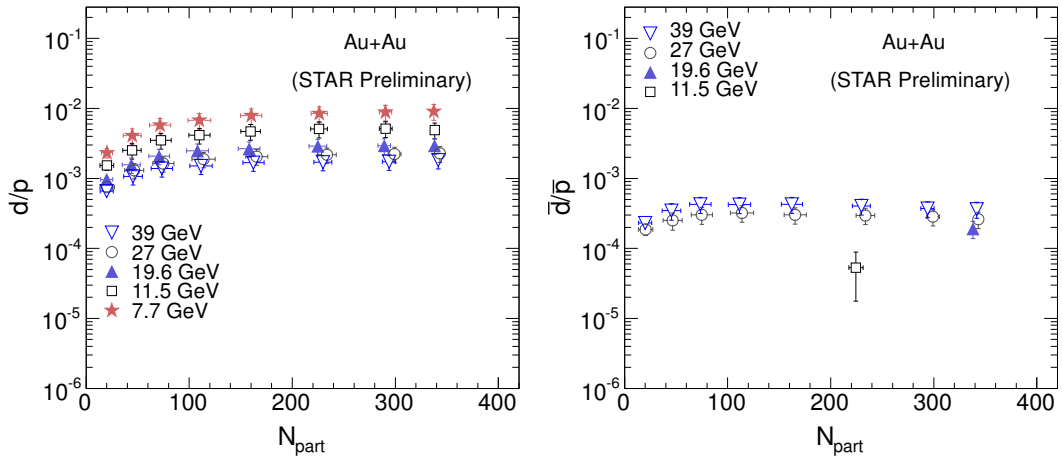


Figure 3.20: $d/p$ and $\bar{d}/\bar{p}$ as a function of centrality ($N_{\text{part}}$) for Au+Au collisions at $\sqrt{s_{NN}}$ = 39, 27, 19.6, 11.5 and 7.7 GeV.

Figure 3.20 shows the centrality dependence of $d/p$ and $\bar{d}/\bar{p}$ ratios in Au+Au collisions at $\sqrt{s_{NN}}$ = 39, 27, 19.6, 11.5, 7.7 GeV. From Fig. 3.20 we see that both $d/p$ and $\bar{d}/\bar{p}$ increase with increasing centrality at first then reaches a plateau region for midcentral to central collisions. The lower $d/p$ and $\bar{d}/\bar{p}$ ratio at peripheral collision may indicate

the reduction of nuclei production at peripheral collisions due to low production of nucleons. We also observe that both $d/p$ and $\overline{d}/\overline{p}$ shows energy dependence for all centrality. $d/p$ ratio increases with decreasing beam energy, indicating the formation of baryon rich system at low beam energies. The $\overline{d}/\overline{p}$ ratio however, decreases with decreasing beam energy. This reduction in $\overline{d}/\overline{p}$ ratio at low beam energy can be attributed to the lower production of anti-nuclei at low beam energies.

### 3.6.5.2 Energy Dependence of $\overline{d}/\overline{p}$ and $d/p$ Ratios

Figure 3.21 shows the variation of $d/p$ and $\overline{d}/\overline{p}$ ratios as a function of center-of-mass energy in central Au+Au collisions at $\sqrt{s_{\mathrm{NN}}}$ = 39, 27, 19.6, 11.5, 7.7 GeV. Data of $\overline{d}/\overline{p}$ ratio from various beam energies and colliding species ($pp$, $\overline{p}p$, $pA$, $AA$) [37, 38, 39, 40, 41, 42, 43, 44, 45, 46, 47] are collected and shown in Fig. 3.21. One very interesting observation is that the ratio increases monotonically with beam energies and reaches a plateau above ISR beam energy regardless of the beam species ($pp$, $pA$, $AA$). Similar behavior has been seen in $\overline{p}/p$ ratio as a function of beam energy [48].
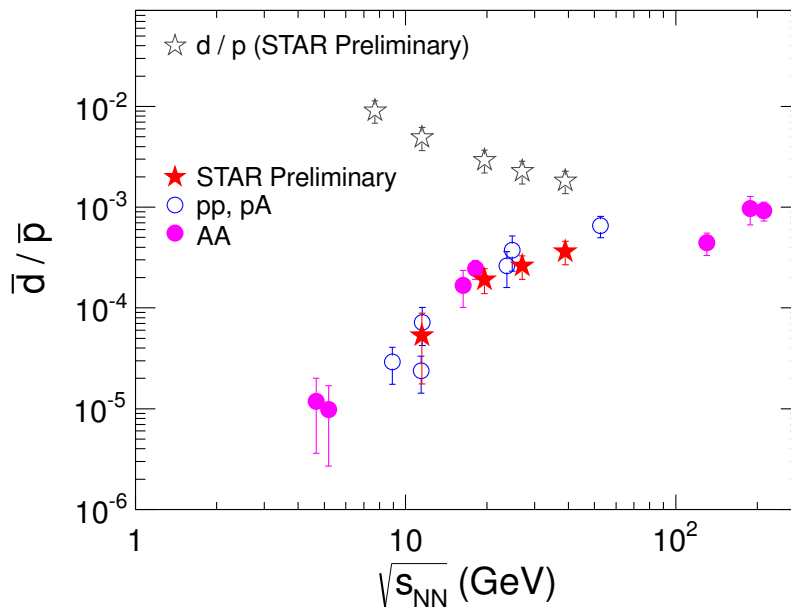


Figure 3.21: $d/p$ and $\overline{d}/\overline{p}$ as a function of $\sqrt{s_{\mathrm{NN}}}$ for Au+Au collisions at $\sqrt{s_{\mathrm{NN}}}$ = 39, 27, 19.6, 11.5 and 7.7 GeV. Data from other published results are also shown.

### 3.6.6 Summary

We have measured the $d$ and $\overline{d}$ production in Au+Au collisions at $\sqrt{s_{\mathrm{NN}}} = 39, 27, 19.6,$ 11.5 and 7.7 GeV. The transverse momentum distributions $d$ and $\overline{d}$ are presented for 0-5%, 5-10%, 10-20%, 20-30%, 30-40%, 40-50%, 50-60%, and 60-80% centrality bins. The bulk properties are studied by measuring the integrated nuclei yield ($dN/dy$), $\langle p_{\mathrm{T}} \rangle$, particle ratios, $B_2$ and $d/p$ ($\overline{d}/\overline{p}$). The results are compared with the corresponding published results from other collision energies and experiments. $\langle N_{\mathrm{part}} \rangle$ scaled $d$ and $\overline{d}$ yield shows weak centrality dependence. The increase in $d$ yield per participating nucleon with the increasing collision centrality indicated large baryon stopping in the lower energies. The yields of $\overline{d}$ is found decrease with decreasing collision energy. However, yields of $d$ increases with decreasing collision energy indicating baryon rich medium at low beam energies. The centrality dependence of $\langle p_{\mathrm{T}} \rangle$ of $d$ and $\overline{d}$ is found to be similar for all beam energies. Increase of $\langle p_{\mathrm{T}} \rangle$ with increasing centrality indicates the existence of higher radial flow for central collisions. The measured $B_2$ for $d$ and $\overline{d}$ shows strong centrality dependence indicating variation of correlation volume with centrality. $B_2$ for $d$ and $\overline{d}$ is consistent with other published results from Bevalac AGS, SPS, RHIC. The measured $B_2$ for $d$ and $\overline{d}$ is found to be of similar magnitude for the beam energies studied in this thesis. $d/p$ and $\overline{d}/\overline{p}$ ratio is found to show slight centrality dependence. The energy dependence of $d/p$ and $\overline{d}/\overline{p}$ is found to be opposite in trend. The $\overline{d}/\overline{p}$ ratios measured in this thesis are consistent with other published results. The $\overline{d}/\overline{p}$ ratio is found to increase monotonically with beam energies and then reaching a plateau above ISR beam energy regardless of the beam species (pp, pA, AA).

# Bibliography

[1] H. H. Gutbrod et al., Phys. Rev. Lett. **37**, 667 (1976).

[2] R. Scheibl and U. Heinz, Phys. Rev. C **59**, 1585 (1999); W. J. Llope et al., Phys. Rev. C **52**, 2004 (1995).

[3] H. Sato and K. Yazaki, Phys. Lett. B **98**, 153 (1981).

[4] S.T. Butler and C.A. Pearson, Phys. Rev. **129**, 836 (1963).

[5] H. H. Gutbrod *et al.*, Phys. Rev. Lett. **37**, 667 (1976);

[6] A. Z. Mekjian, Phys. Rev. C 17, 1051 (1978); S. Das Gupta and A. Z. Mekjian, Phys. Rep. 72, 131 (1981).

[7] C. Adler *et al.*, Nucl. Instrum. Methods A **470**, 488499 (2001).

[8] W. J. Llope *et al.*, Nucl. Instrum. Methods A **522**, 252 (2005).

[9] C. A. Whitten Jr, AIP Conf. Proc. **980**, 390 (2008); J. Kiryluk, arXiv:hep-ex[0501072].

[10] L. Adamczyk *et al.*, Phys. Rev. C **88**, 014902 (2013).

[11] M. Anderson *et al.*, Nucl. Instrum. Methods A **499**, 659 (2003).

[12] H. Bichsel, Nucl. Instrum. Methods A **562**, 154 (2006).

[13] W. J. Llope, Nucl. Instrum. Methods B **241**, 306 (2005).

[14] J. Beringer *et al.*, Phys. Rev. D 86, 010001 (2012).

[15] D. Kharzeev and M. Nardi, Phys. Lett. B **507**, 121 (2001).

[16] H. Masui and A. Schmah, arXiv:1212.3650v1 [nucl-ex].

[17] B. B. Back *et al.*, Phys. Rev. C **70**, 021902(R) (2004).

[18] H. Long, Ph.D. thesis, UCLA, 2002.

[19] `http://geant4.web.cern.ch/geant4/UserDocumentation/UsersGuides/`
`IntroductionToGeant4/html/index.html`

[20] P. Nevski, `http://www.star.bnl.gov/STARAFS/comp/simu/gstar/gstar.html`.

[21] W. M. Yao *et al.*, (Particle Data Group), J. Phys. G **33**, 1 (2006).

[22] J. Adams *et al.*, Phys. Rev. C **70**, 041901 (2004).

[23] B. I. Abelev *et al.*, Phys. Rev. C **79**, 034909 (2009).

[24] STAR collaboration poster, Quark Matter 2012, `https://indico.cern.ch/event/`
`181055/session/37/contribution/308`.

[25] E. Schnedermann and U. W. Heinz, Phys. Rev. C **50**, 1675 (1994).

[26] L. Van Hove, Phys. Lett. B **118**, 138 (1982).

[27] E. Schnedermann *et al.*, Phys. Rev. C **48**, 2462 (1993).

[28] S. Wang *et al.*, Phys. Rev. Lett. **74**, 2646 (1995).

[29] S. Albergo *et al.*, Phys. Rev. C **65**, 034907 (2002). T. A. Armstrong *et al.*, Phys. Rev. Lett. **85**, 2685 (2000).

[30] T. Anticic *et al.*, Phys. Rev. C **69**, 024902 (2004). I. G. Bearden *et al.*, Phys. Rev. Lett. **85**, 2681 (2000).

[31] C. Adler *et al.*, Phys. Rev. Lett. **87**, 262301 (2001). S. S. Adler *et al.*, Phys. Rev. Lett. **94**, 122302 (2005).

[32] K. Adcox *et al.*, Phys. Rev. Lett. **88**, 192302 (2002); C. Adler *et al.*, Phys. Rev. Lett. **87**, 082301 (2001).

[33] R. Bond, P. J. Johnansen, S. E. Koonin, and S. Garpman, Phys. Lett. **71B**, 43 (1977).

[34] A. Z. Mekjian, Phys. Rev. Lett. **38**, 640 (1977); Phys. Rev. C **17**, 1051 (1978); Nucl. Phys. A **312**, 491 (1978).

[35] F. Q. Wang and N. Xu, Phys. Rev. C 61, 021904 (2000); F. Q. Wang, Phys. Lett. B 489, 273 (2000).

[36] P. J. Siemens and J. I. Kapusta, Phys. Rev. Lett. **43**, 1486 (1979); Phys. Rev. Lett. **43**, 1690(E) (1979); L. P. Csernai and J. I. Kapusta, Phys. Rep. **131**, 223 (1986).

[37] T. A. Armstrong *et al.*, Phys. Rev. C **61**, 064908 (2000).

[38] F. Binon *et al.*, Phys. Lett. B **30**, 510 (1969).

[39] J. A. Appel *et al.*, Phys. Rev. Lett. **32**, 428 (1974).

[40] B. Alper *et al.*, Phys. Lett. B **46**, 265 (1973).

[41] T. Alexopoulos *et al.*, Phys. Rev. D **62**, 072004 (2000).

[42] M. Aoki *et al.*, Phys. Rev. Lett. **69**, 2345 (1992).

[43] T. A. Armstrong *et al.*, Phys. Rev. Lett. **85**, 2685 (2000).

[44] G. Ambrosini *et al.*, New J. Phys. **1**, 22.1 (1999); Heavy Ion Phys. **14** 297 (2001), e-print arxiv: nucl-ex/0011016..

[45] I. G. Bearden *et al.*, Phys. Rev. Lett. **85**, 2681 (2000).

[46] C. Adler *et al.*, Phys. Rev. Lett. **87**, 262301 (2001).

[47] S. S. Adler *et al.*, Phys. Rev. Lett. **94**, 122302 (2005).

[48] C. Adler *et al.*, Phys. Rev. Lett. **86**, 4778 (2001); L. Ahle *et al.*, Phys. Rev. Lett. **81**, 2650 (1998); F. Sickler *et al.*, Nucl. Phys. A **661**, 45c (1999); G. E. Copper, Ph.D Thesis, University of California at Berkeley, 2000; A. M. Rossi *et al.*, Nucl. Phys. B **84**, 269 (1975); M. Aguilar-Benitez *et al.*, Z. Phys. C **50**, 405 (1991).

[49] L. Kumar *et al.*, Nuclear Physics A **931**,1114-1119 (2014).

[50] X. Zhu *et al.*, Acta Phys. Polon. Supp. **5** 213-218 (2012); X. Zhu *et al.*, Journal of Physics, **509**, 012004 (2014).

[51] B. I. Abelev *et al.*, Phys. Rev. Lett. **97**, 152301 (2006).

## 3.7 Appendix

### 3.7.1 Refmult Cuts for Determining the Centrality

Table 3.10: Refmult cuts for determining centrality

| $\sqrt{s_{\mathrm{NN}}}$ | 0-5% | 5-10% | 10-20% | 20-30% | 30-40% | 40-50% | 50-60% | 60-70% | 70-80% |
|---|---|---|---|---|---|---|---|---|---|
| 200 GeV | 446 | 379 | 269 | 184 | 119 | 73 | 41 | 21 | 10 |
| 62.4 GeV | 329 | 285 | 199 | 135 | 88 | 54 | 30 | 16 | 7 |
| 39 GeV | 316 | 265 | 185 | 125 | 81 | 50 | 28 | 15 | 7 |
| 27 GeV | 288 | 241 | 168 | 114 | 74 | 45 | 26 | 13 | 6 |
| 19.6 GeV | 263 | 220 | 152 | 102 | 66 | 40 | 23 | 12 | 6 |
| 11.5 GeV | 221 | 184 | 127 | 86 | 56 | 34 | 19 | 10 | 5 |
| 7.7 GeV | 185 | 154 | 106 | 72 | 46 | 28 | 16 | 8 | 4 |

### 3.7.2 $\langle N_{\mathrm{part}} \rangle$ and $\langle N_{\mathrm{coll}} \rangle$ for Au+Au Collisions

Table 3.11: $\langle N_{\mathrm{part}} \rangle$ for different centrality bins

| $\sqrt{s_{\mathrm{NN}}}$ | 39 GeV | 27 GeV | 19.6 GeV | 11.5 GeV | 7.7 GeV |
|---|---|---|---|---|---|
| 0-5% | 341.7±2.2 | 343.3±2.0 | 338.0±2.3 | 338.2±2.0 | 337.4±2.1 |
| 5-10% | 293.9±6.4 | 299.3±6.2 | 289.2±6.0 | 290.6±6.2 | 290.4±6.0 |
| 10-20% | 229.8±8.7 | 233.6±9.0 | 224.9±8.6 | 226.0±8.2 | 226.2±7.9 |
| 20-30% | 162.4±10.2 | 165.5±10.7 | 158.1±10.5 | 159.6±9.5 | 160.2±10.2 |
| 30-40% | 111.4±10.8 | 114.0±11.3 | 108.0±10.6 | 110.0±10.3 | 109.9±11.0 |
| 40-50% | 73.5±10.4 | 75.0±10.3 | 70.8±10.1 | 72.5±10.1 | 71.8±10.2 |
| 50-60% | 45.5±8.9 | 46.7±9.2 | 43.9±8.7 | 44.5±8.9 | 44.7±8.7 |
| 60-80% | 20.0±6.4 | 20.5±7.1 | 19.9±5.9 | 20.1±6.7 | 20.2±5.3 |

### 3.7.3 Correction of $p$, $\bar{p}$ Spectra for Feed-down Effect

The $p$, $\bar{p}$ spectra in [49] is inclusive, *i.e.* it contain primary $p$ ($\bar{p}$) as well as $p$ ($\bar{p}$) coming from weak decays of other particles such as $\Lambda(\bar{\Lambda})$, $\Xi(\bar{\Xi})$. Therefore, corrections have been applied on the inclusive $p$, $\bar{p}$ spectra before calculating the quantities $B_2$ $\left(\overline{B_2}\right)$ and $d/p$ ($\bar{d}/\bar{p}$). To calculate the feed-down $p$ ($\bar{p}$) coming from weak decays, we need

Table 3.12: $\langle N_{\mathrm{coll}} \rangle$ for different centrality bins

| $\sqrt{s_{\mathrm{NN}}}$ | 39 GeV | 27 GeV | 19.6 GeV | 11.5 GeV | 7.7 GeV |
|---|---|---|---|---|---|
| 0-5% | 852.7±26.9 | 841.5±28.4 | 799.8±27.4 | 784.5±27.2 | 773.8±28.2 |
| 5-10% | 687.2±20.9 | 694.0±21.5 | 642.8±19.6 | 635.1±19.9 | 628.6±19.9 |
| 10-20% | 491.7±25.8 | 496.9±26.2 | 458.4±24.1 | 453.3±22.7 | 450.1±22.1 |
| 20-30% | 305.8±26.6 | 311.6±27.6 | 284.5±25.9 | 283.9±22.9 | 283.1±24.5 |
| 30-40% | 182.6±24.4 | 187.7±25.4 | 169.9±22.9 | 171.8±21.7 | 170.6±23.1 |
| 40-50% | 103.6±20.0 | 106.4±19.9 | 96.1±18.4 | 98.2±18.5 | 96.4±18.5 |
| 50-60% | 54.5±14.3 | 56.4±14.7 | 50.9±13.3 | 51.5±13.5 | 51.7±13.1 |
| 60-80% | 19.4±7.7 | 20.0±8.6 | 18.9±6.9 | 19.1±7.8 | 19.2±6.3 |

the $p_{\mathrm{T}}$ distribution of the parent particles ($\Lambda$, $\overline{\Lambda}$, $\Xi$, $\overline{\Xi}$). The $\Lambda$, $\overline{\Lambda}$ spectra for $\sqrt{s_{\mathrm{NN}}} =$ 39, 27, 19.6, 11.5 and 7.7 GeV is used form [50]. The $\Lambda$, $\overline{\Lambda}$ spectra in [50] is feed-down corrected for $\Xi$, $\overline{\Xi}$. Therefore, the $\Lambda$, $\overline{\Lambda}$ spectra from [50] was scaled to include the contribution from $\Xi$, $\overline{\Xi}$ as we want to calculated feed-down from all weak decays. Moreover, we have also included the contribution of $p$ ($\overline{p}$) from $\Sigma$ ($\overline{\Sigma}$) weak decays by scaling the $\Lambda$, $\overline{\Lambda}$ spectra for weak decay feed-down from $\Sigma$ ($\overline{\Sigma}$). The $\Sigma/\Lambda$ ratio of 0.35 is used as it was done in [51].

### 3.7.3.1 Decay Kinematics of $\Lambda$, ($\overline{\Lambda}$)

The $\Lambda$ ($\overline{\Lambda}$) spectra, including the feed-down from $\Xi(\overline{\Xi})$ and $\Sigma$ ($\overline{\Sigma}$), is used as parent particle. Each $\Lambda$ ($\overline{\Lambda}$) particles is then decayed into $\pi^- + p$ ($\pi^+ + \overline{p}$) with 63.9% branching ratio. To account for uniform distribution in $\eta$-$\phi$ plane, the $\eta$ and $\phi$ distribution of input $\Lambda$, ($\overline{\Lambda}$) was uniformly varied within the acceptance of the STAR TPC detector (-1.0 < $\eta$ < 1.0 and 0 < $\phi$ < 2$\pi$). Figure 3.22 shows the $p_{\mathrm{T}}$-correlation plot of input $\Lambda$ ($\overline{\Lambda}$) and daughter $p$ ($\overline{p}$). Since we use corrected $\Lambda$ ($\overline{\Lambda}$) spectra as input in this study, therefore, the daughter $p$ ($\overline{p}$) does not need to be corrected for efficiency and acceptance effect of the TPC detector. The decay daughters $p$ and $\overline{p}$ from parents $\Lambda$ and $\overline{\Lambda}$ have similar rapidity ($y$) and $p_{\mathrm{T}}$ distribution as expected in real experiment. Figure 3.23 shows the rapidity ($y$) vs $p_{\mathrm{T}}$ acceptance of the daughter $p$ and $\overline{p}$ for 0-5% centrality at $\sqrt{s_{\mathrm{NN}}} =$ 39 GeV.
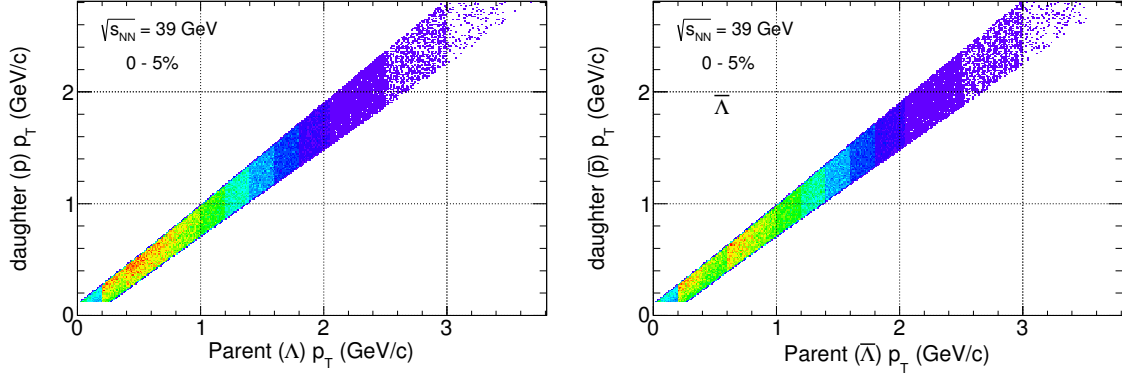
Figure 3.22: $p_T$-correlation plot of input $\Lambda$ ($\overline{\Lambda}$) and daughter $p$ ($\overline{p}$) for 0-5% centrality at $\sqrt{s_{NN}} = 39$ GeV.
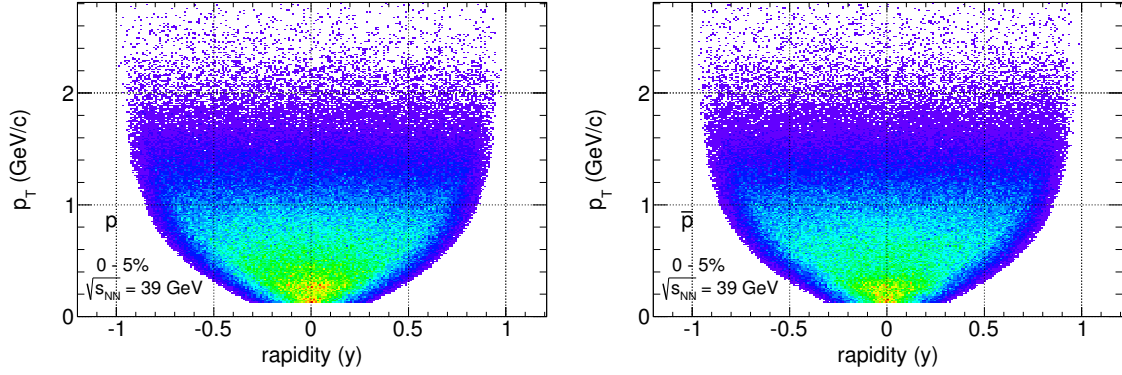


Figure 3.23: $p_T$-$y$ correlation plot of daughter $p$ and $\overline{p}$ for 0-5% centrality at $\sqrt{s_{NN}} = 39$ GeV.

### 3.7.3.2 Calculation of Feed-down Ratio

To quantify the amount of weak-decay $p$ ($\overline{p}$) in the inclusive $p$ ($\overline{p}$) spectra, we define the feed-down ratio as,

$$\text{FD}_{\text{ratio}}(p_T) = \frac{\text{weak decay p}(\overline{\text{p}})}{\text{inclusive p}(\overline{\text{p}})} \qquad (3.22)$$

The $p$, $\overline{p}$ spectra in [49] was measured at mid-rapidity ($|y| < 0.1$). Therefore, we select the daughter $p(\overline{p})$ which are within $|y| < 0.1$ which constitutes the numerator of the equation 3.22. The Denominator is the inclusive $p(\overline{p})$ from [49]. Figure 3.24 shows

the FD ratio of $p$ and $\bar{p}$ for $\sqrt{s_{\mathrm{NN}}} = 39$, 27, 19.6, 11.5 and 7.7 GeV. The error bars corresponds to the systematic error. As seen from Fig. 3.24, the FD ratio is highest for lowest $p_{\mathrm{T}}$ bin. Then the FD ratio decreases as a function of $p_{\mathrm{T}}$. We also observe that the FD ratio is higher for $\bar{p}$ than $p$ and this difference increases as beam energy decreases.
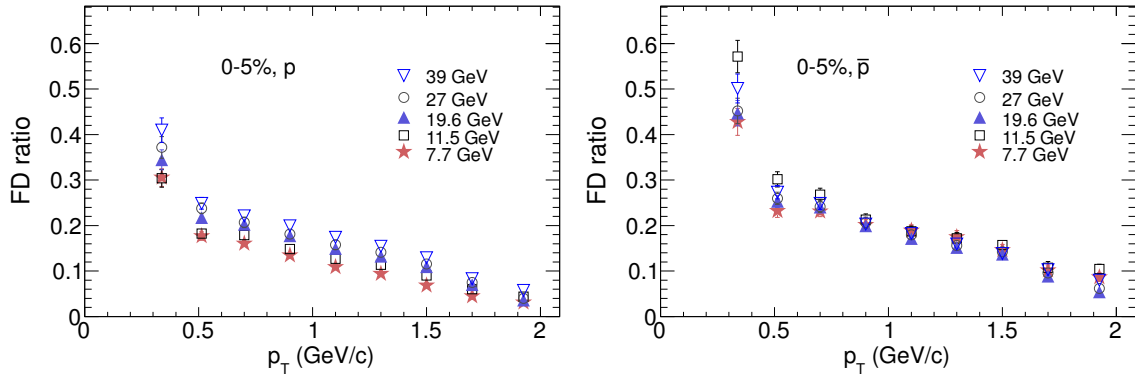


Figure 3.24: FD ratio of $p$ and $\bar{p}$ for 0-5% centrality at $\sqrt{s_{\mathrm{NN}}} = 39$, 27, 19.6, 11.5 and 7.7 GeV.

#### 3.7.3.3 Systematic Error on Feed-Down Ratio

The $\Lambda$ ($\overline{\Lambda}$) spectra is measured experimentally in the $p_{\mathrm{T}}$ range $0.5 < p_{\mathrm{T}} < 2.5$ GeV/c. Therefore, $\Lambda$ ($\overline{\Lambda}$) spectra has been fitted with fit function to get the spectra in the unmeasured region. The $m_{\mathrm{T}}$-exponential fit function is used as default fit function to extrapolate the $p_{\mathrm{T}}$ distribution in the unmeasured region. However, other fit functions (Blast-wave and $p_{\mathrm{T}}$-exponential function) has been also used to calculate the systematic error due to extrapolation. Moreover, we have also varied the amount of feed-down from $\Sigma$ ($\overline{\Sigma}$) and used the results to calculate the systematic error. The systematic error of $\Lambda$ and $\overline{\Lambda}$ spectra has also been used to calculated the systematic error on the feed-down ratio. Table 3.13 and Table 3.14 lists the FD ratios along with the systematic error. These FD ratios were used in this analysis to correct the inclusive $p(\bar{p})$ spectra.

Table 3.13: Feed-down (FD) ratio of midrapidity ($|y| < 0.3$) proton for 0-5% central Au+Au collisions at $\sqrt{s_{NN}}$ = 39, 27, 19.6, 11.5 and 7.7 GeV. First column corresponds to the center values for each $p_T$ bin.

| $p_T$ (GeV/c) | 39 GeV | 27 GeV | 19.6 GeV | 11.5 GeV | 7.7 GeV |
|---|---|---|---|---|---|
| 0.34 | 0.41±0.064 | 0.37±0.054 | 0.34±0.017 | 0.30±0.015 | 0.30±0.015 |
| 0.51 | 0.25±0.012 | 0.24±0.018 | 0.22±0.011 | 0.18±0.009 | 0.18±0.008 |
| 0.70 | 0.22±0.011 | 0.21±0.012 | 0.20±0.010 | 0.18±0.009 | 0.16±0.008 |
| 0.90 | 0.20±0.010 | 0.18±0.009 | 0.18±0.008 | 0.15±0.007 | 0.13±0.007 |
| 1.10 | 0.17±0.009 | 0.16±0.008 | 0.15±0.007 | 0.13±0.006 | 0.11±0.005 |
| 1.30 | 0.15±0.007 | 0.14±0.007 | 0.13±0.005 | 0.11±0.005 | 0.09±0.005 |
| 1.50 | 0.13±0.006 | 0.12±0.006 | 0.11±0.003 | 0.09±0.004 | 0.07±0.003 |
| 1.70 | 0.08±0.004 | 0.07±0.004 | 0.07±0.003 | 0.06±0.003 | 0.04±0.002 |
| 1.92 | 0.06±0.003 | 0.04±0.002 | 0.04±0.002 | 0.04±0.002 | 0.03±0.002 |

Table 3.14: Feed-down (FD) ratio of midrapidity ($|y| <0.3$) anti-proton for 0-5% central Au+Au collisions at $\sqrt{s_{NN}}$ = 39, 27, 19.6 and 11.5 GeV.

| $p_T$ (GeV/c) | 39 GeV | 27 GeV | 19.6 GeV | 11.5 GeV |
|---|---|---|---|---|
| 0.34 | 0.50±0.025 | 0.45±0.022 | 0.45±0.022 | 0.57±0.028 |
| 0.51 | 0.27±0.014 | 0.26±0.013 | 0.25±0.013 | 0.30±0.015 |
| 0.70 | 0.25±0.012 | 0.24±0.012 | 0.24±0.012 | 0.27±0.013 |
| 0.90 | 0.20±0.010 | 0.21±0.010 | 0.20±0.010 | 0.21±0.011 |
| 1.10 | 0.18±0.009 | 0.18±0.009 | 0.17±0.008 | 0.19±0.009 |
| 1.30 | 0.16±0.008 | 0.16±0.008 | 0.15±0.007 | 0.17±0.009 |
| 1.50 | 0.14±0.007 | 0.14±0.007 | 0.14±0.007 | 0.16±0.008 |
| 1.70 | 0.10±0.005 | 0.09±0.005 | 0.09±0.005 | 0.11±0.005 |
| 1.92 | 0.08±0.004 | 0.06±0.003 | 0.05±0.003 | 0.10±0.005 |

## 3.7.4 TOF and TPC Efficiency of $d$

### TOF matching efficiency of $d$
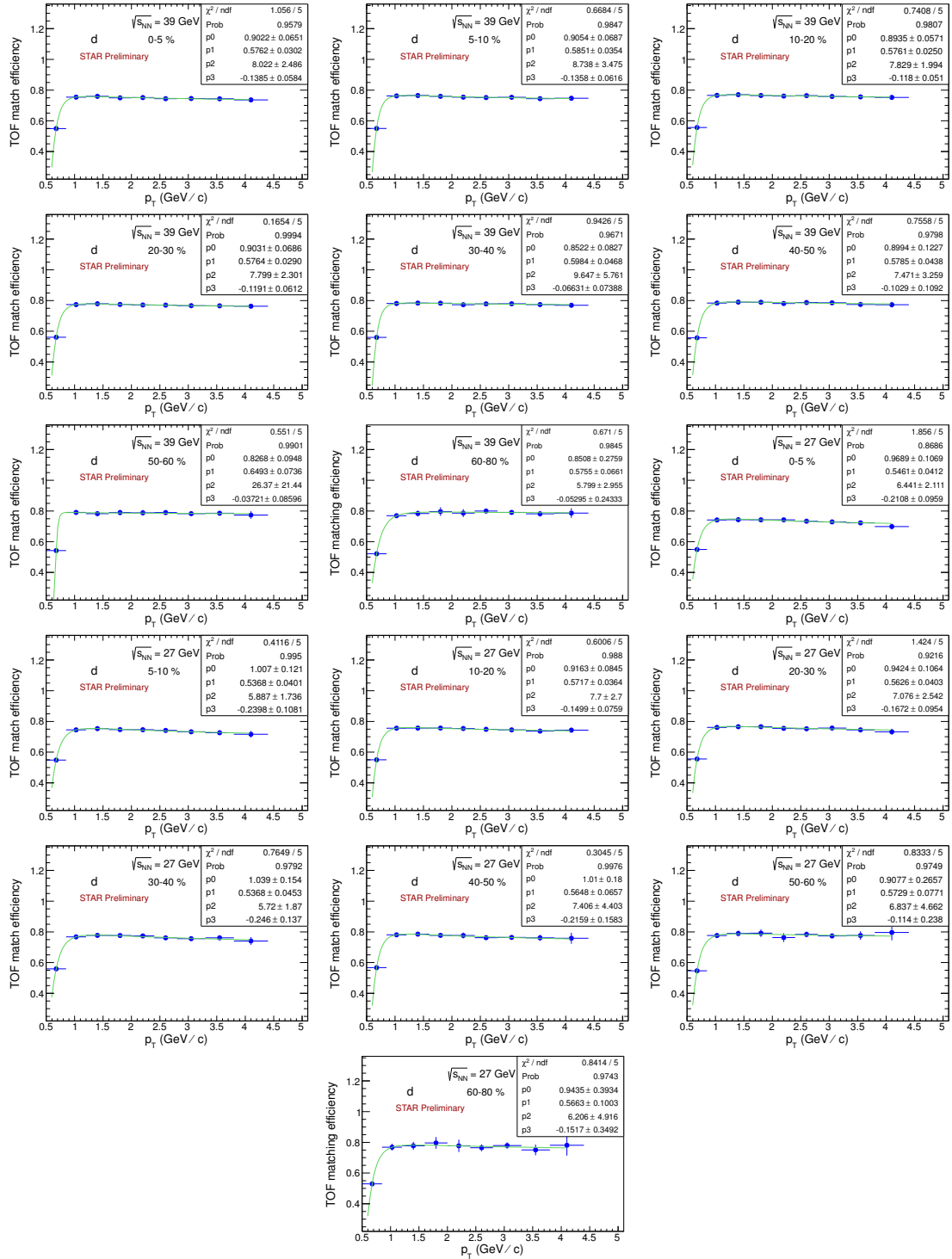
# TOF matching efficiency of $d$ (continued..)
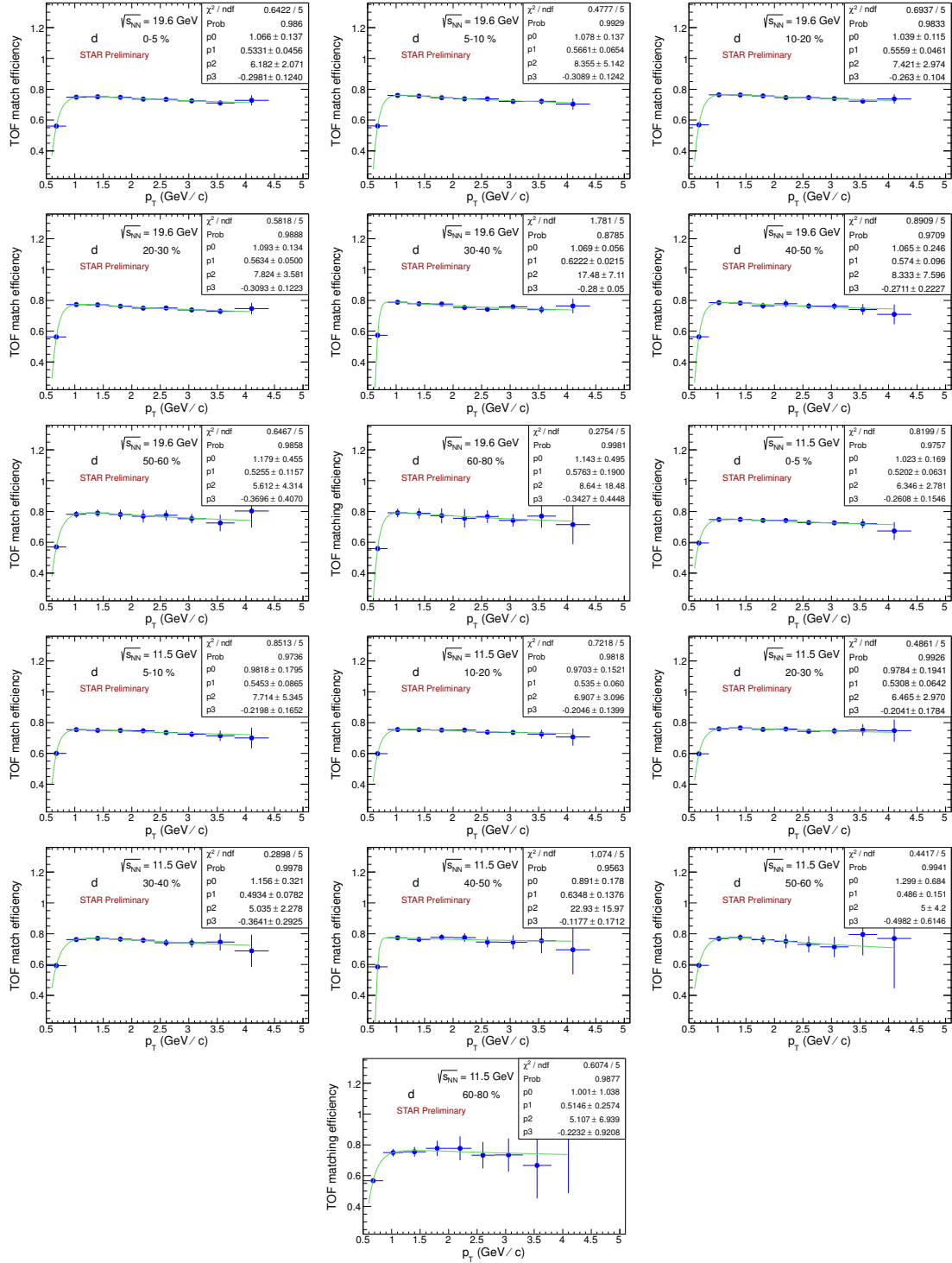
# TOF matching efficiency of $d$ (continued..)
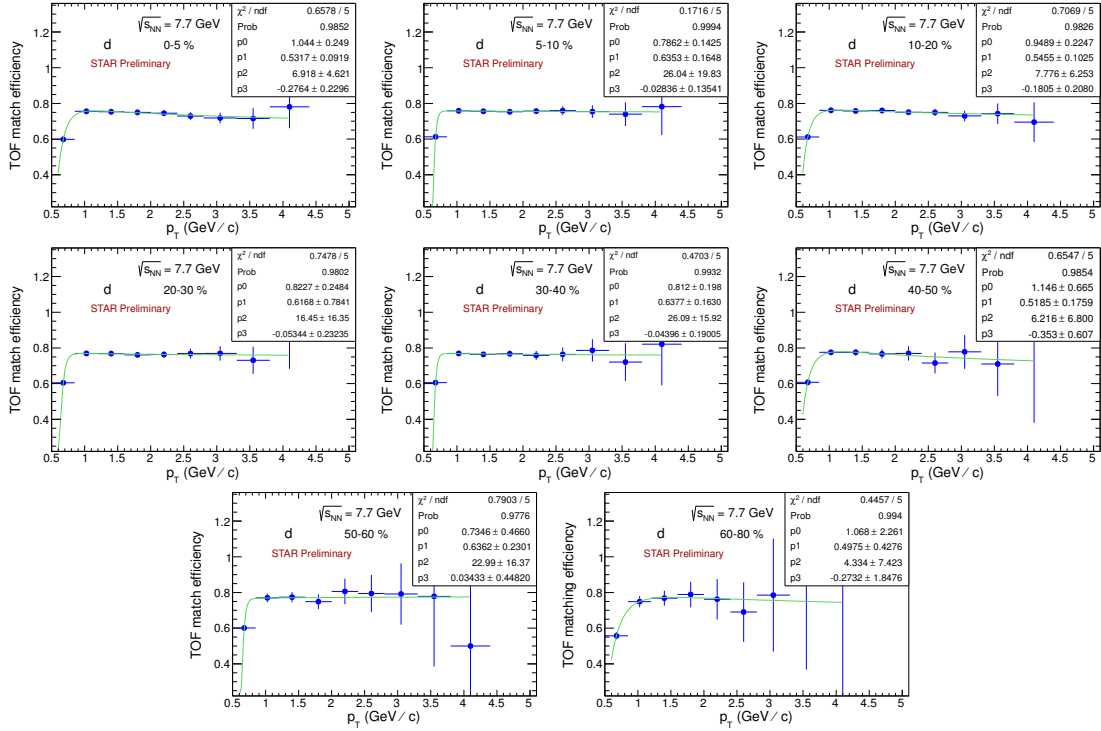
# TPC acceptance efficiency of $d$
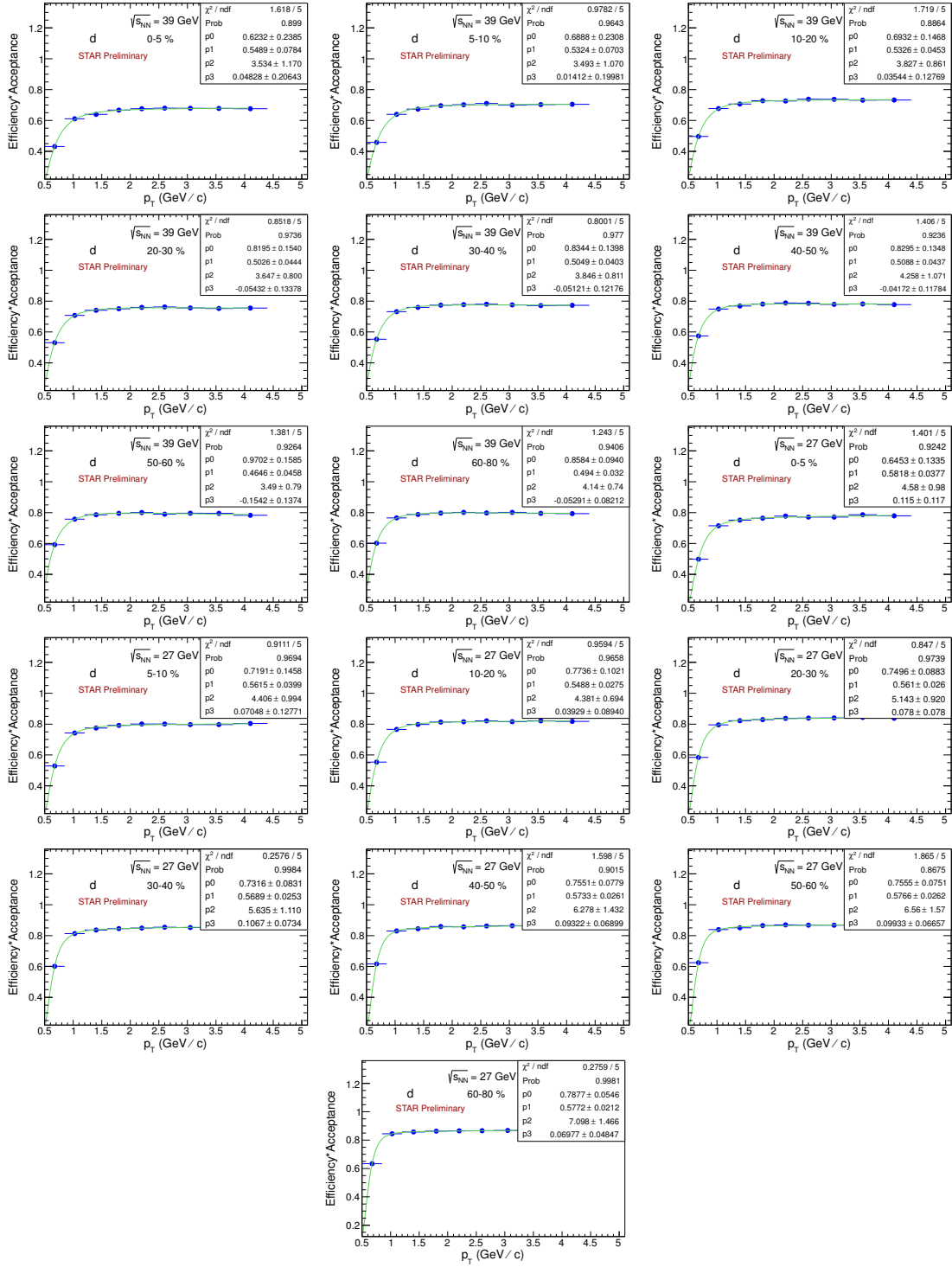
# TPC acceptance efficiency for $d$ (continued..)
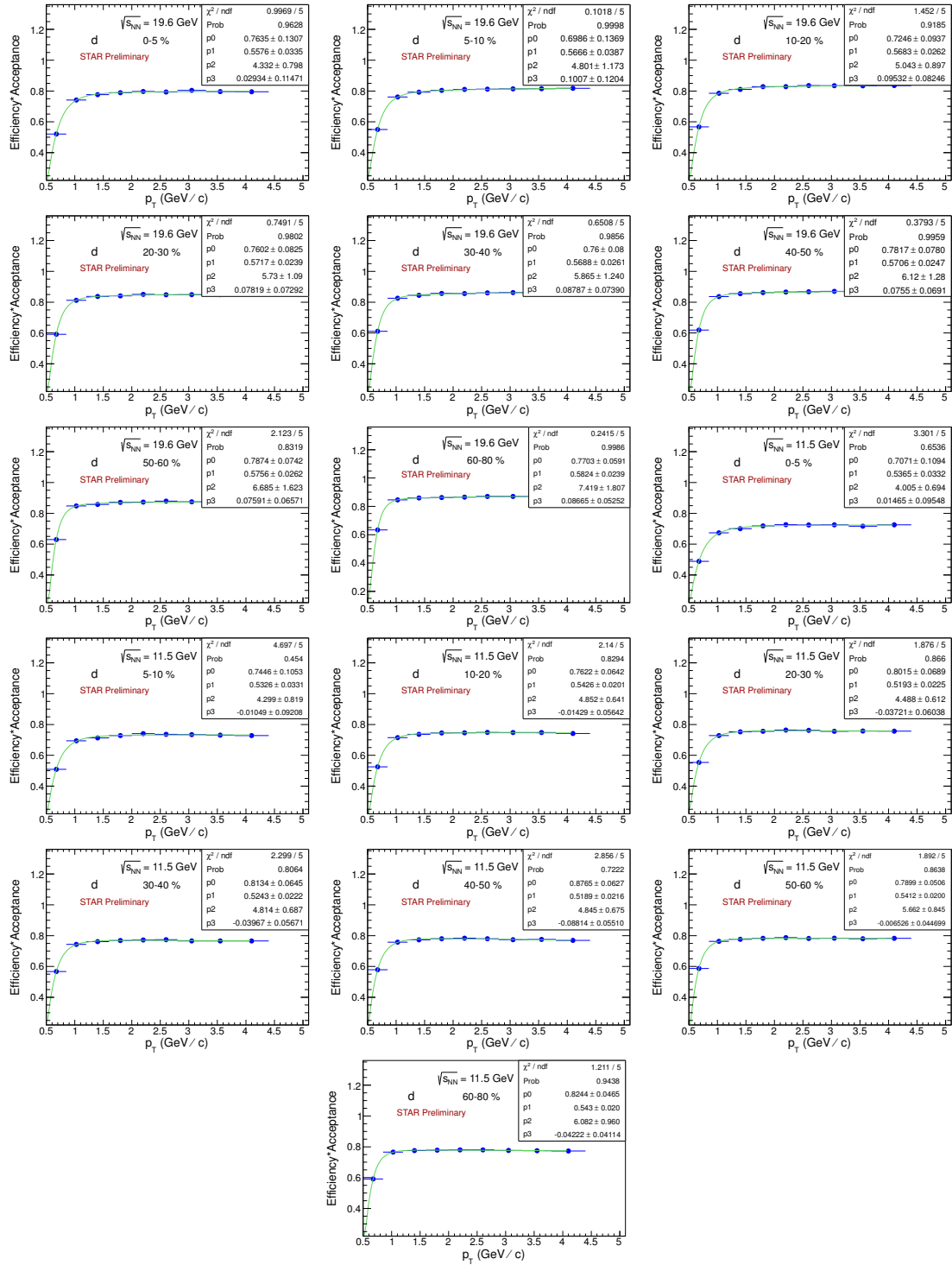
# TPC acceptance efficiency for $d$ (continued..)
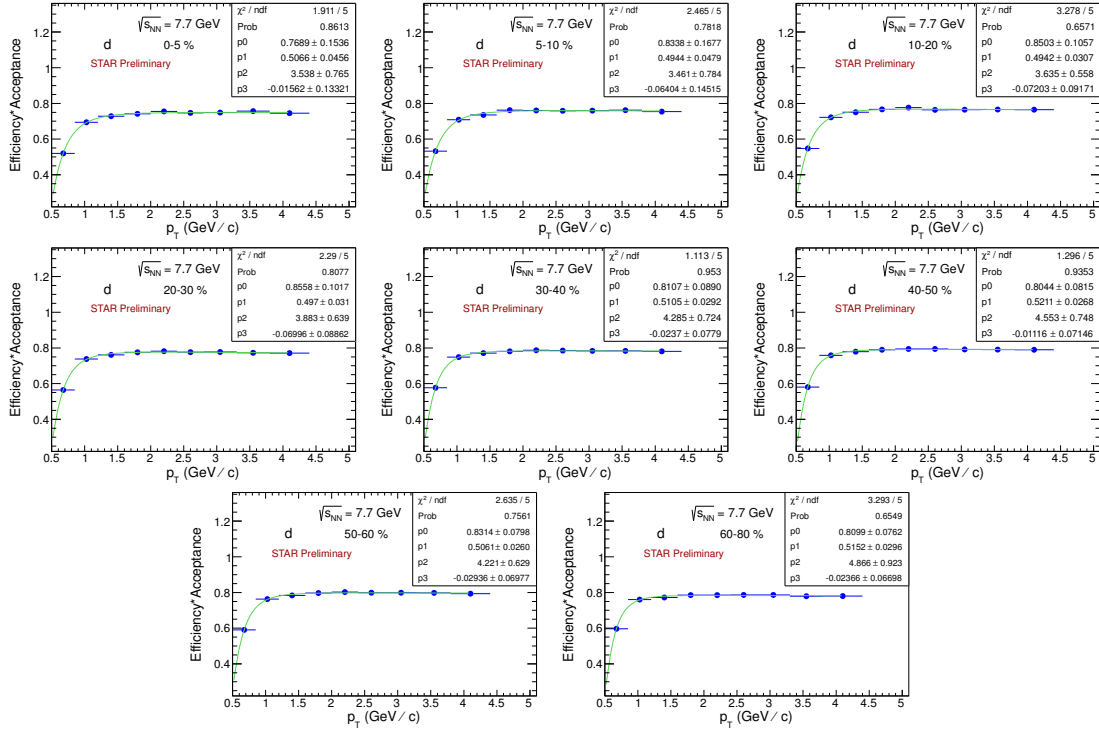
## 3.7.5 TOF and TPC Efficiency of $\overline{d}$

### TOF matching efficiency of $\overline{d}$
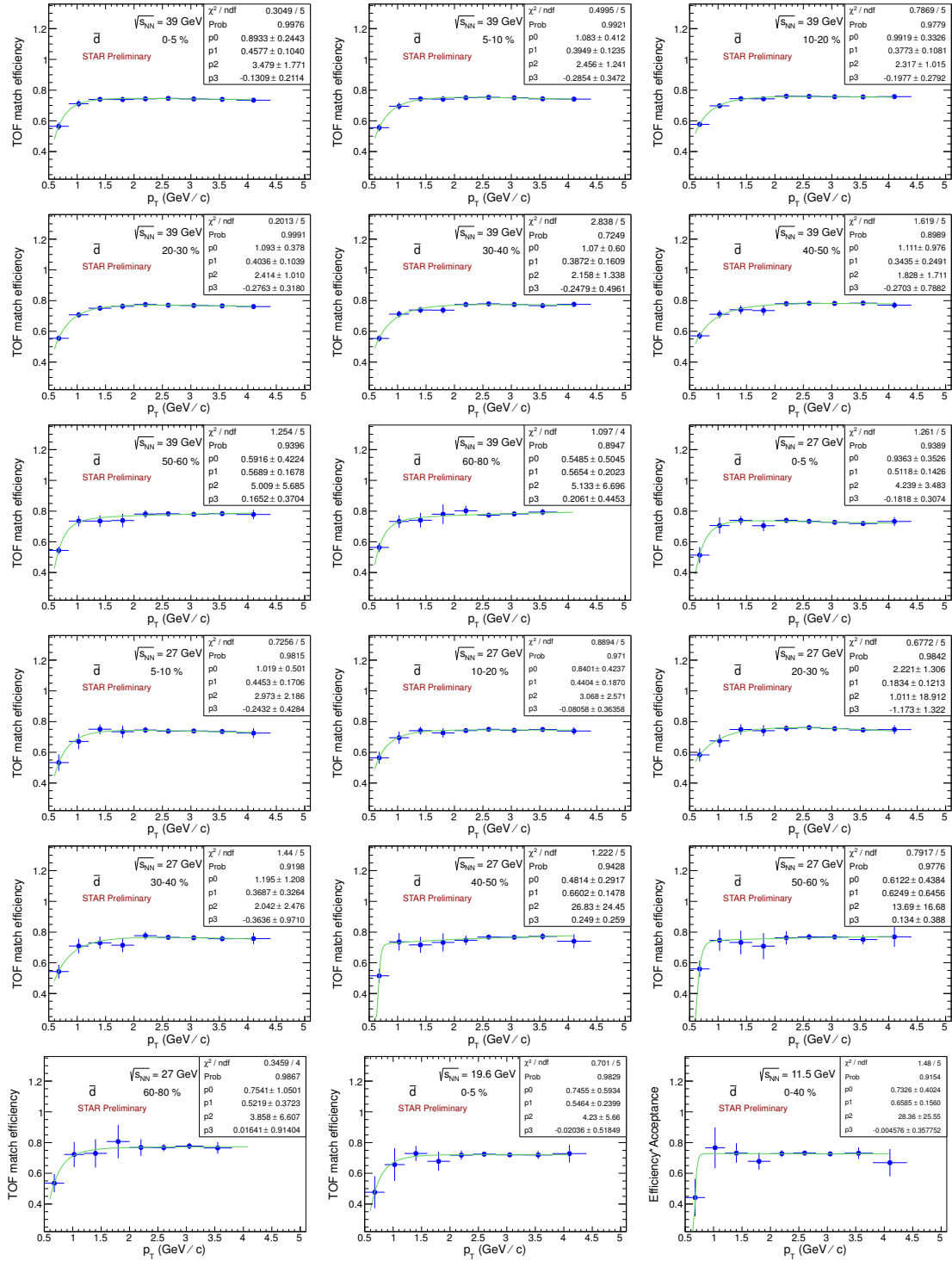
# TPC acceptance efficiency of $\overline{d}$
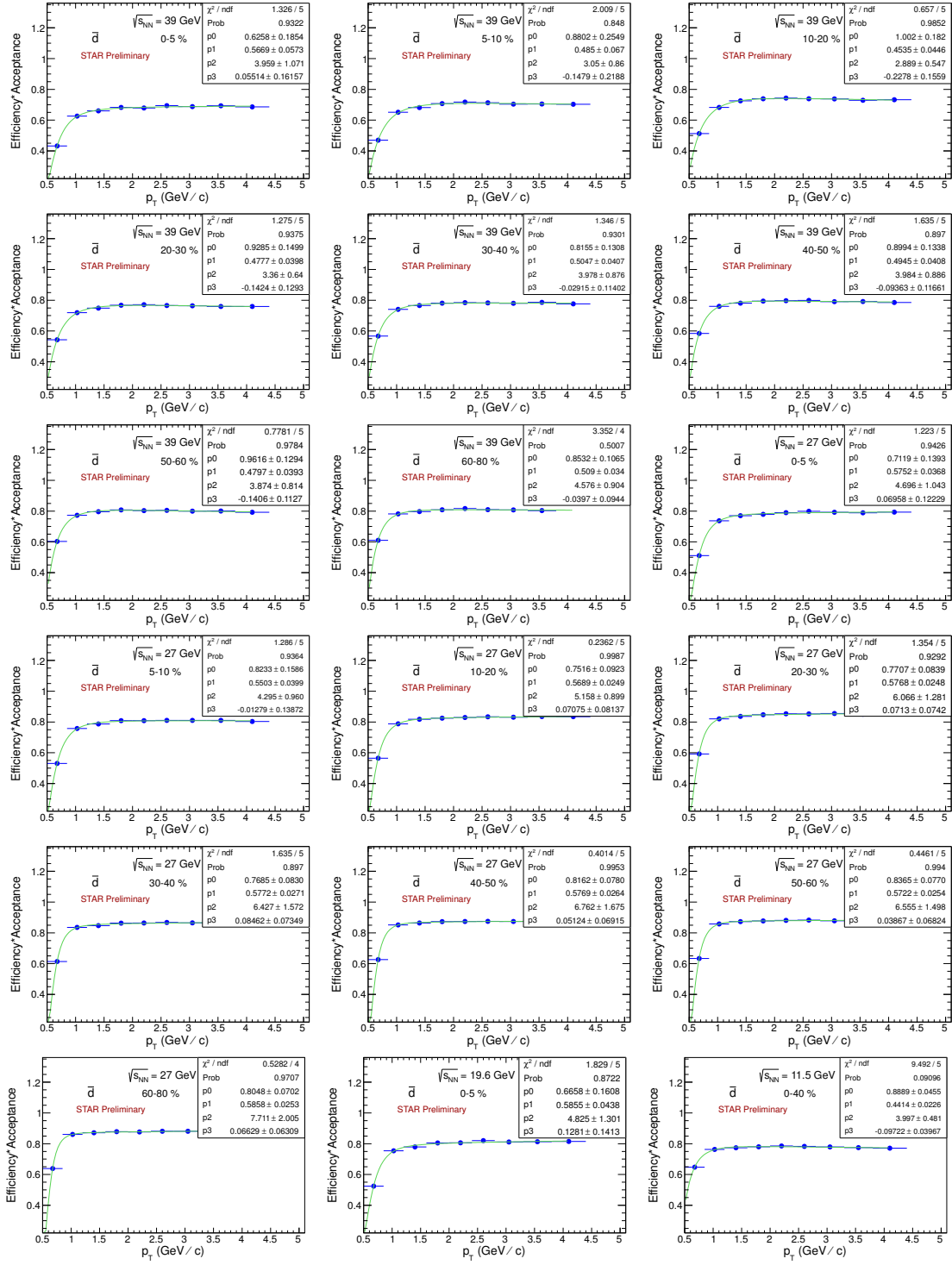
## 3.7.6 Raw Yield of Extraction of $d$ and $\overline{d}$

**Raw yield of extraction of $d$ for $\sqrt{s_{\mathrm{NN}}} = 39$ GeV (0-5%)**
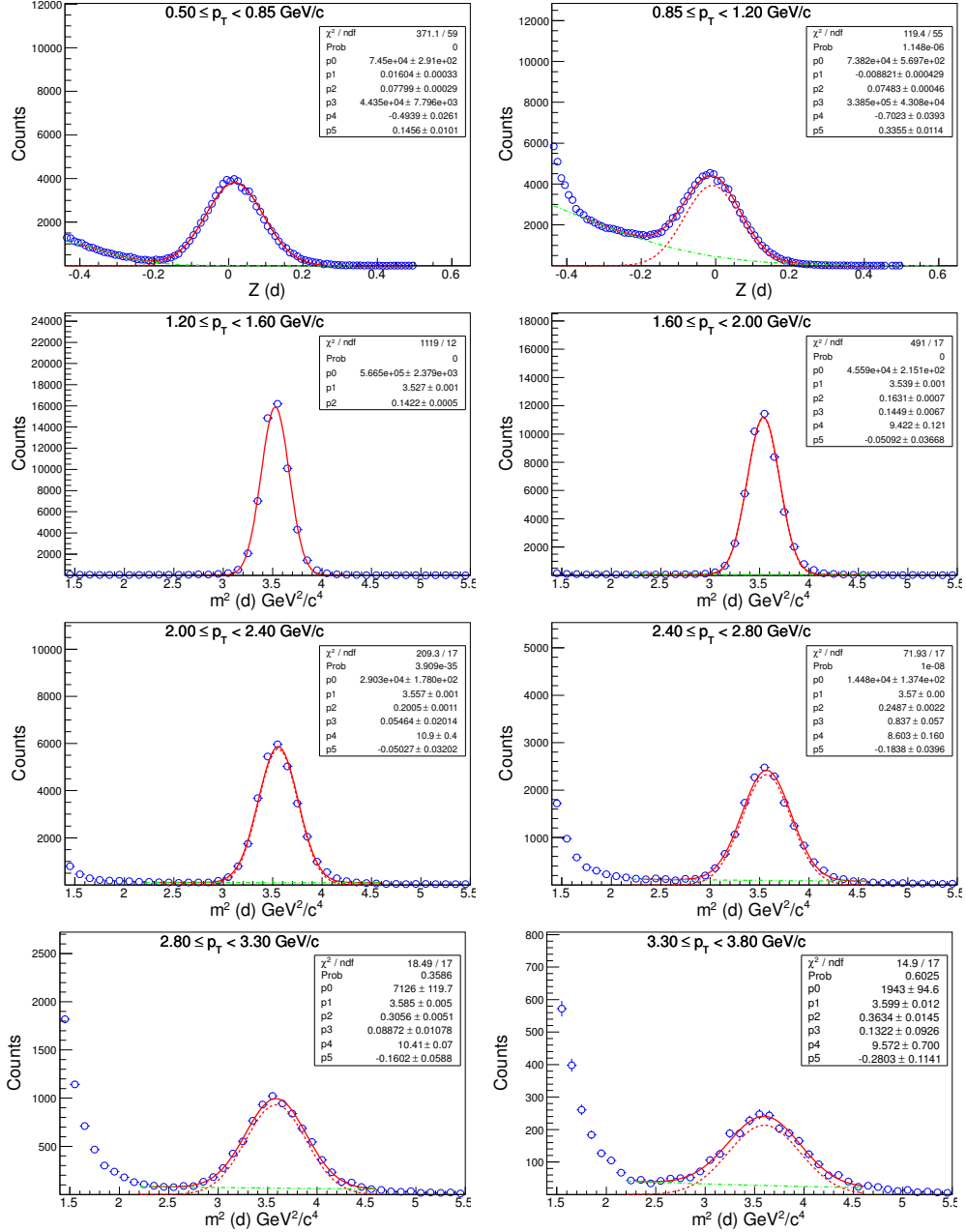
# Raw yield of extraction of $d$ for $\sqrt{s_{\mathrm{NN}}} = 27$ GeV (0-5%)
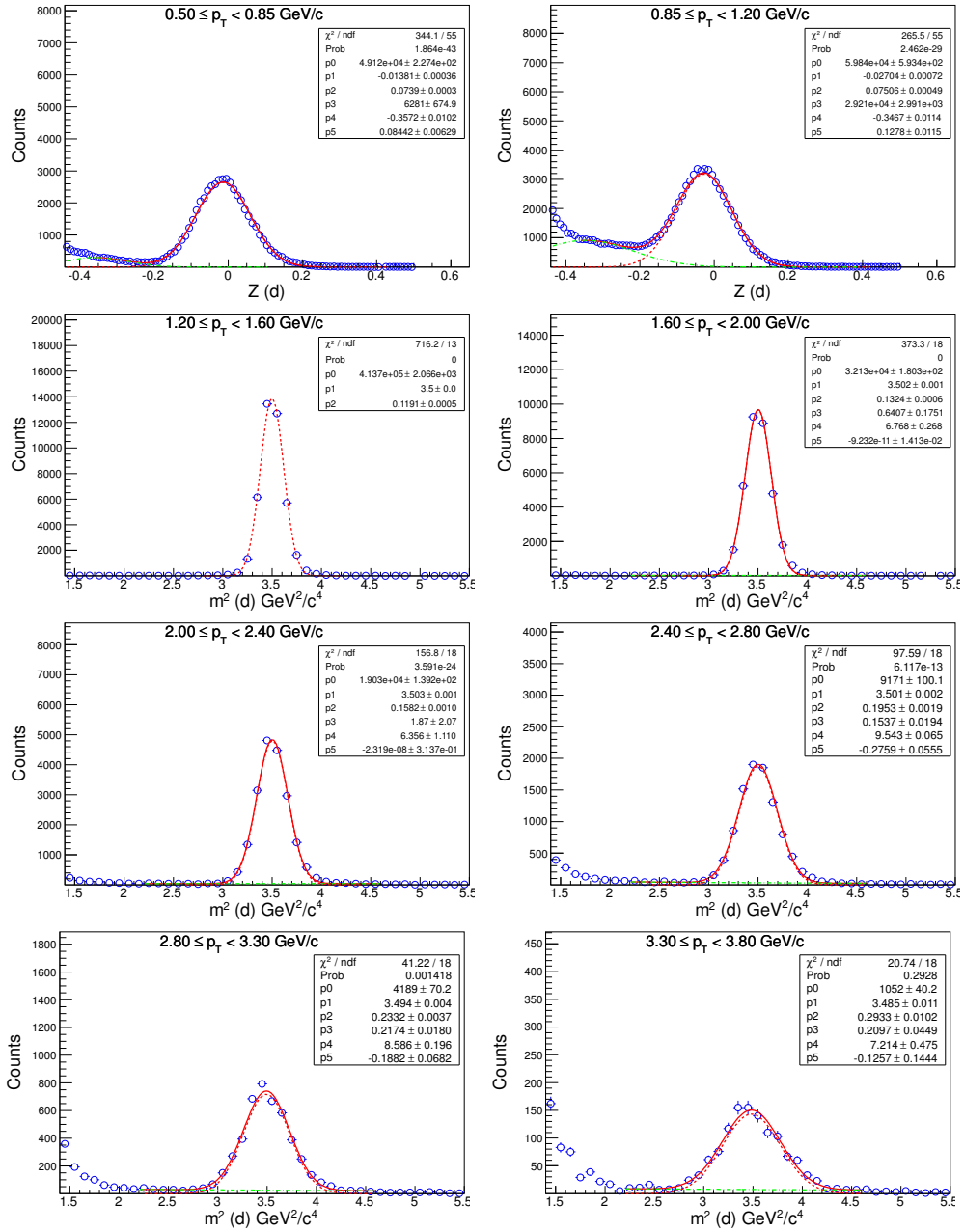
# Raw yield of extraction of $d$ for $\sqrt{s_{\mathrm{NN}}} = 19.6$ GeV (0-5%)
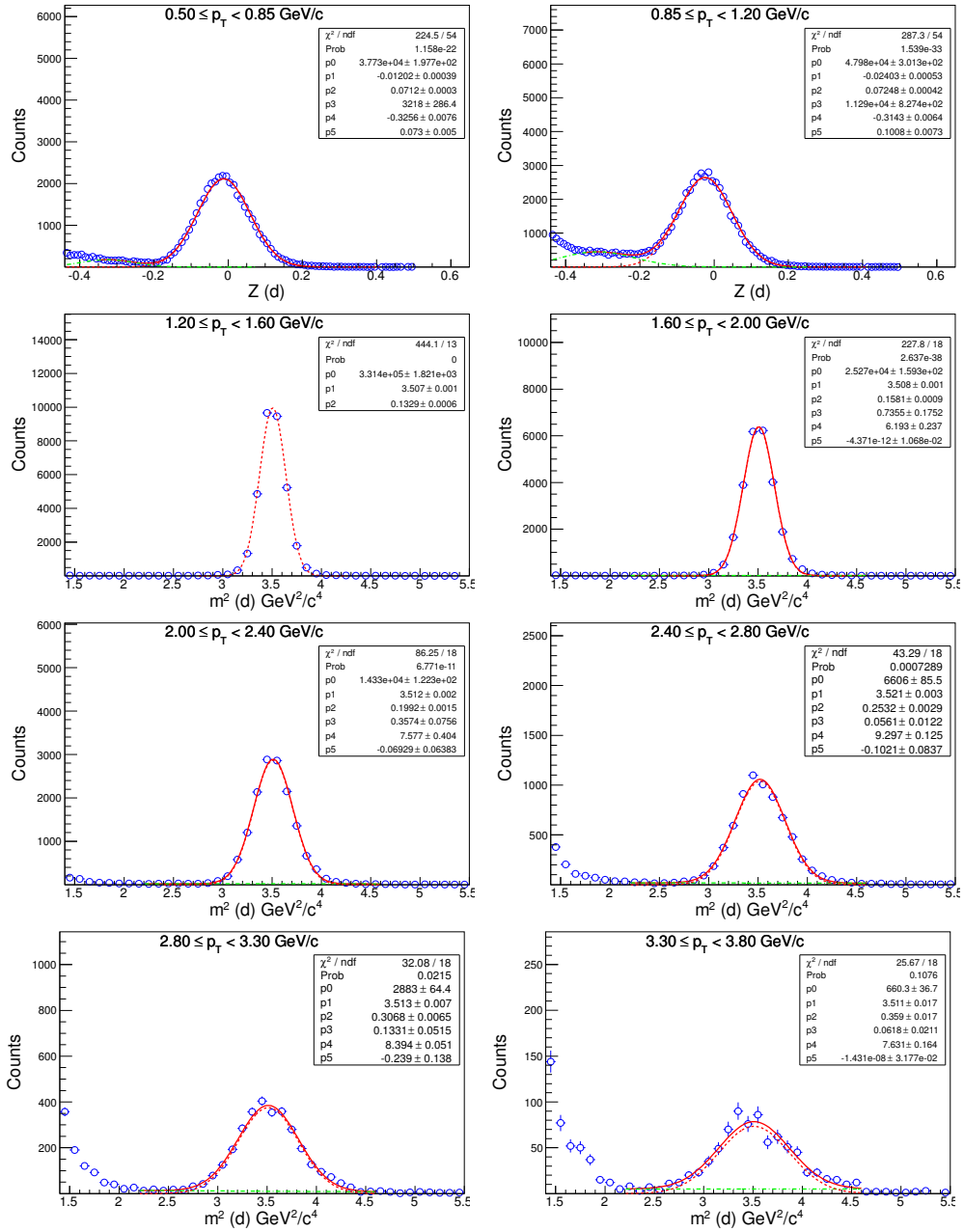
# Raw yield of extraction of $d$ for $\sqrt{s_{\mathrm{NN}}} = 11.5$ GeV (0-5%)
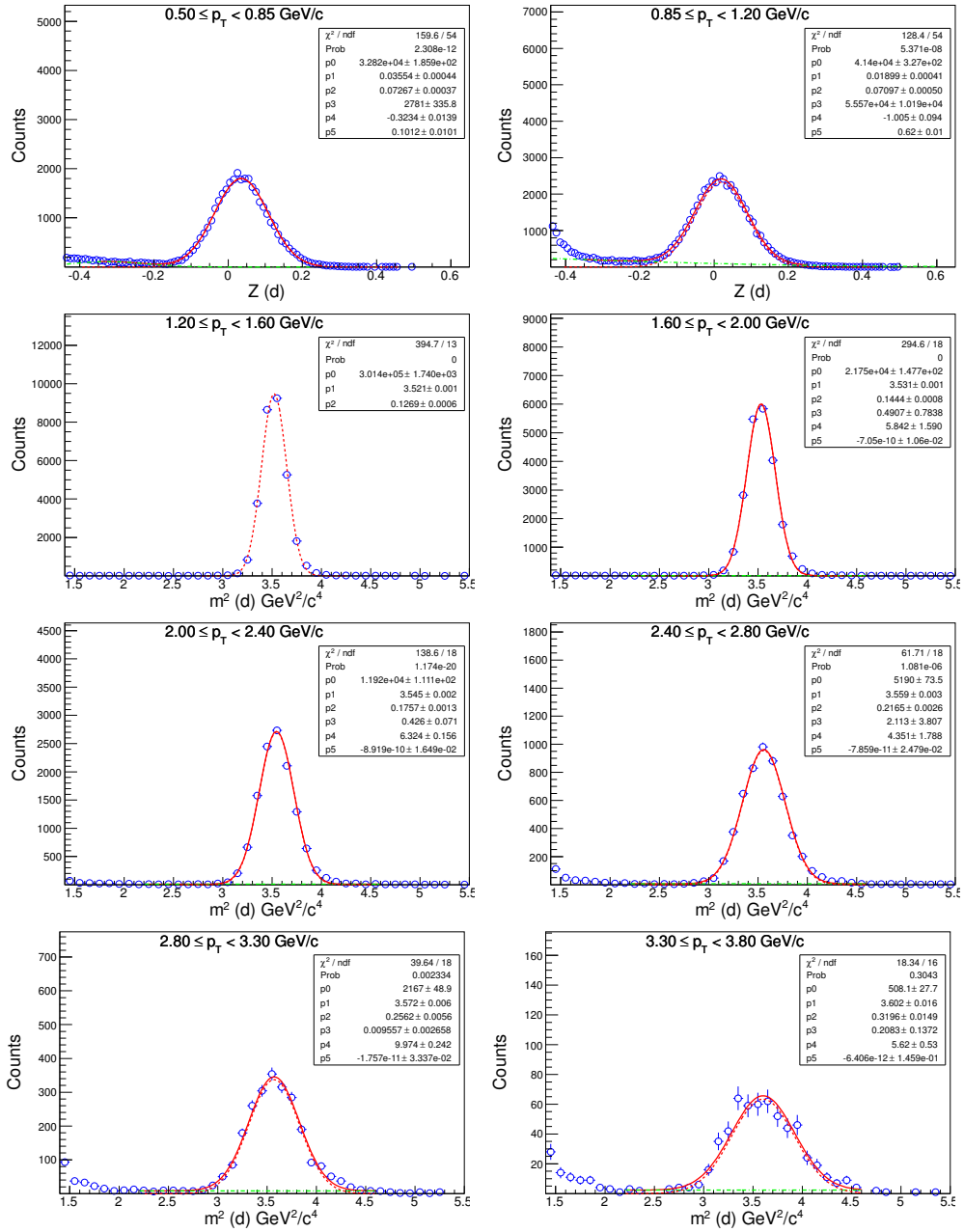
# Raw yield of extraction of $d$ for $\sqrt{s_{NN}} = 7.7$ GeV (0-5%)

# Raw yield of extraction of $\overline{d}$ for $\sqrt{s_{\mathrm{NN}}} = 39$ GeV (0-5%)
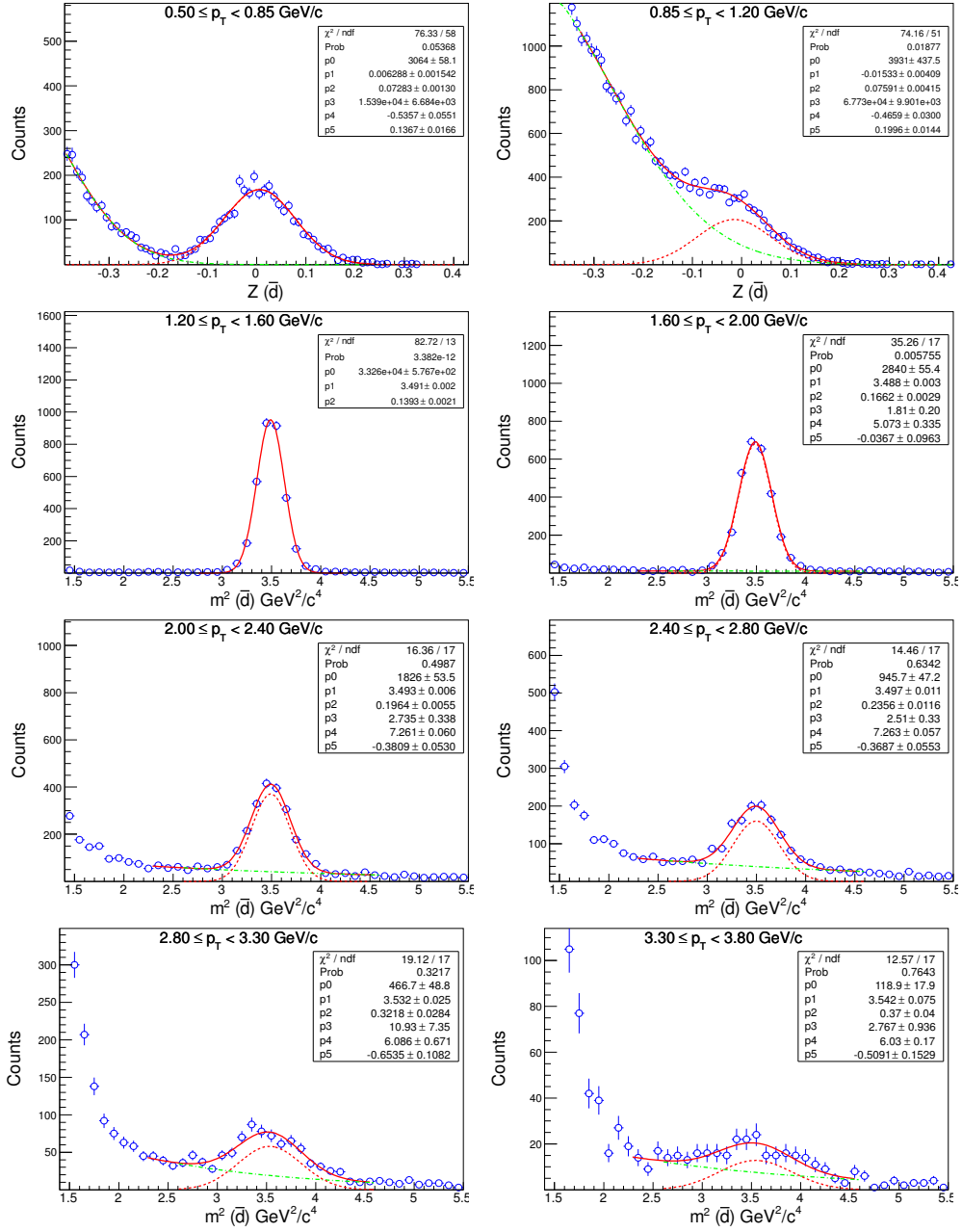


104

**Raw yield of extraction of $\overline{d}$ for $\sqrt{s_{\mathrm{NN}}} = 27$ GeV (0-5%)**
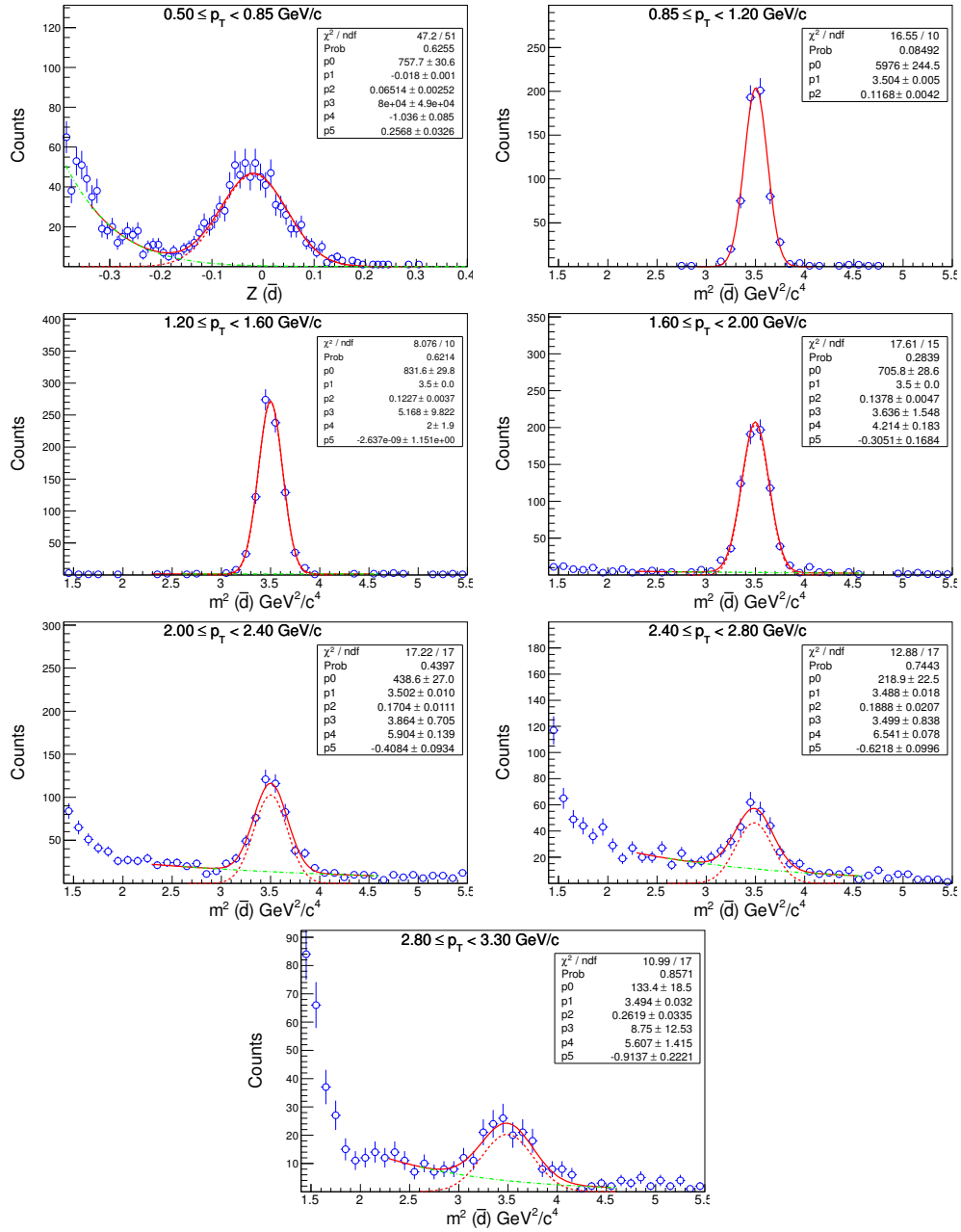
**Raw yield of extraction of $\overline{d}$ for $\sqrt{s_{\mathrm{NN}}} = 19.6$ GeV (0-5%)**
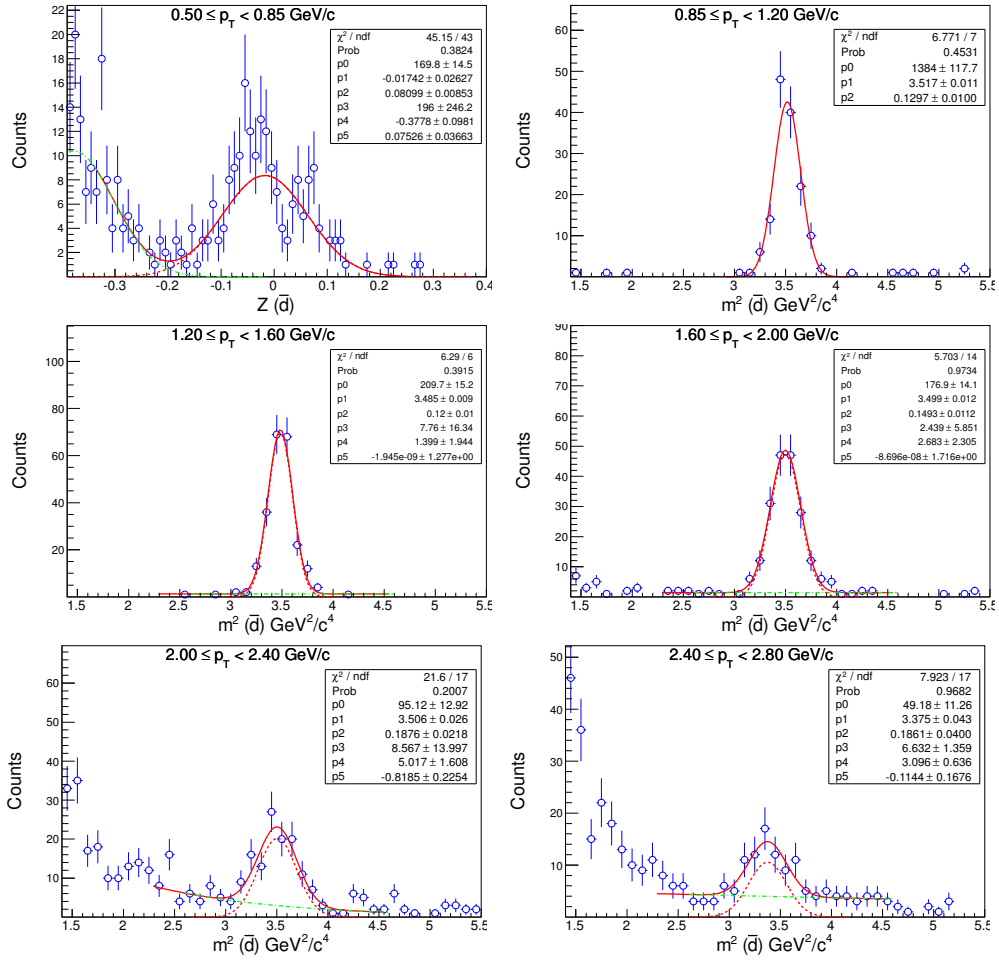
# Raw yield of extraction of $\bar{d}$ for $\sqrt{s_{NN}} = 11.5$ GeV (0-40%)
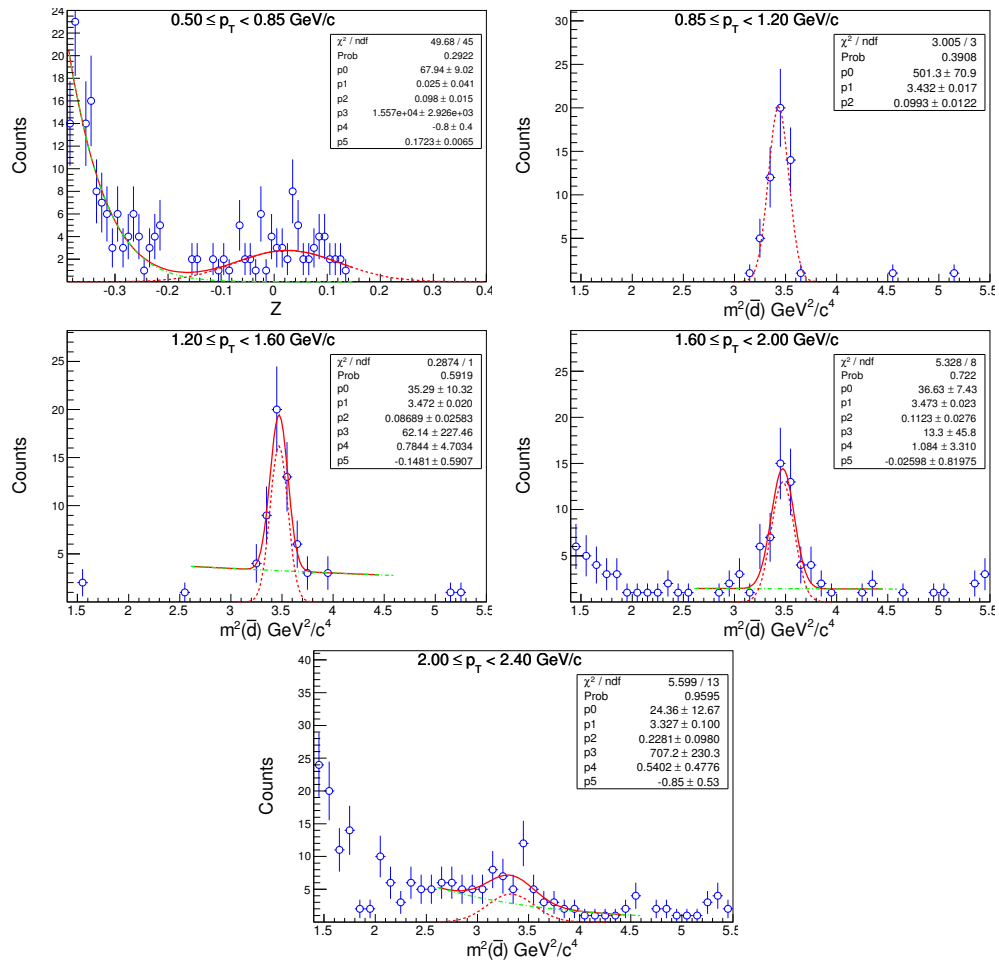
# Chapter 4

# Elliptic Flow of Light Nuclei in Au+Au Collisions at RHIC

## 4.1 Motivation for Studying Light Nuclei $v_2$

One of the main goals of the high energy heavy-ion collision experiments is to study the phase structures in the QCD phase diagram [1]. With this purpose the Relativistic Heavy Ion Collider (RHIC) has finished the first phase of the Beam Energy Scan (BES) program [2, 3, 4]. It has been found that the identified hadron $v_2$ shows number of constituent quark (NCQ) scaling at the higher beam energies. This scaling behavior is a signature of partonic collectivity in the strongly interacting medium of quarks and gluons formed in heavy-ion collisions [5]. Such a scaling behavior also suggests partonic coalescence to be a mechanism for hadron formation. In a relativistic heavy-ion collision, light nuclei (anti-nuclei) can be formed by coalescence of produced nucleons (anti-nucleons) or from the stopped nucleons [6, 7, 8]. Since, the binding energies of light nuclei are very small ($\sim$ few MeV), therefore, it is expected that light nuclei might be formed at a later stage of the evolution, when interactions between the nucleons and other particles become weak. This process is called as

final-state coalescence [6, 9]. The coalescence probability of two nucleon is related to the local nucleon density [10]. Therefore, the production of light nuclei provides an interesting tool to measure collective motion and freeze-out properties at a later stage of the evolution. The advantage of nucleonic coalescence over the partonic coalescence is that both the nuclei and the constituent nucleon space-momentum distributions are measurable quantities in heavy-ion collision experiments. By studying the elliptic flow of light nuclei (anti-nuclei) and comparing to that of proton (anti-proton), we will gain insight in the particle production mechanism in heavy-ion collision via the process of coalescence.

## 4.2  Data Set and Cuts

The results presented in this chapter are from the data collected in Au+Au collisions at $\sqrt{s_{NN}}$ = 7.7, 11.5, 19.6, 27, 39, 62.4 and 200 GeV by the STAR experiment for minimum bias trigger in the years 2010 and 2011. The minimum-bias (0-80%) trigger condition was based on a coincidence of the signals from the Zero-Degree Calorimeters (ZDC) [11], Vertex Position Detectors (VPD) [12] and/or Beam-Beam Counters (BBC) [13].

### 4.2.1  Event Selection

Different cuts on primary vertex position has been used for different collision energies for good quality events selection and maximizing the event statistics. The cuts applied on longitudinal component ($V_Z$) of primary vertex are listed in Table 4.1. These vertex cuts were chosen after extensive quality assurance (QA) studies performed based on the mean transverse momenta, the mean vertex position, the mean interaction rate, and the mean multiplicity in the detector [3]. Events were rejected if any one of the quantities are several $\sigma$ away from the run-period average. The distributions of $z$-positions of vertex are shown in Fig. 4.1 for $\sqrt{s_{NN}}$ = 7.7, 11.5, 19.6, 27, 39, 62.4 and 200 GeV. The triggered events at the lowest beam energies may not solely come

109
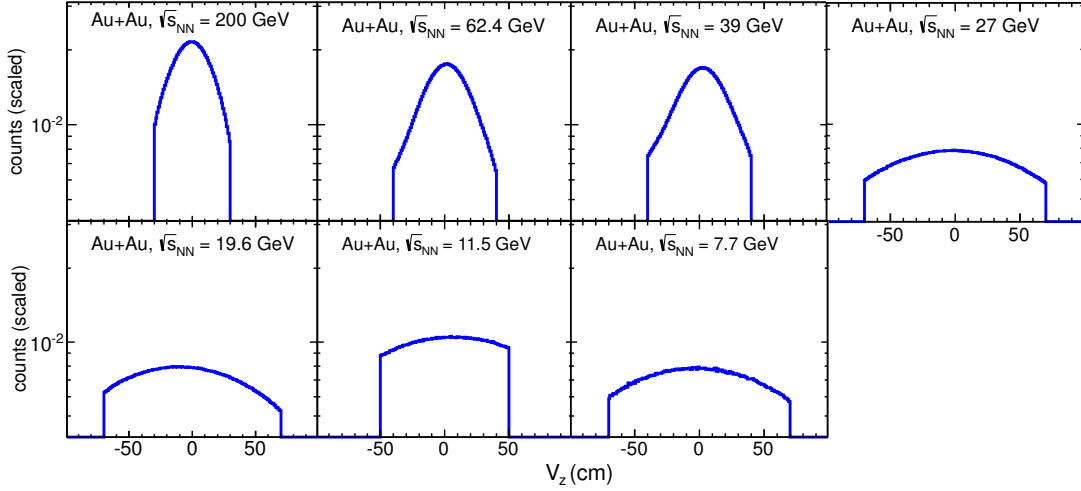
Figure 4.1: The distribution of $z$-component of primary vertex position of the events selected for the analysis at seven different collision energies.
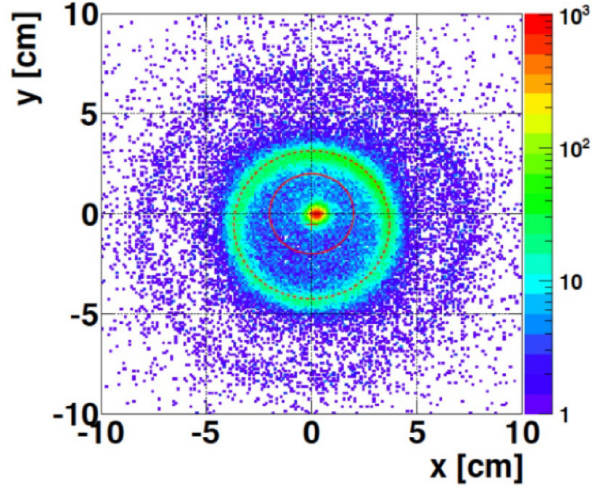


Figure 4.2: The distribution of $x$ and $y$-positions of vertex for $\sqrt{s_{NN}} = 7.7$ GeV in Au+Au collisions. Red dashed circle represent the circumference of beam pipe and solid red curve is a circle of radius 2.0 cm.

from Au+Au collisions, but may also be contaminated by interactions with beam-pipe or detector materials. This happens because of the large beam emittance at low beam energies. To reject these contaminations, an additional cut on transverse vertex position $V_R < 2$ cm has been used. $V_R$ is defined as $V_R = \sqrt{V_X^2 + V_Y^2}$, where

$V_X$ and $V_Y$ are the $x$ and $y$ components of primary vertex position. Figure 4.2 shows distribution of $x$ and $y$-distribution of the primary vertex for $\sqrt{s_{\mathrm{NN}}} = 7.7$ GeV. To remove pileup events, it was required that at least two tracks from the primary vertex were matched to the TOF detector. After applying all events selection cuts, the number of minimum bias events for each collision energy are given in Table 4.1.

Table 4.1: The z-vertex acceptance and total number of MB (minimum bias, defined later) events for each energy.

| Energy ($\sqrt{s_{\mathrm{NN}}}$) | $V_Z$ (cm) | MB events ($10^6$) |
|---|---|---|
| 200 GeV | $\lvert V_Z \rvert < 30$ | 241 |
| 62.4 GeV | $\lvert V_Z \rvert < 40$ | 62 |
| 39 GeV | $\lvert V_Z \rvert < 40$ | 119 |
| 27 GeV | $\lvert V_Z \rvert < 70$ | 60 |
| 19.6 GeV | $\lvert V_Z \rvert < 70$ | 33 |
| 11.5 GeV | $\lvert V_Z \rvert < 50$ | 11 |
| 7.7 GeV | $\lvert V_Z \rvert < 70$ | 4 |

### 4.2.2 Centrality Definition

The centrality of each event was defined based on the uncorrected charged particle multiplicity ($dN_{\mathrm{event}}/dN_{\mathrm{ch}}^{\mathrm{raw}}$) distribution, where $dN_{\mathrm{events}}$ is the number of events and $dN_{\mathrm{ch}}^{\mathrm{raw}}$ is the number of charged particles at midrapidity ($\lvert \eta \rvert < 0.5$) (uncorrected for charged track reconstruction efficiency and acceptance) [3]. The detailed procedure of calculating centrality is explained in previous chapter (sub-section 3.2.3).

## 4.3 Particle Identification

In this analysis, light nuclei are measured using the Time Projection Chamber (TPC) and Time of Flight (TOF) detector at the STAR experiment. The role of both of the detectors in particle identification are explained in the previous chapter (section 3.3). Therefore we only discuss the procedure which are specific for $v_2$ analysis. The track cuts used for light nuclei $v_2$ analysis are listed in Table. 4.2.

Table 4.2: Track cuts used for light nuclei identification

| Variable | Condition |
|---|---|
| Number of fit points in TPC (nHits) | $\geq 25$ |
| Number of points for $\langle dE/dx \rangle$ | $\geq 15$ |
| (nHits/Maximum possible nHits) | $\geq 0.52$ |
| DCA from primary vertex | $\leq 1.0$ cm |
| $p_T$ | $\geq 0.15$ GeV/$c$ |
| pseudo-rapidity ($\eta$) | $\leq 1.0$ |

## 4.4  Elliptic Flow Measurement

The elliptic flow parameter $v_2$ is a good variable for studying the system formed in the heavy-ion collisions at RHIC [21]. It describes the momentum anisotropy of particle emitted from non-central heavy-ion collisions. The azimuthal distribution of produced particles with respect to reaction plane angle ($\Psi_r$) can be expressed in terms of a Fourier series,

$$\frac{dN}{d(\phi - \Psi_r)} \propto 1 + 2v_1 \cos(\phi - \Psi_r) + 2v_2 \cos(2(\phi - \Psi_r)) + ... \qquad (4.1)$$

where $\phi$ is the azimuthal angle of the produced particle and $\Psi_r$ is called the reaction plane angle. $\Psi_r$ is defined as the angle between $x$-axis and impact parameter. Since in a given experiment we can not measure the impact parameter therefore, we can not measure the reaction plane angle. Hence we use event plane angle $\Psi_n$ to measure the azimuthal anisotropy. The second order azimuthal anisotropy is called elliptic flow ($v_2$) and is measured with respect to $2^{\text{nd}}$ order event plane angle ($\Psi_2$). We calculate $\Psi_2$ using the azimuthal distribution of the produced particles [27], i.e.,

$$\Psi_2 = \frac{1}{2} \tan^{-1}\left(\frac{Q_{2y}}{Q_{2x}}\right) \qquad (4.2)$$

where, $Q_{2x}$ and $Q_{2y}$ are components of the second order event flow vector $\vec{Q}_2$. The components, $Q_{2x}$ and $Q_{2y}$ are defined as,

$$Q_2 \cos(2\Psi_2) \;=\; Q_{2x} = \sum_{i=1}^{N} w_i \cos(2\phi_i) \tag{4.3a}$$

$$Q_2 \sin(2\Psi_2) \;=\; Q_{2y} = \sum_{i=1}^{N} w_i \sin(2\phi_i) \tag{4.3b}$$

where the sum runs over $N$, the total number of particles produced in an event, and $w_i$ are the weight which is used to optimise the event plane resolution at best by maximizing the flow contributions to the flow vector [27]. In this analysis, transverse momentum $(p_T)$ of individual tracks has been used as weights in Equation 4.3. Tracks with transverse momentum $p_T < 2$ GeV/$c$ has been used for Event Plane calculation to minimize the contribution from non-flow effects (the effect which are not necessarily correlated with the event plane, for example jets). To remove biases from self-correlation and short range correlation, we have followed sub-event plane method [27]. In this process, each event is divided into two sub-events with equal multiplicity. In this analysis we define two sub-events in two different $\eta$ windows namely $\eta^-$ (-1.0 $< \eta <$ -0.05) and $\eta^+$ (0.05 $< \eta <$ 1.0) and calculate $\Psi_{2\eta^-}$ and $\Psi_{2\eta^+}$, for these two $\eta$ windows respectively. To calculate $v_2$, each particle is then correlated with the event plane of opposite $\eta$ window to remove biases from self-correlation. The $\eta$ gap ($\Delta\eta = 0.1$) in between the sub-events reduces the short-range correlations from the $v_2$ measurements. However, this method is insensitive to the effects of long range correlations [28]. The track selection criteria for event plane reconstruction is listed in Table 4.3.

## 4.4.1   Correction For Detector Acceptance

The event plane angle is random in the laboratory frame and therefore it should be a uniform distribution for a perfect detector. However, in the experiments, the detectors have a finite acceptance which can lead to anisotropic particle distributions

Table 4.3: Track cuts used for event plane calculation

| variable | condition |
|---|---|
| Number of fit points in TPC (nHits) | $\geq 15$ |
| (nHits/Maximum possible nHits) | $\geq 0.52$ |
| DCA from primary vertex | $\leq 2.0$ cm |
| $p_T$ | $0.15 \leq p_T \leq 2.0$ GeV/$c$ |
| pseudo-rapidity ($\eta$) | $\leq 1.0$ |

in the laboratory frame. This anisotropy is not related to the true anisotropic flow arising due to initial spatial anisotropy of the system formed in heavy-ion collision, which we aim to measure. Therefore it is necessary to ensure that event plane angle distribution is flat in the laboratory frame. Several methods have been developed to correct for the detector acceptance [27]. The most commonly used methods, is to use the distribution of the particles themselves as a measure of the correction for the acceptance effect. This is know as $\phi$-weight method [27]. In this method, one can accumulate the azimuthal distribution of the particles, in laboratory frame of reference, and then use the inverse of this distribution as weights in the calculation of the event planes. But this method will not work if the azimuthal distribution of the particles is zero or very low in some part of the phase-space (*e.g.* dead sectors in a detector). This type of situation occurred in the STAR detector system because of few dead sector in the TPC during data collection in the year 2010. For this reason it was not possible to use $\phi$-weight method for event plane correction. Another disadvantage of this method is that, it does not take into account the multiplicity fluctuations around the mean value. The second method, known as re-centering [29], is to recenter the distribution of flow vectors ($Q_X$ , $Q_Y$) by subtracting the flow vectors averaged over all events.

$$Q_{2x} = Q_{2x} - \langle Q_{2x} \rangle \tag{4.4a}$$

$$Q_{2y} = Q_{2y} - \langle Q_{2x} \rangle \tag{4.4b}$$

This method has been followed for event plane correction presented in this thesis. The main limitation of this method is that it does not eliminate the higher harmonics from the distribution of $\Psi_2$. To eliminate the higher harmonics contributions, the event plane has been further corrected by the event-by-event shift method. In this method, one fits the unweighted distribution of the event plane in the lab frame, summed over all events, to a Fourier expansion and devises an event-by-event shifting of the planes needed to make the final distribution isotropic. The equation for shift correction for $n^{th}$ harmonic event plane can be written as,

$$\Delta\Psi_n = \frac{1}{n}\sum_{i=1}^{i_{max}}\frac{2}{i}[-\langle\sin(in\Psi_n)\rangle\cos(in\Psi_n) + \langle\cos(in\Psi_n)\rangle\sin(in\Psi_n)] \qquad (4.5)$$

where $\langle\ \rangle$ denotes average over all events. The minimum value of $i_{max} = 4/n$ where $n$ is the harmonic number of interest.

The final corrected event plane is then given by,

$$\Psi'_n = \Psi_n + \Delta\Psi_n \qquad (4.6)$$

The $\Psi_2$ distributions corrected by re-centering and shift method are shown in Fig. 4.3(a) and Fig. 4.3(b) for Au+Au collisions at $\sqrt{s_{NN}} = 200$, 62.4, 39, 27, 19.6, 11.5 and 7.7 GeV respectively. The event plane distributions have been fitted with a Fourier function,

$$f = p_0[1 + 2p_1\cos(2\Psi_2)], \qquad (4.7)$$

where $p_0$ and $p_1$ are free parameters. Small values of parameters $p_1$ indicates that event plane distributions are flat.

## 4.4.2 Resolution Correction of Event Plane

Due to the finite multiplicity in a single event, the calculated event plane ($\Psi_2$) may not coincide with the true reaction plane ($\Psi_r$). Therefore the observed elliptic flow,

115
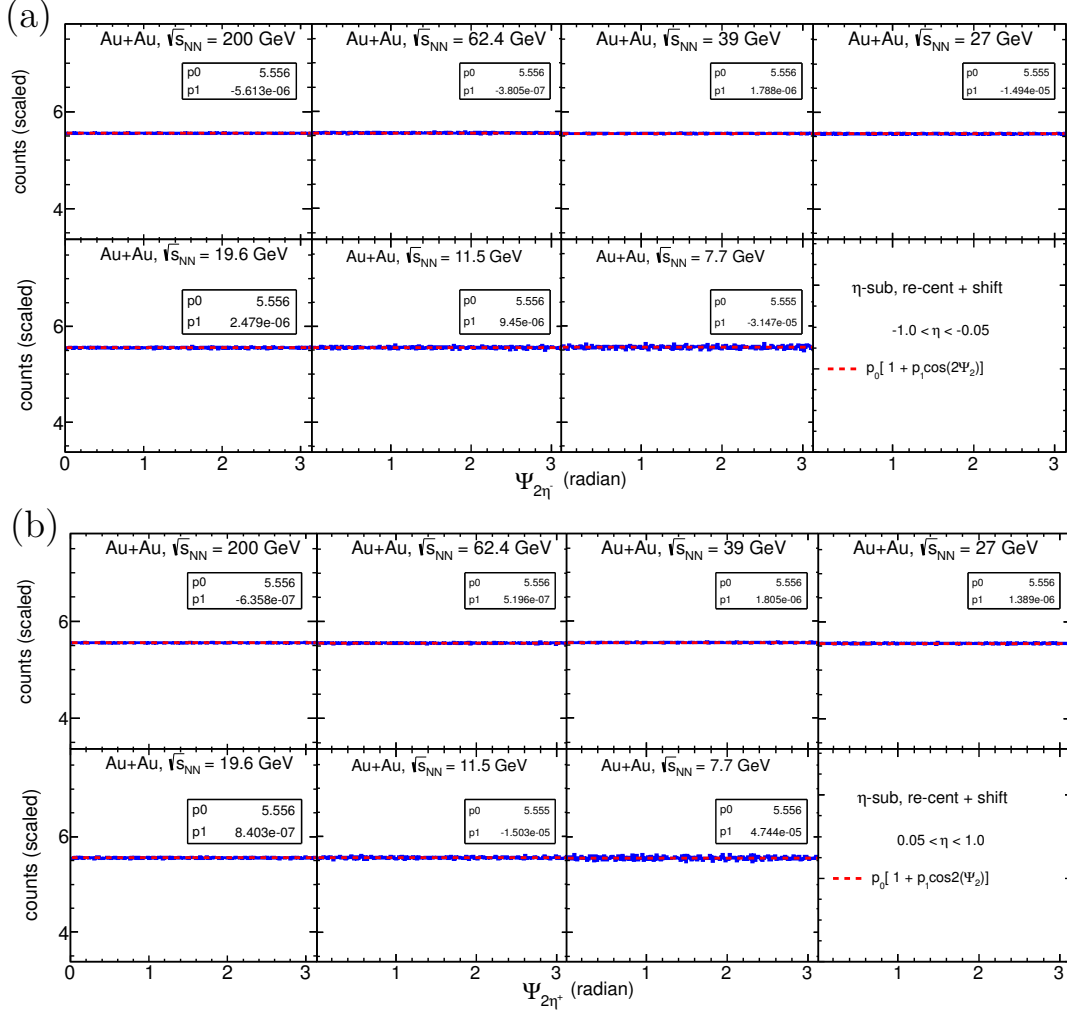
Figure 4.3: Event plane distribution for -1.0 < η < -0.05 (a) and 0.05 < η < 1.0 (b). Dotted line in each panel corresponds to the the 2$^{nd}$ order Fourier function fit (Eq. 4.7). Fit parameter values are shown in the legend.

$v_2^{obs}$, has to be corrected for the event plane resolution ($R$) as,

$$v_2 = \frac{v_2^{obs}}{R} = \frac{v_2^{obs}}{\langle \cos[2(\Psi_2 - \Psi_r)] \rangle} \tag{4.8}$$

where $\Psi_r$ is the true reaction plane angle. Since $\Psi_r$ is unknown, the event plane resolution is estimated by the correlation of the event planes of two sub-events, namely

sub-event A and sub-event B, and is given by,

$$R = \langle \cos[2(\Psi_2 - \Psi_r)] \rangle = C\sqrt{\cos[2(\Psi_2^A - \Psi_2^B)]} \qquad (4.9)$$

where $C$ is a constant calculated from the known multiplicity dependence of the resolution [27]. For this analysis, the sub-events were constructed by dividing the full TPC acceptance into two $\eta-$sub groups so that the multiplicity of each sub-event A and B are approximately the same and hence their respective resolutions should be equal. Fig. 4.4 shows resolution for each sub event plane as function of centrality for different beam energies in Au+Au collisions.
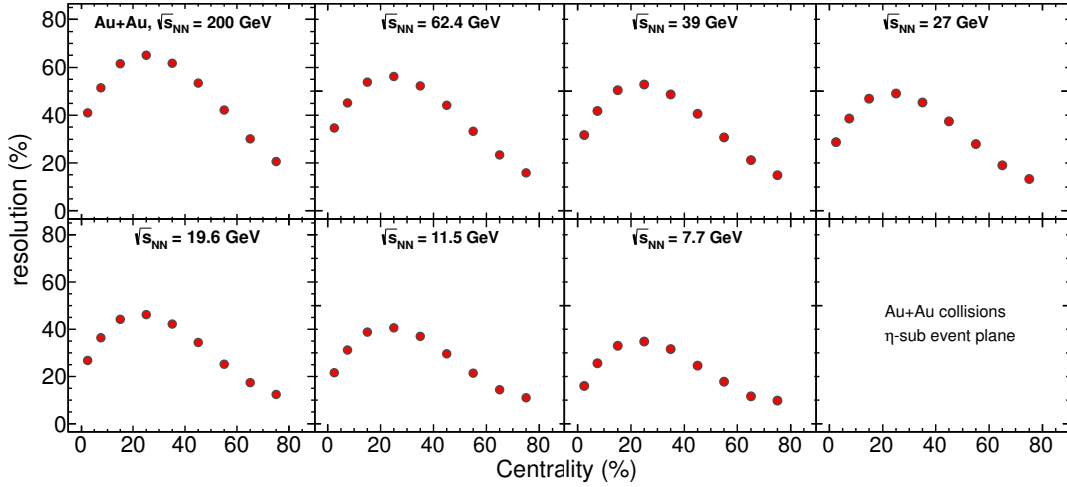


Figure 4.4: Resolution of sub-event planes as a function of centrality for Au+Au collisions at $\sqrt{s_{NN}} = 200$, 62.4, 39, 27, 19.6, 11.5 and 7.7 GeV.

The event plane resolution has been calculated for nine different centrality individually (namely $0-5\%$, $5-10\%$, $10-20\%$, $20-30\%$, $30-40\%$, $40-50\%$, $50-60\%$, $60-70\%$ and $70-80\%$). As the event plane resolution depends on number of particles used for event plane reconstruction, therefore it increases from peripheral to central collisions. On the other hand, since the event plane is calculated using the anisotropic flow of the event itself, the resolution decreases for more central collisions where anisotropic flow is small. Because of this two competing effects the final resolution first increases from

peripheral to mid-central collision and then decreases again. The values of second order TPC event plane resolution for $\eta-$sub events for all nine centrality classes and for all beam energies are shown in Table 4.4. Statistical error on resolution is less than 2% for all the centrality classes and all energies.

Table 4.4: $2^{\text{nd}}$ order event plane resolution for $\eta$-sub event method

| $\sqrt{s_{\text{NN}}}$ | 0-5% | 5-10% | 10-20% | 20-30% | 30-40% | 40-50% | 50-60% | 60-70% | 70-80% |
|---|---|---|---|---|---|---|---|---|---|
| 200 GeV | 0.409 | 0.513 | 0.615 | 0.650 | 0.616 | 0.535 | 0.421 | 0.301 | 0.207 |
| 62.4 GeV | 0.347 | 0.451 | 0.538 | 0.562 | 0.522 | 0.440 | 0.333 | 0.234 | 0.159 |
| 39 GeV | 0.316 | 0.417 | 0.504 | 0.528 | 0.487 | 0.406 | 0.306 | 0.212 | 0.148 |
| 27 GeV | 0.288 | 0.386 | 0.469 | 0.491 | 0.453 | 0.375 | 0.279 | 0.191 | 0.132 |
| 19.6 GeV | 0.267 | 0.364 | 0.442 | 0.463 | 0.421 | 0.344 | 0.253 | 0.174 | 0.124 |
| 11.5 GeV | 0.216 | 0.312 | 0.387 | 0.407 | 0.370 | 0.295 | 0.214 | 0.145 | 0.109 |
| 7.7 GeV | 0.160 | 0.257 | 0.330 | 0.349 | 0.315 | 0.246 | 0.177 | 0.116 | 0.098 |

Most commonly used method for resolution correction for an average $v_2$ over a wide centrality range is,

$$\langle v_2 \rangle = \frac{\langle v_2^{obs} \rangle}{\langle R \rangle}. \tag{4.10}$$

Here $\langle R \rangle$ is the mean resolution in that wide centrality bin and can be calculated as,

$$\langle R \rangle = \frac{\sum N_i \langle R \rangle_i}{\sum N_i}, \tag{4.11}$$

where $N_i$ and $\sum N_i \langle R \rangle_i$ is the multiplicity and resolution of the $i^{th}$ narrow centrality bin, respectively. This procedure works well for narrow centrality bins, but fails for wider centrality bins like for example 0-80%. There is another approach, known as event by event resolution correction, for event plane resolution correction for wide centrality bin [24]. In this method resolution correction for wide centrality bin has been done by dividing the term $\cos[2(\phi - \Psi_2)]$ for each particle by the event plane resolution $(R)$ of the corresponding centrality for each event, i.e.,

$$\langle v_2 \rangle = \langle \frac{v_2^{obs}}{R} \rangle. \tag{4.12}$$

These two method do not give same $\langle v_2 \rangle$ because

$$\frac{\langle v_2^{obs} \rangle}{\langle R \rangle} \neq \langle \frac{v_2^{obs}}{R} \rangle. \tag{4.13}$$

## 4.4.3 The $\eta$-sub Event Plane Method

The $\eta$-sub event plane method helps to reduce the contribution from non-flow effects (which arises mostly due to short-range correlations) by correlating particles in two different pseudo-rapidity window. In this method [27] two event plane angles are calculated in two different $\eta$ windows, (and separated by a small $\Delta\eta$ gap in between them). Then each particle is correlated with event plane angle of opposite hemisphere. Since the particle and event plane angles are from opposite hemispheres, therefore, this method also takes care for the self-correlation effect. Therefore, using $\eta$-sub event plane method, $v_2$ is defined as,

$$v_2(\eta_\pm) = \frac{\langle \cos[2(\phi_{\eta_\pm} - \Psi_{2,\eta_\mp})] \rangle}{\sqrt{\langle \cos[2(\Psi_{2,\eta_+} - \Psi_{2,\eta_-})]}} \tag{4.14}$$

Here $\Psi_{2,\eta_+}$ and $\Psi_{2,\eta_-}$ are the second harmonic event plane angle defined for particles with positive ($0.05 \leq \eta \leq 1.0$) and negative ($-1.0 \leq \eta \leq -0.05$) pseudo-rapidity window respectively. An $\eta$ gap of $|\eta| < 0.1$ between positive and negative pseudo-rapidity sub-events has been introduced to suppress non-flow effects. In Eq. 4.14 the non-flow effects (correlations) are reduced in both the observed flow (numerator) and the event plane resolution (denominator). Depending on the nature of the remaining non-flow effects, $v_2$ measured this way may have values that are either lower or higher than those obtained with the standard plane method [22]. But this method is not sufficient to reduce non-flow effects due to long-range correlations. The results presented in this thesis has been calculated using the $\eta$−sub event plane method.

## 4.5 Extraction of nuclei $v_2$

### 4.5.1 $\phi$-binning Method for $v_2$ Measurement

In this method one has to measure the raw yield of the chosen particle as function of the angle $\phi - \Psi_2$, where the $\phi$ is is the azimuthal angle of the particle in the lab-frame and $\Psi_2$ is the $2^{nd}$ order event plane angle. Then the $\phi - \Psi_2$ distribution is fitted with a Fourier function to extract the $v_2$. Since light nuclei can not be identified event-by-event, therefore, statistical method is followed to find the yield of light nuclei. In this method, we fill histograms of the $Z$ (defined in chapter 3) in bins of $\phi - \Psi_2$. One such representative plot for $Z$ distribution of mid-rapidity $\overline{d}$, $t$ and $^3He$ in Au+Au collisions at $\sqrt{s_{\mathrm{NN}}} = 39$ GeV for 0-80% centrality is shown in Fig. 4.5. The $Z$ distributions, for each transverse momentum $(p_T)$ bin is then fitted with a two Gaussian function, one for the desired nuclei and another for the background. The nuclei yield is then extracted by bin counting the histogram of $Z$-distribution after subtracting the background contribution. The yield calculated by integrating the Gaussian function for desired nuclei gives same yield as bin counting method. However, deuterons at low $p_T$ $(< 1.0$ GeV$/c)$ can be contaminated with the knock out deuterons from the beam-pipe.
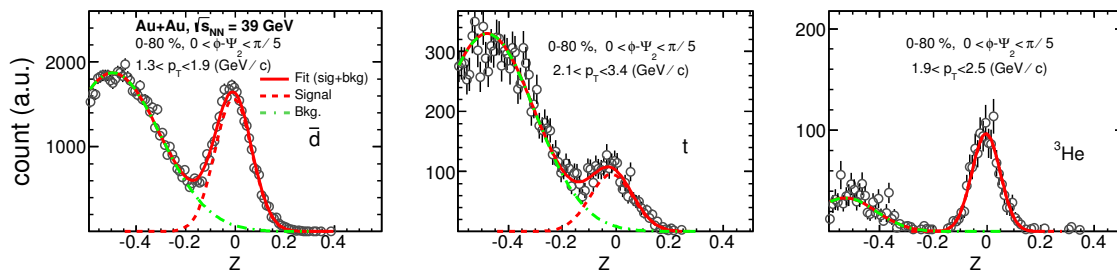


Figure 4.5: $Z$ distribution for mid-rapidity $\overline{d}$, $t$ and $^3$He from Au+Au collisions at $\sqrt{s_{\mathrm{NN}}} = 39$ GeV. The different $p_T$ ranges are for representative purpose. $Z$ distribution of each nuclei is fitted with two Gaussian function (red solid) curve. One Gaussian corresponds to $Z$ of nuclei (red dashed line) and another Gaussian corresponds to the background (dot-dashed line).

We take care for this contamination by fitting the DCA distribution of $d$ with the DCA of $\bar{d}$ as reference since $\bar{d}$ do not have such contaminations. The details of this method is explained in Appendix 3.9.2. In this analysis we have used deuterons that have been produced only from Au+Au events. The yield of light nuclei is then plotted as a function of $\phi - \Psi_2$ and fitted with a Fourier function to extract $v_2$,

$$\frac{dN}{d(\phi - \Psi_2)} = p_0[1 + 2v_2 \cos(2(\phi - \Psi_2))], \tag{4.15}$$

where $p_0$ and $v_2$ are the fit parameters. The raw yields of mid-rapidity light nuclei for different $(\phi - \Psi_2)$ bins in Au+Au collisions at $\sqrt{s_{NN}} = 39$ GeV for 0-80% centrality are shown in Fig. 4.6.
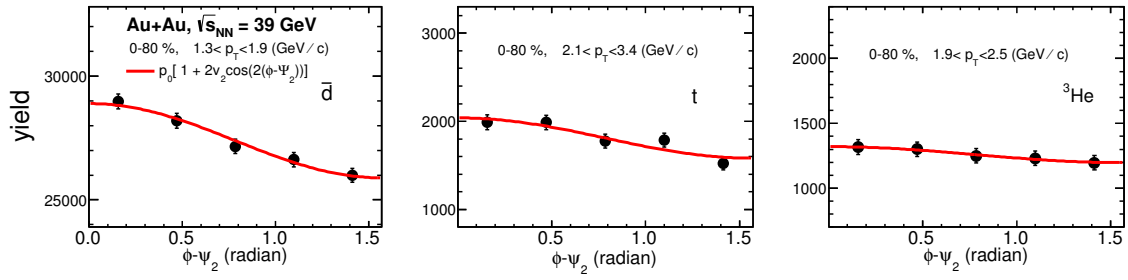


Figure 4.6: $(\phi - \Psi_2)$ distribution for mid-rapidity $\bar{d}$, $t$ and $^3He$ from Au+Au collisions at $\sqrt{s_{NN}} = 39$ GeV. $(\phi - \Psi_2)$ distribution is fitted with Fourier function (red solid line) as mentioned in Eq. 4.15 to get the parameter $v_2$.

The distribution is fitted with the function as described in Eq. 4.15 and the fit is shown by red line. Here the measured $v_2$ has been corrected by event-by-event resolution correction method [24].

## 4.6 Systematic Uncertainties

The systematic uncertainties were evaluated by varying the various parameters used to determine the light nuclei yields. The main source of systematic uncertainty for nuclei yields are discussed in the following subsections.

### 4.6.1 Uncertainty in Particle Identification

Both the TPC and TOF detector has been used to identify light nuclei. The $Z$ variable is used to identify light nuclei using TPC detector and mass ($m^2$) is used from the time-of-flight information using the TOF detector. Hence, by varying the $Z$ and $m^2$ range, systematic uncertainty due to particle identification was studied.

### 4.6.2 Uncertainty from Track Selections

Various track cuts are used to select good quality tracks for the analysis (see Table 4.2). The light nuclei yield depends on these track cuts. Hence these track cuts are varied to study the systematic uncertainty due to track selection.

## 4.7 Results and Discussion

### 4.7.1 Minimum Bias $v_2$

Figure 4.7 shows elliptic flow $v_2$ as a function of transverse momentum $p_T$ at midrapidity for light nuclei in minimum bias (0-80%) events for Au+Au collisions at $\sqrt{s_{\mathrm{NN}}}$ = 200, 62.4, 39, 27, 19.6, 11.5 and 7.7 GeV. $v_2(p_T)$ of $\overline{d}$ is shown only for beam energies $\sqrt{s_{\mathrm{NN}}} > 11.5$ GeV as statistics is insufficient for lower beam energies. For the same reason $v_2(p_T)$ of $^3\overline{He}$ is measured only for $\sqrt{s_{\mathrm{NN}}} = 200$ GeV. In Fig. 4.7, the statistical errors are shown by vertical lines where as systematic errors are shown by bands. The $v_2(p_T)$ for all nuclei species show monotonically increasing trend with increasing $p_T$ (Fig. 4.7). Mass ordering of nuclei $v_2(p_T)$ can also be seen for $p_T < 2.0$ GeV/$c$. The mass ordering of deuteron $v_2(p_T)$ is clearly visible in Fig. 4.8 where the $v_2(p_T)$ of $\pi^+$, $K_s^0$ and $p$ are also included from Ref. [3]. For low transverse momentum ($p_T < 2.0$ GeV/$c$), lower mass particles has higher $v_2(p_T)$ compared to heavier particles. This observed mass ordering of $v_2(p_T)$ occurs naturally in a hydrodynamic model of heavy-ion collisions [21]. The negative $v_2$ observed in the low transverse momentum
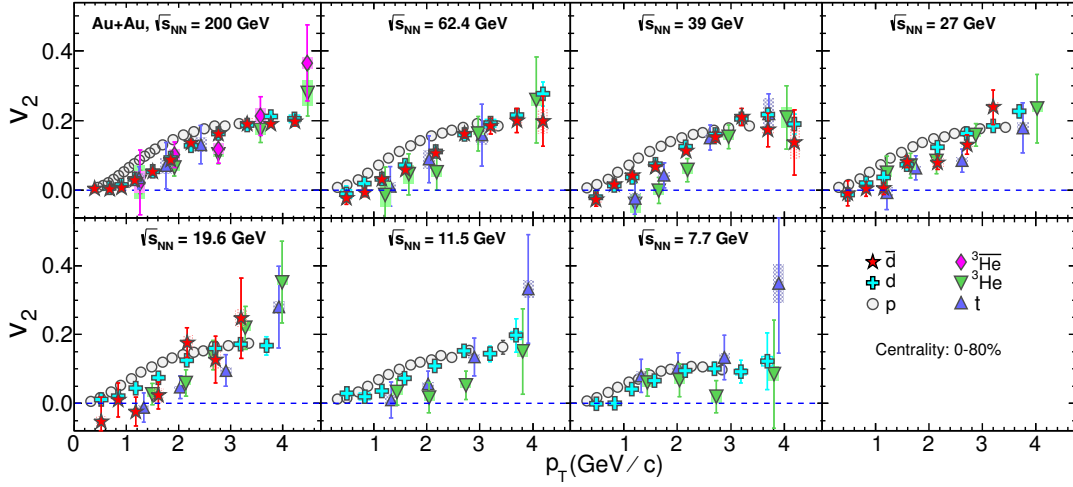
Figure 4.7: Observation of mid-rapidity $v_2(p_T)$ for $d, \bar{d}$, $t$ and $^3$He,$^3\overline{\text{He}}$ from minimum bias (0-80%) Au+Au collisions. For comparison, proton $v_2(p_T)$ also shown as open circles in the figure. Vertical line in each marker corresponds to statistical error and band corresponds to systematic error. Proton $v_2$ are from Ref. [3].
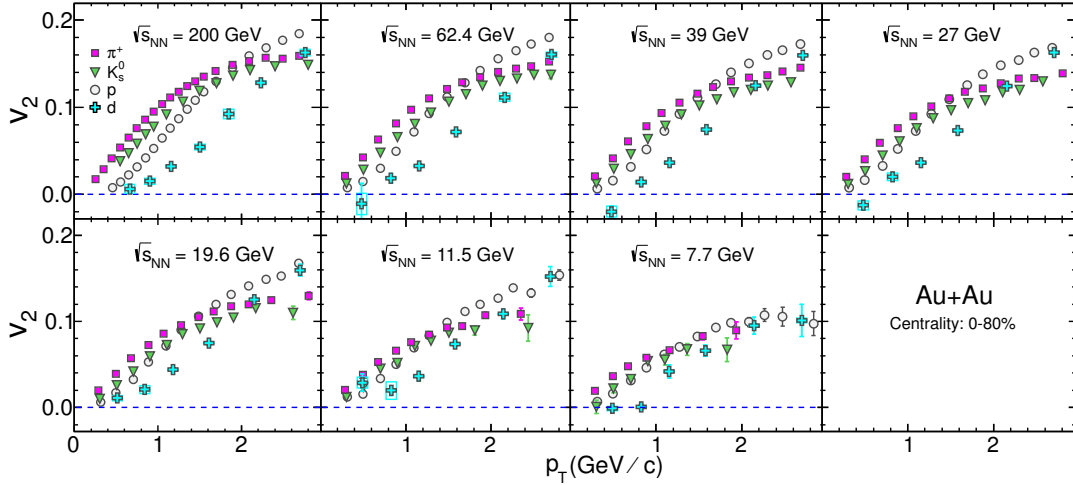


Figure 4.8: Mass dependence of mid-rapidity $v_2(p_T)$ for $\pi^+$ (square), $K_s^0$ (triangle), $p$ (open circle), and $d$ (cross) for minimum bias (0-80%) Au+Au collisions.

for some beam energies could be attributed to the interplay of radial and elliptic flow as the Blast-Wave model predicts [15]. With the available large statistics in the analyzed data set, it was possible to study the difference of $v_2(p_T)$ of $d$ and $\bar{d}$ in a wide energy range. Fig. 4.9 presents the difference of $v_2(p_T)$ of $d$ and $\bar{d}$ for Au+Au collision at $\sqrt{s_{\text{NN}}} = 200$, 62.4, 39, 27 and 19.6 GeV. For comparison, difference of $v_2$
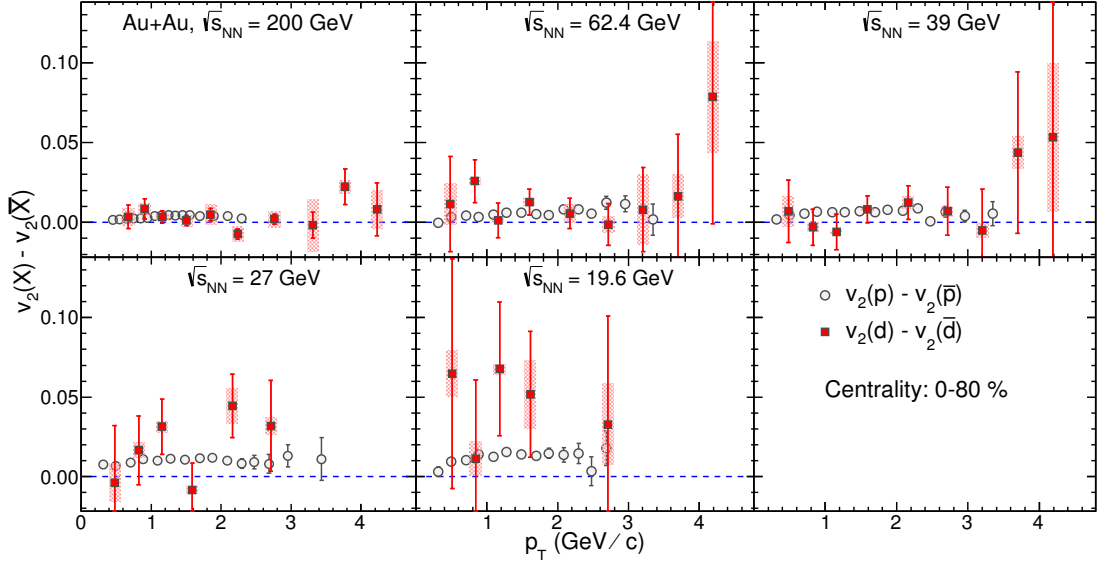
Figure 4.9: Energy dependence of $v_2$ difference: $v_2(d)$ - $v_2(\bar{d})$ as a function of transverse momentum for minimum bias (0-80%) Au+Au collisions at $\sqrt{s_{NN}}$ = 200, 62.4, 39, 27, 19.6 GeV.

of $p$ and $\bar{p}$ from [3] are also shown. Fig. 4.9 shows that the $v_2$ of nuclei and anti-nuclei is almost same for $\sqrt{s_{NN}} \geq 39$ GeV. However, although the statistical errors are large, the $v_2$ of nuclei and anti-nuclei starts to differ for beam energies $(\sqrt{s_{NN}}) \leq 27$ GeV. The difference increases as collision energy $(\sqrt{s_{NN}})$ decreases and the difference is qualitatively similar to the difference in $v_2$ observed in $p$ and $\bar{p}$. The increased difference in $v_2$ at low beam energies for both hadrons and nuclei might be the result of the increased hadronic interactions [3]. Figure 4.10 shows the comparison of $v_2(p_T)$ of $t$ and $^3He$. The $t$ and $^3He$ nuclei have same atomic mass number $(A)$ but different composition of protons and neutrons inside them. The $t$ and $^3He$ nuclei exhibit similar magnitude of $v_2$ within the statistical error. This observation suggests that the $v_2$ of light nuclei are independent of the composition of nucleons inside them if the atomic mass number is same. It also suggests that individual components (proton and neutron) are carrying equal amount of collectivity so that any combination, keeping the same atomic mass number $(A)$, results in similar magnitude of collective flow.
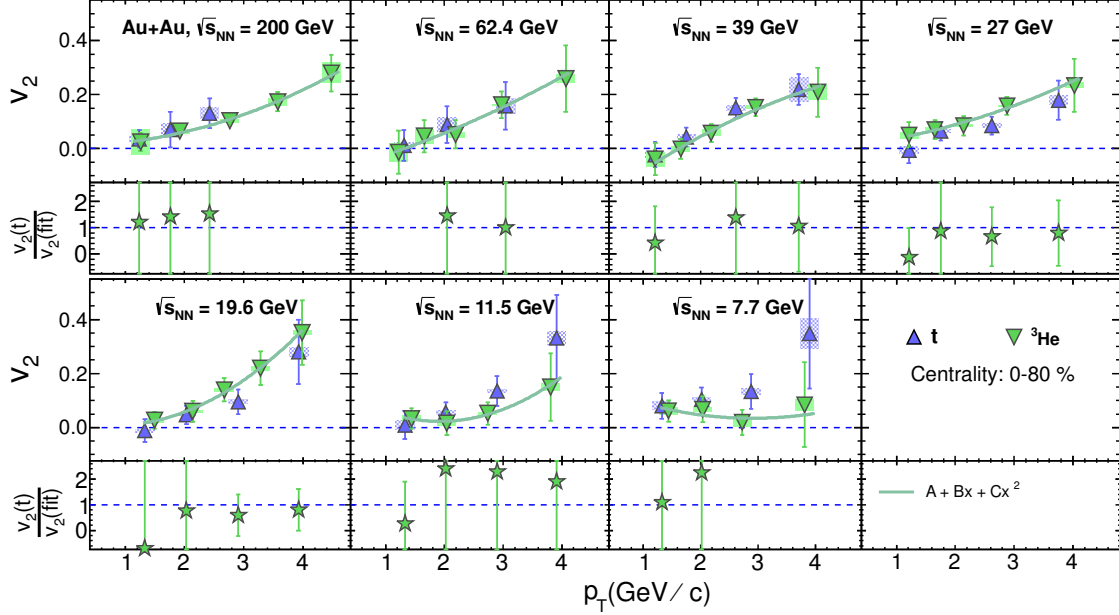
Figure 4.10: Comparison of mid-rapidity $^3He$ $v_2$ with that of $t$ for minimum bias (0-80%) Au+Au collisions. The solid line in the upper panels is $2^{nd}$ order polynomial fit to the $^3He$ $v_2$ data and the ratio to that of $t$ $v_2$ is shown in the lower plot at each corresponding collision energy.

## 4.7.2 Centrality Dependence of Nuclei $v_2$

The event statistics is sufficient for the measurement of the centrality dependence of $v_2$ of $d$ in Au+Au collisions at $\sqrt{s_{NN}}$ = 200, 62.4, 39, 27, 19.6, 11.5 and 7.7 GeV and down to $\sqrt{s_{NN}}$ = 27 GeV for $\bar{d}$. The statistics is insufficient for measurement of the centrality dependence of $v_2$ of $\bar{d}$ for beam energies $\sqrt{s_{NN}} < 27$ GeV. Figure 4.11 shows the $v_2$ of $d$ and $\bar{d}$ in 0-30% and 30-80% central events in Au+Au collisions for $\sqrt{s_{NN}}$ = 62.4, 39, 27, 19.6, 11.5 and 7.7 GeV. For the Au+Au collision at $\sqrt{s_{NN}}$ = 200 GeV, $v_2$ of $d$ and $\bar{d}$ are measured in three different centralities, namely 0-10%, 10-40% and 40-80% central events. The $v_2$ of both $d$ and $\bar{d}$ show clear centrality dependence for the measured energy ranges. From Fig. 4.11, it is also observed that $d$ and $\bar{d}$ show similar magnitude of $v_2$ for each centrality.
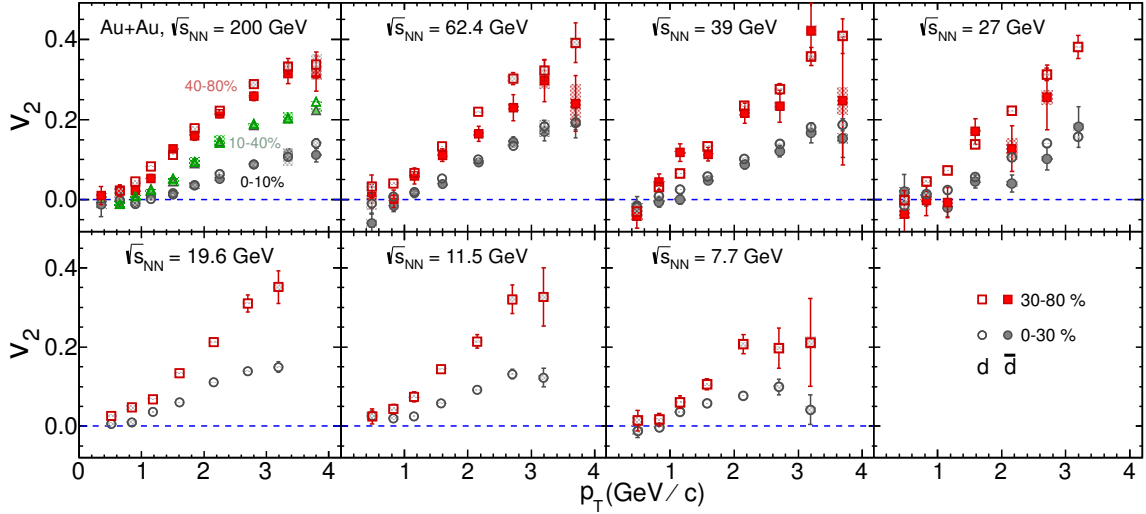
Figure 4.11: Centrality dependence of mid-rapidity $v_2(p_T)$ of $d$ (open markers) and $\bar{d}$ (solid markers) for Au+Au collisions at $\sqrt{s_{NN}} = 200$, 62.4, 39, 27, 19.6, 11.5 and 7.7 GeV. For $\sqrt{s_{NN}} = 200$ GeV, circles corresponds to 0-10%, triangles corresponds to 10-40% and squares corresponds to 40-80% central events. In rest of the collision energies, circles corresponds to 0-30% and squares corresponds to 30-80% central events.

## 4.7.3   Atomic Mass Number Scaling and Coalescence Model

Figure 4.12 presents the nuclei $v_2/A$ as a function of $p_T/A$ where $A$ is the atomic mass number of the corresponding nuclei. The main goal of this study is to understand whether the light nuclei (anti-nuclei) are produced via coalescence of nucleons (anti-nucleons). Coalescence model predicts that if a composite particle is produced by coalescence of $n$ number of particles, very close to each other in phase-space, then the elliptic flow $v_2(p_T)$ of the composite will be the $n$-times the $v_2(p_T)$ of the individual particles [10]. In Fig 4.12 it is observed that the nuclei (anti-nuclei) $v_2$, scaled by atomic mass number ($A$), follows $v_2$ of $p$ ($\bar{p}$) for $p_T/A$ up to 1.5 GeV/$c$. This indicates that $d$ ($\bar{d}$) within $p_T < 3.0$ GeV/$c$ and $t$, $^3He$ ($^3\overline{He}$) within $p_T < 4.5$ GeV/$c$ might have formed via coalescence of proton (anti-proton) and neutron (anti-neutron). There is another possibility of light nuclei formation via the coalescence of quarks produced in heavy-ion collisions as observed for identified hadrons [3]. However, there is a major drawback to this assumption as the binding energies of light nuclei are very low ($\sim$few MeV). Since the average temperature of the quark-gluon system is very high
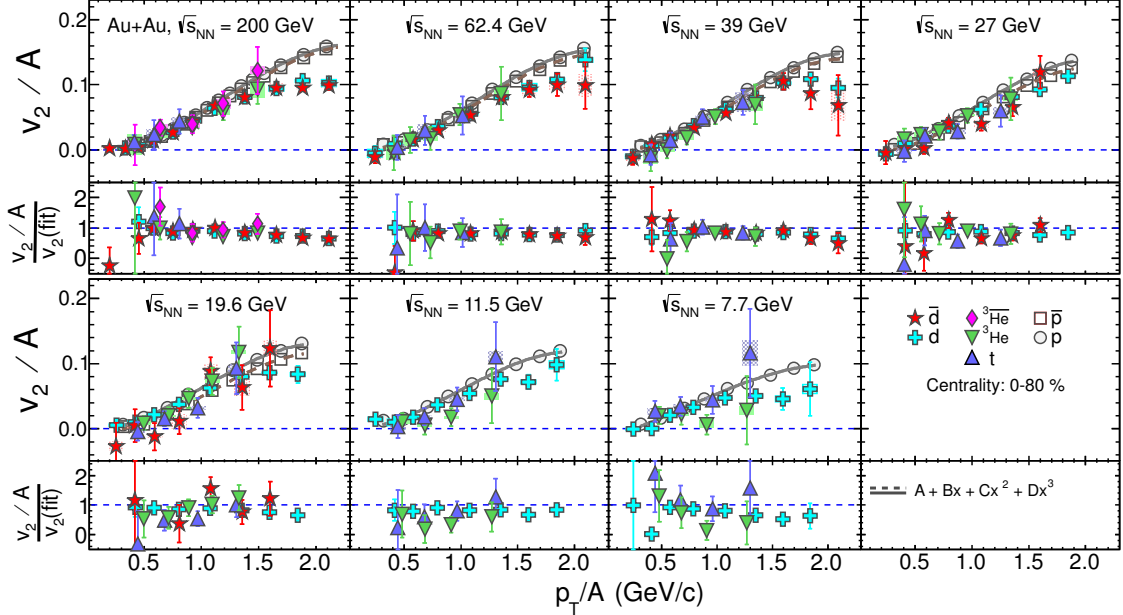
Figure 4.12: Atomic mass ($A$) scaling of the mid-rapidity light nuclei $v_2$ of $p(\bar{p})$, $d$, $(\bar{d})$ and $t$ and $^3He$, $(^3\overline{He})$ from minimum bias (0-80%) Au+Au collisions. Solid (dotted) line corresponds to the polynomial fit to the of $p$ ($\bar{p}$) $v_2$ data. The ratios of $[v_2/A]$/fit results for $d$, $\bar{d}$, $t$ and $^3He$ are shown in the lower panels at each corresponding collision energy.

compared to the binding energy of the light nuclei, it is highly unlikely that any nuclei would survive during the quark coalescence process. To verify the applicability of coalescence of nucleons to be source of nuclei production in heavy-ion collision, we have carried out a model based study on light nuclei production. The dynamic coalescence model study has been carried out using a transport model namely A Multi Phase Transport (AMPT) model (version v2.25t7d) [31]. The AMPT model, which is a hybrid transport model has four main stages: the initial conditions, partonic interactions, the conversion from the partonic to the hadronic matter, and the hadronic interactions. It uses the same initial conditions as in HIJING [32]. Scattering among partons are modelled by Zhang's parton cascade [33], which calculates two-body parton scatterings using cross sections from pQCD with screening masses. In the default AMPT model, partons are recombined with their parent strings and when they stop interacting, the resulting strings fragment into hadrons according to the Lund string fragmentation model [34]. However in the string melting scenario, these strings are

127
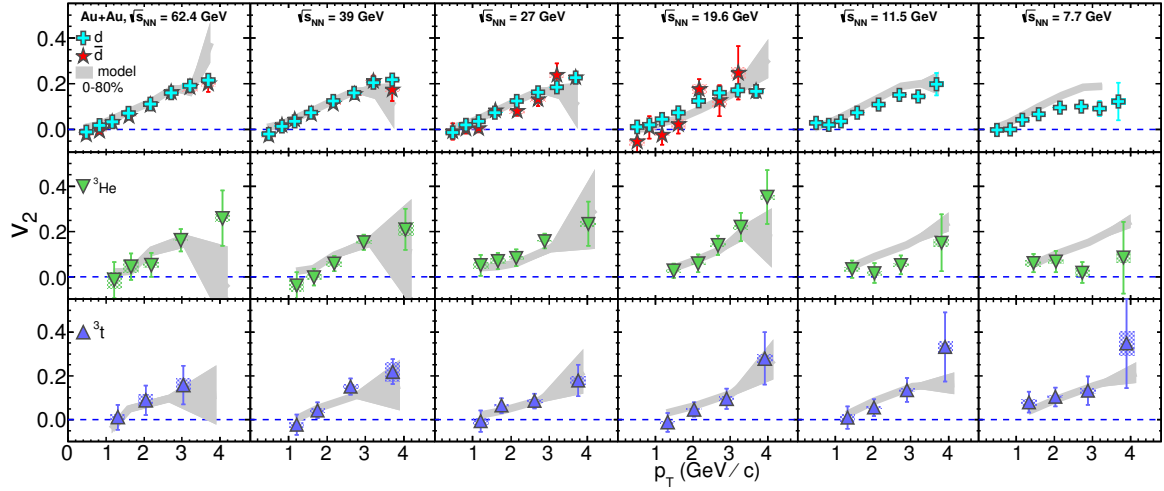
Figure 4.13: Mid-rapidity $v_2$ of $d$, $t$ and $^3He$ are compared with the results of AMPT + Coalescence calculations (hatched bands).

converted into soft partons and a quark coalescence model is used to combine parton into hadrons. The evolution dynamics of the hadronic matter is described by A Relativistic Transport (ART) model [37]. For this study we have used nucleon phase space information from the string melting version of the AMPT model. The dynamical coalescence model has been used extensively at both intermediate [35] and high energies [36]. In this model, the probability for producing a cluster is determined by the overlap of the cluster's Wigner phase-space density with the nucleon phase-space distribution at freeze-out. For light nuclei, the Wigner phase-space densities are obtained from their internal wave functions, which are taken to be those of a spherical harmonic oscillator [38]. The $v_2$ results of $d$, $t$ and $^3He$ from dynamic coalescence model are shown in solid bands in Fig. 4.13. The figure shows that the coalescence model results agree with the measured light nuclei $v_2$ in the data. This observation supports the idea that in heavy-ion collisions, light nuclei might be produced via coalescence of nucleons.

## 4.8 Summary

The measurement of the $2^{nd}$ order azimuthal anisotropy, namely, $v_2(p_T)$ for $d$, $\bar{d}$, $t$, $^3He$ in mid-rapidity ($|\eta| < 1.0$) for Au+Au collisions at center of mass energy $\sqrt{s_{\mathrm{NN}}} = 200$, 62.4, 39, 27, 19.6, 11.5 and 7.7 GeV is presented. It is found that the elliptic flow ($v_2$) of all nuclei for minimum bias events of Au+Au, shows monotonically increasing trend with increasing $p_T$. Light nuclei $v_2$ show mass ordering at low $p_T$ similar to hadrons (Fig. 4.7 and Fig. 4.8) as well as a collision centrality dependence (Fig. 4.11). It is observed that $v_2$ of nuclei and anti-nuclei are almost of similar magnitude for beam energies ($\sqrt{s_{\mathrm{NN}}}$) = 39 GeV and above. Although the errors are large for $\sqrt{s_{\mathrm{NN}}} < 39$ GeV, it is found that the difference of $v_2$ of nuclei and anti-nuclei starts increasing as collision energy decreases, similar to that observed for $p$ and $\bar{p}$ (Fig. 4.9). The $t$ and $^3He$ nuclei have same magnitude of $v_2$ for collision energies $\sqrt{s_{\mathrm{NN}}} = 200$, 62.4, 39, 27, 19.6, 11.5 and 7.7 GeV (Fig. 4.10). The $v_2$ of light nuclei is found to depend only on their mass and not on the composition of the individual nuclei. The light nuclei $v_2$ follows an atomic mass number scaling up to $p_T/A \sim 1.4$ GeV/c (Fig. 4.12) which indicates the coalescence of nucleons might be underlying mechanism of light nuclei formation in heavy-ion collisions. This fact is further corroborated by carrying out a model based study of nuclei $v_2$ using transport+coalescence model. It is observed that the coalescence model reproduces the light nuclei $v_2$, as measured in the data (Fig. 4.13). This supports the general idea of coalescence of nucleons to be the process behind light nuclei formation in heavy-ion collisions.

# Bibliography

[1] I. Arsene *et al.*, Nucl. Phys. A **757**, 1 (2005); B. B. Back *et al.*, Nucl. Phys. A **757**, 28 (2005); J. Adams *et al.*, Nucl. Phys. A **757**, 102 (2005); K. Adcox *et al.*, Nucl. Phys. A **757**, 184 (2005).

[2] L. Adamczyk *et al.*, Phys. Rev. C **86**, 054908 (2012).

[3] L. Adamczyk *et al.*, Phys. Rev. C **88**, 014902 (2013).

[4] L. Adamczyk *et al.*, Phys. Rev. Lett. **110**, 142301 (2013).

[5] X. Dong *et al.* Phys. Lett. B **597**, 328332 (2004); Nu Xu, J. Phys. Conf. Ser. **50**, 243 (2006).

[6] H. H. Gutbrod et al., Phys. Rev. Lett. **37**, 667 (1976).

[7] R. Scheibl and U. Heinz, Phys. Rev. C **59**, 1585 (1999); W. J. Llope et al., Phys. Rev. C **52**, 2004 (1995).

[8] H. Sato and K. Yazaki, Phys. Lett. B **98**, 153 (1981).

[9] S.T. Butler and C.A. Pearson, Phys. Rev. **129**, 836 (1963).

[10] H. H. Gutbrod *et al.*, Phys. Rev. Lett. **37**, 667 (1976); H. Sato and K. Yazaki, Phys. Lett. B **98**, 153 (1981); W. J. Llope et al., Phys. Rev. C **52**, 2004 (1995); R. Scheibl and U. Heinz, Phys. Rev. C **59**, 1585 (1999).

[11] C. Adler *et al.*, Nucl. Instrum. Methods A **470**, 488499 (2001).

[12] W. J. Llope *et al.*, Nucl. Instrum. Methods A **522**, 252 (2005).

[13] C. A. Whitten Jr, AIP Conf. Proc. **980**, 390 (2008); J. Kiryluk, arXiv:hep-ex[0501072].

[14] S. Afanasiev *et al.*, Phys. Rev. Lett. **99**, 052301 (2007).

[15] B. I. Abelev *et al.*, arXiv:0909.0566v1 [nucl-ex].

[16] C. Jena *et al.*, arXiv:1101.4196 [nucl-ex].

[17] K. H. Ackermann *et al.*, Nucl. Instrum. Methods A **499**, 624 (2003).

[18] M. Anderson *et al.*, Nucl. Instrum. Methods A **499**, 659 (2003).

[19] H. Bichsel, Nucl. Instrum. Methods A **562**, 154 (2006).

[20] W. J. Llope, Nucl. Instrum. Methods B **241**, 306 (2005).

[21] P. F. Kolb and U. Heinz Nucl. Phys. A **715**, 653c (2003).

[22] B.I. Abelev *et al.*, Phys. Rev. C **77**, 054901 (2008).

[23] D. Kharzeev and M. Nardi, Phys. Lett. B **507**, 121 (2001).

[24] H. Masui and A. Schmah, arXiv:1212.3650v1 [nucl-ex].

[25] B. B. Back *et al.*, Phys. Rev. C **70**, 021902(R) (2004).

[26] J. Beringer *et al.*, Phys. Rev. D **86**, 010001 (2012).

[27] A. M. Poskanzer and S. A. Voloshin, Phys. Rev. C **58**, 1671 (1998).

[28] A. M. Poskanzer and S. A. Voloshin, arXiv:0809.2949v2 [nucl-ex].

[29] P. Danielewicz *et al.*, Phys. Rev. C **38**, 120 (1988); J. Barrette *et al.*, Phys. Rev. Lett. **55**, 1420 (1997); J. Barrette *et al.*, Phys. Rev. C **56**, 3254 (1997).

[30] B. I. Abelev *et al.* Phys. Rev. C **81**, 044902 (2010).

[31] Z. Lin, C. M. Ko, B. A. Li, B. Zhang, and S. Pal, Phys. Rev. C **72**, 064901 (2005).

[32] X. N. Wang and M. Gyulassy, Phys. Rev. D **44**, 3501 (1991).

[33] B. Zhang, Comput. Phys. Commun. **109**, 193 (1998).

[34] B. Andersson *et al.* Phys. Rep. **97**,31 (1983).

[35] M. Gyulassy, K. Frankel, E. A. Relmer, Nucl. Phys. A **402**, 596 (1983); J. Aichelin et al., Phys. Rev. Lett. **58**, 1926 (1987); V. Koch et al., Phys. Lett. B **241**, 174 (1990); L. W. Chen, C.M. Ko, B. A. Li, Phys. Rev. C **68**, 017601 (2003).

[36] J. L. Nagle, B. S. Kumar, D. Kusnezov, H. Sorge, and R. Mattiello, Phys. Rev. C **53**, 367 (1996); R. Mattiello, H. Sorge, H. Stöcker, and W. Greiner, Phys. Rev. C **55**, 1443 (1997); L. W. Chen and C. M. Ko, Phys. Rev. C **73**, 044903 (2006).

[37] B. A. Li and C. M. Ko, Phys. Rev. C **52**, 2037 (1995); B. A. Li, A. T. Sustich, B. Zhang, and C. M. Ko, Int. J. Phys. E **10**, 267 (2001).

[38] R. Scheibl and U. Heinz, Phys. Rev. C **59**, 1585 (1999); A. T. M. Aerts and C. B. Dover, Phys. Rev. D **28**, 450 (1983).

[39] G. E. Brown and M. Rho, Phys. Rev. Lett. **66**, 2720 (1991).

[40] R. Rapp and E. Shuryak, Phys. Rev. Lett. **86**, 2980 (2001).

[41] K. Aamodt *et al.* (ALICE Collaboration), Phys. Lett. B **696**, 328 (2011).

[42] J. Adams *et al.* (STAR Collaboration), Phys. Rev. C **71**, 064902 (2005).

## 4.9 Appendix

### 4.9.1 Removing Beam Pipe Contamination from $d$ Yield

The region of beam pipe running through the TPC detector is made of low $Z$ material (Beryllium). The particles coming from the primary vertex can hit the beam pipe material and generate large numbers of secondary particles with low $Z$, including deuterons. The low momentum deuterons from collision vertex have a significant contamination from these background deuterons knocked out from the beam pipe. These background deuterons cannot be easily distinguished by the TPC as their ionization energy loss characteristics are similar to the primary deuterons from the primary vertex. The background deuteron tracks is not generated in the actual event and hence they are not related to the primary vertex. The characteristic quantity which defines how close the track is from the primary vertex is the distance of closest approach (DCA). For this analysis primary tracks which have DCA < 1.0 cm has been used as shown in Table 4.2. The DCA of primary deuterons is small, while the DCA of background deuterons could be either large or small. $\overline{d}$ is not knocked out from the beam pipe, and it is expected that the DCA distributions of primary $d$ tracks should have equivalent shapes as the DCA distributions of $\overline{d}$. Fig. 4.14 shows the DCA distributions of $d$ and $\overline{d}$ in two different transverse momentum range. From the Fig. 4.14, it is obvious that DCA distributions of $d$ is not similar to that of $\overline{d}$ due to added contribution of knocked out deuterons from the beam pipe. Therefore, this secondary deuterons has been be removed from this analysis. To account for the beam-pipe generated deuterons, we fitted the DCA distribution of $d$ in each $p_T$ range by a function,

$$\text{DCA(d)} = \text{DCA}(\overline{\text{d}}) + \text{A}[1 - \exp(\frac{\text{DCA}}{\text{DCA}_0})]^c \tag{4.16}$$

Where, $\text{DCA}(\overline{d})$ is the scaled DCA distribution of $\overline{d}$ and $A$, $\text{DCA}_0$ and $c$ are fit parameters. Hence, we obtained the beam pipe conribution of deuteron as given by
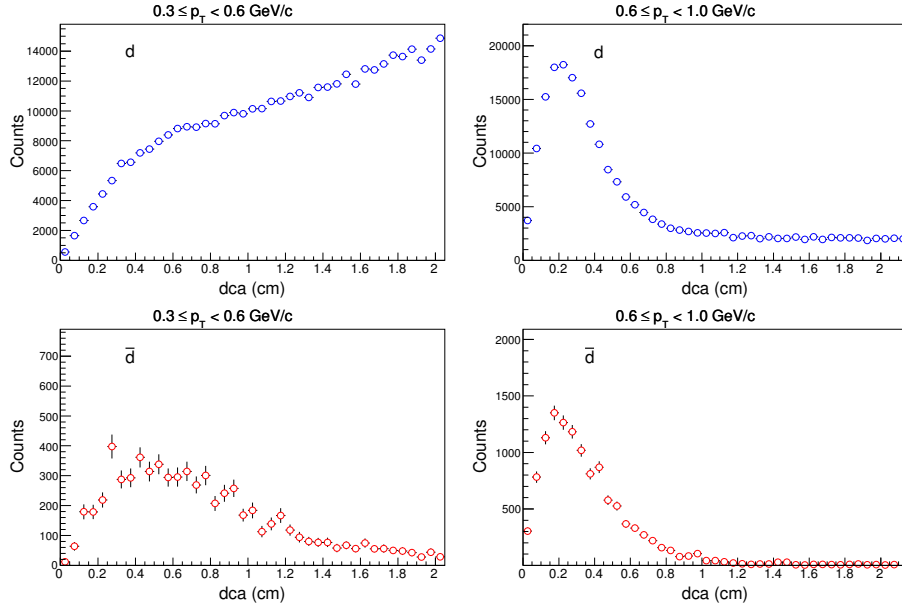
133

Figure 4.14: DCA ditribution of $d$ (upper panel) and $\bar{d}$ (lower panel) for $0 < (\phi - \Psi_2) < \frac{\pi}{10}$ and for 0-80% central events in Au+Au at $\sqrt{s_{NN}} = 39$ GeV.

the second part of the above equation. Once we get the fit parameters, then the correct yield of $d$ can be extracted as,

$$\text{Yield}(d) = \text{Integral of DCA(d)} - \text{Integral of A}[1 - \exp(\frac{\text{DCA}}{\text{DCA}_0})]^{\text{C}} \qquad (4.17)$$

Therefore, after subtracting the beam-pipe contribution from the DCA distribution of all the deuterons, it becomes identical to the DCA distribution of $\bar{d}$ as shown in Fig. 4.15. In this analysis, $d$ yield has been calculated for $p_T < 1.0 \ GeV/c$ following the method mentioned above. For $p_T > 1.0 \ GeV/c$, the usual $Z$-distribution method has been followed to calculate yield of $d$, $t$ and $^3He$. To get $\bar{d}$ yield $Z$-distribution method has been followed for all $p_T$ range. The DCA and $Z$-distribution for minimum bias Au+Au collisions for all beam energies is shown in the following. Subsequently, the $\phi - \Psi_2$ distributions are also shown.
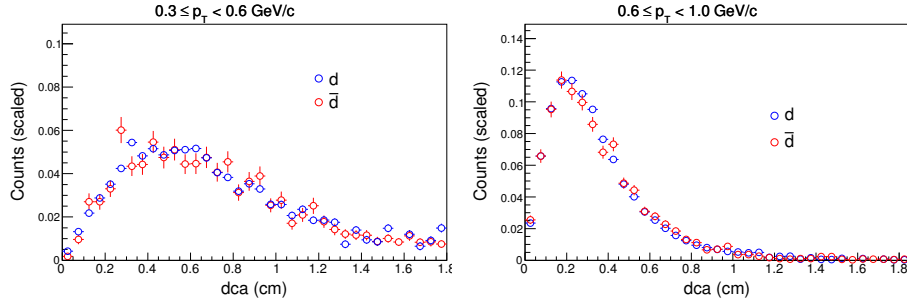
134

Figure 4.15: DCA ditribution of $d$ (after removing beam pipe contamination) and $\bar{d}$ for $0 < (\phi - \Psi_2) < \frac{\pi}{10}$ and 0-80% central events in Au+Au at $\sqrt{s_{\mathrm{NN}}} = 39$ GeV.

## 4.9.2 DCA and Z distributions of light nuclei

The DCA and $Z$ distributions for few $p_{\mathrm{T}}$ bins are shown. Each $p_{\mathrm{T}}$ has five figure corresponding to five $(\phi - \Psi_2)$ bins namely, 0-$\frac{\pi}{10}$, $\frac{\pi}{10} - \frac{2\pi}{10}$, $\frac{2\pi}{10} - \frac{3\pi}{10}$, $\frac{3\pi}{10} - \frac{4\pi}{10}$ and $\frac{4\pi}{10} - \frac{5\pi}{10}$. The method of yield extraction are same for other $p_{\mathrm{T}}$ bins.

**DCA-distribution of $d$ ($\sqrt{s_{\mathrm{NN}}} = 200$ GeV, 0-80%)**



135
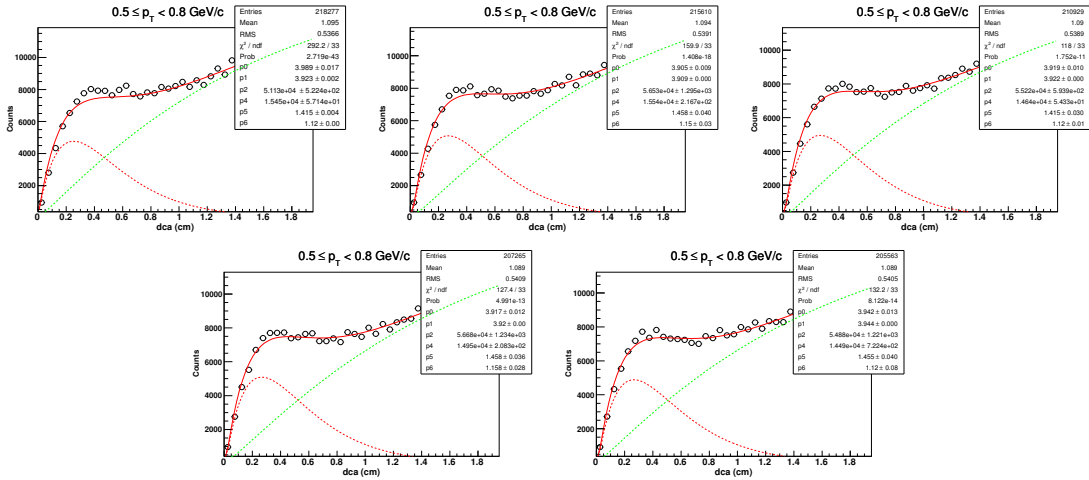
**Z-distribution of $d$ ($\sqrt{s_{\mathrm{NN}}} = 200$ GeV, 0-80%)**
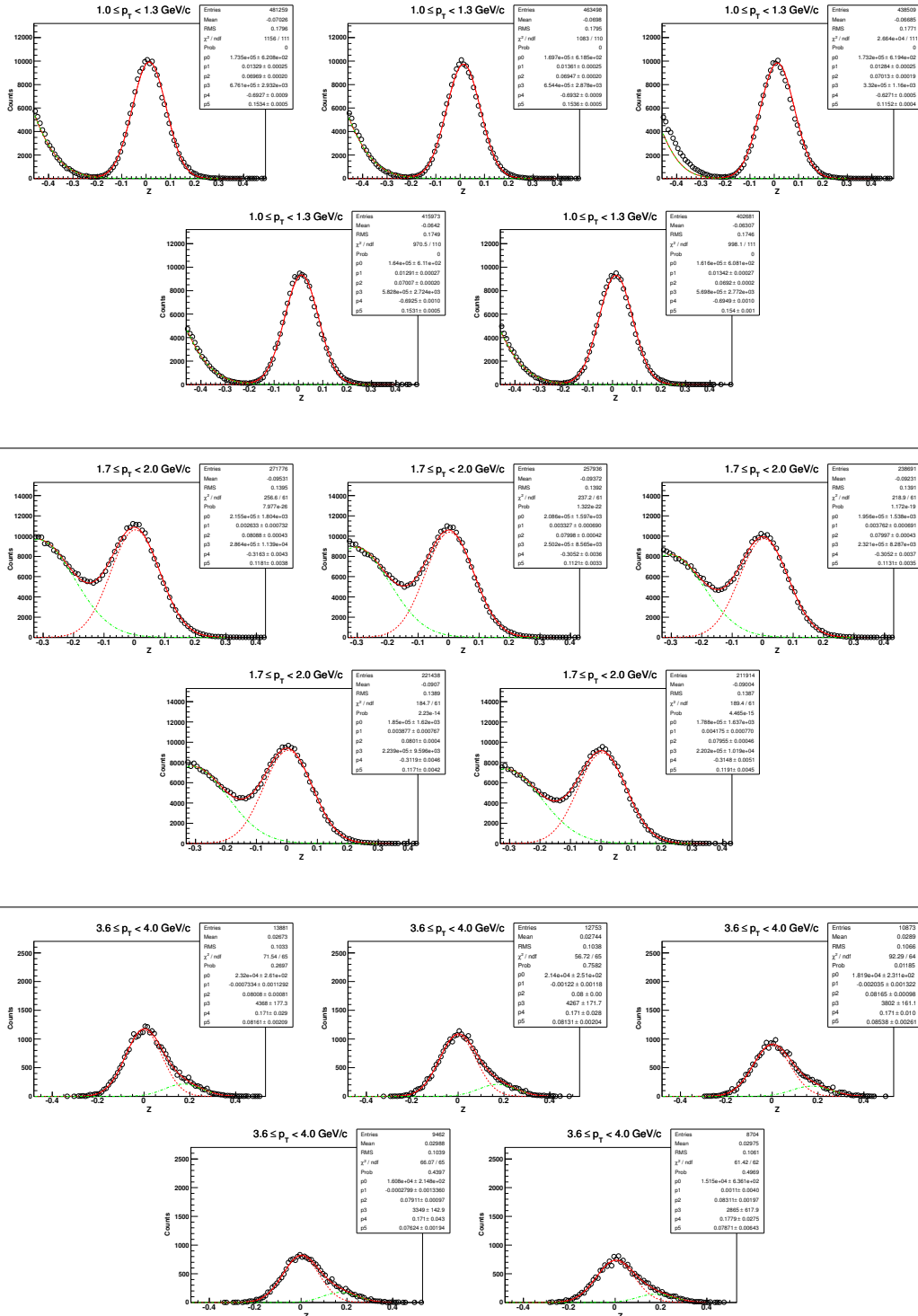
$Z$-distribution of $\overline{d}$ for Au+Au at $\sqrt{s_{\mathrm{NN}}} = 200$ GeV, centrality 0-80%
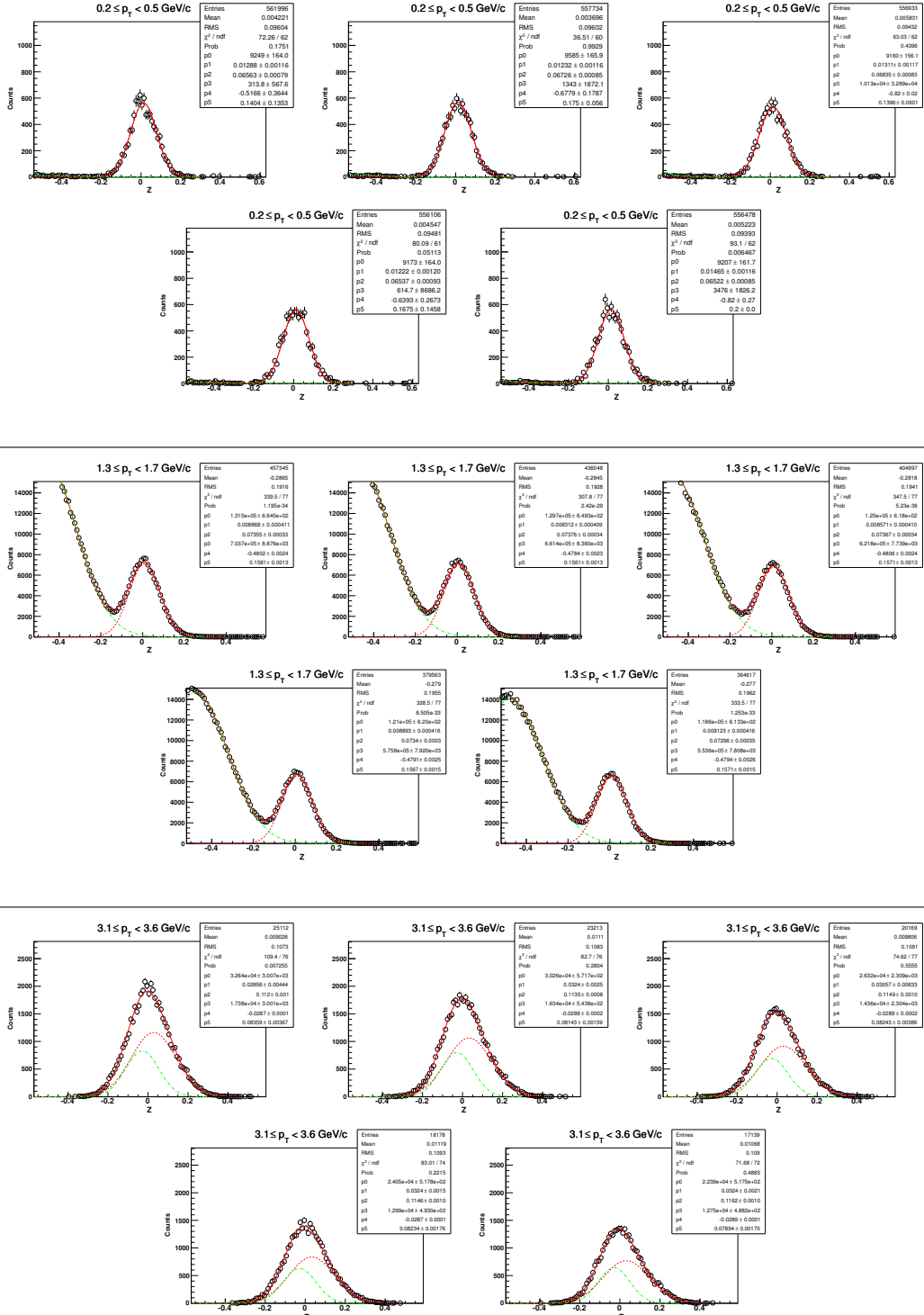
# $(\phi - \Psi_2)$ distribution of $d$ in Au+Au at $\sqrt{s_{\mathrm{NN}}} = 200$ GeV (0-80%)
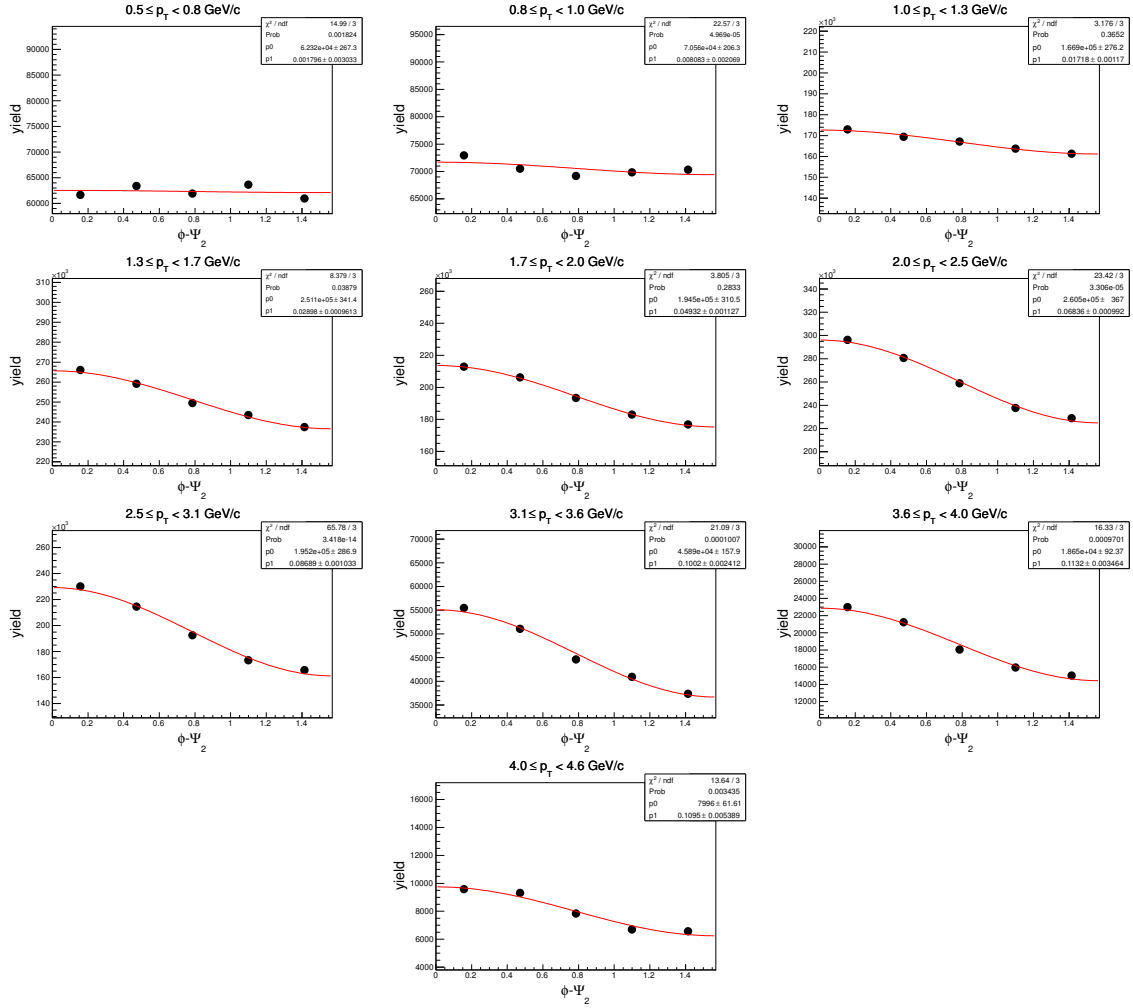
# $(\phi - \Psi_2)$ distribution of $\overline{d}$ in Au+Au at $\sqrt{s_{\mathrm{NN}}} = 200$ GeV (0-80%)
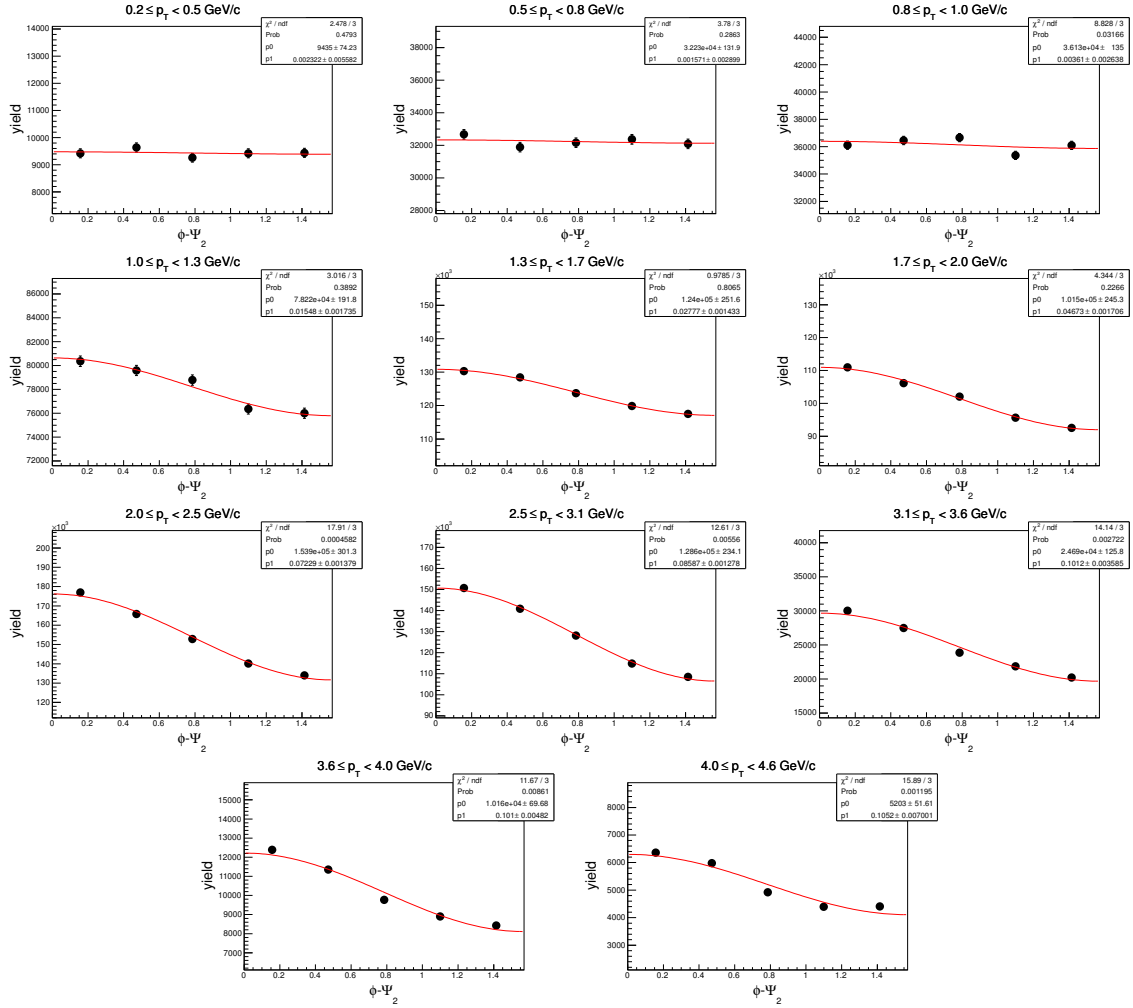
$Z$ distribution of $^3He$ in Au+Au at $\sqrt{s_{\mathrm{NN}}} = 200$ GeV (0-80%)
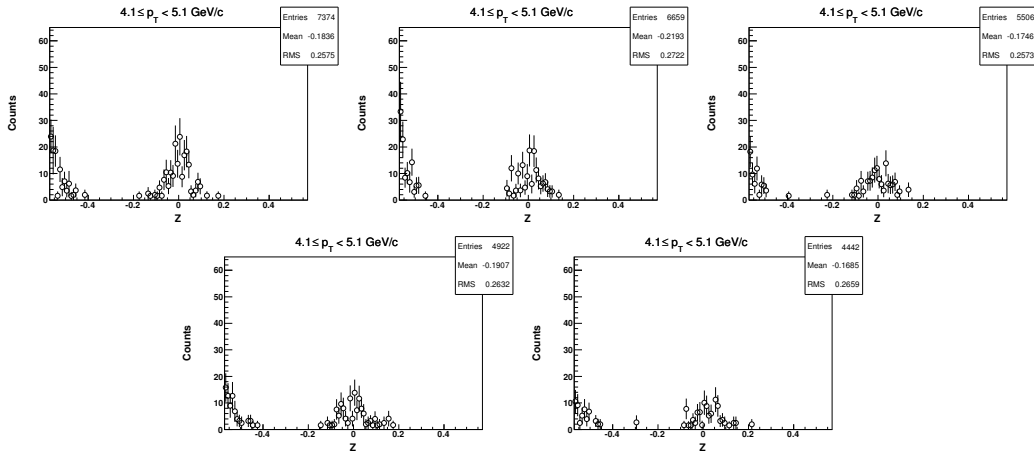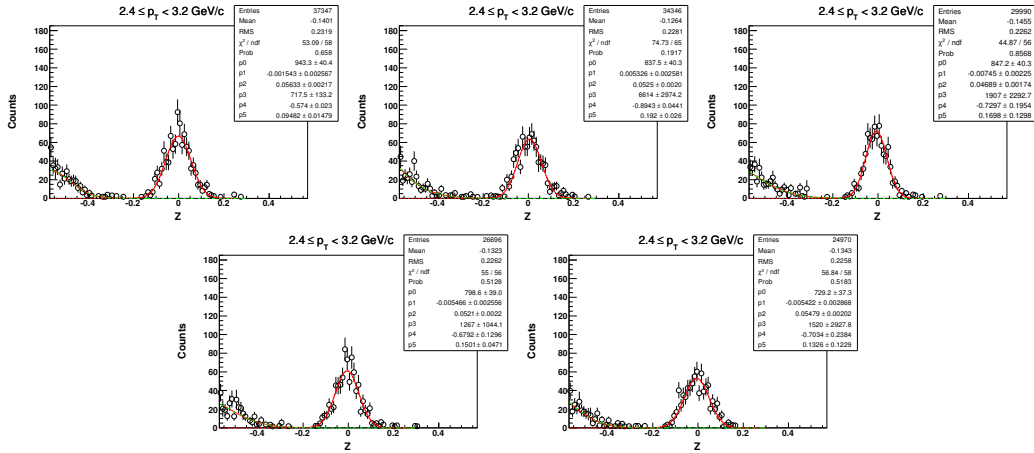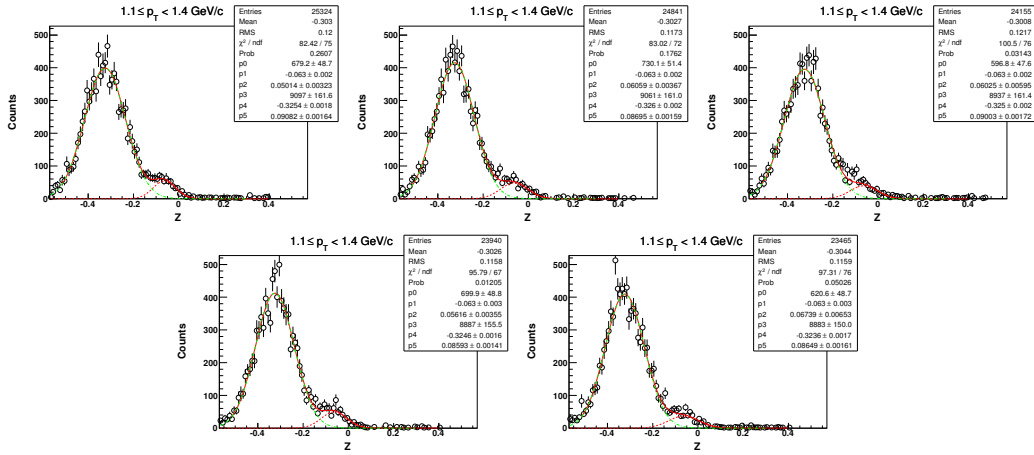
# $Z$ distribution of $t$ in Au+Au at $\sqrt{s_{\mathrm{NN}}} = 200$ GeV (0-80%)
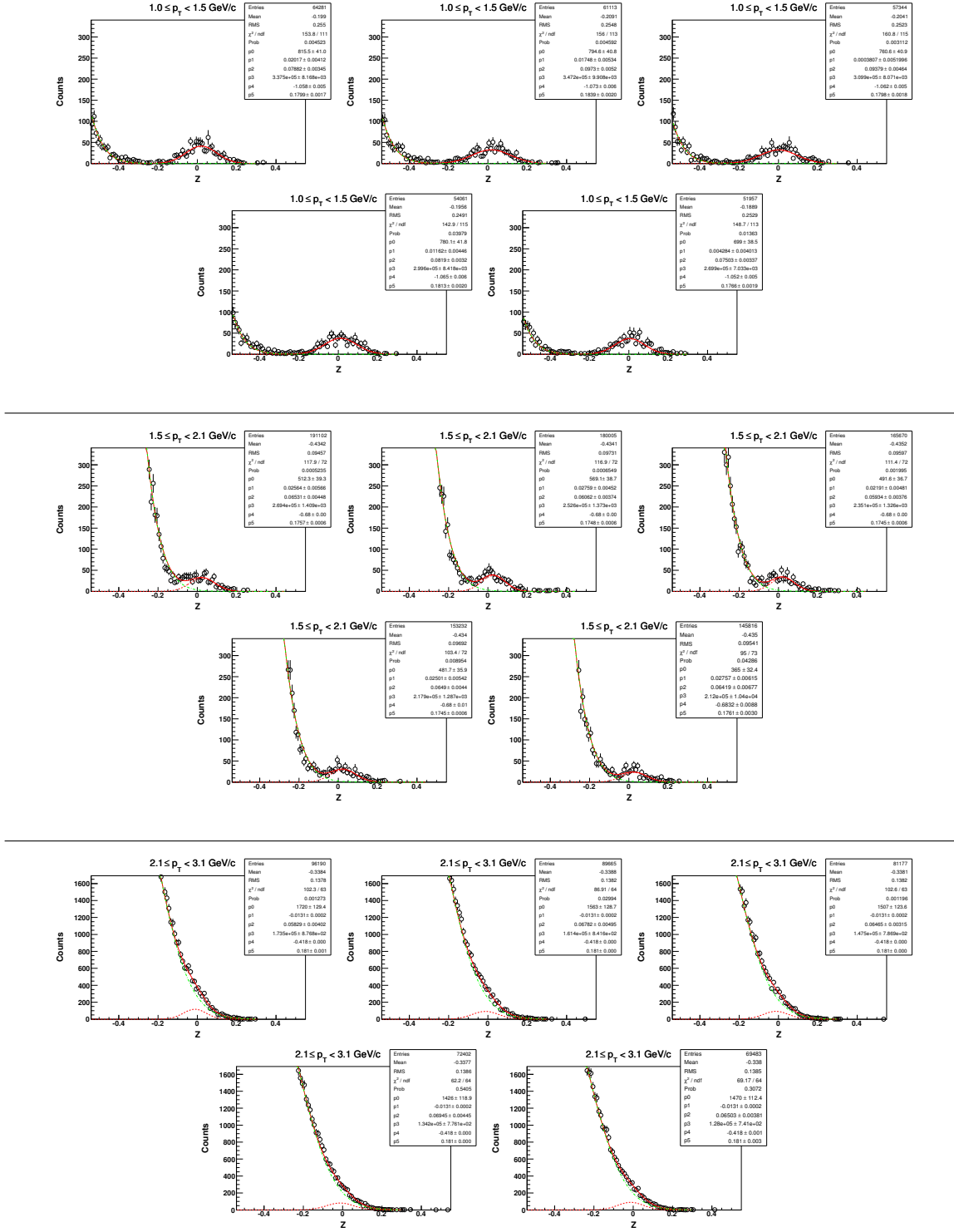
$(\phi - \Psi_2)$ distributions of $^3$He in Au+Au at $\sqrt{s_{\mathrm{NN}}} = 200$ GeV (0-80%)
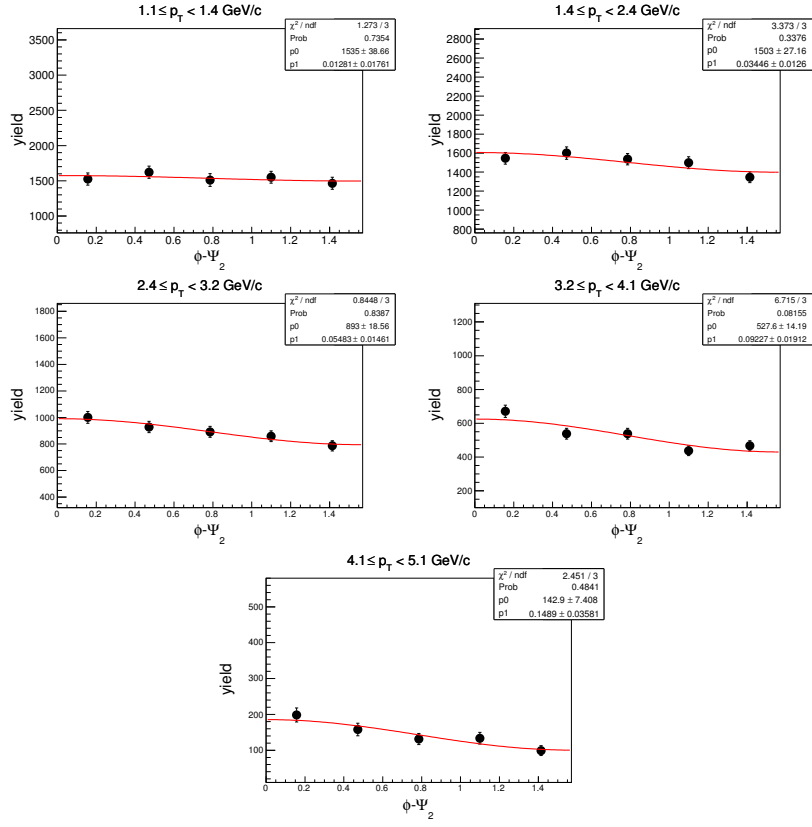


$(\phi - \Psi_2)$ distributions of $t$ in Au+Au at $\sqrt{s_{\mathrm{NN}}} = 200$ GeV (0-80%)

# DCA and $Z$ distribution of $d$ ($\sqrt{s_{\mathrm{NN}}} = 62.4$ GeV, (0-80%))

# Z-distribution of $\overline{d}$ ($\sqrt{s_{NN}}$ = 62.4 GeV, (0-80%))
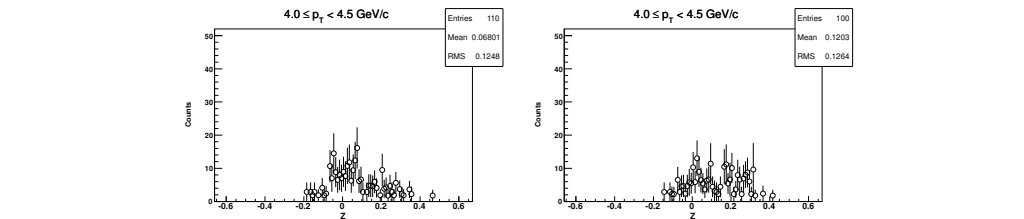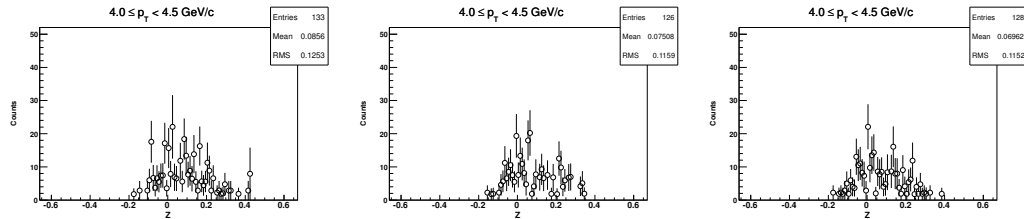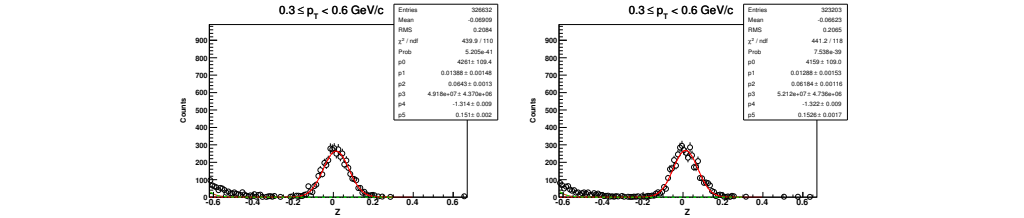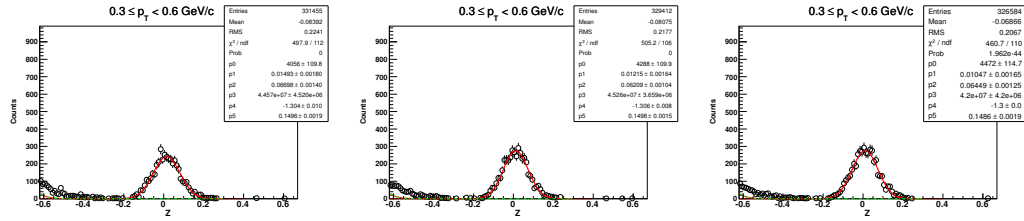


144

$(\phi - \Psi_2)$ distributions of $d$ in Au+Au at $\sqrt{s_{\mathrm{NN}}} = 62.4$ GeV (0-80%)
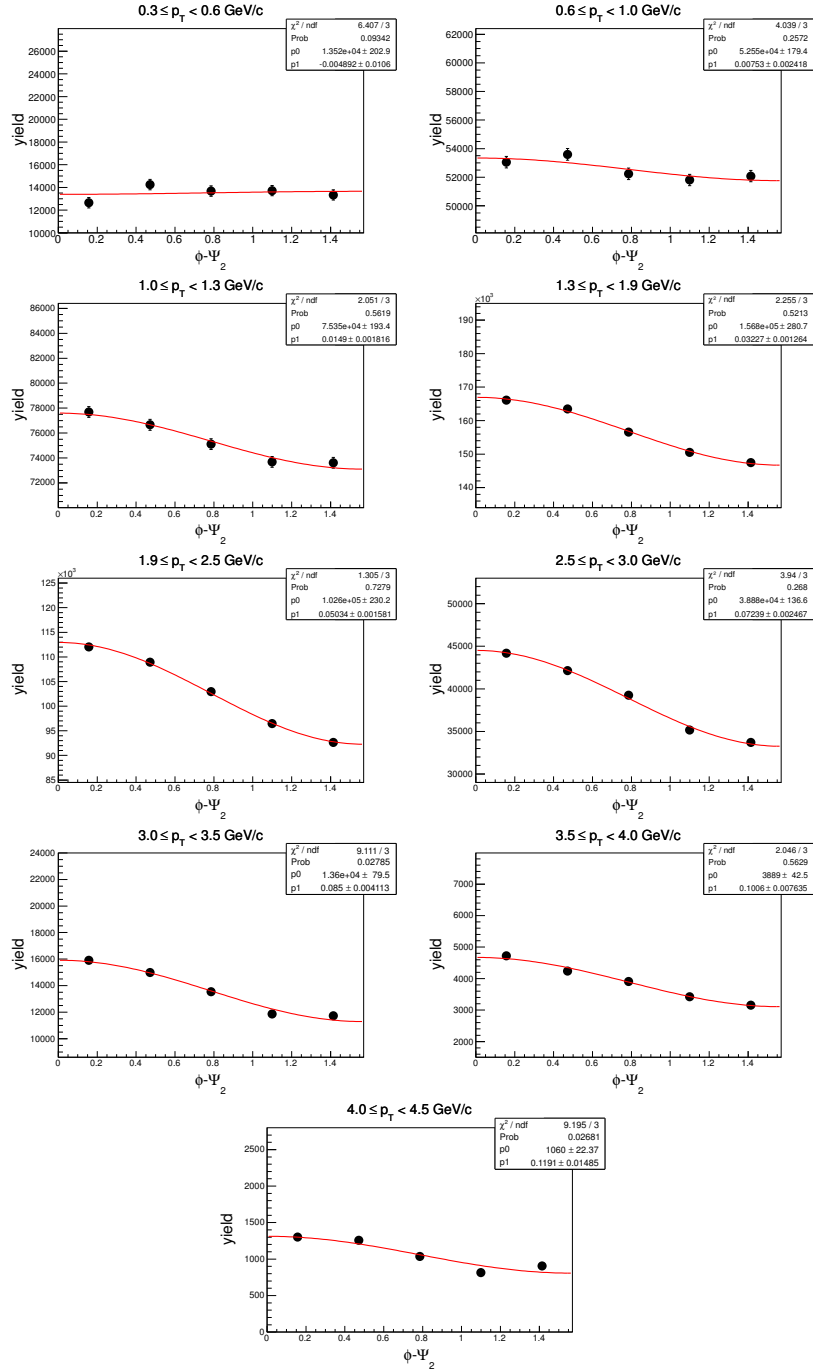
# $(\phi - \Psi_2)$ distributions of $\overline{d}$ in Au+Au at $\sqrt{s_{\mathrm{NN}}} = 62.4$ GeV (0-80%)
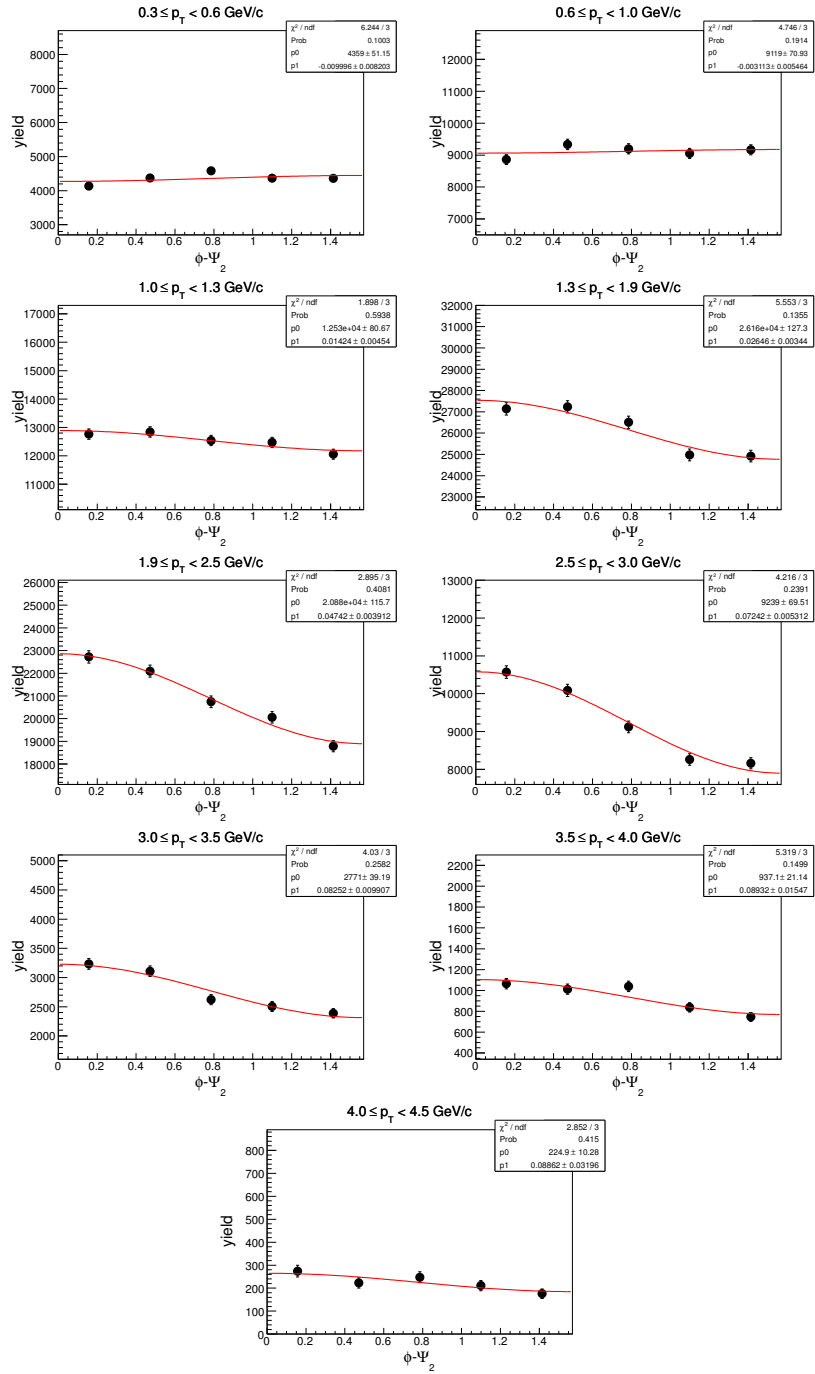
Z distribution of $^3He$ in Au+Au at $\sqrt{s_{\mathrm{NN}}} = 62.4$ GeV, (0-80%))
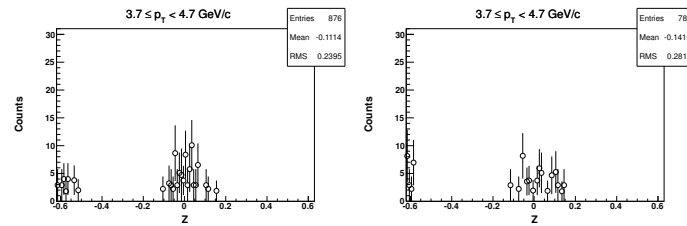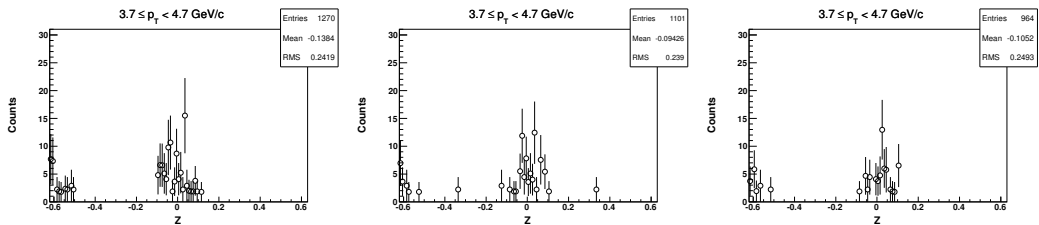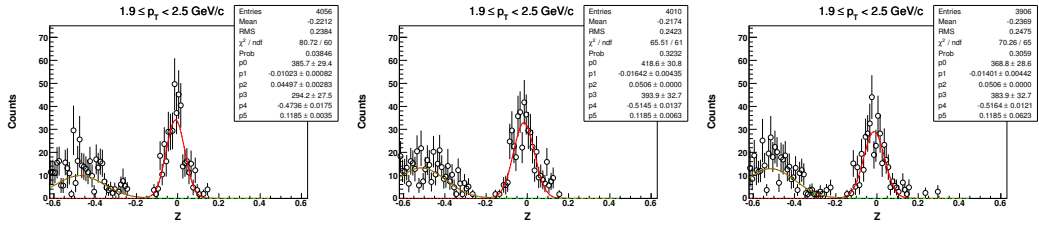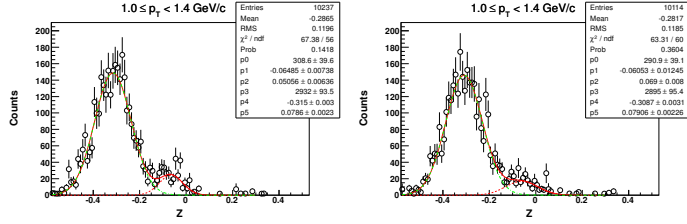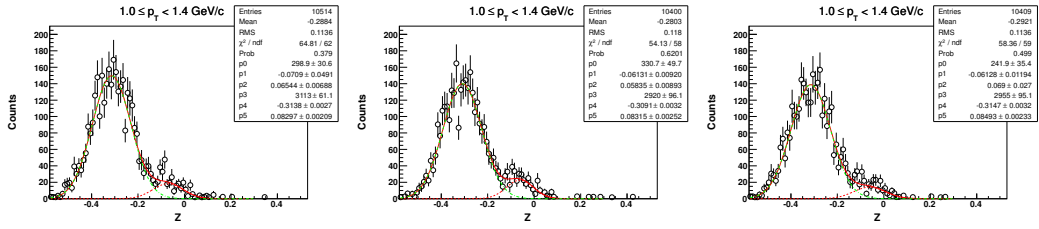
**Z-distribution of $t$ in Au+Au at $\sqrt{s_{\mathrm{NN}}} = 62.4$ GeV, (0-80%))**
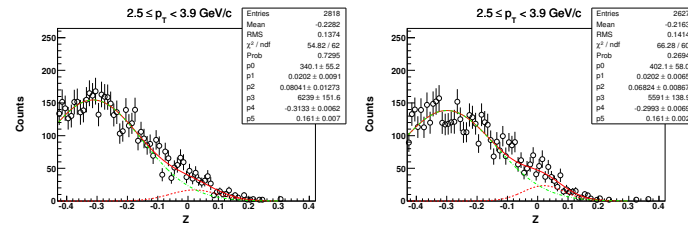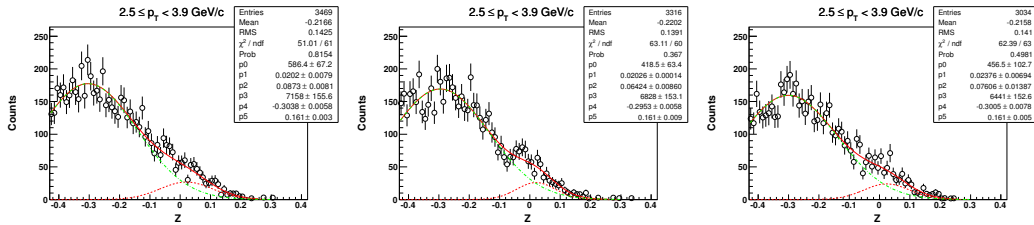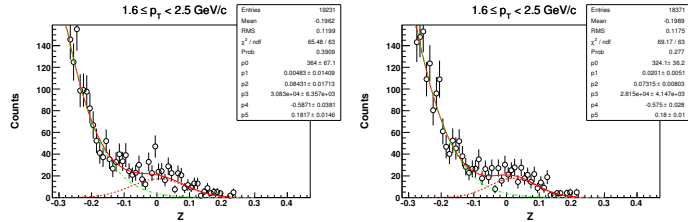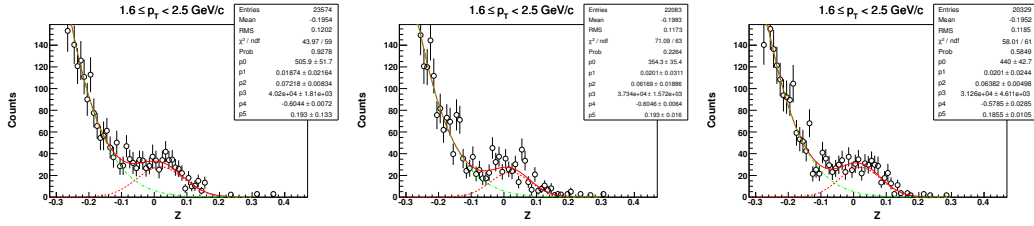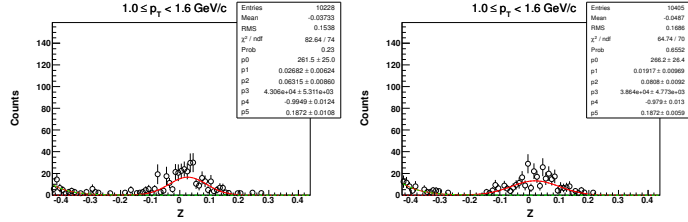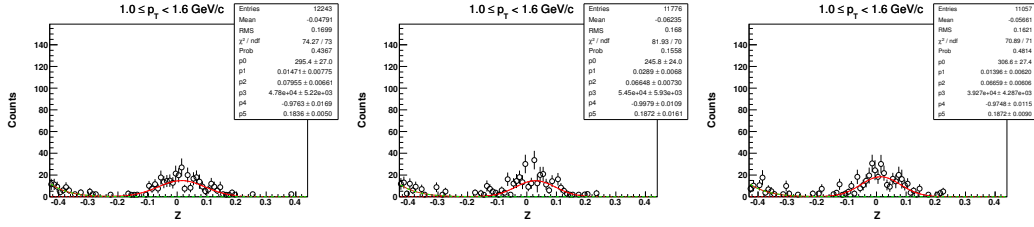
$(\phi - \Psi_2)$ distributions of $^3$He in Au+Au at $\sqrt{s_{\mathrm{NN}}} = 62.4$ GeV (0-80%)
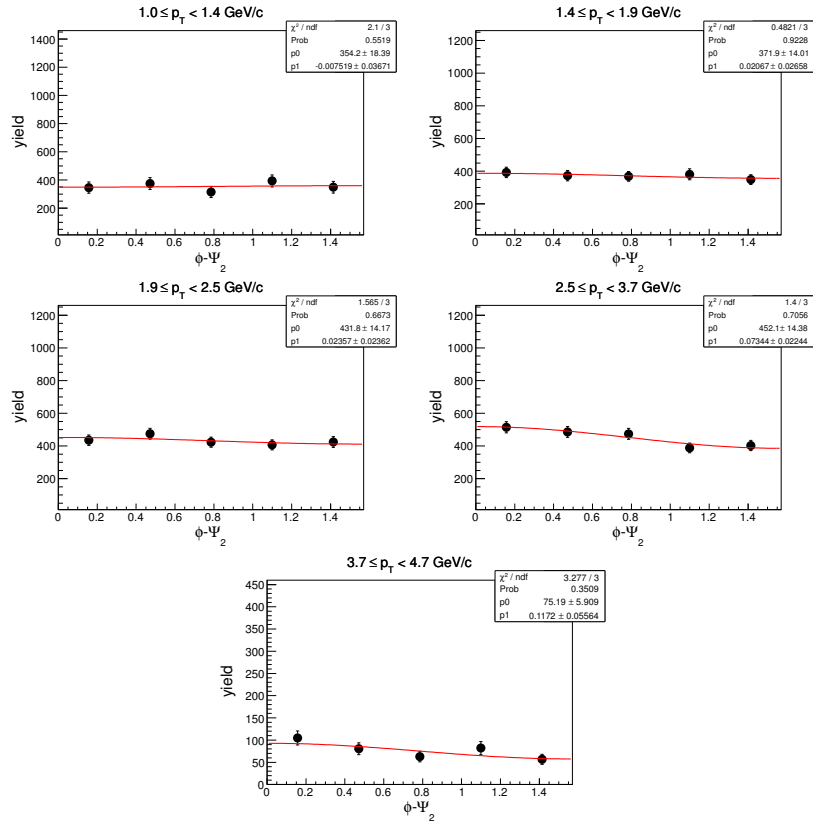


$(\phi - \Psi_2)$ distributions of $t$ in Au+Au at $\sqrt{s_{\mathrm{NN}}} = 62.4$ GeV (0-80%)

# DCA and $Z$ distribution of $d$ in Au+Au at $\sqrt{s_{\mathrm{NN}}} = 39$ GeV (0-80%)
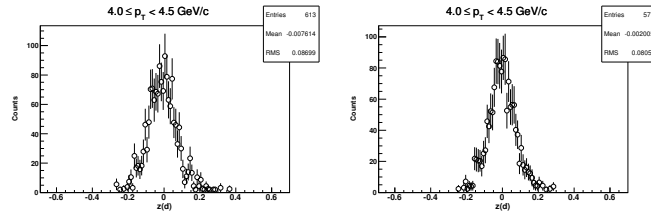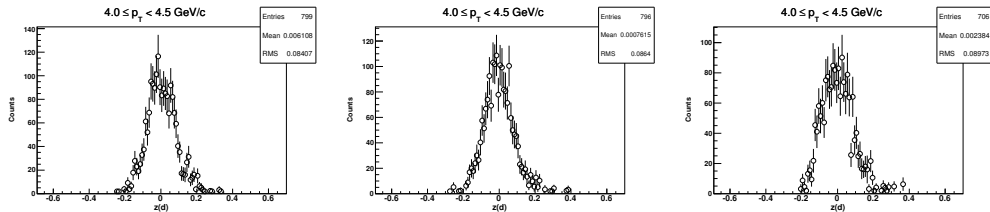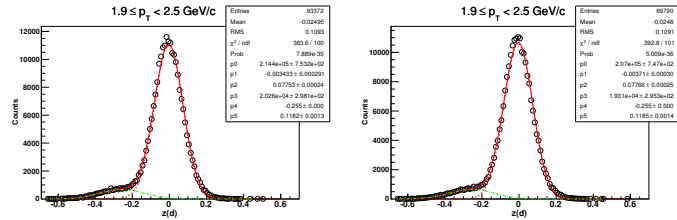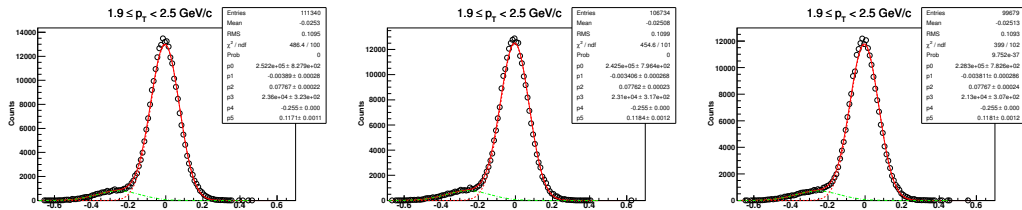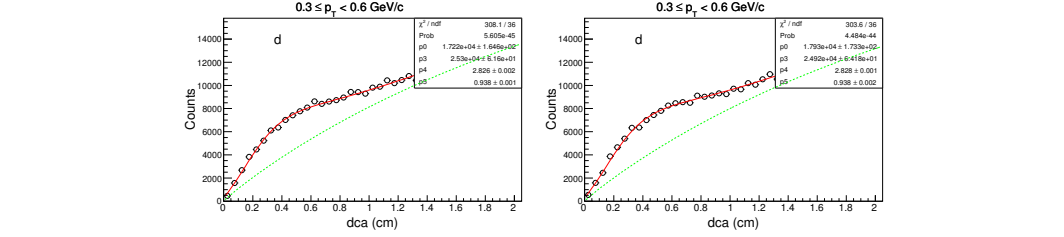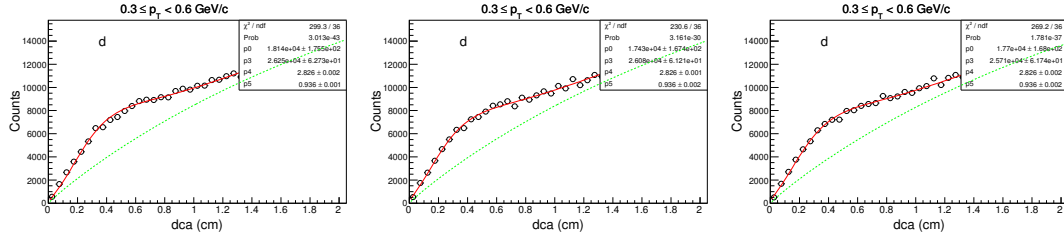
# $Z$ distribution of $\overline{d}$ in Au+Au at $\sqrt{s_{\mathrm{NN}}} = 39$ GeV (0-80%))
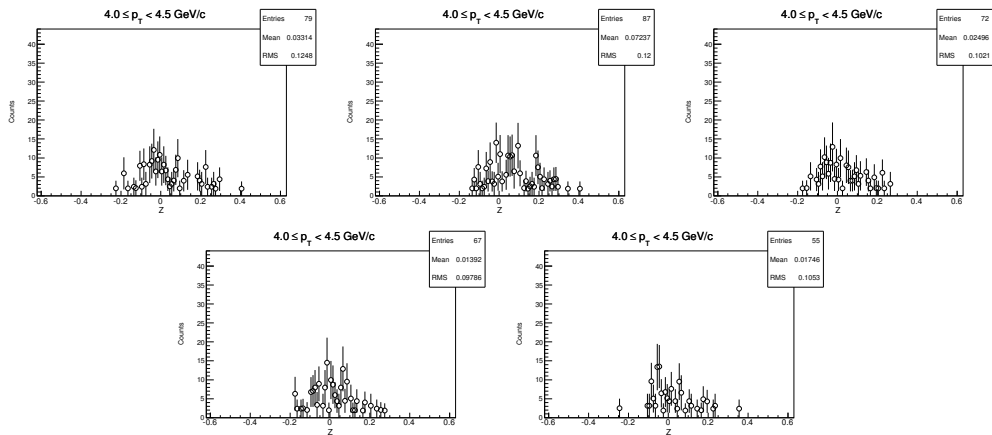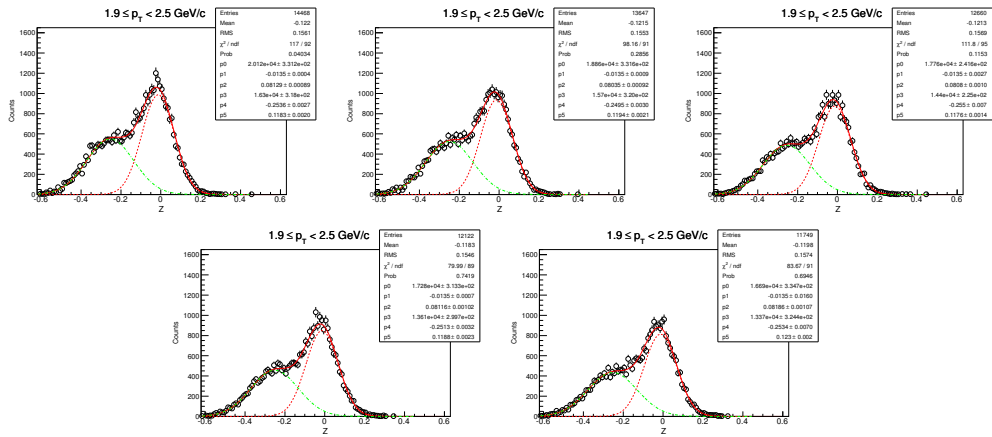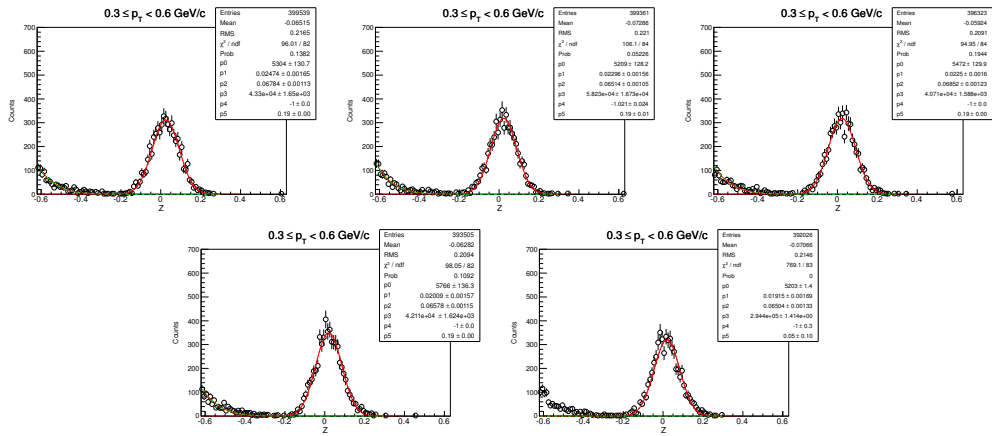
$(\phi - \Psi_2)$ distributions of $d$ in Au+Au at $\sqrt{s_{\mathrm{NN}}} = 39$ GeV (0-80%)
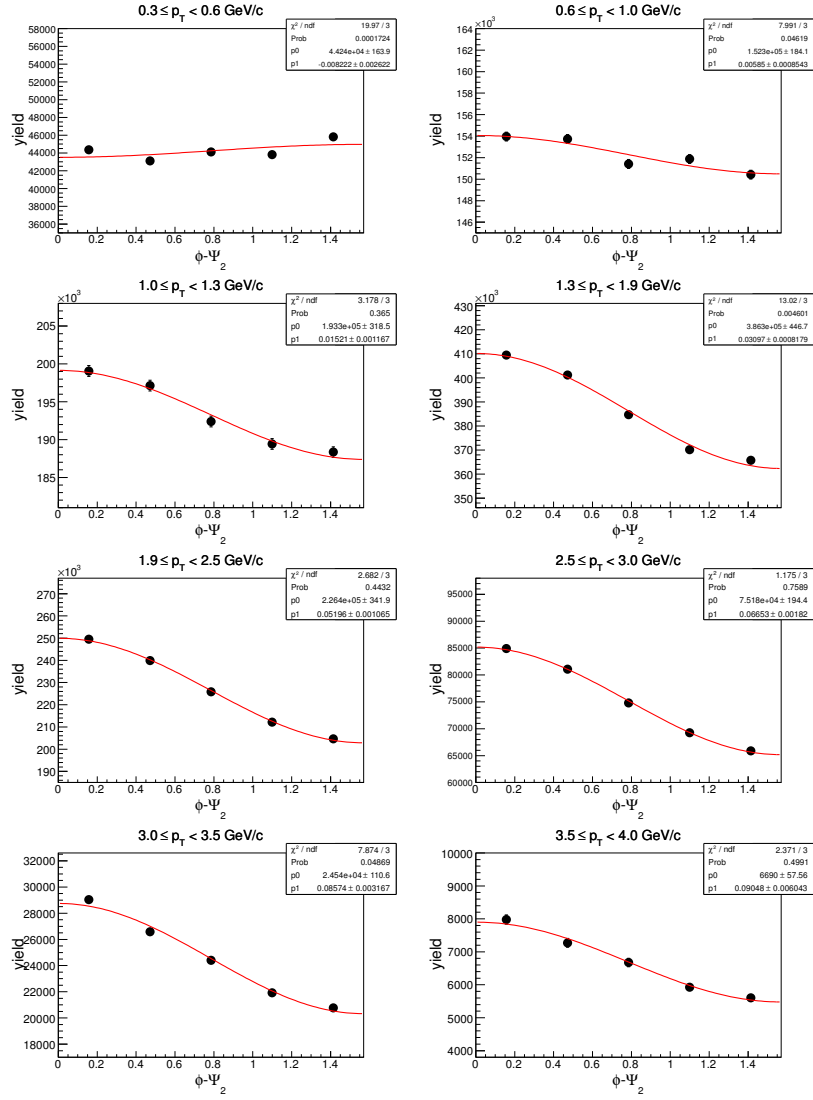
$(\phi - \Psi_2)$ distributions of $\overline{d}$ in Au+Au at $\sqrt{s_{\mathrm{NN}}} = 39$ GeV (0-80%)
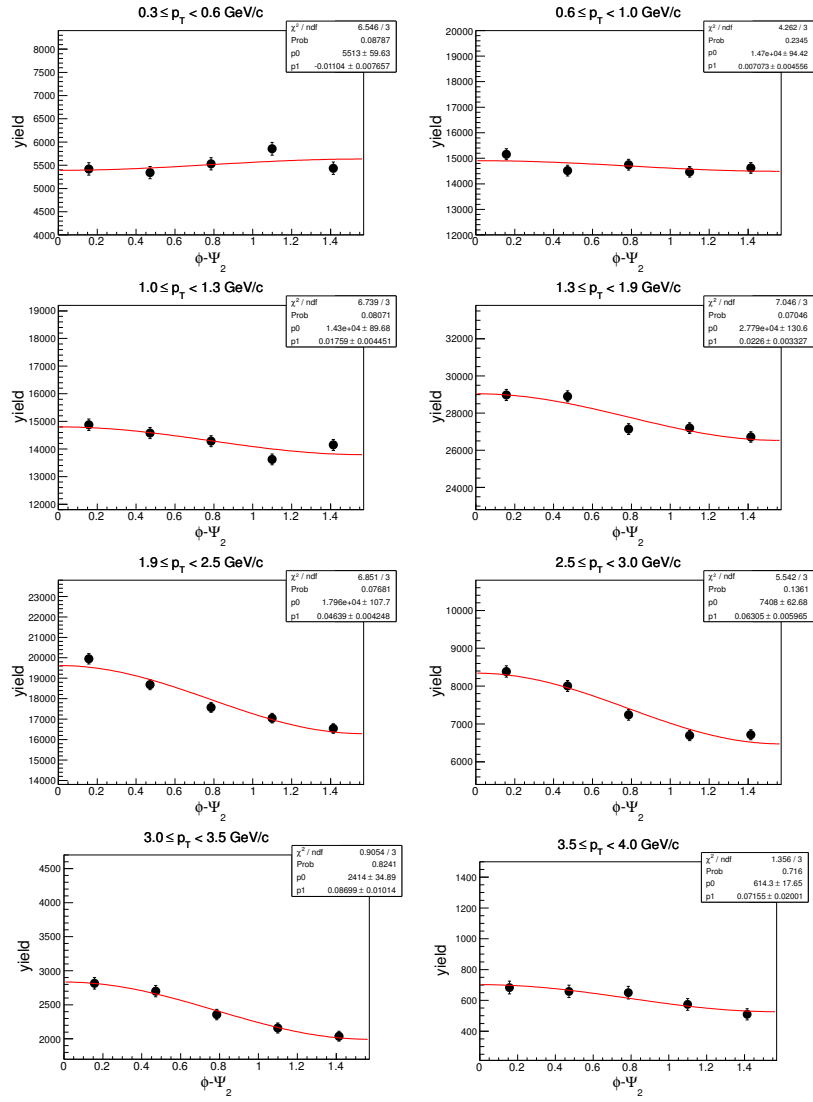
# $Z$ distribution of $^3$He in Au+Au at $\sqrt{s_{\mathrm{NN}}} = 39$ GeV (0-80%))
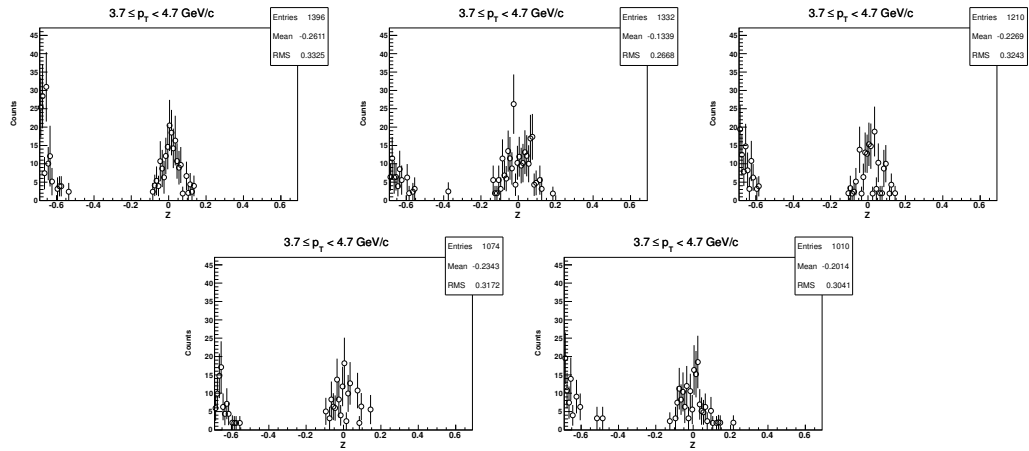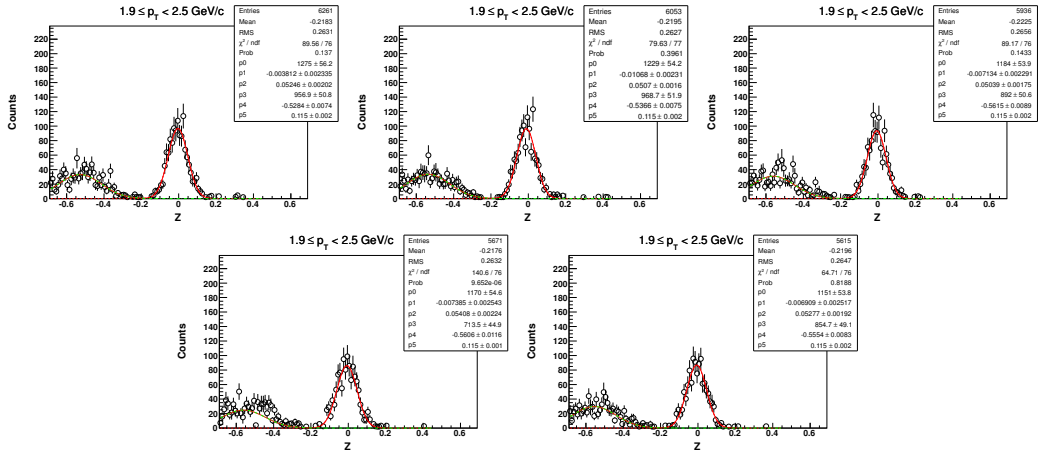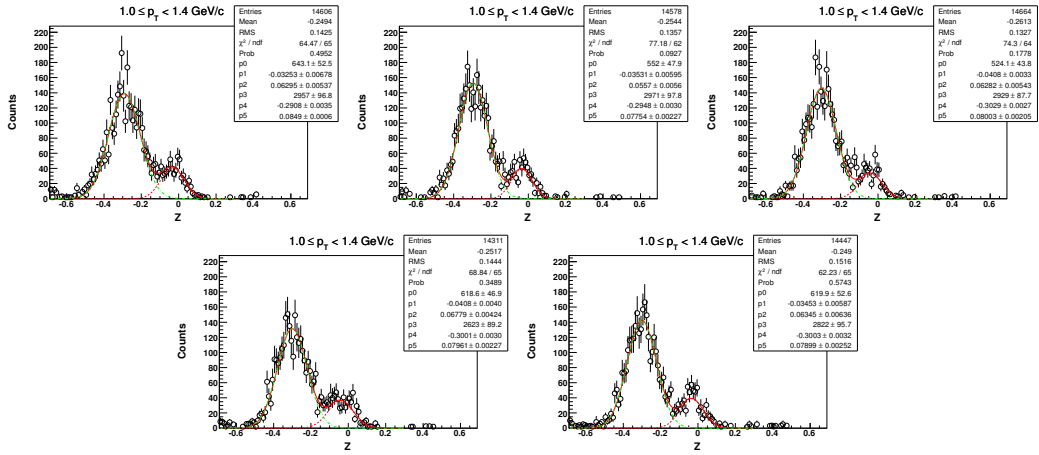
# $Z$ distribution of $t$ in Au+Au at $\sqrt{s_{\mathrm{NN}}} = 39$ GeV, (0-80%))
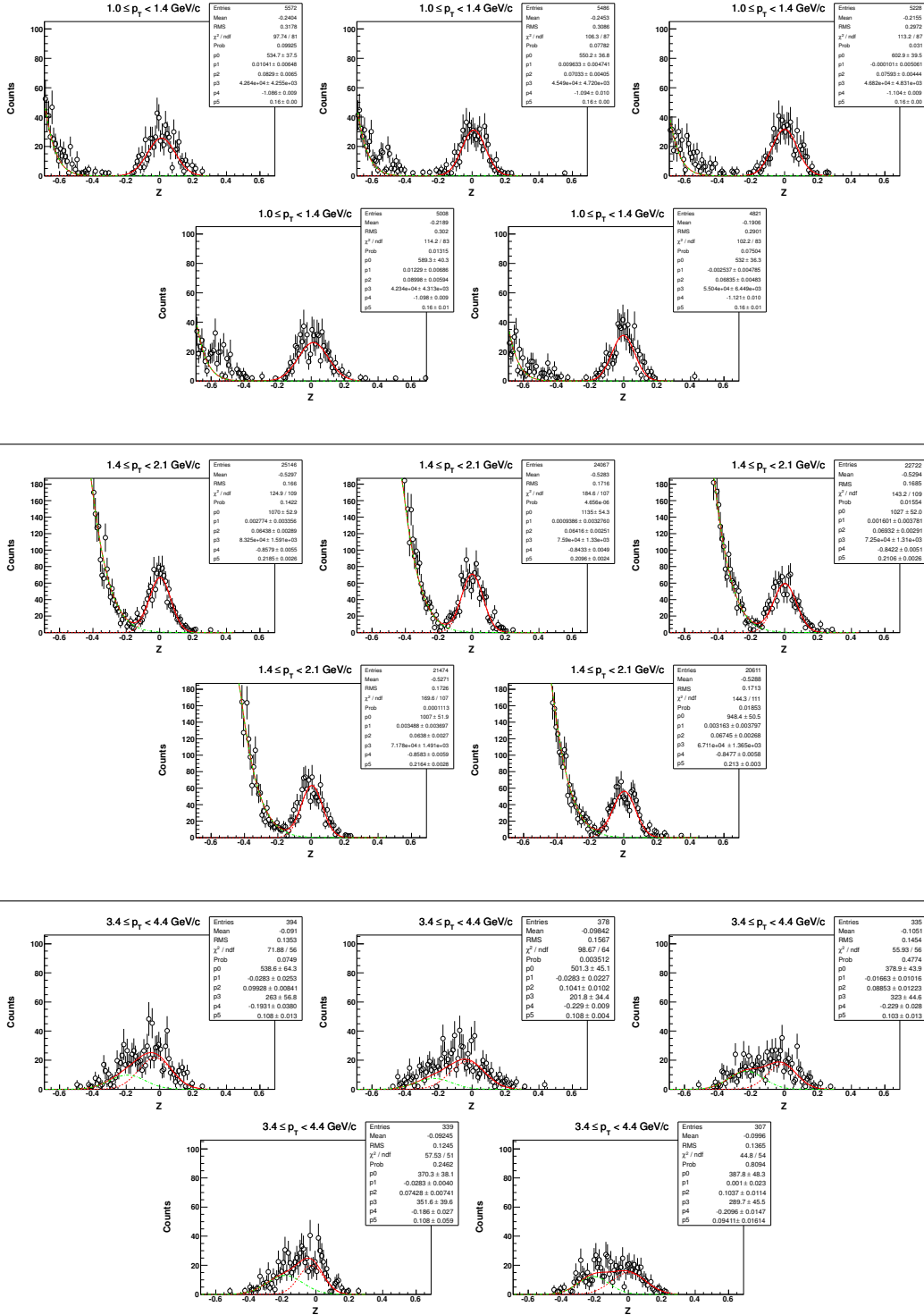
$(\phi - \Psi_2)$ distributions of $^3$He in Au+Au at $\sqrt{s_{\text{NN}}} = 39$ GeV (0-80%)
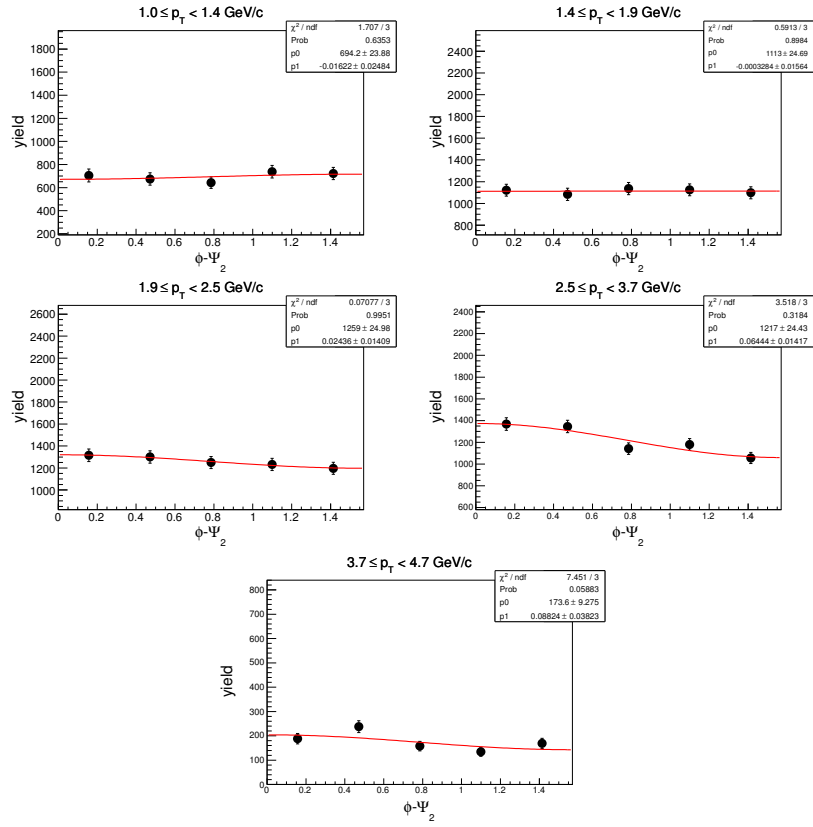


$(\phi - \Psi_2)$ distributions of $t$ in Au+Au at $\sqrt{s_{\text{NN}}} = 39$ GeV (0-80%)

# DCA and $Z$ distribution of $d$ ($\sqrt{s_{\mathrm{NN}}} = 27$ GeV, (0-80%))
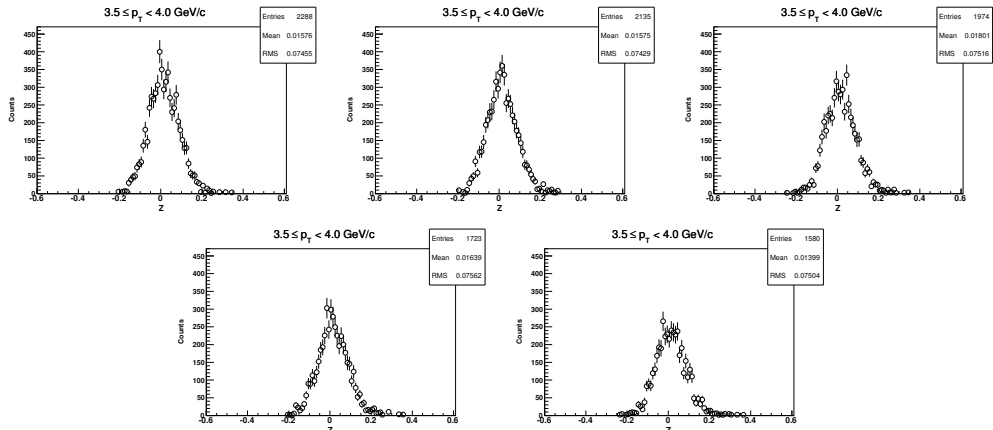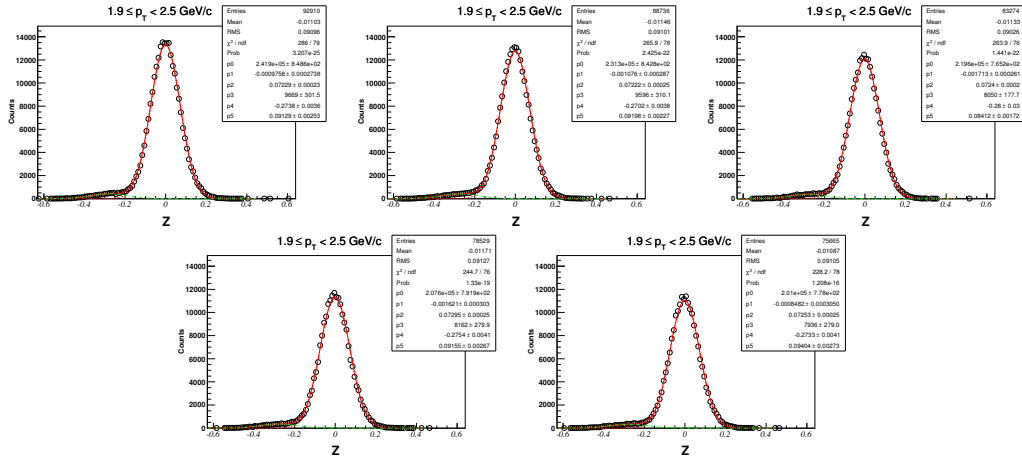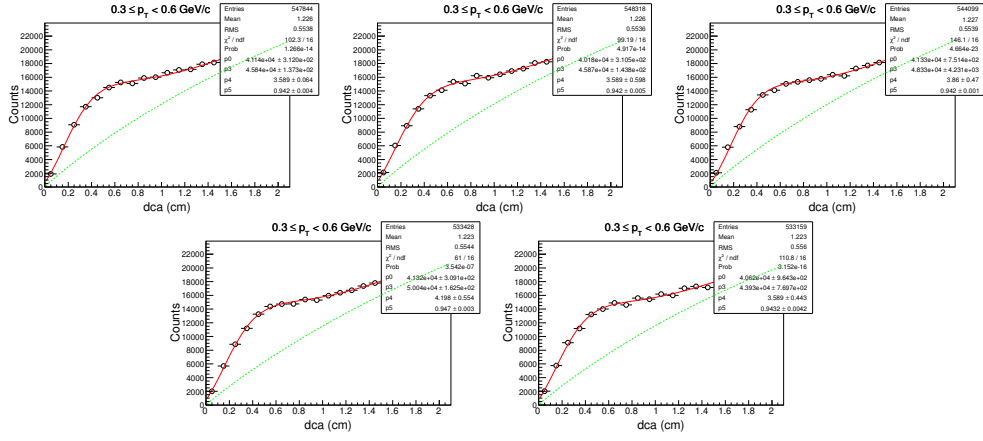
# $Z$ distribution of $\overline{d}$ in Au+Au at $\sqrt{s_{\mathrm{NN}}} = 27$ GeV, (0-80%))
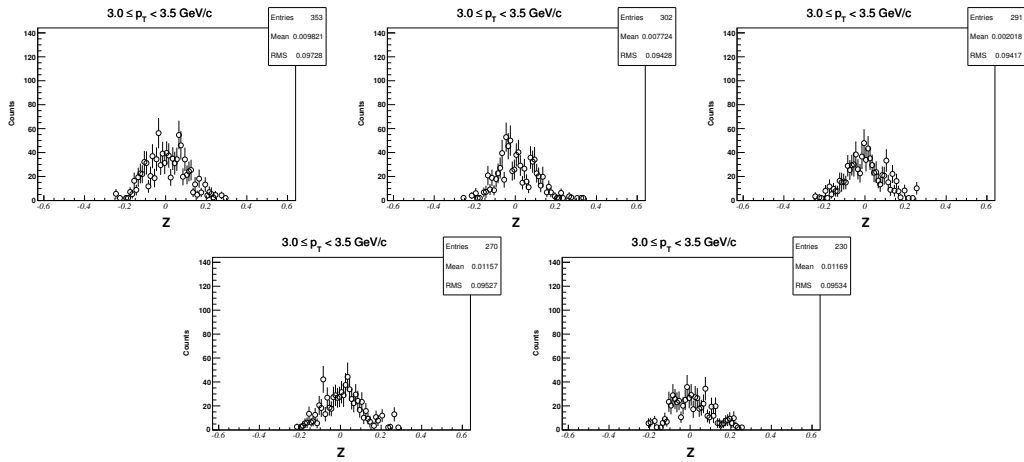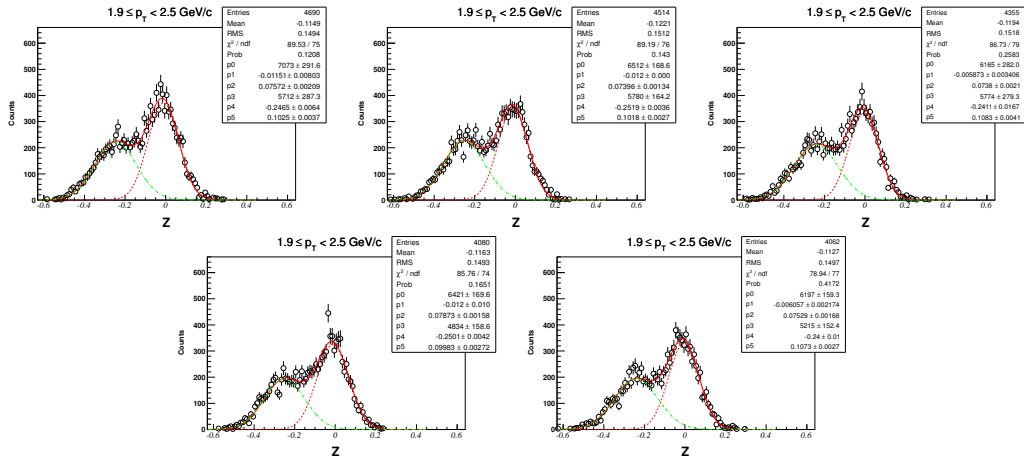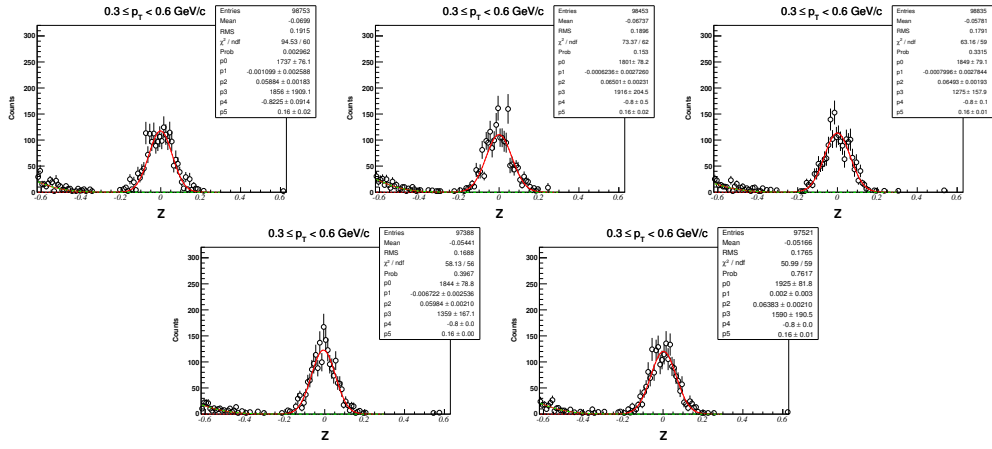
$(\phi - \Psi_2)$ distributions of $d$ in Au+Au at $\sqrt{s_{\mathrm{NN}}} = 27$ GeV (0-80%)
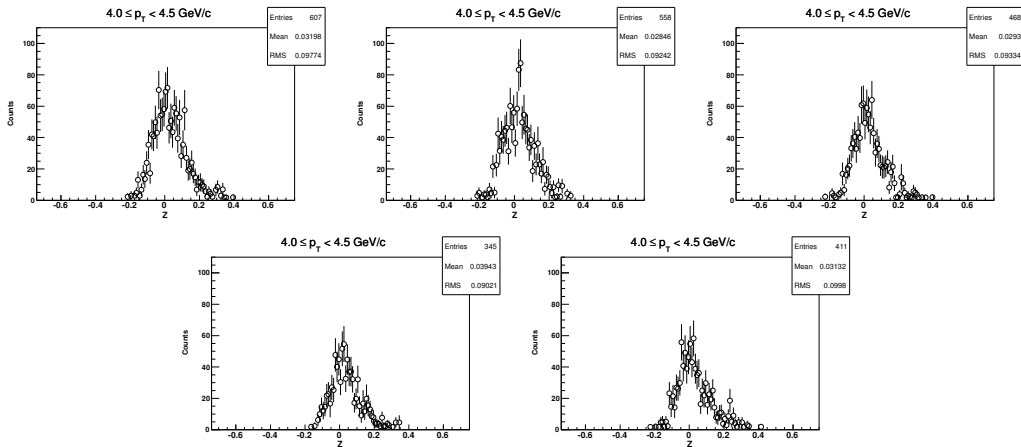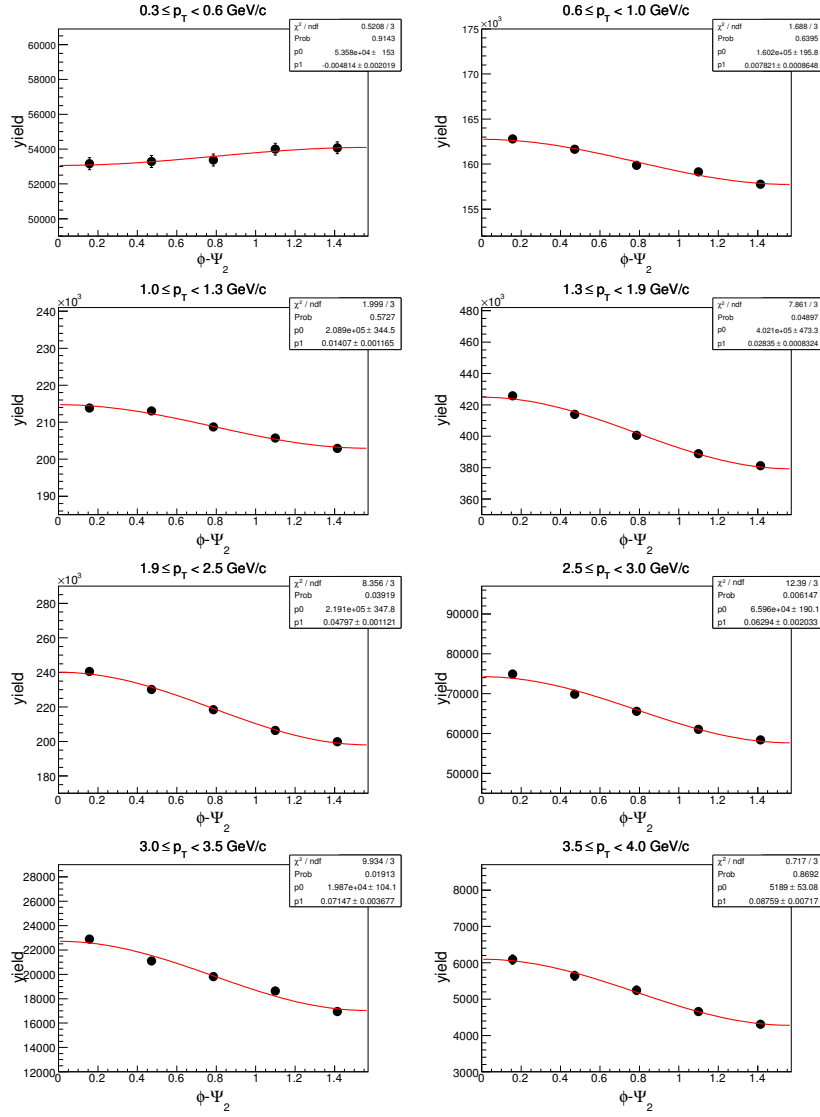
$(\phi - \Psi_2)$ distributions of $\overline{d}$ in Au+Au at $\sqrt{s_{\mathrm{NN}}} = 27$ GeV (0-80%)
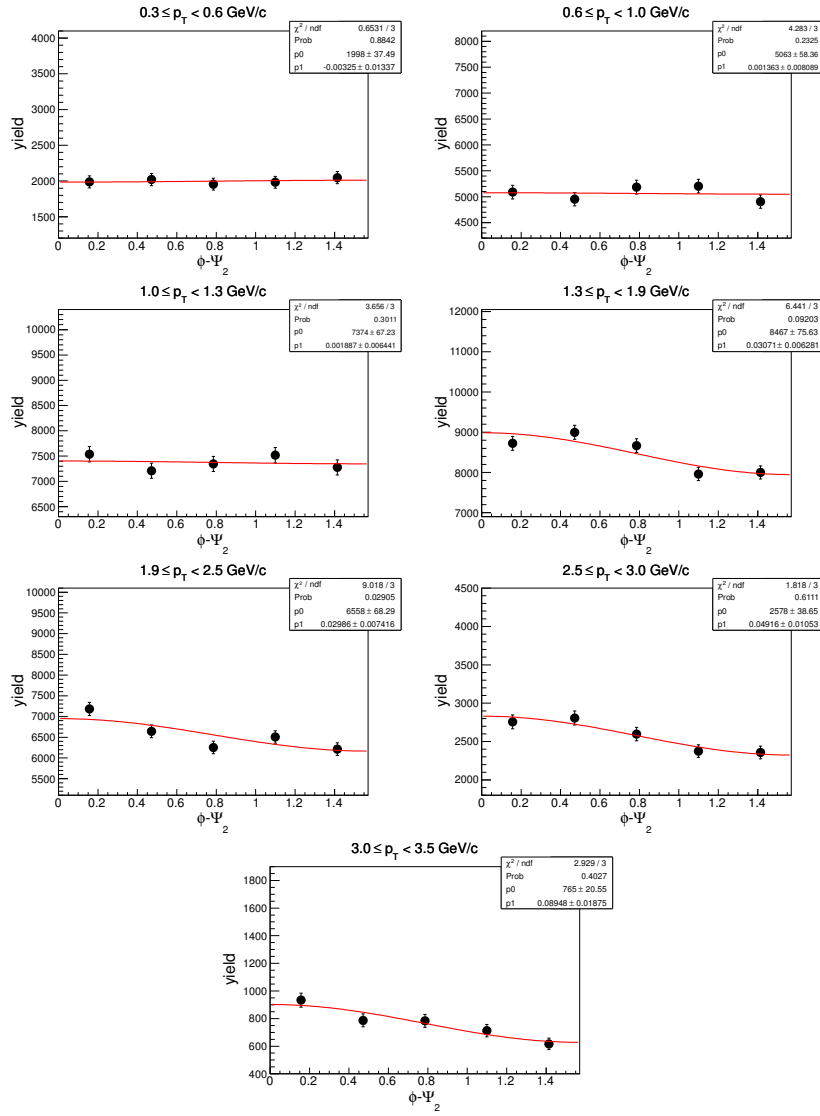
# $Z$ distribution of ${}^3$He ($\sqrt{s_{\rm NN}} = 27$ GeV, (0-80%))
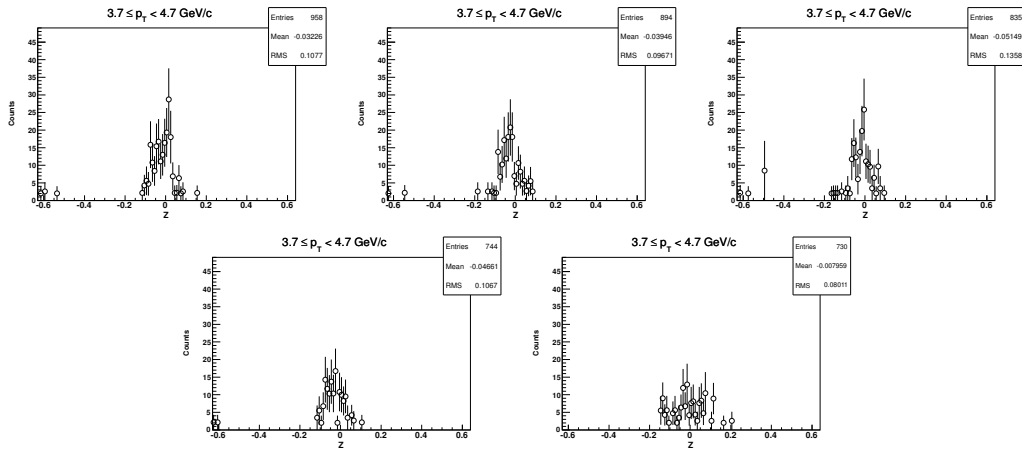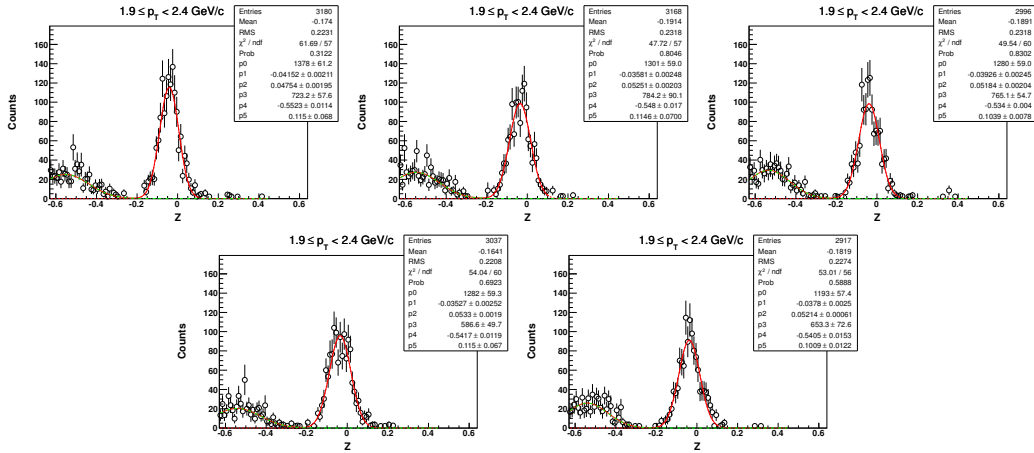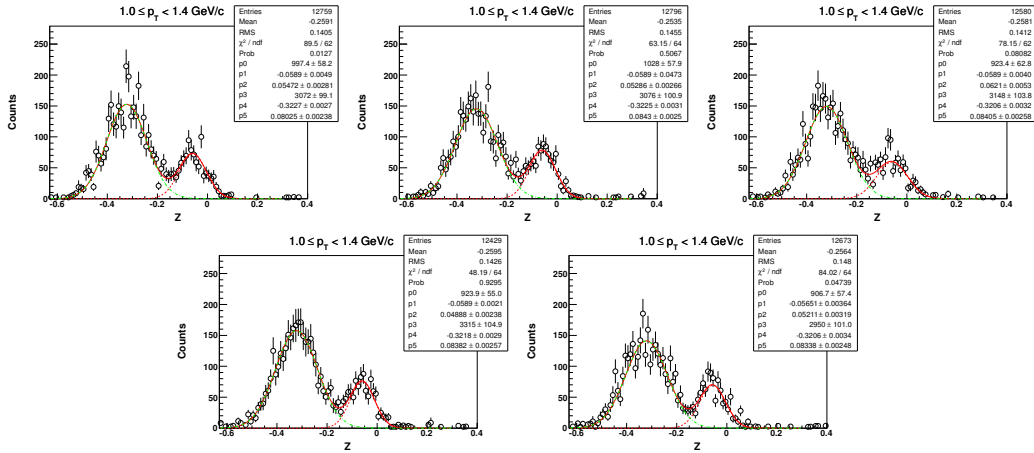
# $Z$ distribution of $t$ ($\sqrt{s_{\mathrm{NN}}} = 27$ GeV, (0-80%))
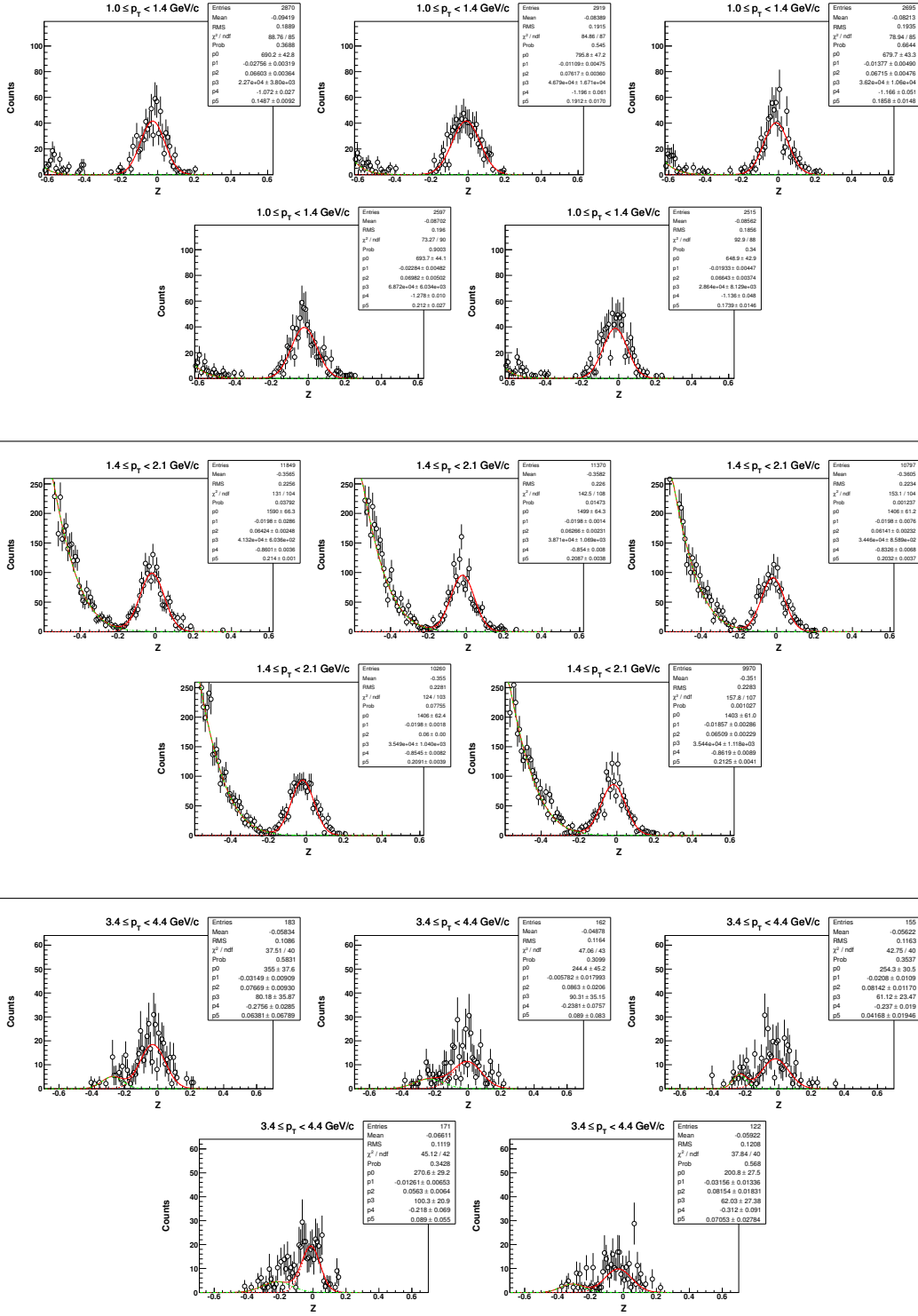
$(\phi - \Psi_2)$ distributions of $^3$He in Au+Au at $\sqrt{s_{\mathrm{NN}}} = 27$ GeV (0-80%)
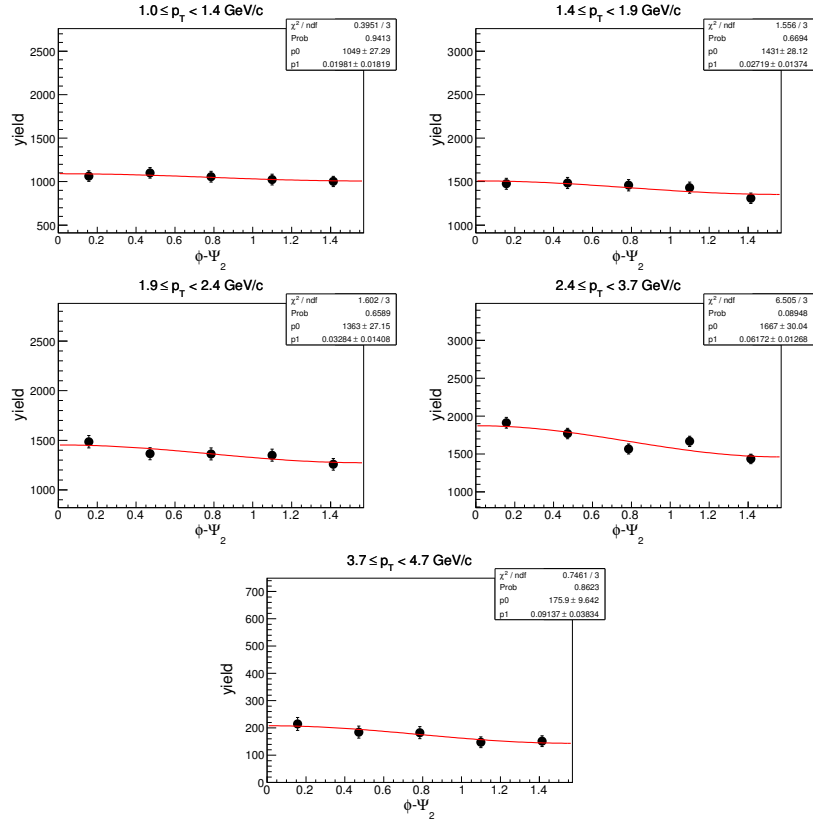


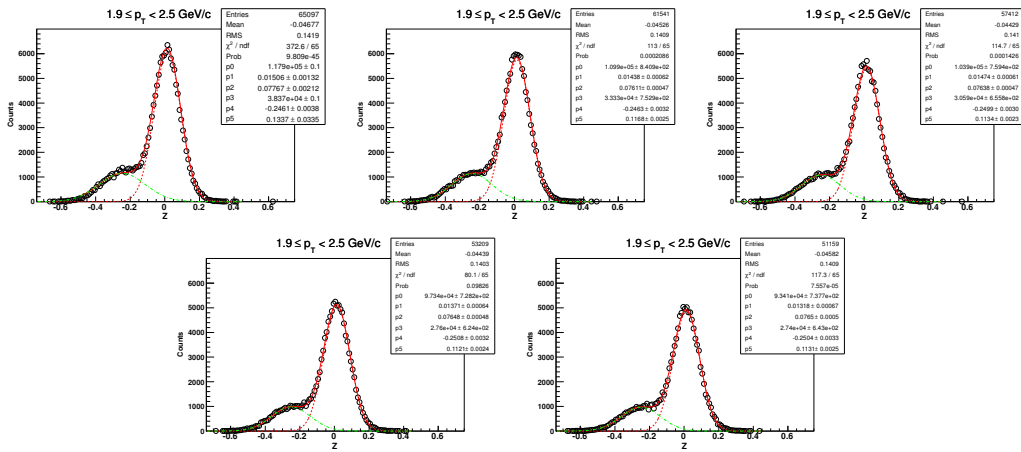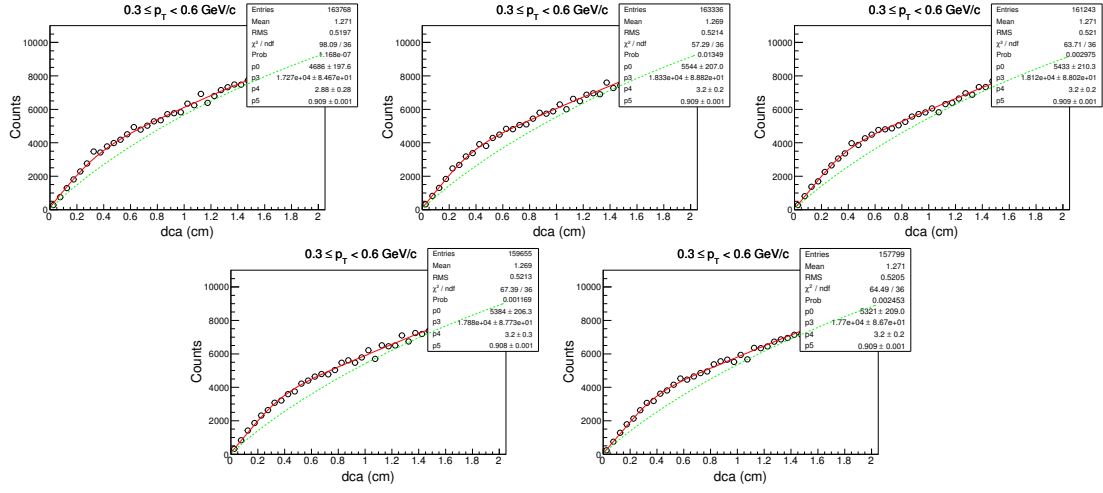$(\phi - \Psi_2)$ distributions of $t$ in Au+Au at $\sqrt{s_{\mathrm{NN}}} = 27$ GeV (0-80%)

# DCA and $Z$ distribution of $d$ in Au+Au at $\sqrt{s_{\mathrm{NN}}} = 19.6$ GeV (0-80%))
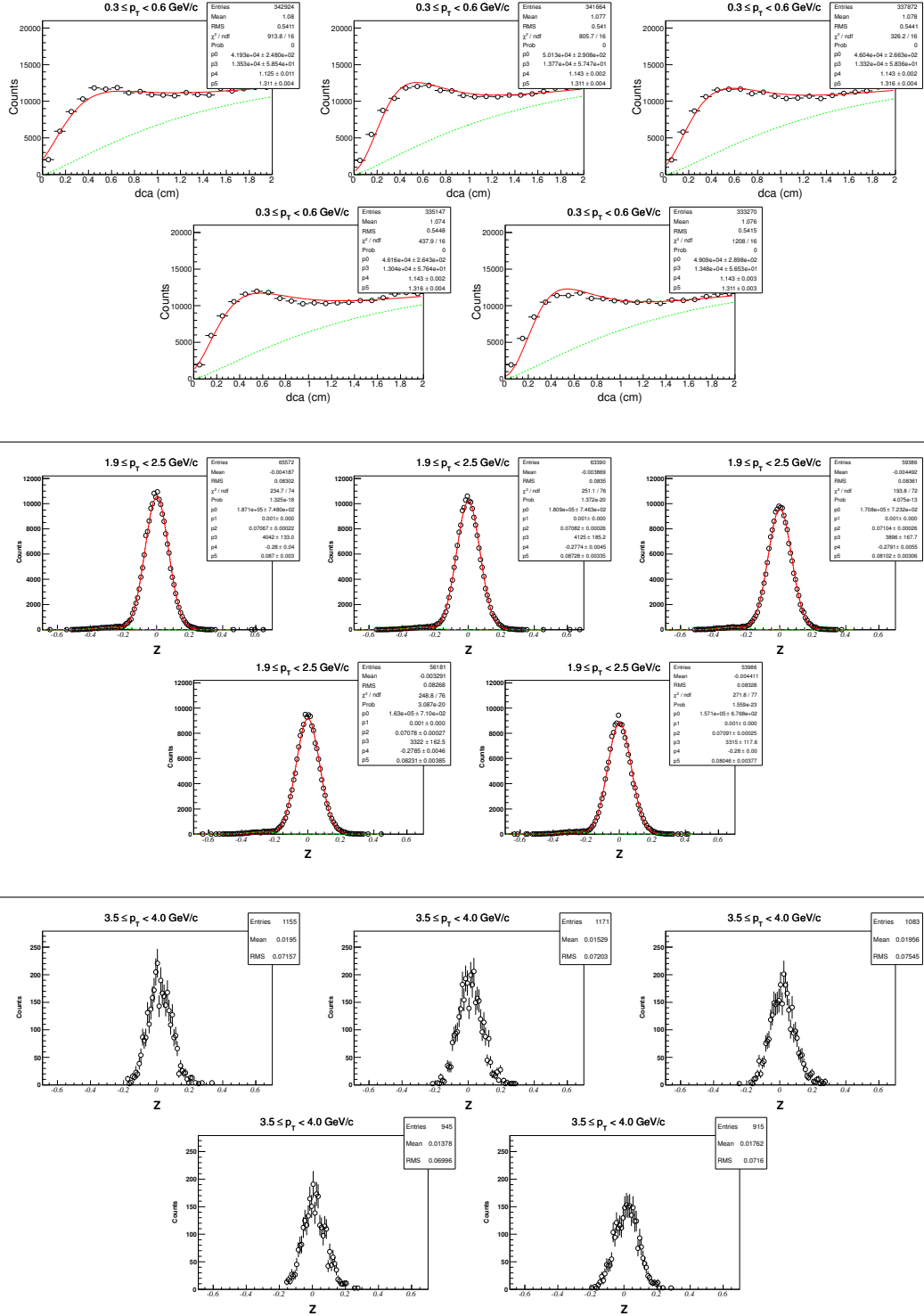
# $Z$ distribution of $\overline{d}$ in Au+Au at $\sqrt{s_{\mathrm{NN}}} = 19.6$ GeV (0-80%))
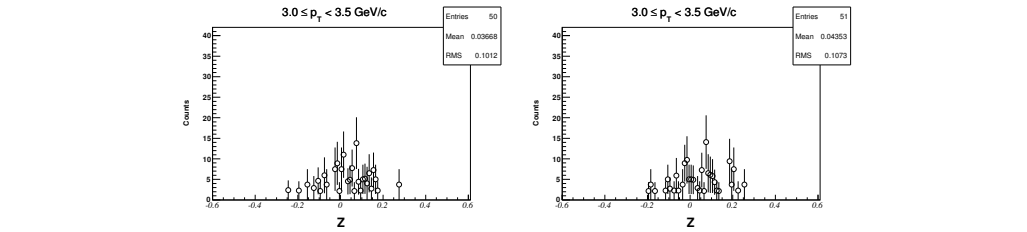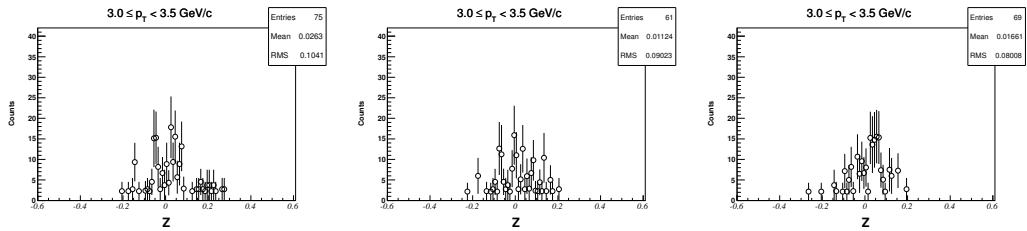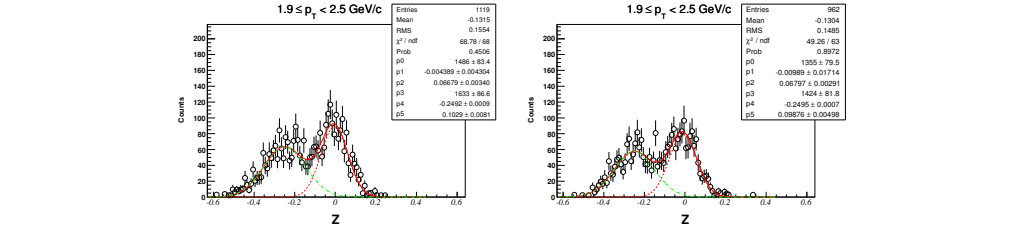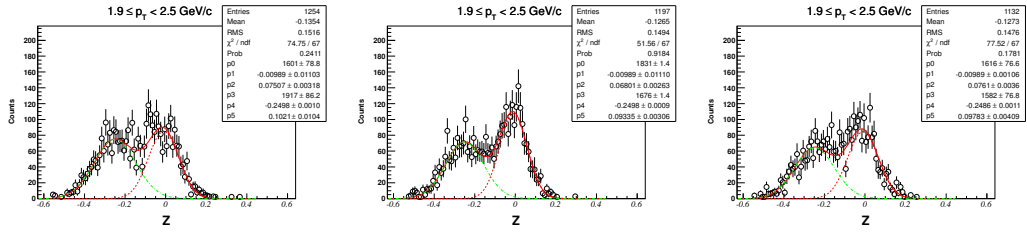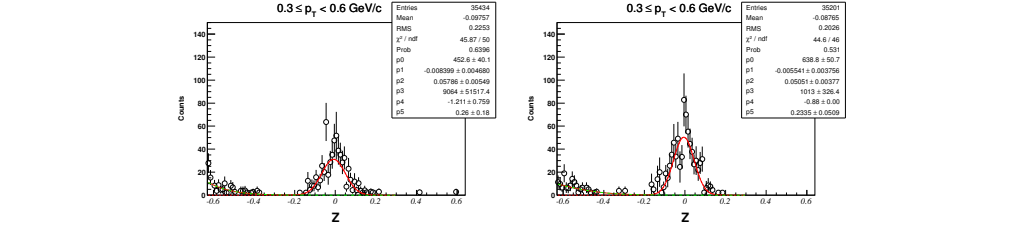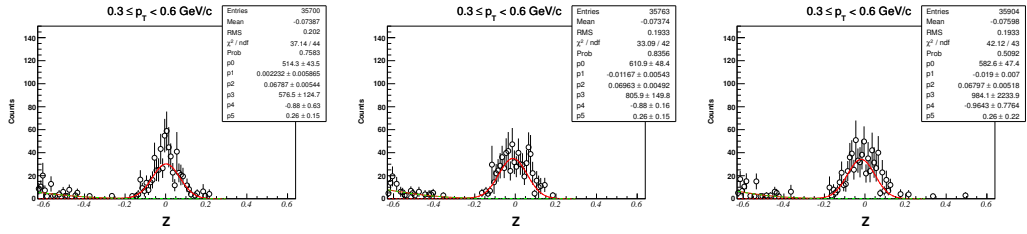
$(\phi - \Psi_2)$ distributions of $d$ in Au+Au at $\sqrt{s_{NN}} = 19.6$ GeV (0-80%)
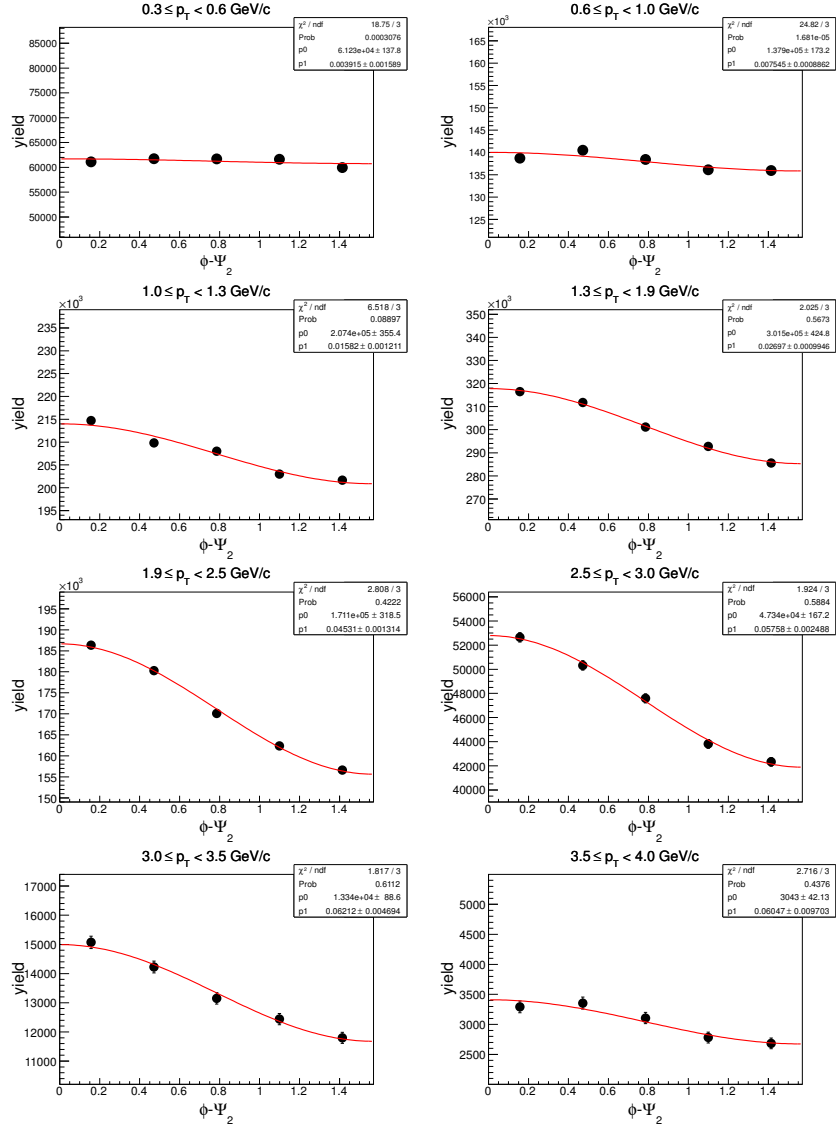
$(\phi - \Psi_2)$ distributions of $\overline{d}$ in Au+Au at $\sqrt{s_{\text{NN}}} = 19.6$ GeV (0-80%)
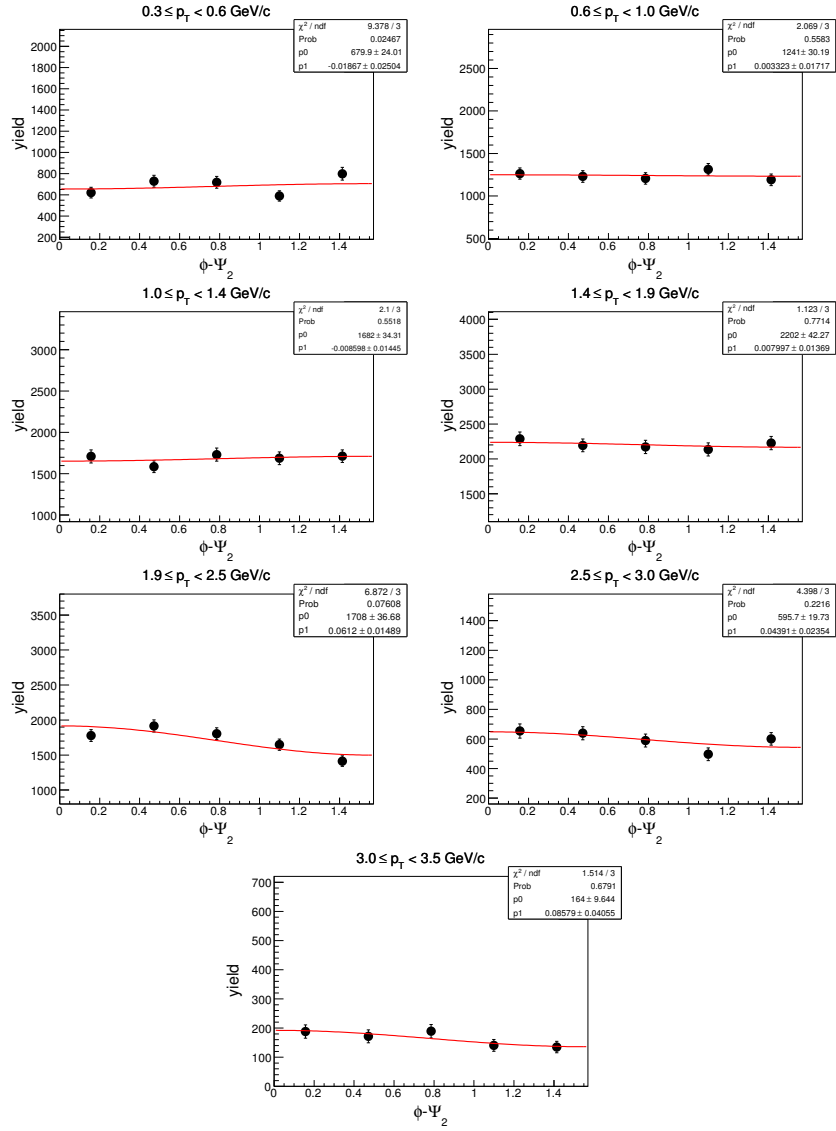
# $Z$ distribution of $^3$He in Au+Au at $\sqrt{s_{NN}} = 19.6$ GeV, (0-80%))
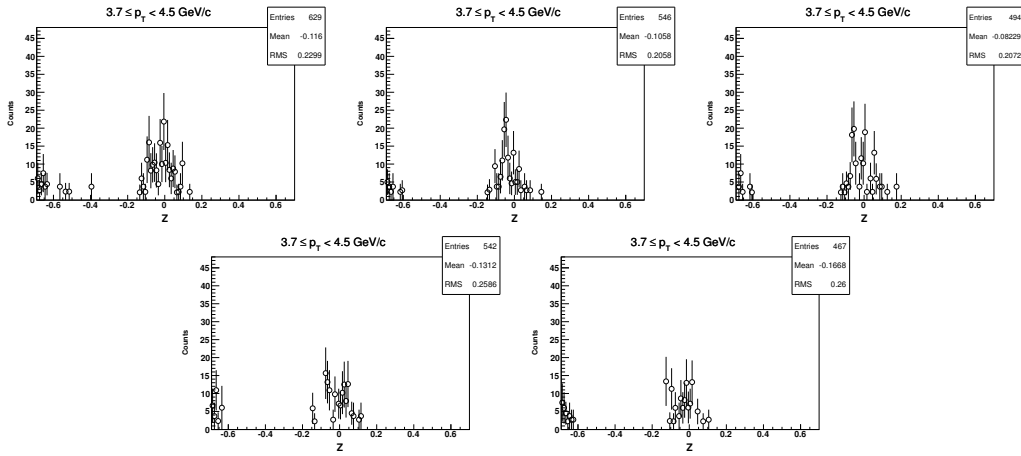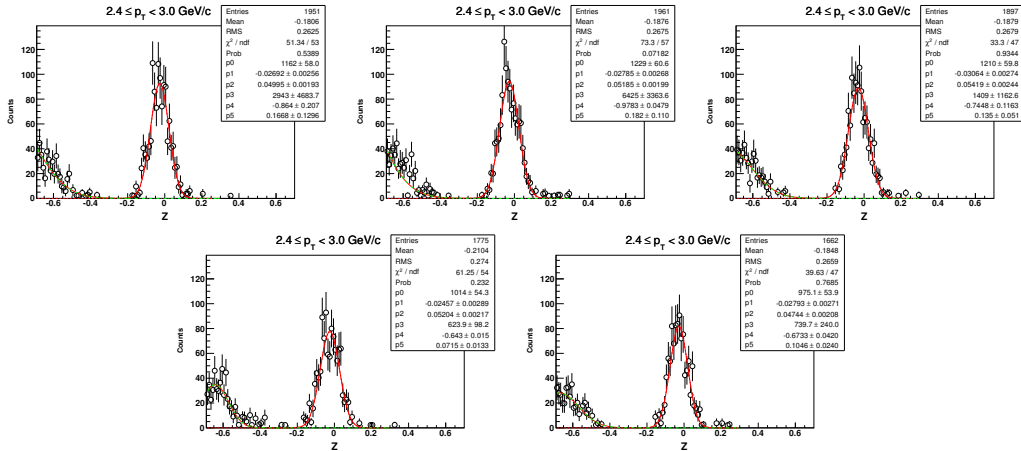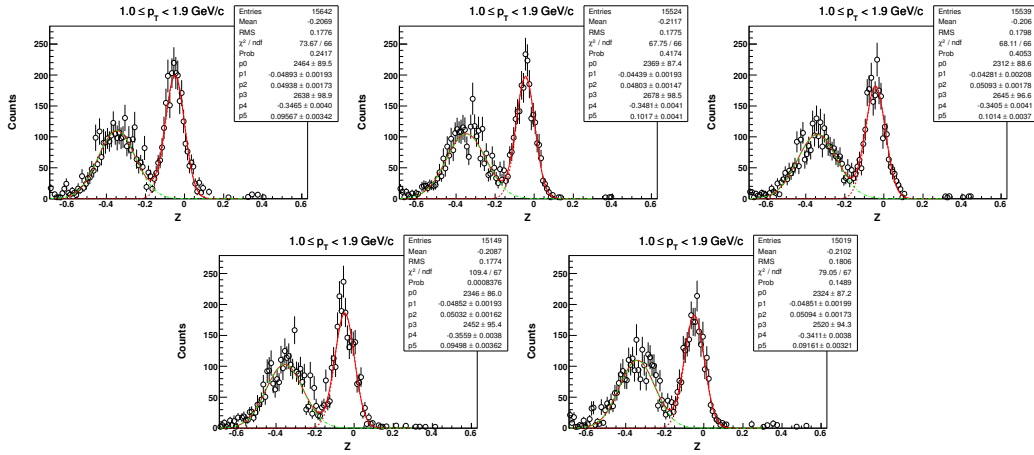
# $Z$ distribution of $t$ in Au+Au at $\sqrt{s_{\mathrm{NN}}} = 19.6$ GeV, (0-80%))
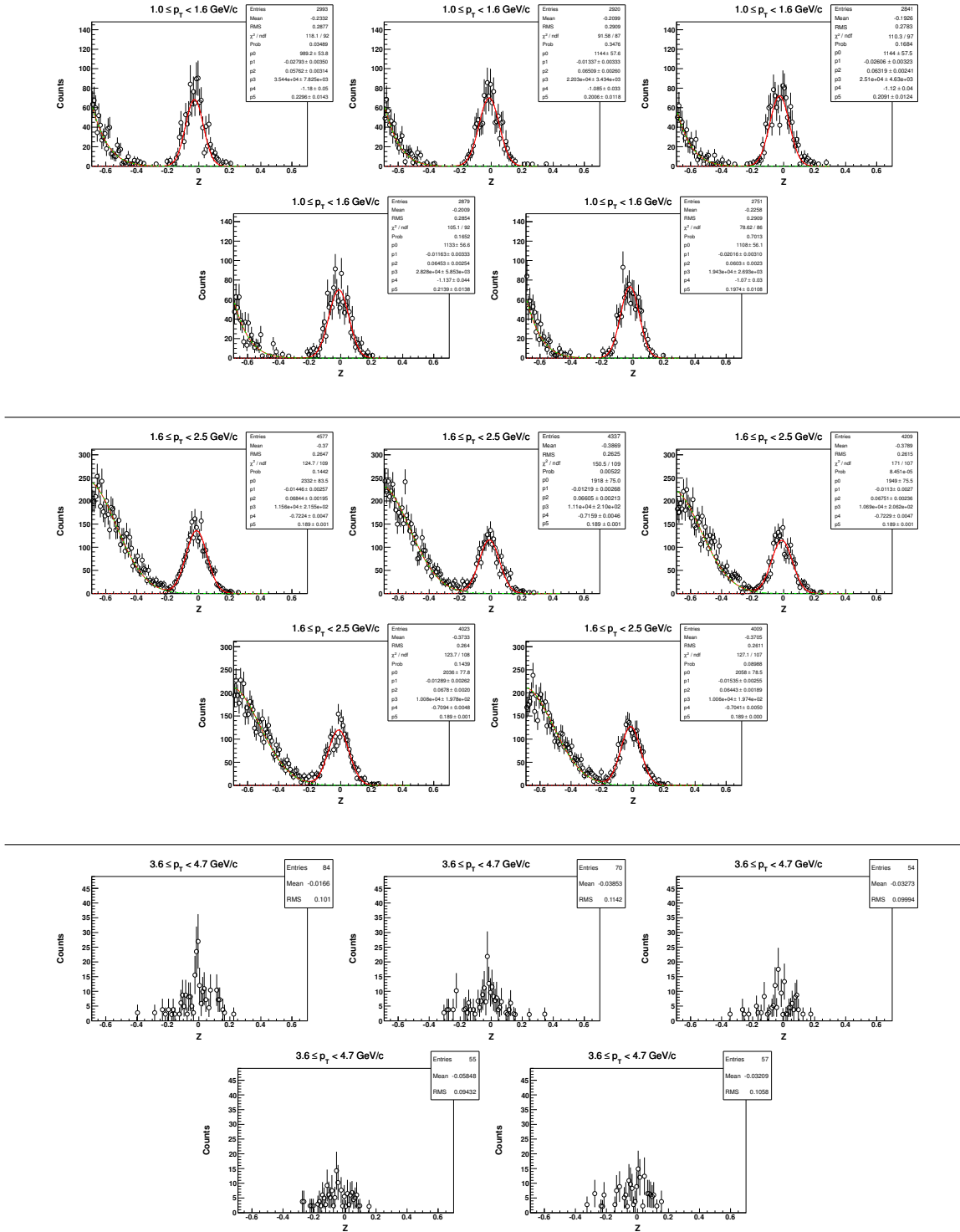
$(\phi - \Psi_2)$ **distributions of** $^3$**He in Au+Au at** $\sqrt{s_{\mathrm{NN}}} = 19.6$ **GeV (0-80%)**
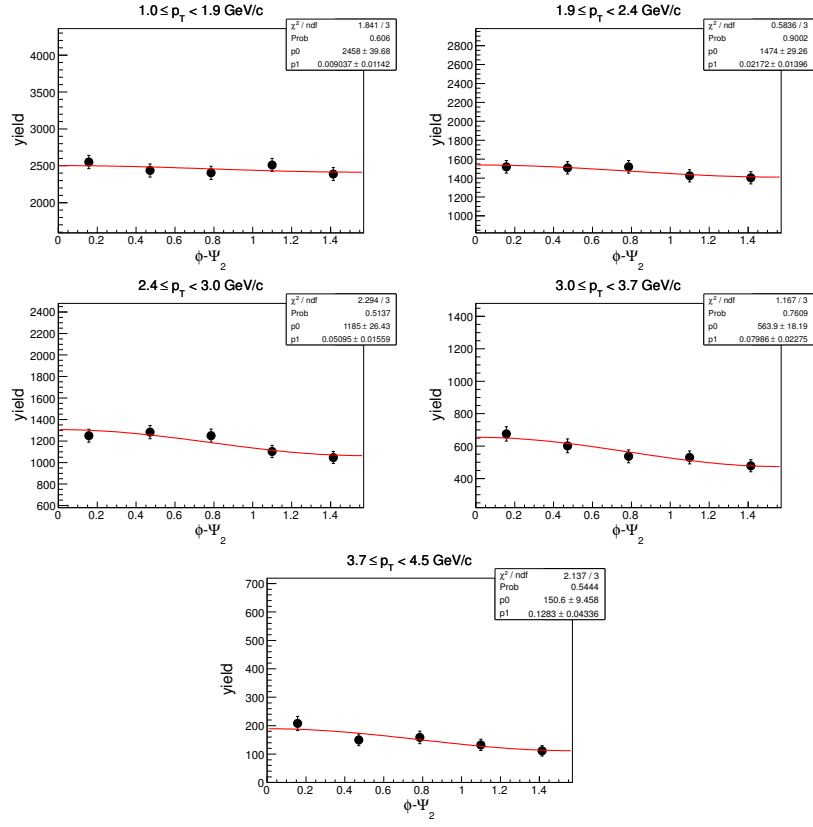


$(\phi - \Psi_2)$ **distributions of** $t$ **in Au+Au at** $\sqrt{s_{\mathrm{NN}}} = 19.6$ **GeV (0-80%)**
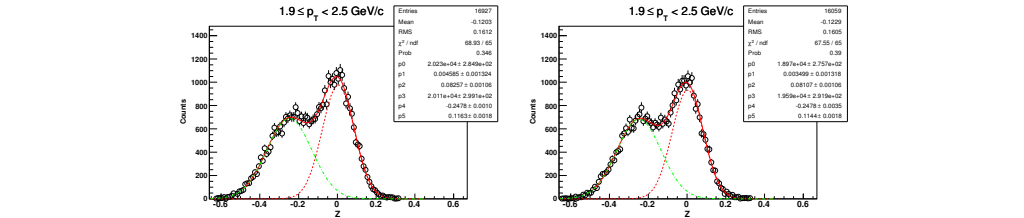
# DCA and $Z$ distribution of $d$ ($\sqrt{s_{NN}} = 11.5$ GeV, (0-80%))
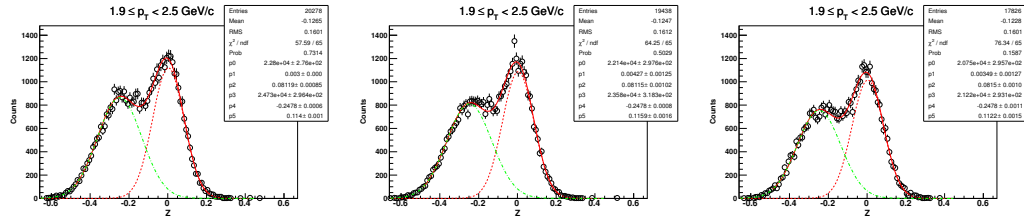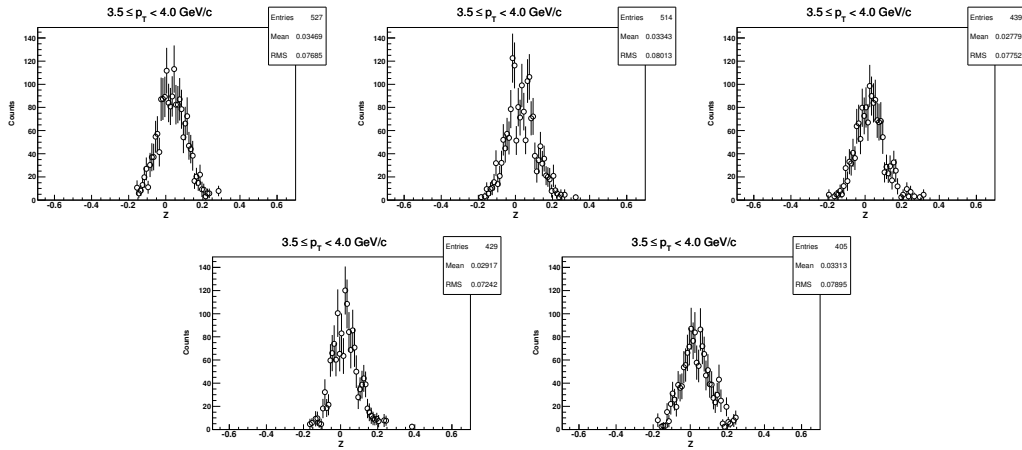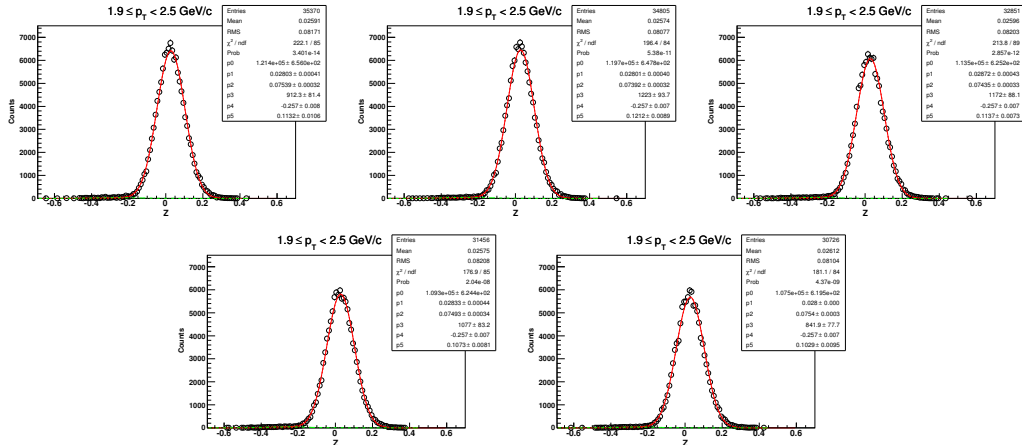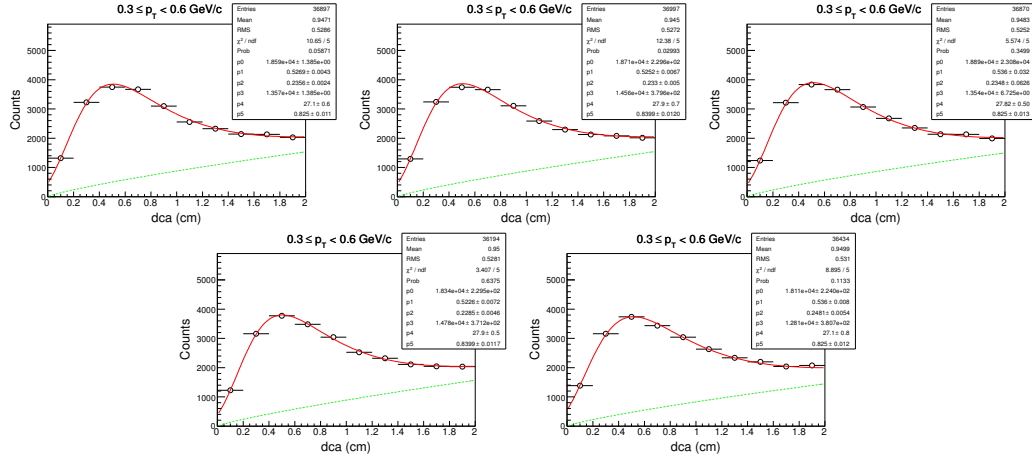
$(\phi - \Psi_2)$ distributions of $d$ in Au+Au at $\sqrt{s_{\mathrm{NN}}} = 11.5$ GeV (0-80%)
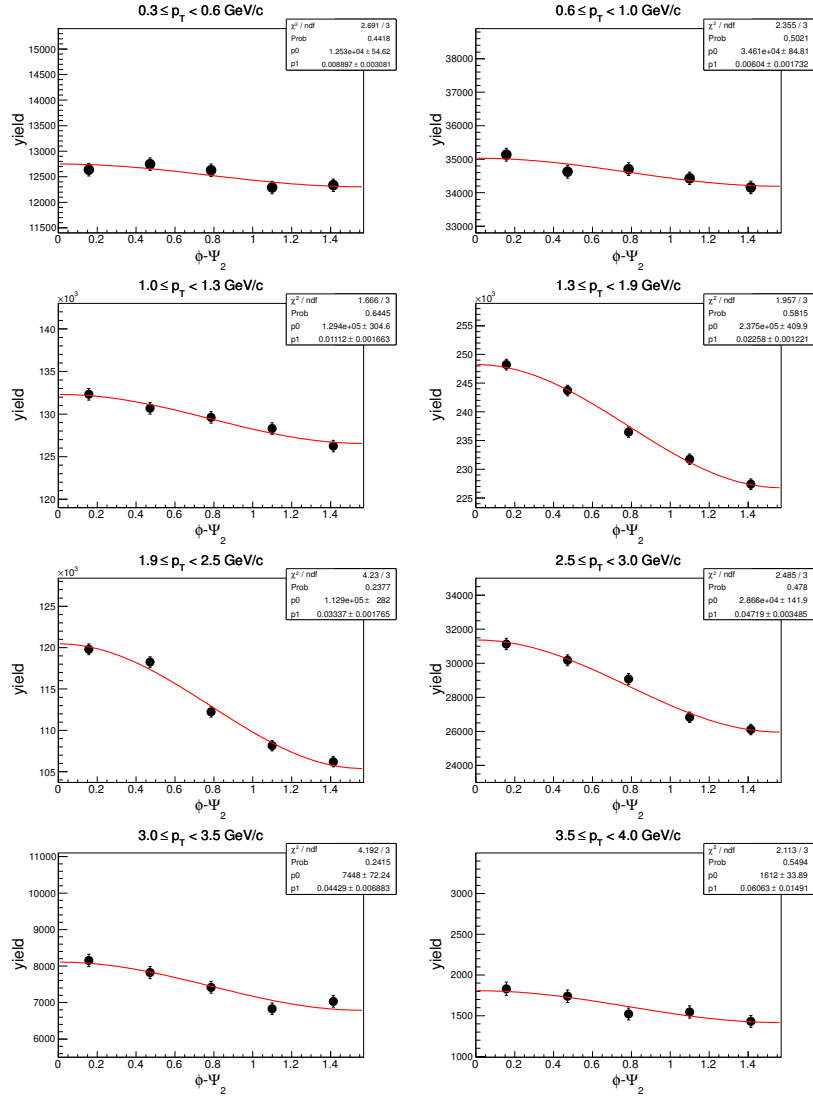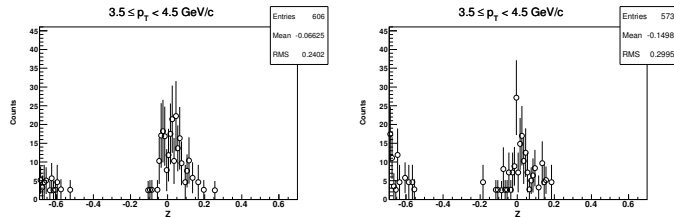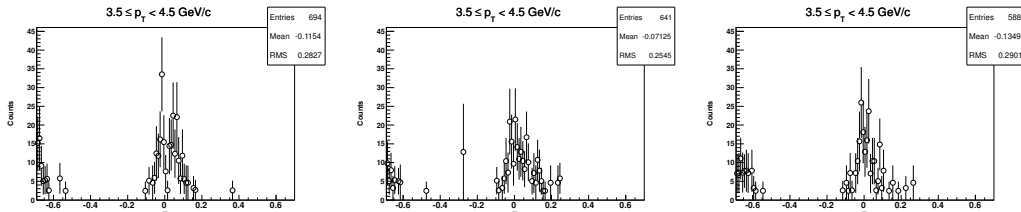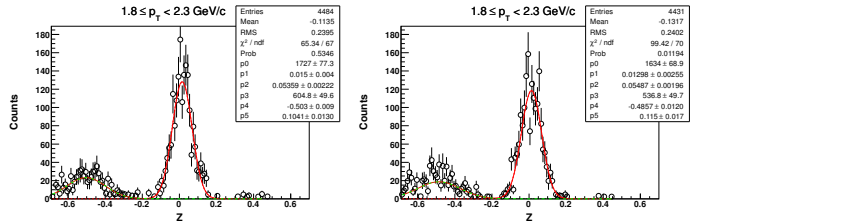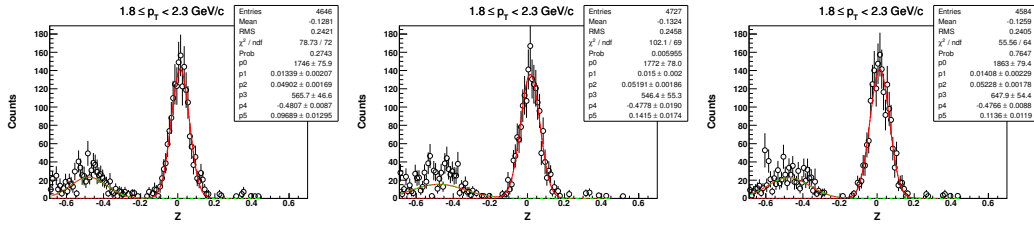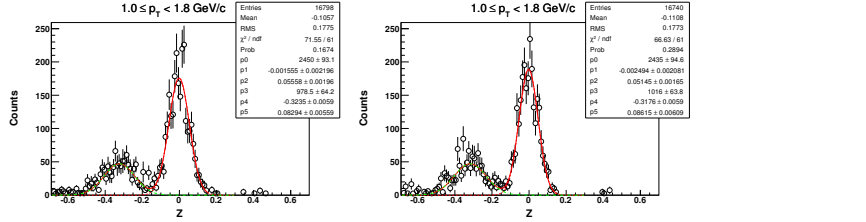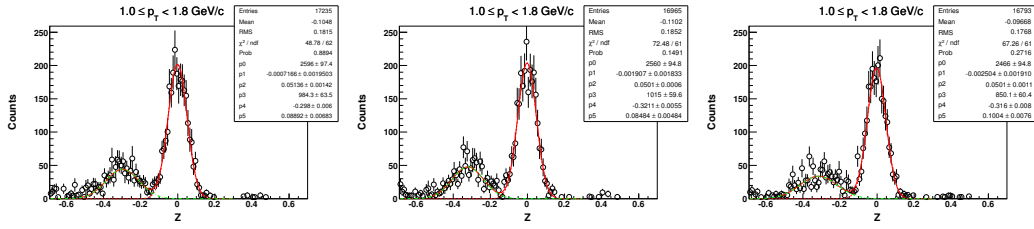
Z distribution of $^3$He in Au+Au at $\sqrt{s_{NN}} = 11.5$ GeV, (0-80%))

# $Z$ distribution of $t$ in Au+Au at $\sqrt{s_{\mathrm{NN}}} = 11.5$ GeV (0-80%))
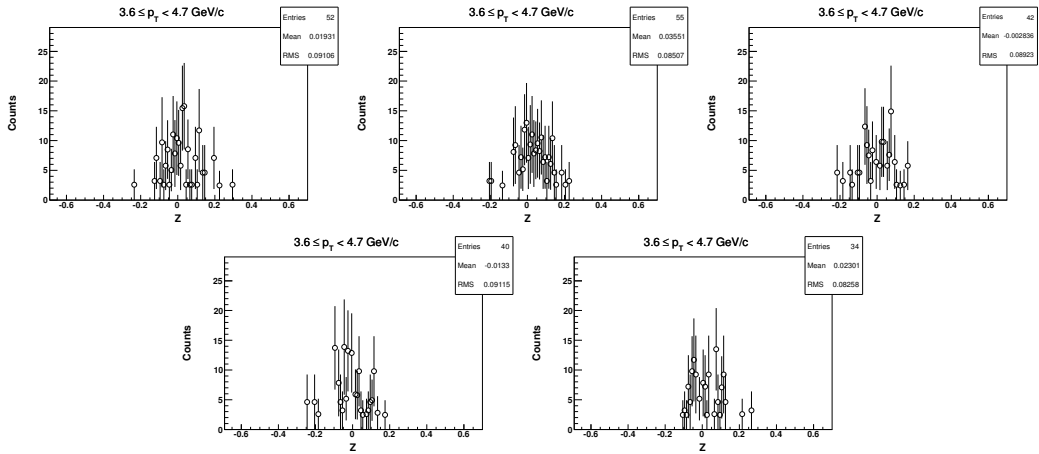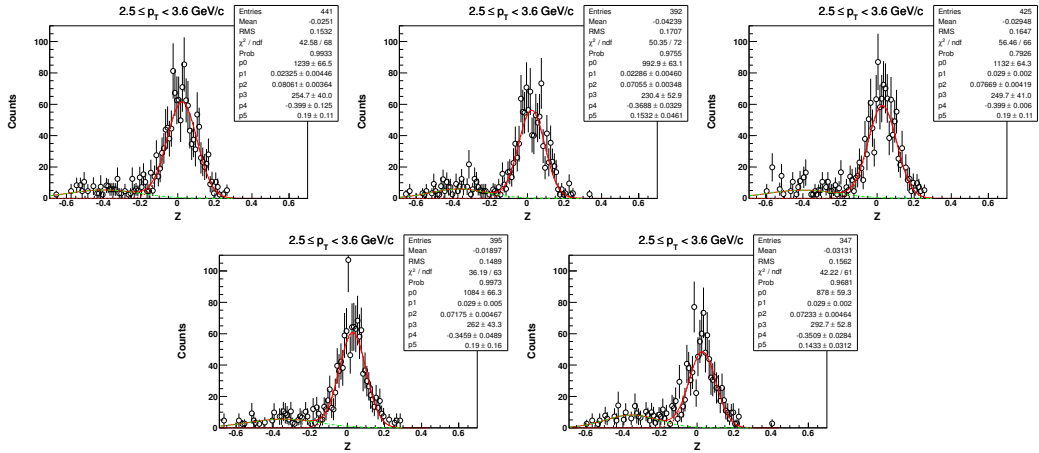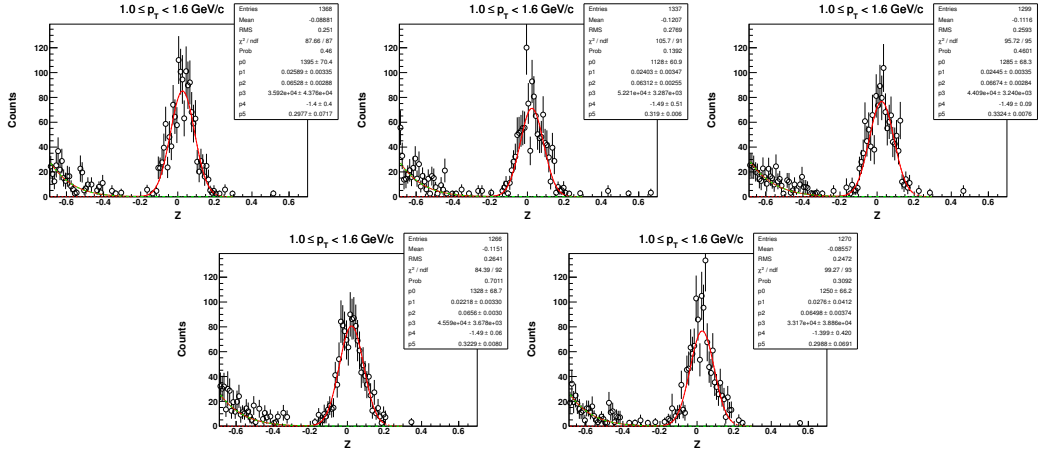
$(\phi - \Psi_2)$ distributions of $^3$He in Au+Au at $\sqrt{s_\mathrm{NN}} = 11.5$ GeV (0-80%)
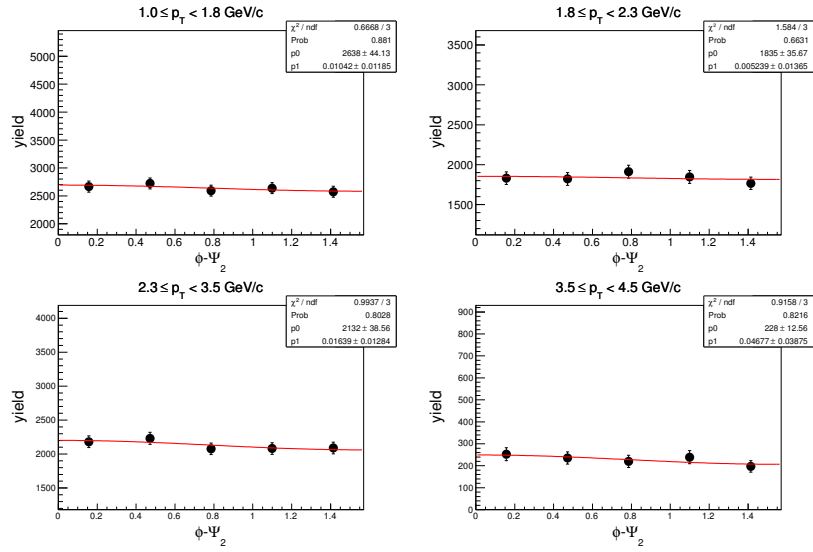


$(\phi - \Psi_2)$ distributions of $t$ in Au+Au at $\sqrt{s_\mathrm{NN}} = 11.5$ GeV (0-80%)
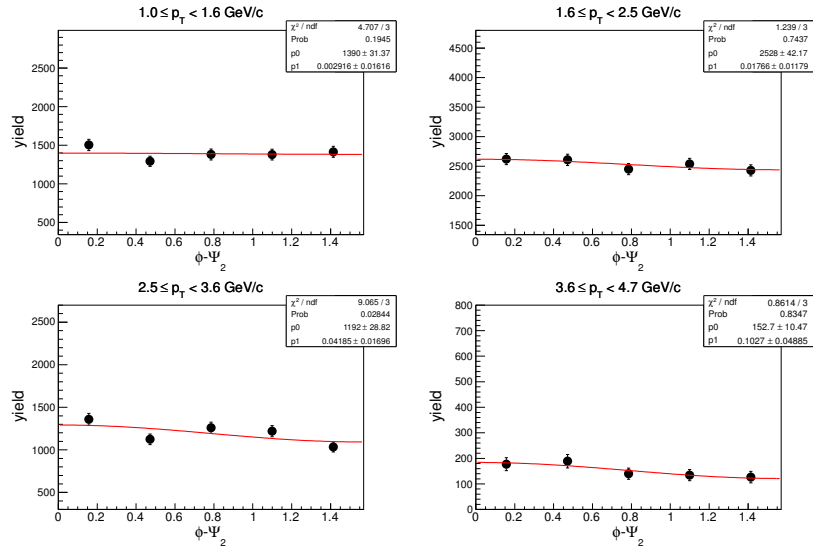
DCA and $Z$ distribution of $d$ in Au+Au at $\sqrt{s_{\mathrm{NN}}} = 7.7$ GeV, (0-80%))
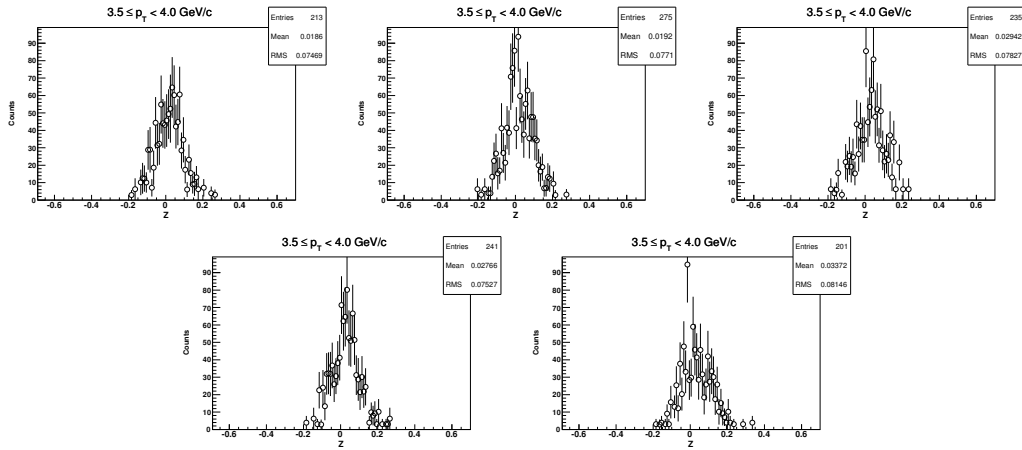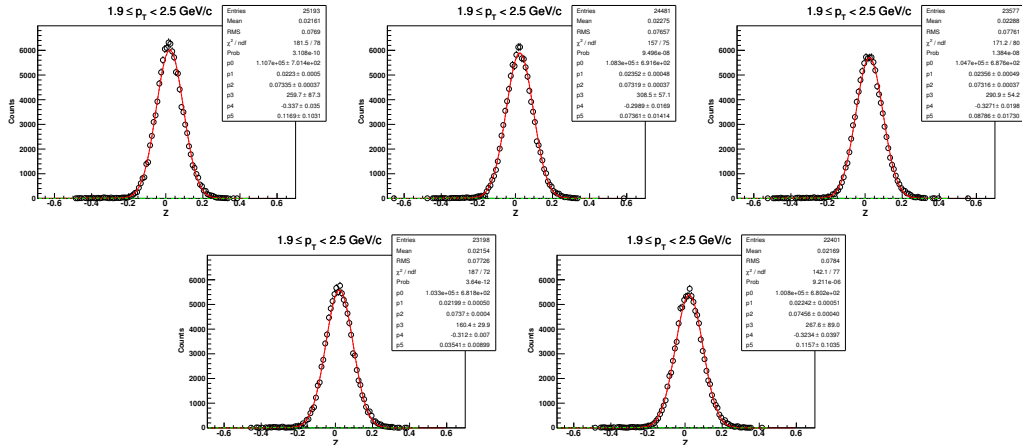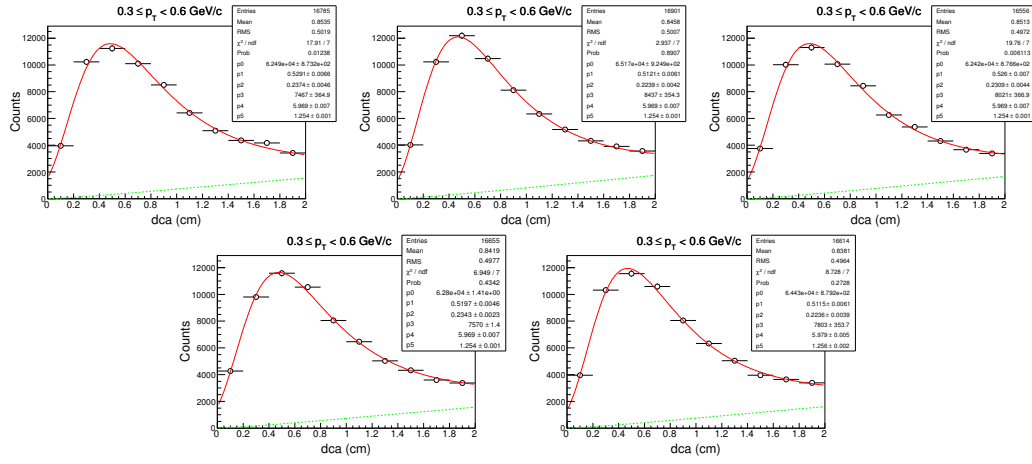
$(\phi - \Psi_2)$ distributions of $d$ in Au+Au at $\sqrt{s_{\mathrm{NN}}} = 7.7$ GeV (0-80%)
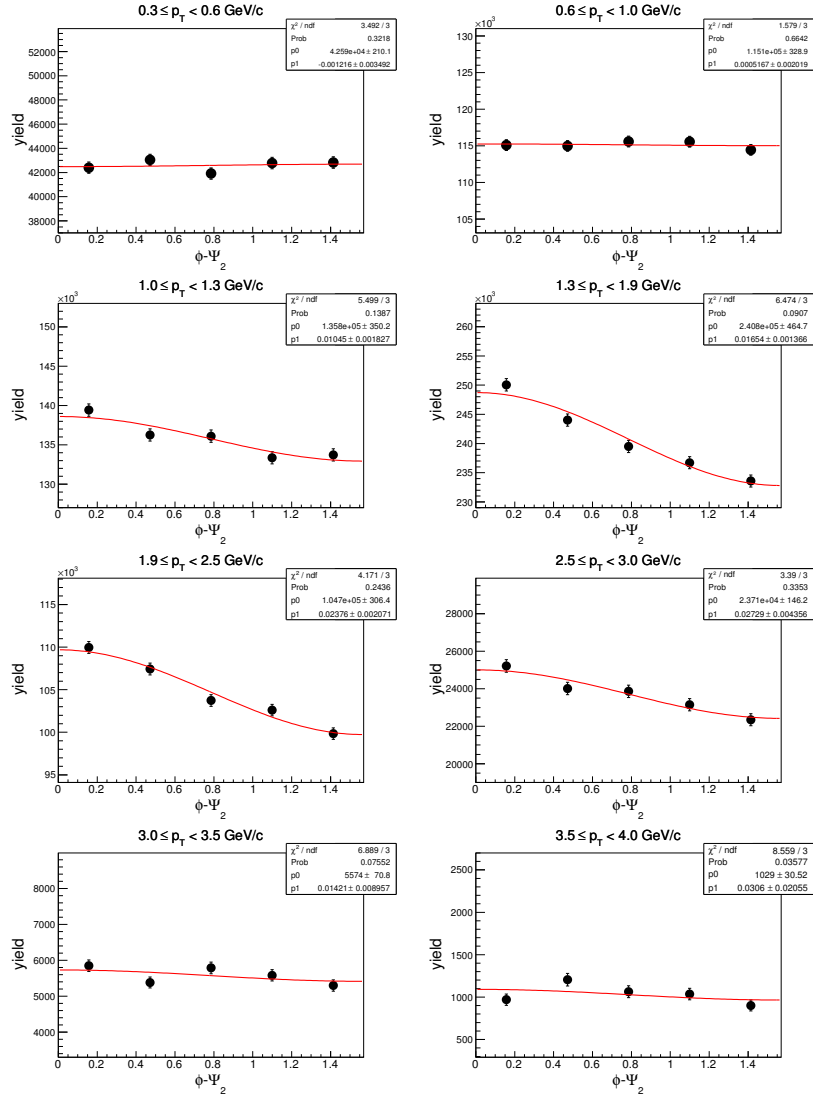
# Z distribution of $^3$He in Au+Au at $\sqrt{s_{NN}} = 7.7$ GeV (0-80%))
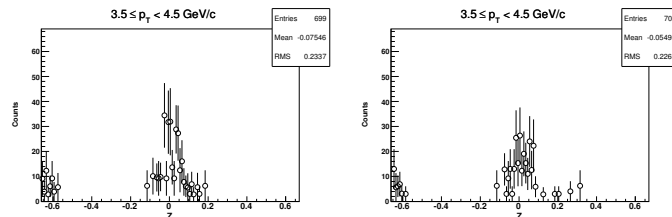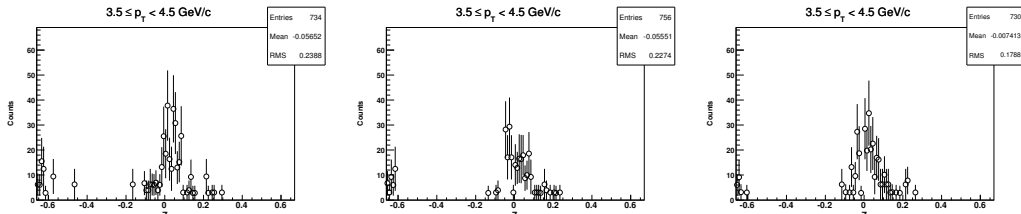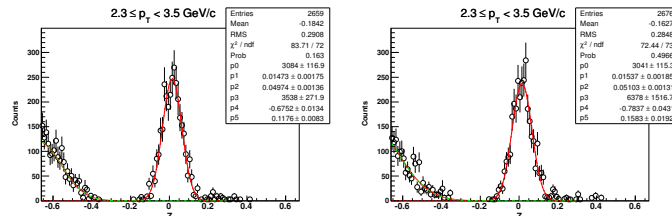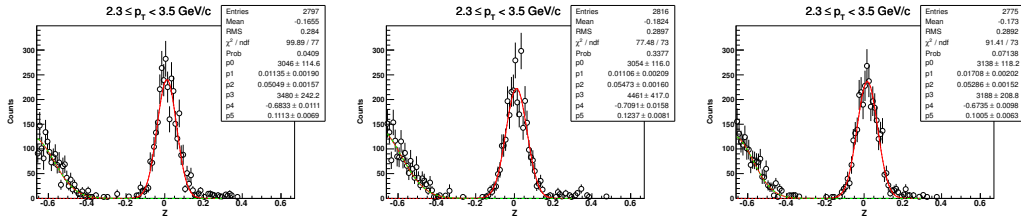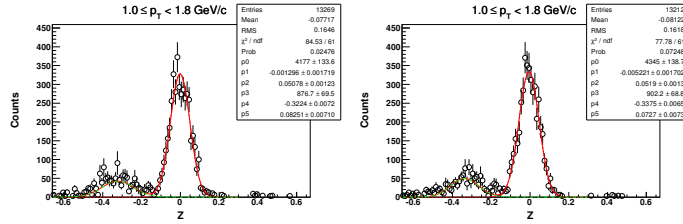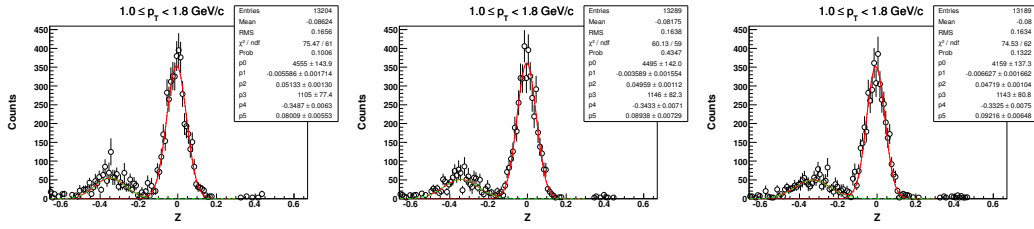
# Z distribution of $t$ in Au+Au at $\sqrt{s_{NN}} = 7.7$ GeV (0-80%))
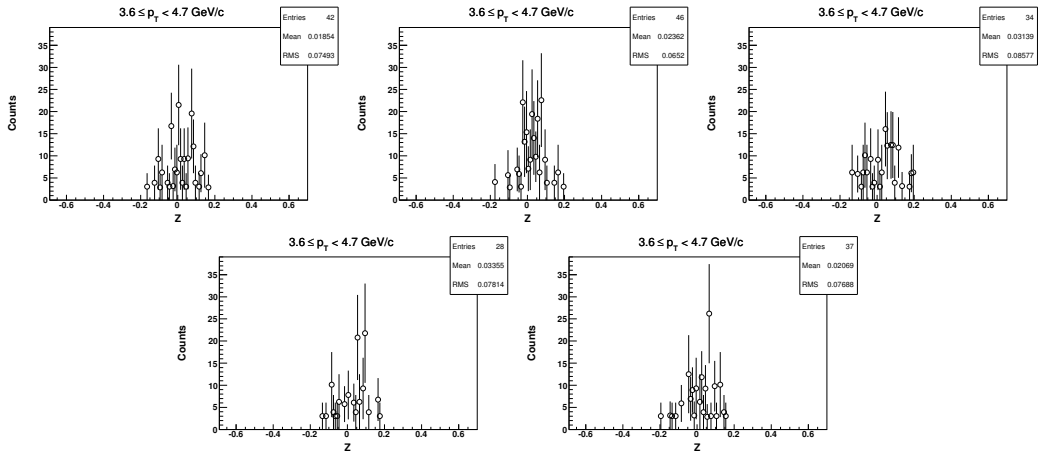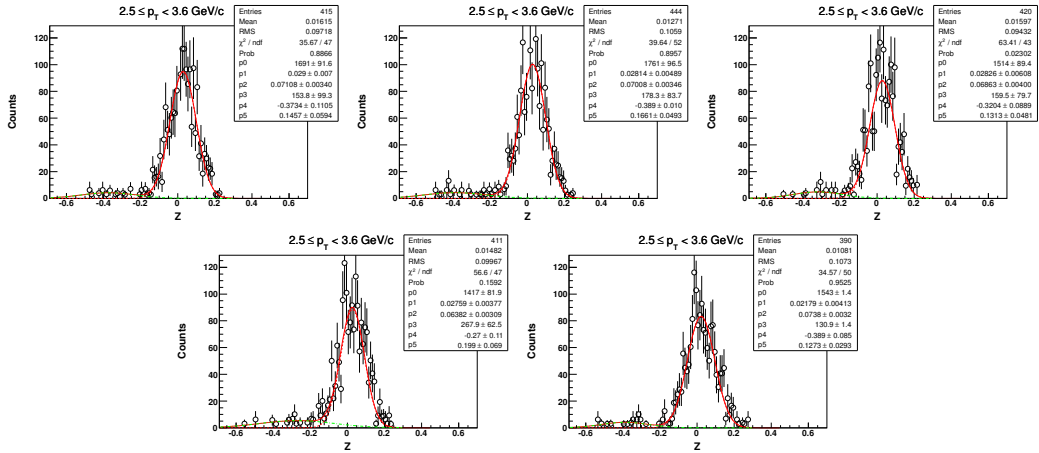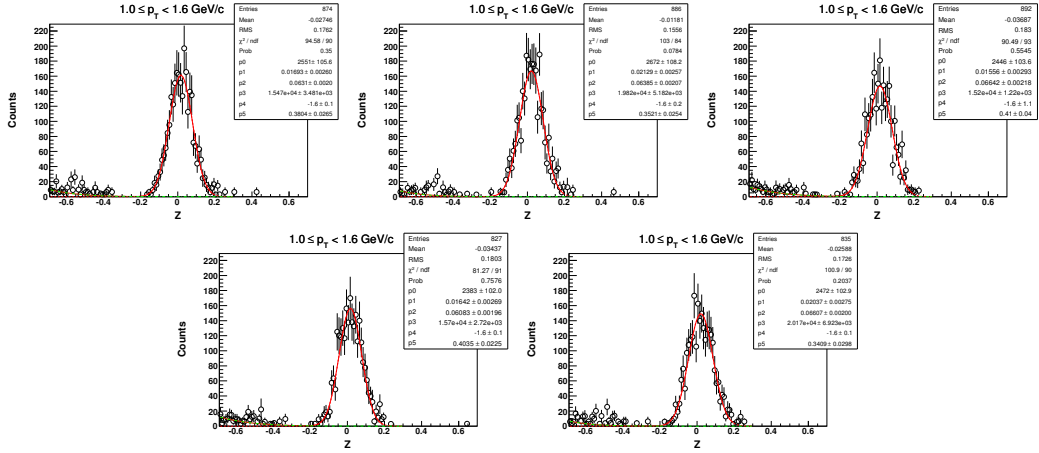
$(\phi - \Psi_2)$ distributions of $^3$He in Au+Au at $\sqrt{s_{\mathrm{NN}}} = 7.7$ GeV (0-80%)
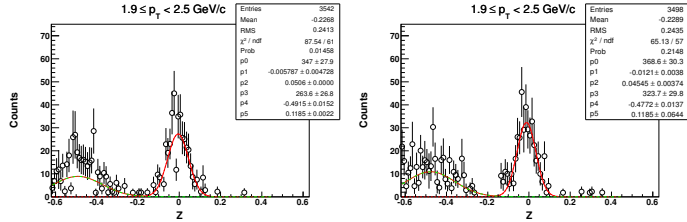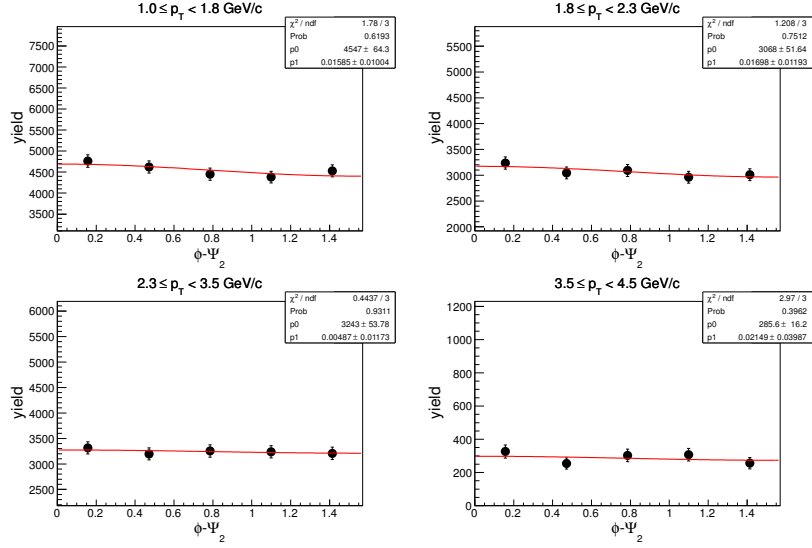


$(\phi - \Psi_2)$ distributions of $t$ in Au+Au at $\sqrt{s_{\mathrm{NN}}} = 7.7$ GeV (0-80%)
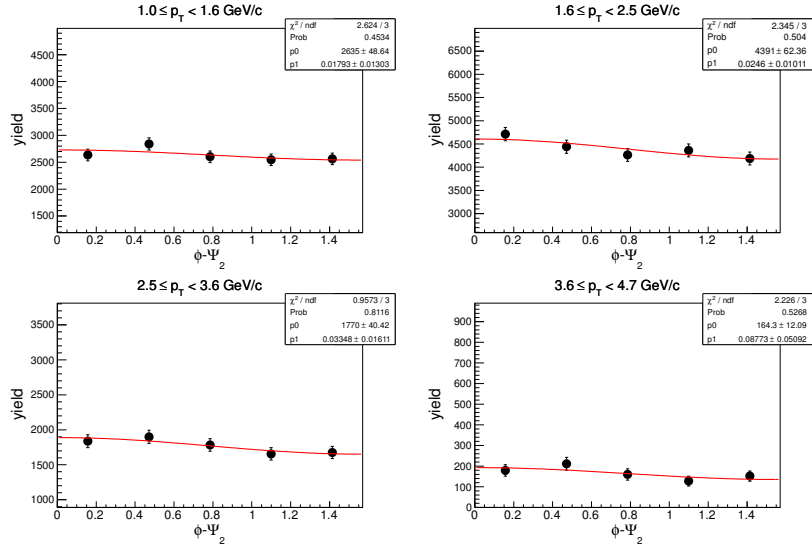
# Chapter 5

# Anisotropic Flow of Charged Particles in AMPT Model

The systematic study of inclusive charged hadron $v_2$, $v_3$ and there fluctuations in different asymmetric heavy-ion collisions for top RHIC energy ($\sqrt{s_{NN}} = 200$ GeV) are presented. Charged particle multiplicity $dN_{ch}/d\eta$, average transverse momentum ($\langle p_T \rangle$) and inclusive charged hadron $v_2$, $v_3$ are also presented in this chapter for deformed U+U collisions for $\sqrt{s_{NN}} = 200$ GeV. Both the studies are made using a transport based model [1].

## 5.1  Flow Measurement Method in Transport Model

The elliptic flow signal is proportional to the eccentricity, $\varepsilon_2$, of the initial collision region defined by the overlap of the colliding nuclei [2]. However, it has been suggested that fluctuations of the initial collision geometry may lead to higher order Fourier components in the azimuthal correlation function through collective effects [3]. Traditional hydrodynamic calculations start from a smooth matter distribution given by the transverse overlap of two Woods-Saxon distributions. In such calculations, elliptic flow is aligned with the orientation of the reaction plane defined by the impact param-

181

eter direction and the beam axis. Therefore, by symmetry, no $v_3$ component arises in the azimuthal distribution of the produced particle. To describe this component, fluctuations in the initial collision geometry has to be taken care in an event-by-event basis. In a Glauber Monte Carlo event, the minor axis of eccentricity of the region defined by nucleon-nucleon interaction points does not necessarily coincide with the reaction plane vector. Therefore, the participant eccentricity [4, 6] calculated with respect to this tilted axis can be finite even for most central events and significantly larger than the reaction plane eccentricity. In the current model based work, the participant eccentricity $\varepsilon_2$ and triangularity $\varepsilon_3$ has been calculated using the position distribution of the initial participants (nucleon which take part in the collision). The participant eccentricity is defined as,

$$\varepsilon_2 = \frac{\sqrt{(\sigma_y^2 - \sigma_x^2)^2 + 4(\sigma_{xy})^2}}{\sigma_x^2 + \sigma_y^2} \tag{5.1}$$

where $\sigma_x^2$, $\sigma_y^2$ and $\sigma_{xy}$, are the event-by-event (co)variances of the participant nucleon distributions along the transverse directions $x$ and $y$ [4]. If the coordinate system coincide with the center of mass of the participating nucleons such that $\langle x \rangle = \langle y \rangle = 0$, then definition of eccentricity is equivalent to

$$\varepsilon_2 = \frac{\sqrt{\langle r^2 \cos(2\phi_{part}) \rangle^2 + \langle r^2 \sin(2\phi_{part}) \rangle^2}}{\langle r^2 \rangle} \tag{5.2}$$

where, $r$ and $\phi_{part}$ are the polar coordinate positions of participating nucleons. The minor axis of the ellipse defined by this region is given as,

$$\Psi_2 = \frac{\arctan(\langle r^2 \sin(2\phi_{part}) \rangle, \langle r^2 \cos(2\phi_{part}) \rangle) + \pi}{2} \tag{5.3}$$

The definition of $v_2$ with respect to this participant plane is then defined as,

$$v_2 = \langle \cos(2(\phi - \Psi_2)) \rangle \tag{5.4}$$

182

where, $\phi$ is the azimuthal angle of the produced particles. In analogy to eccentricity and elliptic flow, the initial spatial and final momentum space triangular anisotropies can be quantified as participant triangularity $\varepsilon_3$, and triangular flow $v_3$, are defined as,

$$\varepsilon_3 = \frac{\sqrt{\langle r^2 \cos(3\phi_{part})\rangle^2 + \langle r^2 \sin(3\phi_{part})\rangle^2}}{\langle r^2 \rangle} \tag{5.5}$$

and,

$$v_3 = \langle \cos(3(\phi - \Psi_3))\rangle \tag{5.6}$$

respectively, where $\Psi_3$ is the minor axis of participant triangularity. The $\Psi_3$ is defined as,

$$\Psi_3 = \frac{\arctan(\langle r^2 \sin(3\phi_{part})\rangle, \langle r^2 \cos(3\phi_{part})\rangle) + \pi}{3}. \tag{5.7}$$

The minor axis of triangularity is found to be uncorrelated with the reaction plane angle and the minor axis of eccentricity in Glauber Monte Carlo calculations. In other words, the average triangular flow ($v_3$) calculated with respect to the reaction plane angle ($\Psi_r$) is zero. The participant triangularity defined in Eq. 5.6, is however calculated with respect to $\Psi_3$ (Eq. 5.7) and therefore, always finite.

## 5.2   The AMPT Model and the Observables

We have used AMPT transport model [1] to study azimuthal anisotropy of produced charged particles. The AMPT model has been described previously in chapter 4 (section 4.7.3). In AMPT, a Glauber model prescription is followed for obtaining the number of participating nucleons ($N_{part}$). The minijet partons are made to undergo scattering before they are allowed to fragment into hadrons. These interactions could give rise to anisotropy in particle production along azimuthal direction. The event plane in AMPT is set along the $x$ axis. In the default version of the AMPT model, partons are recombined with their parent strings and when they stop interacting, the resulting strings fragment into hadrons according to the Lund string fragmentation

model. The string-melting version of the AMPT model (labeled here as SM) is based on the idea that for energy densities beyond a critical value of $\sim 1$ GeV/fm$^3$, it is difficult to visualize the coexistence of strings (or hadrons) and partons. Hence there is a need to melt the strings to partons. This is done by converting the mesons to a quark and antiquark pair, baryons to three quarks, etc. The scattering of the quarks is based on parton cascade Zhangs Parton Cascade [5]. Once the interactions stop, the partons then hadronize through the mechanism of parton coalescence. The interactions between the mini-jet partons in the default AMPT model and those between partons in the AMPT-SM model could give rise to substantial $\langle v_2 \rangle$. The parton-parton interaction cross section is taken as 10 mb. The results presented below use both the default and SM versions of the AMPT model. The detailed input parametrization of AMPT model is given in the Appendix at the end of this chapter. The notations for the various observables (Eq. 5.2 − Eq. 5.7) has been followed as presented in Ref. [7].

We have studied azimuthal anisotropy of charged particles using the AMPT model in asymmetric collisions (Ag+Au, Cu+Au, and Si+Au) and symmetric collisions (Au+Au, Cu+Cu) at $\sqrt{s_{NN}} = 200$ GeV. We have also estimated azimuthal anisotropy of charged particles in various collision configurations in deformed U+U collisions at $\sqrt{s_{NN}} = 200$ GeV. The deformation of uranium nuclei was implemented in the AMPT model for the later study. The reason for these studies being carried out with asymmetric and deformed heavy-ion collisions was to provide the model based expectation of various flow observables, so that physics case can be build for collision of such nuclei in the RHIC experiments. RHIC has collided Au+Cu and U+U in the year 2012. The following subsection describe the model studies in details.

## 5.3 Azimuthal Anisotropy in Asymmetric Heavy-ion Collisions

Knowing the initial geometry and fluctuations in heavy-ion collisions has recently been shown to have important consequences on interpreting the data from the Relativistic Heavy Ion Collider (RHIC) and the Large Hadron Collider (LHC) experiments [7, 8]. The contribution from the odd harmonics associated with the particle azimuthal angle distribution (originally thought to be zero due the left-right symmetry in the transverse plane of symmetric heavy-ion collisions) to dihadron correlations are found to be important. It is being widely discussed that nonzero odd harmonic contributions could arise from fluctuations in the transverse positions of nucleons undergoing hadronic scattering. Further it is now known that even the ideal hydrodynamics calculations under predicts the measured elliptic flow in central heavy-ion collisions at RHIC [9]. Only inclusion of flow fluctuations arising due to the eccentricity fluctuations can provide some satisfactory explanation of the data. It is also believed that measurement of higher order flow coefficients and their fluctuations can substantially improve the constraints on the transport properties of the system formed in high energy heavy-ion collisions [11]. Experimentally it has not been possible to separate the contribution from elliptic flow ($v_2$), fluctuations, and nonflow from the data [10]. This is due to the lack of knowledge of the probability distributions for flow fluctuations. The fluctuations in $v_2$ can arise due to fluctuations in the eccentricity of the overlap region of the two colliding nuclei or deviations of the participant plane from the reaction plane. While nonflow effects are those correlations among particles that are not related to the reaction plane (e.g., due to resonance decay and jets).

Asymmetric heavy-ion collisions could provide density profiles that are different or not accessible through symmetric heavy-ion collisions. For example a midcentral Cu on Au collision could lead to the Cu nucleus being occluded in the Au, leading to nonzero odd harmonic of flow and being highly sensitive to early time dynamics.

Keeping these and other physics aspects in mind, RHIC then proposed an asymmetric heavy-ion collisions program[8]. This study concentrates on the variation of $\varepsilon_2$, $\varepsilon_3$, their fluctuations, $v_2$ and $v_3$ for Au+Au, Au+Ag, Au+Cu, Cu+Cu, and Au+Si collisions at $\sqrt{s_{NN}} = 200$ GeV using AMPT with default settings. The goal being to simulate the expectation of above observables in asymmetric heavy-ion collisions relative to symmetric heavy-ion collisions.
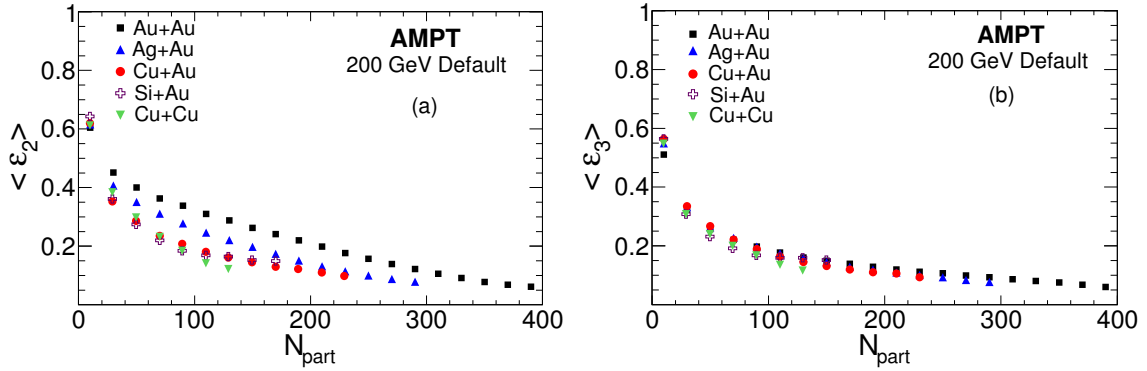


Figure 5.1: (a) Average eccentricity ($\langle\varepsilon_2\rangle$) and (b) average triangularity ($\langle\varepsilon_3\rangle$) as a function of $N_{\mathrm{part}}$ for the various heavy-ion collisions at $\sqrt{s_{\mathrm{NN}}} = 200$ GeV from AMPT model. Error bars are statistical only.

Figure 5.1 shows the $\langle\varepsilon_2\rangle$ and $\langle\varepsilon_3\rangle$ for asymmetric heavy-ion collisions (Ag+Au, Cu+Au, and Si+Au) compared to symmetric heavy-ion collisions (Au+Au and Cu+Cu) at $\sqrt{s_{\mathrm{NN}}} = 200$ GeV as a function of $N_{\mathrm{part}}$. We find for a given $N_{\mathrm{part}}$, the $\langle\varepsilon_2\rangle$ values are higher for larger colliding ion sizes. However for the low mass number colliding ions (Cu+Cu collisions and smaller) they are similar. No such large differences are observed for $\langle\varepsilon_3\rangle$. This suggests that within the framework of the AMPT model, the asymmetric heavy-ion collisions can be used to constrain the models dealing with second harmonic flow coefficient and its fluctuations. However, such collisions may not be that sensitive to studies dealing directly with triangularity and triangular flow.

Figure 5.2 shows the fluctuations in $\langle\varepsilon_2\rangle$ and $\langle\varepsilon_3\rangle$ expressed as the ratio of the corresponding root mean square (rms) values to their average values for both asymmetric heavy-ion collisions and symmetric heavy-ion collisions at $\sqrt{s_{\mathrm{NN}}} = 200$ GeV as a function of Npart. We observe that for midcentral collisions ($60 < N_{\mathrm{part}} < 250$)
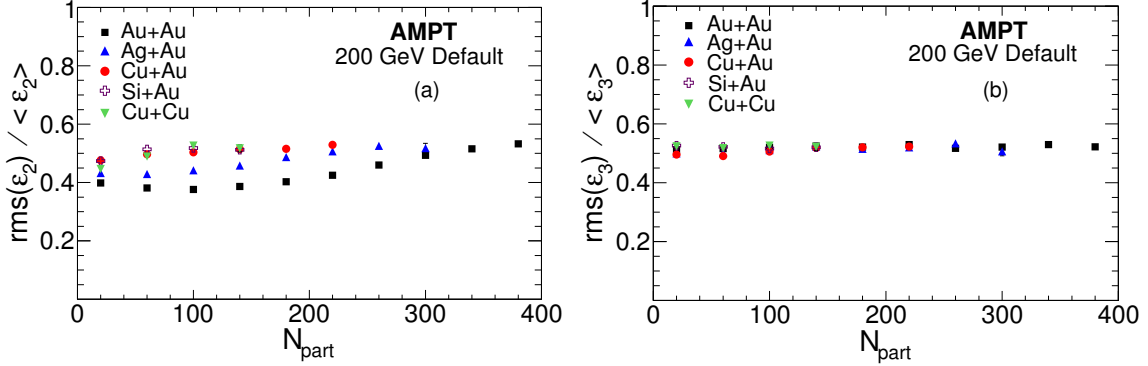
Figure 5.2: (a) Ratio of root mean square (rms) value of $\varepsilon_2$ to $\langle\varepsilon_2\rangle$ and (b) rms of $\varepsilon_3$ to $\langle\varepsilon_3\rangle$ for various heavy-ion collisions at $\sqrt{s_{NN}} = 200$ GeV using AMPT model. Error bars are statistical only.

the fluctuations in $\varepsilon_2$ increases as the system size decreases and then saturates for colliding systems of size comparable or smaller to Cu+Cu. In contrast the variation in fluctuation of $\varepsilon_3$ as a function of system size is very small.
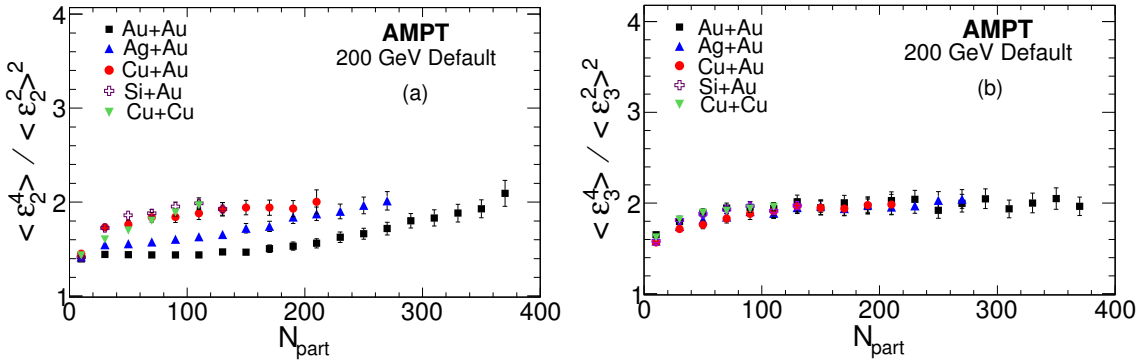


Figure 5.3: $\langle\varepsilon_n^4\rangle/\langle\varepsilon_n^2\rangle^2$, with n = 2, 3, versus $N_{npart}$ for various heavy-ion collisions at $\sqrt{s_{NN}} = 200$ GeV using the AMPT model. Error bars are statistical only.

Similar conclusions are obtained using a slightly different observable as proposed in Ref. [11]. The results of which from the AMPT model are shown in Fig. 5.3. It has been shown that the relative magnitude of $v_n\{4\}$ and $v_n\{2\}$ depends on the event-by-event fluctuations of $v_n$ if the nonflow effects are small. Where the 4 and 2 represents the four-particle and two-particle cumulant methods to extract flow coefficients, re-

spectively. It has been shown in Ref. [11] that,

$$\left(\frac{v_n\{4\}}{v_n\{2\}}\right)^4 = \left(\frac{\varepsilon_n\{4\}}{\varepsilon_n\{2\}}\right)^4 \equiv 2 - \frac{\langle \varepsilon_n^4 \rangle}{\langle \varepsilon_n^2 \rangle^2} \tag{5.8}$$

Figure 5.4 shows the same results as in Fig. 5.3 but as a function of fraction of collision centrality. Where 0 corresponds to the most central collisions and 1 corresponds to the most peripheral collisions. In addition we also show for comparison results from a Glauber model simulation for Pb+Pb collisions at $\sqrt{s_{\mathrm{NN}}} = 2.76$ TeV from Ref. [11]. Since the colliding ion species have different maximum $N_{\mathrm{part}}$ values, it is desirable to study how the fluctuations in $\varepsilon_2$ and $\varepsilon_3$ vary for the case of same fraction of collision centrality. From Fig. 5.4 one observes that although the fluctuations in $\varepsilon_3$ is still similar for all the colliding ion species studied, those for $\varepsilon_2$ now starts showing the ion size dependence more clearly. For a given fraction of collision centrality the fluctuations in $\varepsilon_2$ starts to increase as the colliding ion species size decreases, except for the most central and peripheral collisions. These results show that a systematic
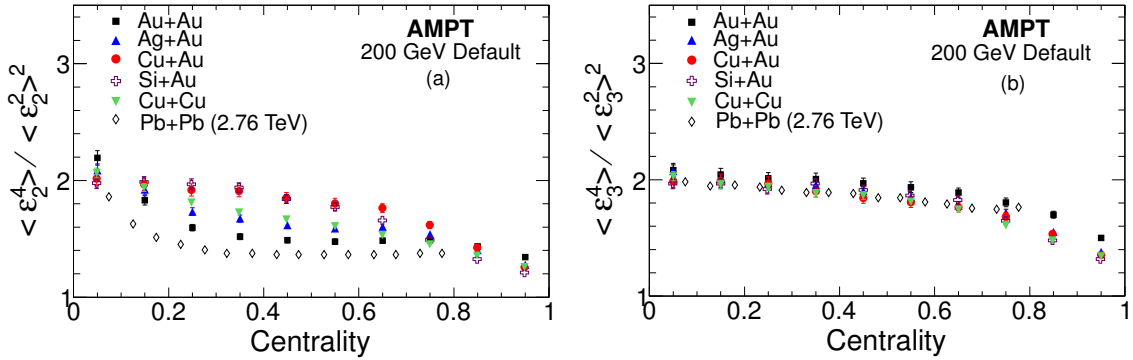


Figure 5.4: $\langle \varepsilon_n^4 \rangle / \langle \varepsilon_n^2 \rangle^2$ with n = 2, 3, versus centrality for various heavy-ion collisions at $\sqrt{s_{\mathrm{NN}}} = 200$ GeV. The Pb+Pb results corresponds to Glauber model simulations from Ref. [11] at $\sqrt{s_{\mathrm{NN}}} = 2.76$ TeV. Error bars are statistical only.

study of heavy-ion collisions with colliding system sizes ranging between Cu+Cu and Au+Au may provide a better handle on understanding $\varepsilon_2$ fluctuations and its relevance to $v_2$ fluctuations in the experimental measurements.
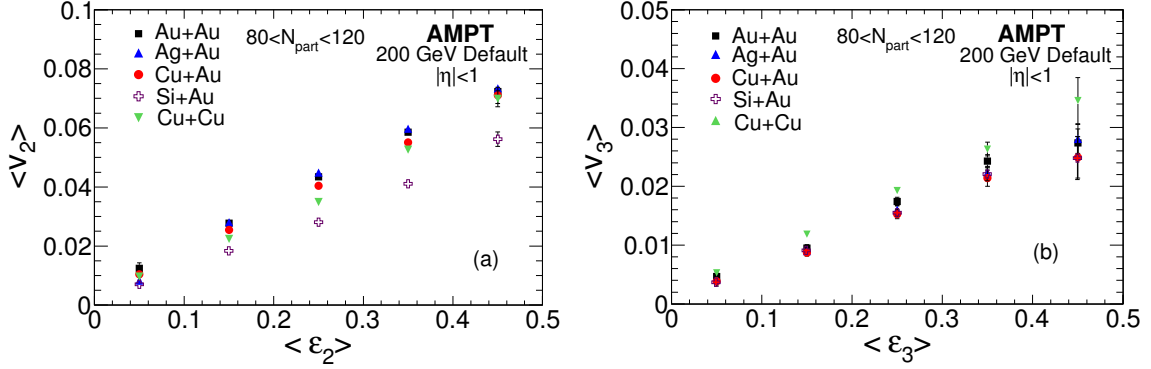
Figure 5.5: (a) $\langle v_2 \rangle$ and (b) $\langle v_3 \rangle$ of charged particles at midrapidity for $80 < N_{\text{part}} < 120$ versus $\langle \varepsilon_2 \rangle$ and $\langle \varepsilon_3 \rangle$, respectively. The results shown are for various species of heavy-ion collisions at $\sqrt{s_{\text{NN}}} = 200$ GeV from AMPT model. The errors shown are statistical.

Collective flow is mostly driven by the initial spatial anisotropy, hence it is expected that $v_2$ and $v_3$ should be proportional to $\varepsilon_2$ and $\varepsilon_3$ , respectively, in high energy heavy-ion collisions. Figure 5.5 shows $\langle v_2 \rangle$ versus $\langle \varepsilon_2 \rangle$ and $\langle v_3 \rangle$ versus $\langle \varepsilon_3 \rangle$ from the AMPT model at midrapidity for $80 < N_{\text{part}} < 120$ in heavy-ion collisions studied at $\sqrt{s_{\text{NN}}} = 200$ GeV. We observed that $\langle v_2 \rangle$ and $\langle v_3 \rangle$ are proportional to $\langle \varepsilon_2 \rangle$ and $\langle \varepsilon_3 \rangle$, respectively, for all the collision systems studied.

However for a given value of $\langle \varepsilon_2 \rangle$, the observed $\langle v_2 \rangle$ decreases with a decrease in the colliding system size. This could be due to larger fluctuations in $\langle \varepsilon_2 \rangle$ for the smaller systems compared to the larger colliding systems. However there is no such observed differences for $\langle v_3 \rangle$ versus $\langle \varepsilon_3 \rangle$. This is consistent with not much difference in fluctuations of $\langle \varepsilon_3 \rangle$ for various colliding ions.

Finally in Fig. 5.6(a) we show the $v_2$ for charged particles at midrapidity for midcentral collisions as a function of transverse momentum ($p_{\text{T}}$) for various colliding systems at $\sqrt{s_{\text{NN}}} = 200$ GeV from the AMPT model. For the centrality range studied we see a clear dependence of $v_2$ on the colliding system size. It increases with an increase in the colliding ion size. This is consistent with the results on variation of $\langle v_2 \rangle$ with $\langle \varepsilon_2 \rangle$ as shown in Fig. 5.5 and the fluctuations in $\varepsilon_2$ shown in Fig. 5.3 and 5.4. In Fig. 5.6(b) the $v_3$ versus $p_{\text{T}}$ shows a much smaller dependence on colliding
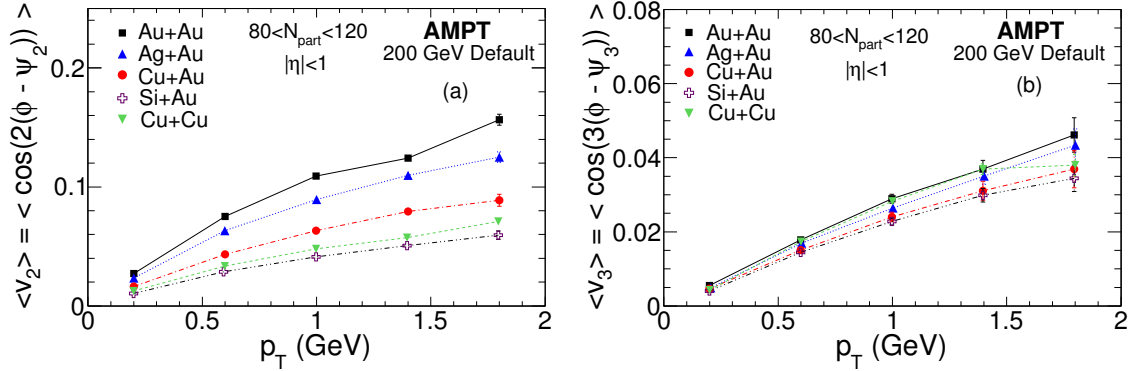
Figure 5.6: (a) $\langle v_2 \rangle$ versus $p_T$ and (b) $\langle v_3 \rangle$ versus $p_T$ of charged particles at midrapidity for $80 < N_{\text{part}} < 120$. The results shown are for various species of heavy-ion collisions at $\sqrt{s_{\text{NN}}} = 200$ GeV from AMPT model. The errors shown are statistical.

system size compared to that of $v_2$ versus $p_T$ shown in Fig. 5.6(a).

## 5.4 Charged Particle Production and Azimuthal Anisotropy in U+U Collisions

In Au+Au collisions at the Relativistic Heavy Ion Collider (RHIC) facility, large values of elliptic flow and large suppression in high transverse momentum ($p_T$) hadron production relative to p+p collisions have been reported [15]. The dominant interpretation of these measurements has indicated that the relevant degrees of freedom in these collisions are quarks and gluons [12, 13, 14]. Heavy-ion collisions using deformed nuclei such as U+U will allow us to investigate the initial conditions, hydrodynamic behavior, path length dependence of partonic energy loss [16, 17, 18], possible local parity violation [19], and other physics topics beyond what we have learned from Au+Au collisions.

In contrast to central Au+Au collisions, because of the prolate shape of uranium, there are configurations (e.g., body-to-body, defined later) in which central U+U collisions are not spherical in the transverse plane but have an elliptic shape. At RHIC we have observed an increase in $v_2/\varepsilon_2$ with an increase in transverse particle

density [15]. This corresponds to the dilute-regime predictions in kinetic theory [22]. For the hydrodynamic regime, one expects $v_2/\varepsilon_2$ to saturate with an increase in transverse particle density [22]. One way to extend the transverse particle density beyond what has been achieved at RHIC is by performing U+U collisions or going to higher beam energies as at the Large Hadron Collider (LHC). Studies suggest that the maximum transverse particle density attended in U+U collisions could be about 6-35% higher than Au+Au collisions depending on the colliding configuration [16, 17, 23]. Furthermore, several possible configurations of U+U collisions can occur, depending on the angles of the two incoming uranium nuclei relative to the reaction plane. This will help in constraining the initial conditions in various models by the measurement of $v_2$, $v_3$, and their fluctuations in U+U and comparing the same to the corresponding results in Au+Au collisions. Glauber-based model simulations suggest an increased value of $\langle \varepsilon_2 \rangle$ (up to 30%) and eccentricity fluctuations in deformed U+U collisions relative to Au+Au collisions [18, 24].

Furthermore it has been shown from the space-time evolution of high-energy noncentral symmetric heavy-ion collisions using relativistic hydrodynamics that the matter expands preferentially in the impact parameter direction and the expanding shells leave a rarefaction behind. As a consequence of this early pressure gradient, this could at freeze-out lead to three distinct fireballs being produced. This was referred to as the nutcracker scenario [25]. Subsequently, it has been pointed out that such phenomena is missing for U+U collisions due to the time evolution of the initial transverse energy density profile within a hydrodynamical framework [26]. The energy loss of partons in a hot and dense colored QCD matter depends not only on the medium density and color factor but also on the path length traversed by the parton. Theories of energy loss for fast partons support a nonlinear dependence of parton energy loss on the path length, but this has not yet been fully tested in experiment, due to the small difference in path lengths for the parton traversing in-plane and out-of-plane for Au+Au collisions. Body-to-body U+U collisions are expected to provide almost twice as much difference between the in-plane and out-of-plane path

lengths for the same eccentricity as semi-peripheral Au+Au collisions. This in turn is expected to increase by 100% the absolute value of radiative energy loss and its difference between in-plane and out-of-plane directions [16].

Parity is conserved globally in the strong interaction, but local parity violation is possible because of the topological structure of QCD [27]. It has been proposed that heavy-ion collisions at high energies provide a unique opportunity to observe local parity violation [28]. The magnetic field required for the parity-violating signal exists in noncentral heavy-ion collisions and is produced by the spectators. In central U+U body-to-body collisions, there are no spectators (small or zero magnetic field), while in certain configurations the geometry of the collision zone induces finite $v_2$. Background processes to local parity violation are expected to be related to $v_2$, while the signal is expected to be related to the magnetic field strength [19]. One can then use a comparative study of local parity violation observables for Au+Au and U+U collisions at similar energies to interpret the measurements [29].

Most of the previous model-based studies of U+U collisions have made use of Monte Carlo Glauber simulation [18, 24] or have used coupling to the hydrodynamic evolution [16, 17]. Some investigations exist for selecting special orientations of U+U collisions using event generators [23]. In this work, we have focused on the centrality dependence of $dN_{ch}/d\eta$, $\langle p_T \rangle$, $\varepsilon_2$, $\varepsilon_3$, their fluctuations, $v_2$, and $v_3$ for several configurations of U+U collisions using the AMPT model. The results are also compared to corresponding observations in Au+Au collisions.

### 5.4.1 Implementing Uranium Collisions in AMPT

In this work, U+U collisions were implemented in the AMPT model as follows. The nucleon density distribution is parametrized as a deformed Woods-Saxon profile [30],

$$\rho = \frac{\rho_0}{1 + \exp([r - R']/a)} \,, \tag{5.9}$$

$$R' = R[1 + \beta_2 Y_2^0(\theta) + \beta_4 Y_4^0(\theta)] \,, \tag{5.10}$$

where $\rho_0$ is the normal nuclear density, $R$ is the radius of the nucleus, and $a$ denotes the surface diffuseness parameter. We have used $R = 6.81$ fm and $a = 0.55$ fm for the $^{238}$U nucleus. $Y_l^m(\theta)$ denote spherical harmonics and $\theta$ is the polar angle with respect to the symmetry axis of the nucleus. The deformation parameters are $\beta_2 = 0.28$ [16] and $\beta_4 = 0.093$ [31] for uranium. The presence of $\beta_4$ modifies the shape of uranium compared to that only with $\beta_2$ [16, 23]. The radius increases $\sim$6% (3%) at $\theta = 0$ ($\theta = \pi/2$), while it decreases $\sim$3% around $\theta = \pi/4$ [18]. The positions of nucleons are sampled by $4\pi r^2 \sin(\theta)\rho(r)d\theta d\phi$, where the absolute normalization of $\rho(r)$ is irrelevant. Both projectile and target U nuclei are randomly rotated along the polar and azimuthal directions event by event with probability distribution $\sin\Theta$ and uniform distribution for $\Theta$ and $\Phi$, respectively. The $\sin\Theta$ weight needs to be implemented to simulate unpolarized nucleus-nucleus collisions [18].
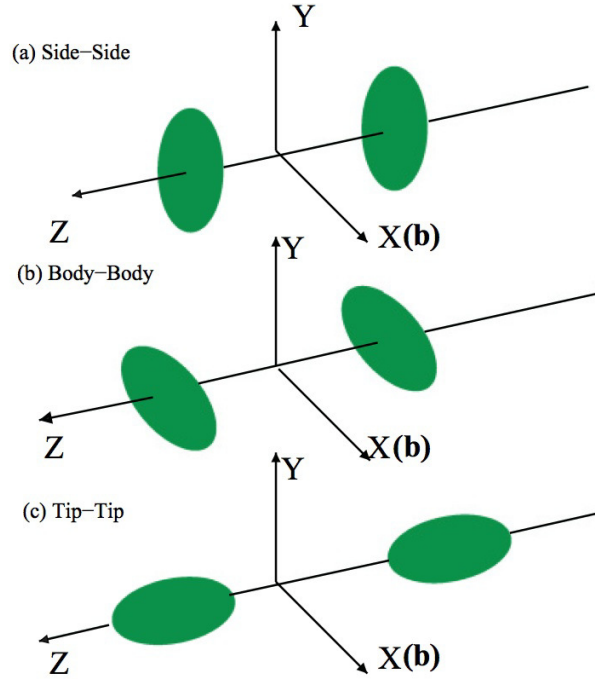


Figure 5.7: Different configurations of U+U collisions studied in the present work. The Z axis is the beam direction. X(b) represents the impact parameter direction along the X axis. For more details refer to the text and Table 5.1

In this work primarily three types of configuration of U+U collisions are studied and compared to U+U collisions without any specific choice of orientation and Au+Au

193

collisions. These specific configurations will be termed as body-to-body, side-on-side, and tip-to-tip in the rest of the paper and are shown in Fig. 5.7. The details in terms of $\theta$ and $\phi$ angles of the orientation of the nuclei for these configurations studied in this paper are given in Table 5.1.

Table 5.1: Details of the angular configuration of U+U collisions used in this study. The subscripts $p$ and $t$ denote the projectile and target, respectively. In the simulations, for the tip-to-tip configuration $\theta$ is varied as $0 \pm 0.07$ rad; for the body-to-body configuration $\theta$ is varied as $\pi/2 \pm 0.005$ rad and $\phi$ as $0 \pm 0.0025$ rad, and for the side-on-side configuration $\theta$ and $\phi$ are varied as $\pi/2 \pm 0.005$ and $\pi/2 \pm 0.17$ rad, respectively.

| Configuration | $\theta_p$ | $\theta_t$ | $\phi_p$ | $\phi_t$ | Impact parameter |
|---|---|---|---|---|---|
| general | 0-$\pi$ | 0-$\pi$ | 0-$2\pi$ | 0-$\pi$ | random |
| tip-to-tip | 0 | 0 | 0-$2\pi$ | 0-$\pi$ | minor axis |
| body-to-body | $\pi/2$ | $\pi/2$ | 0 | 0 | major axis |
| side-on-side | $\pi/2$ | $\pi/2$ | $\pi/2$ | $\pi/2$ | minor axis |

## 5.4.2   Results and Discussion

Figure 5.8 shows the default AMPT model simulated minimum-bias charged particle multiplicity ($N_{ch}$) and charged particle transverse energy ($E_T$) distributions at midrapidity ($|\eta| < 0.5$) in U+U collisions for different configurations for $\sqrt{s_{\mathrm{NN}}} = 200$ GeV. For comparison also shown in Fig. 5.8 are the results from Au+Au (symmetric nuclei) collisions for the same kinematic conditions. The shapes of the distributions are very similar for different configurations of U+U collisions and those from Au+Au collisions. However, the maximum values of $N_{ch}$ and $E_T$ attained for U+U collisions in various configurations is found to be about $15-35\%$ higher than the corresponding values from Au+Au collisions. The tip-to-tip configuration in U+U collisions allows us to attain the maximum $N_{ch}$ and $E_T$ values among the various cases studied. The remaining configurations for U+U seem to give similar values.

Figure 5.9 shows the corresponding results using the string-melting (denoted as SM) version of the AMPT model. The inset of the figure shows the distributions for
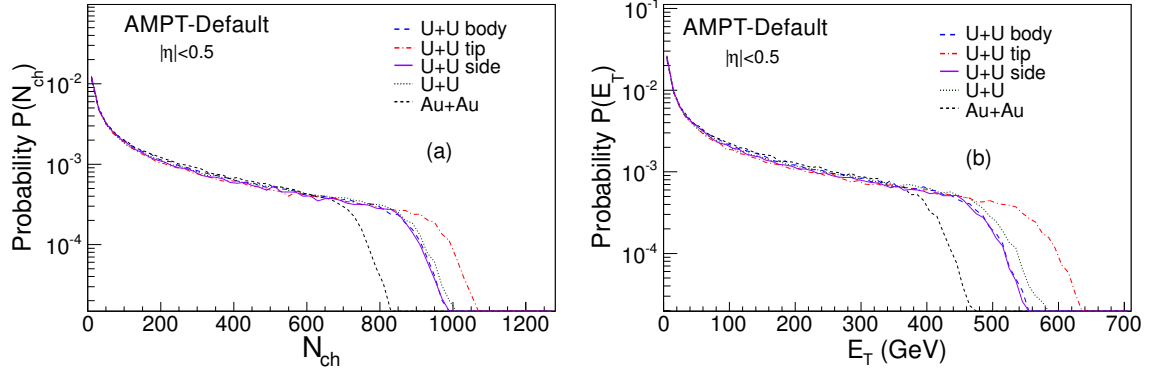
Figure 5.8: Probability distribution of (a) total charged particle multiplicity ($N_{ch}$) and (b) charged particle transverse energy ($E_T$). Both results are at midrapidity ($|\eta| < 0.5$) for minimum bias U+U collisions at $\sqrt{s_{NN}} = 200$ GeV from the default AMPT model. The different colored lines correspond to different configurations of U + U collisions. Also shown for comparison are the results from Au+Au collisions at $\sqrt{s_{NN}} = 200$ GeV from the default AMPT model as short dashed lines.

central collisions on an expanded scale. In general, the charged particle multiplicity
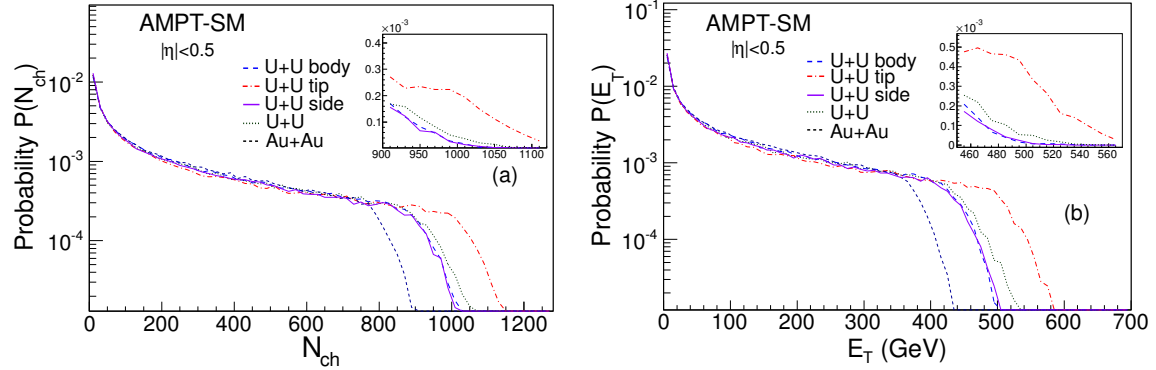


Figure 5.9: Same as Fig. 5.8 for the AMPT string-melting version. The inset shows the distributions for central collisions on an expanded scale.

is about 8% higher compared to the default case. However, the transverse energy of charged particles at midrapidity is about 10% lower for the string-melting case compared to the default version of the AMPT model.

The rest of the trends for different configurations for U+U collisions relative to each other and to the Au+Au collisions are similar in both versions of the model.

Figure 5.10(a) shows $dN_{ch}/d\eta$ for central collisions (impact parameter b < 3.65
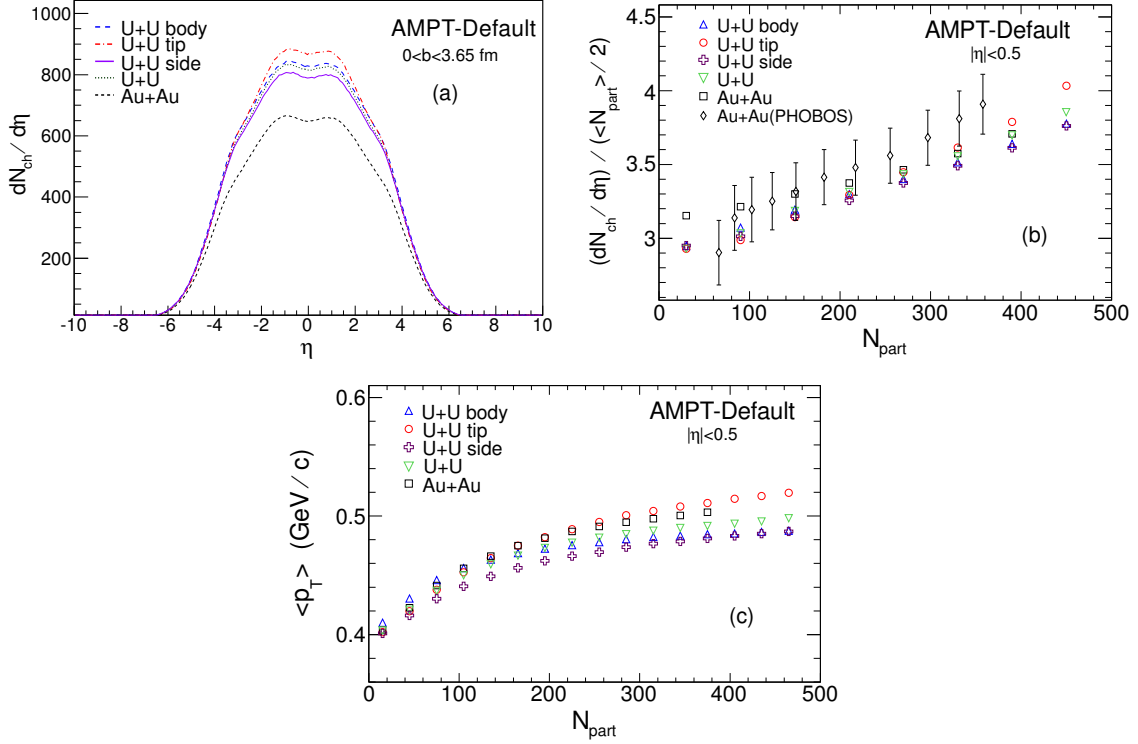
Figure 5.10: Charged particle pseudorapidity ($dN_{ch}/d\eta$) distribution for central collisions (impact parameter = 3.65 fm) as a function of pseudorapidity ($\eta$) for U+U collisions with different configurations of collision and Au+Au collisions at $\sqrt{s_{NN}} = 200$ GeV using the default AMPT model. (b) $dN_{ch}/d\eta$ per participating nucleon ($N_{part}$) pair versus Npart at midrapidity ($|\eta| < 0.5$) for the above cases. Also shown are the experimental results from Au+Au collisions from the PHOBOS experiment at RHIC [32]. (c) Average transverse momentum ($\langle p_T \rangle$) of charged particles as a function of $p_T$ at midrapidity ($|\eta| < 0.5$) for the above collision configurations.

fm) versus $\eta$, Fig. 5.10(b) shows $(dN_{ch}/d\eta)/(N_{part}/2)$ versus $N_{part}$, and Fig. 5.10(c) shows the charged particle average transverse momentum $\langle p_T \rangle$ versus $N_{part}$ for different collision configuration of U+U collisions and Au+Au collisions at $\sqrt{s_{NN}} = 200$ from the default AMPT model, where Npart is the number of participating nucleons. The shapes of the $dN_{ch}/d\eta$ curves are similar for all collision configurations studied and in terms of multiplicity the conclusions are the same as seen in Fig. 5.10(a). $(dN_{ch}/d\eta)/(N_{part}/2)$ at midrapidity ($|\eta| < 0.5$) in U+U collisions extends to higher $N_{part}$ values compared to Au+Au collisions. As expected, it increases with an increase in $N_{part}$. The charged particle multiplicity in most central collisions studied
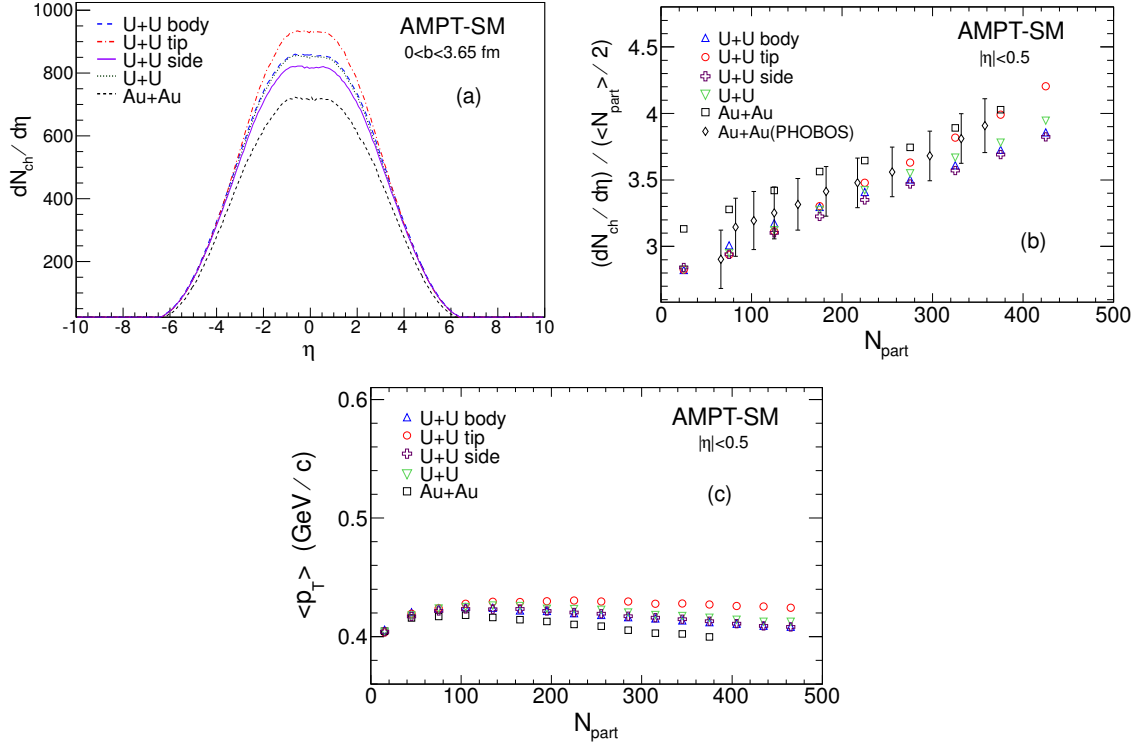
Figure 5.11: Same as Fig. 5.10 for the AMPT string-melting version.

shows a trend of body-to-body and side-on-side values being similar and lower than the values for the tip-to-tip case with $(dN_{ch}/d\eta)/(N_{\text{part}}/2)$ values for the general U+U collisions lying in between. The Au+Au collision values for central collisions are similar to those from the general U+U configuration case for similar $N_{\text{part}}$. The charged particle $\langle p_T \rangle$ at midrapidity increases with an increase in $N_{\text{part}}$. For central collisions, $\langle p_T \rangle$ for the tip-to-tip case is about 30 MeV higher than for the body-to-body case, with the general U+U configuration $\langle p_T \rangle$ values lying in between. The increase in $\langle p_T \rangle$ at midrapidity ($|\eta| < 0.5$) for U+U tip-to-tip collisions relative to Au + Au collisions is small and is about 10 MeV.

Figure 5.11 shows the same results as in Fig. 5.10 using the string-melting version of the AMPT model. The conclusions from $dN_{ch}/d\eta$ are similar to those for the default case, except that the $dN_{ch}/d\eta$ values are higher in the string-melting version. The charged particle $\langle p_T \rangle$ trend with respect to $N_{\text{part}}$ is however different. The $\langle p_T \rangle$ values are lower for the string-melting version compared to the default case and it

saturates or slightly decreases as one goes to central collisions. The saturation of $\langle p_{\mathrm{T}} \rangle$ values for central collisions in the string-melting version could be due to additional partonic interactions and the quark coalescence process in the model relative to that for the default case.
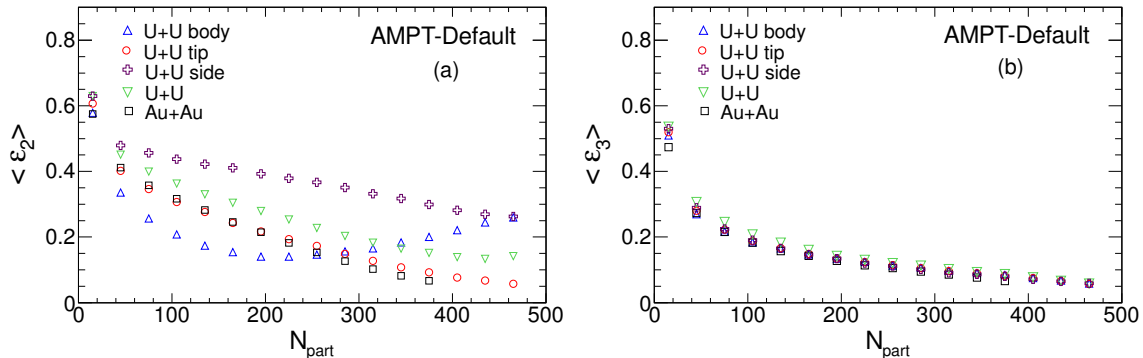


Figure 5.12: (a) Participant eccentricity ($\langle \varepsilon_2 \rangle$) and (b) triangularity ($\langle \varepsilon_3 \rangle$) as a function of number of participating nucleons ($N_{\mathrm{part}}$) for various configurations of U+U collisions and Au+Au collisions at $\sqrt{s_{\mathrm{NN}}} = 200$ GeV from the default AMPT model.

Figure 5.12 shows $\langle \varepsilon_2 \rangle$ and $\langle \varepsilon_3 \rangle$ versus $N_{\mathrm{part}}$ for various configurations of U+U collisions at $\sqrt{s_{\mathrm{NN}}} = 200$ GeV and Au+Au collisions at $\sqrt{s_{\mathrm{NN}}} = 200$ GeV from the default AMPT model. For the same $N_{\mathrm{part}}$ the U+U collisions without any specific selection of collision configuration have higher $\langle \varepsilon_2 \rangle$ compared to Au+Au collisions. For U+U collisions the tip-to-tip configuration has a lower $\langle \varepsilon_2 \rangle$ compared to no specific selection of collision configuration. The side-on-side configuration has the largest values of $\langle \varepsilon_2 \rangle$ for the systems studied. $\langle \varepsilon_2 \rangle$ for the body-to-body configuration shows a specific trend as a function of $N_{\mathrm{part}}$, which is similar to side-on-side and tip-to-tip in most peripheral collisions, then decreases sharply to values below those from tip-to-tip collisions for mid-central collisions, which is followed by an increase in values of $\langle \varepsilon_2 \rangle$ with $N_{\mathrm{part}}$ to reach the same values as side-on-side for the most central collisions. This clearly reflects the specific geometrical configuration traversed by the two uranium nuclei in different cases. $\langle \varepsilon_3 \rangle$ however is found to be similar for all configurations in U+U studied and for Au + Au collisions as a function of $N_{\mathrm{part}}$. Since these are specific to geometrical configurations of the nuclei, we observe no difference in this
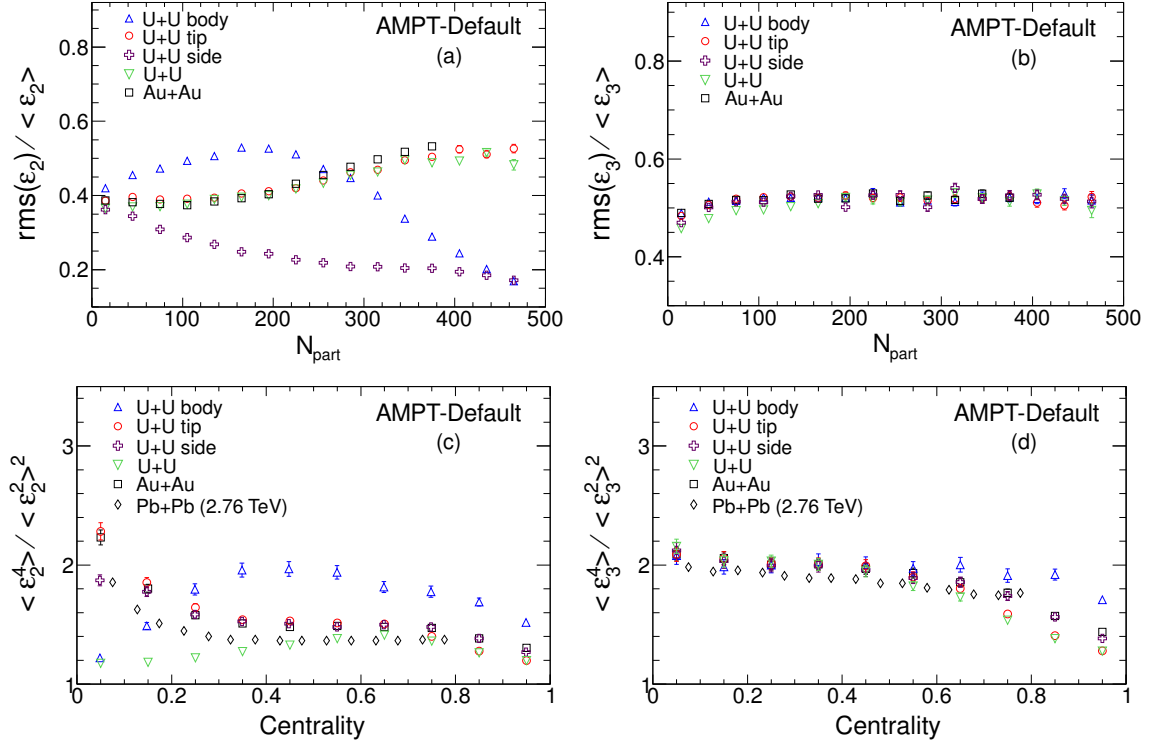
Figure 5.13: (a) Ratio of rms value of $\varepsilon_2$ to $\langle\varepsilon_2\rangle$ and (b) rms of $\varepsilon_3$ to $\langle\varepsilon_3\rangle$ vs $N_{\mathrm{part}}$ for various configurations of U+U collisions and Au+Au collisions at $\sqrt{s_{\mathrm{NN}}} = 200$ GeV using the default AMPT model. (c) and (d) $\langle\varepsilon_n^4\rangle/\langle\varepsilon_n^2\rangle^2$, with n = 2, 3 vs fraction of collision centrality for U+U and Au+Au collisions at $\sqrt{s_{\mathrm{NN}}} = 200$ GeV using the default AMPT model. The Pb+Pb results correspond to Glauber model simulations from Ref. [11] at $\sqrt{s_{\mathrm{NN}}} = 2.76$ TeV.

variable for the string-melting version of the model. Next we study the fluctuation in $\varepsilon_2$ and $\varepsilon_3$ as it has important consequences on understanding the initial conditions in heavy-ion collisions as well as flow fluctuations. The observables used are the ratio of the rms value of $\varepsilon_2$ to $\langle\varepsilon_2\rangle$, the rms of $\varepsilon_3$ to $\langle\varepsilon_3\rangle$, and those suggested in Ref. [11]: $\langle\varepsilon_n^4\rangle/\langle\varepsilon_n^2\rangle^2$ ($n = 2, 3$ in this work). Figures 5.13 (a) and 5.13(b) show the event-by-event fluctuations in $\varepsilon_2$ and $\varepsilon_3$ as a function of $N_{\mathrm{part}}$ for U+U and Au+Au collisions at $\sqrt{s_{\mathrm{NN}}} = 200$ GeV, respectively. The fluctuations in $\varepsilon_2$ for U+U collisions with no specific selection on collision configuration closely follow those for Au+Au collisions; however, for the most central collisions the fluctuations are slightly smaller for U+U collisions. The fluctuations in $\varepsilon_2$ for the tip-to-tip configuration are comparable to

those for Au+Au collisions. The fluctuations in $\varepsilon_2$ for the side-on-side configuration are the smallest among the configurations studied. On the other hand, those for body-to-body U+U collisions reflect a unique trend, with fluctuations in $\varepsilon_2$ being largest in mid-central collisions and then decreasing with increase in centrality to reach the corresponding values of side-on-side for the central-most collisions. Exactly similar trends are observed using the variable $\langle \varepsilon_n^4 \rangle / \langle \varepsilon_n^2 \rangle^2$ as a function of the fraction of collision centrality [Figs. 5.13(c) and 5.13(d)]. In Figs. 5.13(c) and 5.13(d) an x-axis value near 0 means the most-peripheral collisions and a value near 1 means the most-central collisions. The centrality is determined from the impact parameter distribution. The fluctuations in $\varepsilon_3$ are observed to be independent of the collision configuration in U+U and similar to those in Au+Au collisions, except perhaps for the central-most collisions. For comparison, results from a Glauber model simulation for Pb+Pb collisions at $\sqrt{s_{\mathrm{NN}}} = 2.76$ TeV from Ref. [11] are also shown. Our study shows that, if different U+U configurations can be selected in experimental data, it would lead to interesting variations of flow and flow fluctuations as a function of collision centrality, thereby providing a way to understand initial conditions in heavy-ion collisions at high energies. Figures 5.14(a) and 5.14(b) show $\langle v_2 \rangle$ and $\langle v_3 \rangle$ as a function of $N_{\mathrm{part}}$ at midrapidity ($|\eta| < 0.5$) for different configurations of U+U collisions and Au+Au collisions at $\sqrt{s_{\mathrm{NN}}} = 200$ GeV. The characteristic trend of centrality dependence (i.e., smaller values for central collisions and larger values for mid-central collisions) of $\langle v_2 \rangle$ is observed for most of the configurations studied except for U+U body-to-body collisions. In fact, the body-to-body collisions show a minimum $\langle v_2 \rangle$ for mid-central collisions, which is consistent with the variation of $\langle \varepsilon_2 \rangle$ with centrality as shown in Fig. 5.13(a). Figure 5.14(b) shows the corresponding results for $v_3$. $v_3$ is seen to be slightly higher for Au+Au collisions compared to U+U collisions without any choice of configuration. For U+U collisions with various configurations, the largest $v_3$ seems to be from the body-to-body condition, while those for side-on-side are smaller. Also shown in Fig. 5.14(b) are the $\langle v_3 \rangle$ values (close to zero) when calculated using $\Psi_2$ instead of $\Psi_3$. The $\langle v_3 \rangle$ value of zero shows
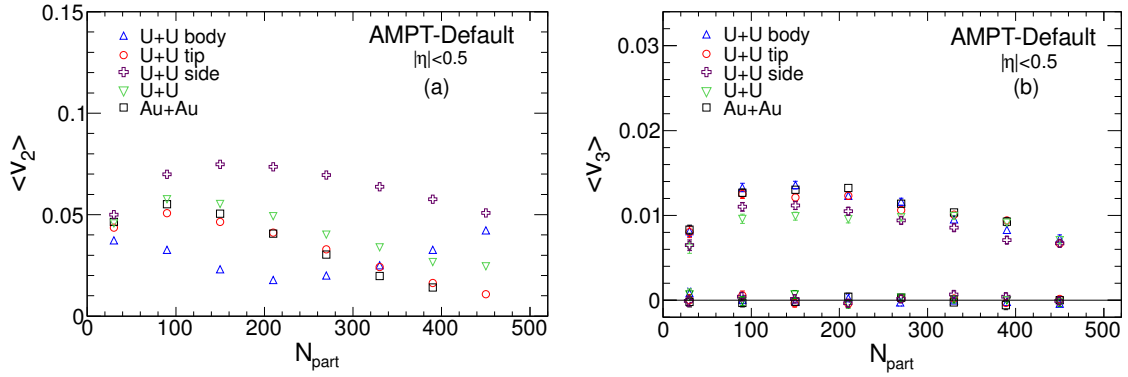
Figure 5.14: (a) Average elliptic flow ($\langle v_2 \rangle$) and (b) triangular flow ($\langle v_3 \rangle$) vs $N_{\mathrm{part}}$ for different collision configurations of U+U and Au+Au collisions at midrapidity for $\sqrt{s_{\mathrm{NN}}} = 200$ GeV from the default AMPT model. In (b), the $\langle v_3 \rangle$ values close to zero are those corresponding to $\langle v_3 \rangle$ calculated using $\Psi_2$.
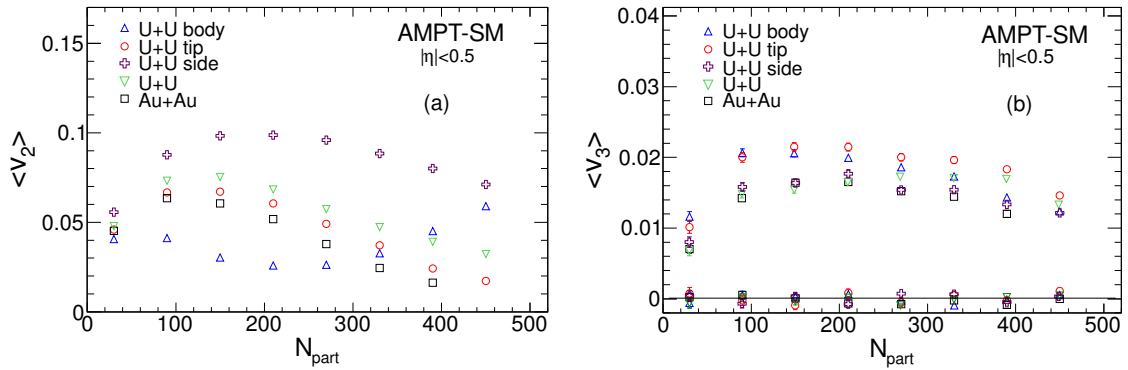


Figure 5.15: Same as Fig. 5.14 for the AMPT string- melting version.

that the minor axis of triangularity is found to be uncorrelated with the reaction plane angle for both U+U and Au+Au collisions. The corresponding results for the string-melting version are shown in Fig. 5.15. The conclusions are the same as for the default case, except that the magnitude of $\langle v_2 \rangle$ and $\langle v_3 \rangle$ are typically 40% and 80% higher, respectively. Also the tip-to-tip configuration has the largest $\langle v_3 \rangle$ values while those from Au+Au collisions have the smallest values.

Figures 5.16 and 5.17 shows the transverse momentum ($p_{\mathrm{T}}$) dependence of $v_2$ and $v_3$ for different collision configuration of U+U and Au+Au collisions at midrapidity ($|\eta| < 0.5$) at $\sqrt{s_{\mathrm{NN}}} = 200$ GeV for $80 < N_{\mathrm{part}} < 120$ and for $160 < N_{\mathrm{part}} < 200$, respectively. The values of $v_2(p_{\mathrm{T}})$ for U+U collisions without any specific collision
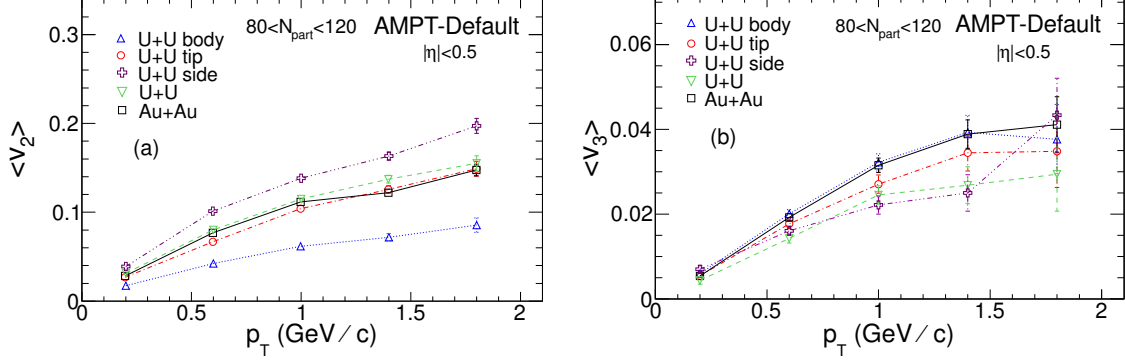
Figure 5.16: (a) Elliptic flow ($v_2$) and (b) triangular flow ($v_3$) as a function of transverse momentum ($p_T$) at midrapidity for $80 < N_{part} < 120$ U+U collisions for different configurations and Au+Au collisions at $\sqrt{s_{NN}} = 200$ GeV from the default AMPT model.
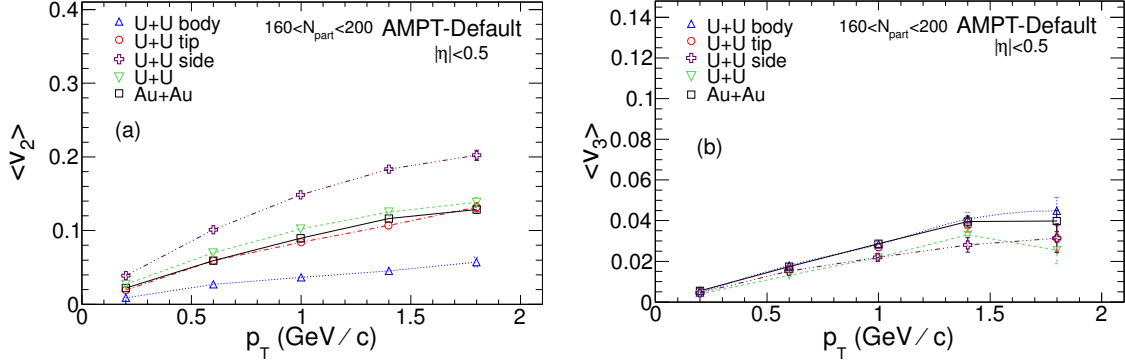


Figure 5.17: Same as Fig. 5.16 for $160 < N_{part} < 200$.

configuration, tip-to-tip and Au+Au collisions have similar values for the $p_T$ range studied. The results for $v_2(p_T)$ from body-to-body U+U collisions are smaller and those for the side-on-side configuration in U+U collisions are higher compared to Au+Au collisions at similar $p_T$ values. Figure 5.16(b) shows the corresponding results for $v_3$. The general trend as observed for $p_T$-integrated $v_3$ [shown in Fig. 5.14(b)] is also followed by $v_3(p_T)$. The $v_3(p_T)$ values for Au+Au and U+U body-to-body configurations seem to be slightly higher compared to those from U+U tip-to-tip and U+U with no specific configuration selected. Figures 5.18 and 5.19 show the corresponding results as given in Figs. 5.16 and 5.17, respectively, for the string-melting version of the AMPT model.
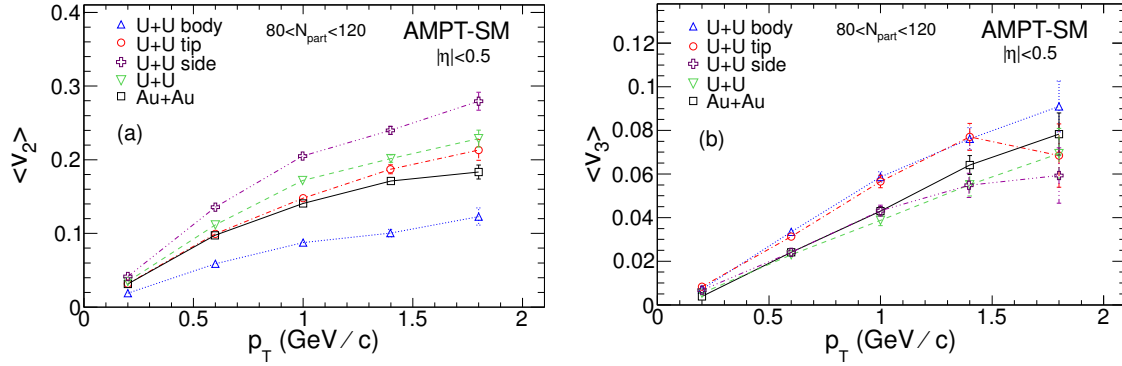
Figure 5.18: Same as Fig. 5.16 for AMPT string-melting version.
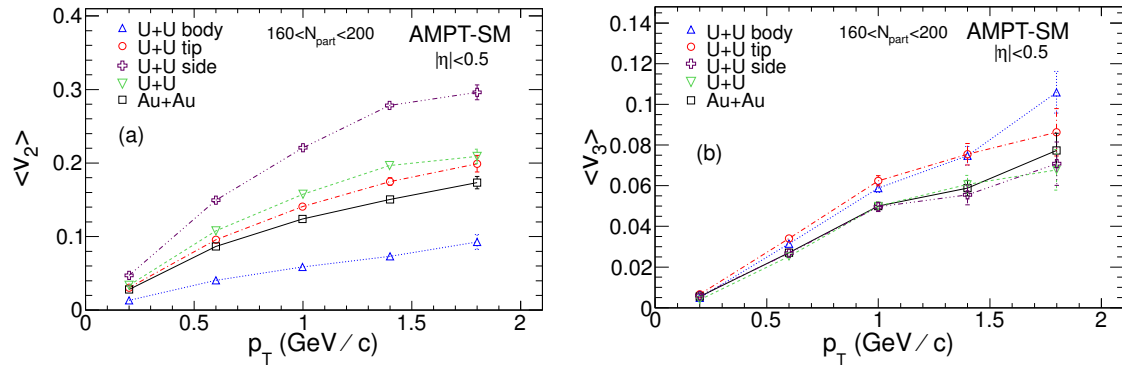


Figure 5.19: Same as Fig. 5.17 for AMPT string-melting version.

The general conclusions are similar, except the magnitudes of the $v_2$ and $v_3$ values are higher for the string-melting case relative to the default case. Furthermore, one notices that the difference in both $v_2(p_T)$ and $v_3(p_T)$ for various collision configuration seems to have increased for the string-melting case compared to the default case. For the several configurations studied the $v_3(p_T)$ values in the default AMPT model for U+U collisions are mostly below the corresponding values from Au+Au collisions, while for the string-melting case the U+U collision $v_3(p_T)$ values are mostly higher than the corresponding values from Au+Au collisions.

## 5.5   Summary

A transport (AMPT) model based study of $\varepsilon_2$, $v_2$, $\varepsilon_3$, $v_3$ and fluctuations in $\varepsilon_2$ and $\varepsilon_3$ for various asymmetric colliding ion species (Ag+Au, Cu+Au, and Si+Au) as well as in various collision configurations of U+U is presented for $\sqrt{s_{\mathrm{NN}}} = 200$ GeV. The results has been presented as a function of the number of participating nucleons ($N_{\mathrm{part}}$), fraction of collision centrality and transverse momentum ($p_{\mathrm{T}}$). The results have been compared to the same observables from symmetric colliding systems of Au+Au (Cu+Cu) collisions.

We found that $\varepsilon_2$ and its fluctuations, for a given number of participating nucleons or fraction of collision centrality, are highly dependent on the colliding ion type (Fig. 5.1). However, those for $\varepsilon_3$ and its fluctuations are very similar for all the colliding species studied (Fig. 5.1). These results are reflected in the experimental observables such as $v_2$ and $v_3$. For the same $\varepsilon_2$ at midrapidity and for midcentral collisions, the proportionality constant between $v_2$ and $\varepsilon_2$ seems to depend on the colliding system size (Fig. 5.5). On the other hand, $v_2$ vs. $p_{\mathrm{T}}$ decreases as the colliding system size decreases for the collision centrality range studied (Fig. 5.6). However no such large sensitivity to colliding ion type on $v_3$, $\varepsilon_3$ and fluctuations in $\varepsilon_3$ are observed from this AMPT model based study. The study thus indicates that asymmetric heavy-ion collisions can be used to constrain models dealing with flow fluctuations in heavy-ion collisions but with greater sensitivity for $v_2$ related observables than for $v_3$.

Azimuthal anisotropy, initial eccentricity and the corresponding fluctuations has also been presented for three specific configurations of U+U collisions for $\sqrt{s_{\mathrm{NN}}} = 200$ GeV. The results from these collisions have been compared to U+U collisions with no specific choice of orientation and Au+Au collisions at the same beam energy. For most of the observables, the results for both default and string-melting configurations of the AMPT model have been presented.

The charged particle multiplicity and charged particle transverse energy is found to be about $15-35\%$ higher for the different U+U configurations relative to Au+Au

collisions (Fig. 5.8, 5.9). For the string-melting version the multiplicities are higher by about 8% for U+U collisions compared to the default model, whereas for the transverse energy they are lower by about 10% compared to the default model. The average transverse momentum for charged particles increases with number of participating nucleons for the default case, whereas they saturate for central collisions in the string-melting version (Fig. 5.10, 5.11). This is perhaps due to additional partonic interactions and the quark coalescence process in the string-melting model relative to the default case. Within the different configurations studied, the multiplicity, transverse energy, and average transverse momentum at midrapidity are largest for the tip-to-tip configuration. This observation may be used in future to select events of particular configuration for U+U collisions.

The average eccentricity and fluctuations in eccentricity show a rich dependence on collision centrality (Fig. 5.12, 5.13). The side-on-side configuration possesses the maximum eccentricity and minimum eccentricity fluctuations as a function of collision centrality among the configurations studied. In contrast, the body-to-body configuration has the minimum eccentricity and maximum eccentricity fluctuations for peripheral and mid-central collisions. The tip-to-tip configuration has minimum eccentricity and maximum eccentricity fluctuations for central collisions. We did not observe large variation in triangularity and its fluctuations for different configurations of U+U collisions studied or between U+U collisions and Au+Au collisions.

The variation of eccentricity and its fluctuation gets reflected in the dependence of $v_2$ and $v_3$ as a function of collision centrality (Fig. 5.14, 5.15). In both the default and string-melting versions of the model, the side-on-side configuration has maximum $v_2$ compared to all other configurations and Au+Au collisions studied for all collision centralities. $v_2$ is smallest for the body-to-body configuration in peripheral and mid-central collisions while it is minimum for the tip-to-tip configuration in central collisions. For peripheral collisions, $v_2$ in U+U can be about 40% larger than in Au+Au, whereas for central collisions, it can be a factor of 2 higher depending on the collision configuration. These features in $v_2$ closely follow the features in $\varepsilon_2$. $v_3$ does

205

not show much dependence on the U+U configuration for the AMPT calculations in the default version; however, in the string-melting version, it seems the body-to-body and tip-to-tip configurations have higher $v_3$ values as a function of collision centrality compared to other cases studied.

The $p_\mathrm{T}$ dependence of $v_2$ is presented for $80 < N_\mathrm{part} < 120$ and $160 < N_\mathrm{part} < 200$. It is observed that the U+U side-on-side configuration has the largest $v_2$ while the U+U body-to-body configuration has the smallest $v_2$ (Fig. 5.16, 5.17). For the other configurations, tip-to-tip, U+U, and Au+Au, the values are similar. A clearer $p_\mathrm{T}$ dependence of $v_3$ is observed in the string-melting case compared to the default case (Fig. 5.18, 5.19). In the string-melting case, $v_3$ values of tip-to-tip and body-to-body configurations are similar and higher than those in U+U, U+U side-on-side, and Au+Au collisions.

# Bibliography

[1] Z. W. Lin and C. M. Ko, Phys. Rev. C 65, 034904 (2002); Z. W. Lin, C. M. Ko, B. A. Li, B. Zhang, and S. Pal, ibid. 72, 064901 (2005).

[2] J.-Y. Ollitrault, Phys. Rev. D 46, 229 (1992).

[3] Paul Sorensen, J. Phys. G 37, 094011 (2010).

[4] B. Alver et. al., (PHOBOS), Phys. Rev. Lett. 98, 242302 (2007).

[5] Z. W. Lin and C. M. Ko, Phys. Rev. C 65, 034904 (2002); Z. W. Lin, C. M. Ko, B. A. Li, B. Zhang, and S. Pal, ibid. 72, 064901 (2005).

[6] B. Alver et. al., (PHOBOS), Phys. Rev. C77, 014906 (2008).

[7] B. Alver and G. Roland, Phys. Rev. C 81, 054905 (2010).

[8] K. Aamodt et. al., (ALICE Collaboration), Phys. Rev. Lett. 107, 032301 (2011).

[9] V. Roy and A. K. Chaudhuri, arXiv:1109.1630 [nucl-th]; B. Schenke, S. Jeon, and C. Gale, Phys. Rev. Lett. 106, 042301 (2011).

[10] J.-Y. Ollitrault, A. M. Poskanzer, and S. A. Voloshin, Phys. Rev. C 80, 014904 (2009); S. A. Voloshin, A. M. Poskanzer, A. Tang, and G. Wang, Phys. Lett. B 659, 537 (2008); L. Yi, F. Wang, and A. Tang, arXiv:1101.4646 [nucl-ex].

[11] R. S. Bhalerao, M. Luzum, and J.-Y. Ollitrault, Phys. Rev. C 84, 054901 (2011).

[12] F. Karsch, Nucl. Phys. A 698, 199 (2002).

[13] S. Bethke, Prog. Part. Nucl. Phys. 58, 351 (2007).

[14] G. Baym, Nucl. Phys. A 698, XXIII (2002).

[15] I. Arsene *et. al.*, (BRAHMS Collaboration), Nucl. Phys. A 757, 1 (2005); B. B. Back *et. al.*, (PHOBOS Collaboration), ibid. 757, 28 (2005); J. Adams *et. al.*, (STAR Collaboration), ibid. 757, 102 (2005); K. Adcox *et. al.*, (PHENIX Collaboration), ibid. 757, 184 (2005).

[16] U. Heniz and A. Kuhlman, Phys. Rev. Lett. 94, 132301 (2005); A. Kuhlman and U. Heniz, Phys. Rev. C 72, 037901 (2005).

[17] T. Hirano, P. Huovinen, and Y. Nara, Phys. Rev. C 83, 021902(R) (2011).

[18] H. Masui, B. Mohanty, and N. Xu, Phys. Lett. B 679, 440 (2009).

[19] S. A. Voloshin, Phys. Rev. Lett. 105, 172301 (2010).

[20] A. Pikin *et. al.*,, JINST 5, C09003 (2010).

[21] BNL program advisory committee recommendations, June 6−8, 2011, `http://www.bnl.gov/npp/docs/pac0611/Overall\%20recommendations\%20final.pdf`.

[22] H. Heiselberg and A. M. Levy, Phys. Rev. C 59, 2716 (1999).

[23] C. Nepali, G. Fai, and D. Keane, Phys. Rev. C 76, 051902(R) (2007); 73, 034911 (2006).

[24] P. Filip, R. Lednicky, H. Masui, and N. Xu, Phys. Rev. C 80, 054903 (2009).

[25] D. Teaney and E. V. Shuryak, Phys. Rev. Lett. 83, 4951 (1999).

[26] P. F. Kolb, J. Sollfrank, and U. W. Heinz, Phys. Rev. C 62, 054909 (2000).

[27] D. Kharzeev, R. D. Pisarski, and M. H. G. Tytgat, Phys. Rev. Lett. 81, 512 (1998).

[28] L. E. Finch, A. Chikanian, R. S. Longacre, J. Sandweiss, and J. H. Thomas, Phys. Rev. C 65, 014908 (2001); S. A. Voloshin, ibid. 62, 044901 (2000).

[29] B. I. Abelev *et. al.*, (STAR Collaboration), Phys. Rev. Lett. 103, 251601 (2009).

[30] K. Hagino, N. W. Lwin, and M. Yamagami, Phys. Rev. C 74, 017310 (2006).

[31] P. Moller, J. R. Nix, W. D. Myers, and W. J. Swiatecki, At. Data Nucl. Data Tables 59, 185 (1995).

[32] X. N. Wang and M. Gyulassy, Phys. Rev. D 44, 3501 (1991). [20] B. Alver *et. al.*, (PHOBOS Collaboration), Phys. Rev. C 83, 024913 (2011).

## 5.6   Appendix

### 5.6.1   Input Parameters of AMPT Model

$200 \rightarrow$ EFRM ($\sqrt{s_{NN}}$ in GeV if FRAME is CMS).

CMS $\rightarrow$ FRAME.

A $\rightarrow$ Projectile.

A $\rightarrow$ Target.

$238 \rightarrow$ IAP (projectile A number).

$92 \rightarrow$ IZP (projectile Z number).

$238 \rightarrow$ IAT (target A number).

$92 \rightarrow$ IZT (target Z number).

$10000 \rightarrow$ NEVNT (total number of events).

$0. \rightarrow$ BMIN (mininum impact parameter in fm).

$18. \rightarrow$ BMAX (maximum impact parameter in fm).

$4 \rightarrow$ ISOFT (D=1): select Default AMPT or String Melting (4).

$150 \rightarrow$ NTMAX: number of timesteps (D=150).

$0.2 \rightarrow$ DT: timestep in fm (hadron cascade time = DT*NTMAX) (D=0.2).

$2.2 \rightarrow$ PARJ(41): parameter a in Lund symmetric splitting function.

$0.5 \rightarrow$ PARJ(42): parameter b in Lund symmetric splitting function.

$1 \rightarrow$ (D=1, yes; 0, no) flag for popcorn mechanism (netbaryon stopping).

$1.0 \rightarrow$ PARJ(5) to control BMBbar vs BBbar in popcorn (D=1.0).

$1 \rightarrow$ shadowing flag (Default=1, yes; 0, no).

$0 \rightarrow$ quenching flag (D=0, no; 1, yes).

$2.0 \rightarrow$ quenching parameter -dE/dx (GeV/fm) in case quenching flag=1.

$2.0 \rightarrow$ p0 cutoff in HIJING for minijet productions (D=2.0).

$1.76717d0 \rightarrow$ parton screening mass in fm$^{-1}$ (D=3.2264d0).

$0 \rightarrow$ IZPC: (D=0 forward-angle parton scatterings; 100,isotropic).

$0.471404d0 \rightarrow$ alpha in parton cascade.

1d6 → dpcoal in GeV.

1d6 → drcoal in fm.

11 → ihjsed: take HIJING seed from below (D=0) or at runtime(11).

53153511→ random seed for HIJING.

8 → random seed for parton cascade.

0 → flag for K0s weak decays (D=0, no; 1, yes).

0 → flag for phi decays at end of hadron cascade (D=1, yes; 0, no).

1 → flag for pi0 decays at end of hadron cascade (D=0, no; 1, yes).

0 → optional OSCAR output (D=0, no; 1, yes; 2 & 3, more parton info).

0 → flag for perturbative deuteron calculation (D=0,no; 1or2,yes).

1 → integer factor for perturbative deuterons ($\geq 1$ & $\leq 10000$).

1 → choice of cross section assumptions for deuteron reactions.

-7. → Pt in GeV: generate events with $\geq 1$ minijet above this value.

1000 → maxmiss (D=1000): maximum # of tries to repeat a HIJING event.

3 → flag to turn off initial and final state radiation (D=3).

1 → flag to turn off Kt kick (D=1).

0 → flag to turn on quark pair embedding (D=0, no; 1, yes).

7., 0. → Initial Px and Py values (GeV) of the embedded quark (u or d).

0., 0. → Initial x & y values (fm) of the embedded back-to-back q/qbar.

1, 5., 0. → nsembd (D=0), psembd (in GeV),tmaxembd (in radian).

0 → Flag to enable users to modify shadowing (D=0, no; 1, yes).

1.d0 → Factor used to modify nuclear shadowing.

0 → Flag for random orientation of reaction plane (D=0, no; 1, yes).

# Chapter 6

# Anisotropic Flow of Charged Particles in Hydrodynamic Model

The systematic study on inclusive charged hadron $v_n$ ($n$ = 2, 3, 4, 5), and there correlation with the corresponding eccentricities ($\varepsilon_n$) were studied using a hydrodynamic model (AZHYDRO-KOLKATA [1]). The effect of smoothening of Glauber Monte Carlo initial conditions on elliptic and triangular flow were estimated. Moreover, $N_{ch}$, $\langle v_n \rangle$ and their correlation with initial $\langle \varepsilon_n \rangle$ were studied for different centralities of Au + Au collusions at $\sqrt{s_{\mathrm{NN}}}$ = 200 GeV using the event-by-event hydrodynamic calculations. Experimental data on $\varepsilon_n$, $dN_{ch}/d\eta$ and $v_n$ for Au+Au collision at $\sqrt{s_{\mathrm{NN}}}$ = 200 GeV are compared to the hydrodynamic model calculations.

## 6.1 Flow Measurement Method in Hydrodynamic Model

A simple fluid, in an arbitrary state, is fully specified by primary variables: particle current ($N_\mu$), energy-momentum tensor ($T^{\mu\nu}$) and entropy current ($S$) and a number of additional (unknown) variables [1]. In relativistic fluid dynamics, one defines

a time-like hydrodynamic 4-velocity, $u^\mu$ (normalized as $u^2 = 1$). One also define a projector, $\Delta^{\mu\nu} = g^{\mu\nu} - u^\mu u^\nu$, orthogonal to the 4-velocity ($\Delta^{\mu\nu} u_\nu = 0$). In equilibrium, an unique 4-velocity ($u^\mu$) exists from which the particle density ($n$), energy density ($\epsilon$) and the entropy density ($s$) can be obtained [1]. With proper (continuous) initial energy density, space-time evolution of ideal fluid, in each event, is obtained by solving the energy-momentum conservation equations,

$$\partial T^{\mu\nu} = 0, \tag{6.1}$$

$$\text{where,} \quad T^{\mu\nu} = (\epsilon + p)u^\mu u^\nu - pg^{\mu\nu}, \tag{6.2}$$

and $p$ is pressure. Heavy ion collisions are best described in $(\tau, x, y, \eta)$ coordinates, where $\tau = \sqrt{t^2 - z^2}$ is the longitudinal proper time and $\eta = \frac{1}{2}\log\frac{t+z}{t-z}$ is the space-time rapidity. Hydrodynamics equations are closed with an equation of state (EoS) $p = p(\epsilon)$. Currently, there is consensus that the confinement-deconfinement transition is a crossover for QCD matter high temperature and zero chemical potential. The crossover or the pseudocritical temperature for the quark−hadron transition is $T_c \approx 170$ MeV [10, 11, 12, 13, 14]. In this study, we have used an equation of state where the Wuppertal−Budapest [10, 12] lattice simulations for the deconfined phase are smoothly joined at $T = T_c = 174$ MeV, with hadronic resonance gas EoS comprising all of the resonances below mass $m_{res} = 2.5$ GeV. Details of the EoS can be found in Ref. [14].

In addition to the initial energy density for which we used the Monte Carlo Glauber model, solution of hydrodynamic equations requires one to specify the thermalization or the initial time $\tau_i$ and fluid velocity $[v_x(x, y), v_y(x, y)]$ at the initial time. A freeze-out prescription is also needed to convert the information about fluid energy density and velocity to invariant particle distribution. We assume that the fluid is thermalized at $\tau_i = 0.6$ fm and the initial fluid velocity is zero, $v_x(x, y) = v_y(x, y) = 0$. Freeze-out mechanism for granular initial condition is sometimes very delicate (for example, presence of multivalued hypersurface). Holopainen and Huovinen in Ref. [18]

studied the freeze-out mechanism for granular initial conditions. Two types of freeze-out critera were used: (i) dynamical freeze-out, which compares the hydrodynamical expansion rate with the pion scattering rate and (ii) constant temperature freeze-out. It was concluded that the effect of different freeze-out criterion on $p_\text{T}$ spectra and elliptic flow are quite small. Presently, we assume the fluid freeze-out at temperature $T_F = 130$ MeV. We use Cooper-Frye formalism to obtain the invariant particle distribution of $\pi^-$ from the freeze-out surface [22]. Resonance production is included. Considering that pions constitute $\sim 20\%$ of all the charged particles, $\pi^-$ invariant distribution is multiplied by the factor $2 \times 1.2$ to approximate the charged particles invariant distribution. From the invariant distribution, harmonic flow coefficients are obtained as [23],

$$v_n(y, p_\text{T}) e^{in\Psi_n(y, p_\text{T})} = \frac{\int d\phi \, e^{in\phi} \frac{dN}{dy p_\text{T} dp_\text{T} d\phi}}{\frac{dN}{dy p_\text{T} dp_\text{T}}}, \tag{6.3}$$

$$v_n(y) e^{in\Psi_n(y)} = \frac{\int p_\text{T} dp_\text{T} d\phi \, e^{in\phi} \frac{dN}{dy p_\text{T} dp_\text{T} d\phi}}{\frac{dN}{dy}}, \tag{6.4}$$

where, $v_n$ is the flow coefficient, $p_\text{T}$ is the transverse momentum and $\phi$ is the azimuthal angle of the produced particles. In a boost-invariant version of hydrodynamics, flow coefficients are rapidity independent. The hydrodynamic simulations are suitable only for central rapidity, $y \approx 0$, where boost invariance is most justified. $\Psi_n$ in Eqs. 6.3 and 6.4 is the participant plane angle for the $n^{th}$ flow harmonic. We characterize the asymmetry of the initial collision zone in terms of various moments of the eccentricity [19, 20, 21],

$$\varepsilon_n e^{in\Psi_n} = \frac{\iint \epsilon(x, y) r^n e^{in\phi} dx dy}{\iint \epsilon(x, y) r^n dx dy}, \quad n = 2, 3, 4, 5.. \tag{6.5}$$

where $x = r\cos\phi$ and $y = r\sin\phi$. Asymmetry measures $\varepsilon_2$ and $\varepsilon_3$ are called eccentricity and triangularity. $\varepsilon_4$ and $\varepsilon_5$ essentially measure the squareness and five sidedness of the initial distribution. In the following subsections, $\varepsilon_4$ will be called rectangularity. In the same vein, $\varepsilon_5$ will be called pentangularity. We also refer

fourth flow coefficient $v_4$ as the rectangular flow and $v_5$ as the pentangular flow for the following subsections.

## 6.2 Fluctuating Initial Conditions and Smoothening Effect on Elliptic and Triangular Flow

In heavy-ion collisions, momentum space anisotropy is best studied by decomposing it in a Fourier series,

$$\frac{dN}{d\phi} = \frac{N}{2\pi}[1 + 2\sum_n v_n cos(n\phi - n\Psi_n)] \qquad (6.6)$$

where $\phi$ is the azimuthal angle of the produced particle and $\Psi_n$ is the plane of the symmetry of initial collision zone. For smooth initial matter distribution, plane of symmetry of the collision zone coincides with the reaction plane (the plane containing the impact parameter and the beam axis), i.e., $\Psi_n \equiv \Psi_{RP}$, $\forall\ n$. The odd Fourier coefficients are zero by symmetry. However, fluctuations in the positions of the participating nucleons can lead to nonsmooth density distribution, which will fluctuate on event-by-event basis. The participating nucleons then determine the symmetry plane ($\Psi_{PP}$), which fluctuate around the reaction plane [2]. As a result odd harmonics, which were exactly zero for smoothed initial distribution, can be developed (see more discussion in Chapter 4). It has been conjectured that third hadronic $v_3$, which is response of the initial triangularity of the medium, is responsible for the observed structures in two particle correlation in Au+Au collisions [3, 4, 5, 6, 7, 8]. The ridge structure in p+$\overline{\text{p}}$ collisions also has a natural explanation if odd harmonic flow develops. Recently, the ALICE collaboration has observed odd harmonic flows in Pb+Pb collisions [9]. In most central collisions, the elliptic flow ($v_2$) and triangular flow ($v_3$) are of similar magnitude. In peripheral collisions however, elliptic flow dominates.

In a hydrodynamic model, collective flow is a response of the spatial asymmetry of the initial state. For example, elliptic flow is the response of ellipticity of the initial medium, triangular flow is the response of the initial triangularity of the medium and so on. In theoretical simulations, one generally uses Monte Carlo Glauber model to obtain the event-by-event initial conditions. In a Monte Carlo Glauber model, according to the density distribution of the colliding nuclei, two nucleons are randomly chosen. If the transverse separation between them is below a certain distance, they are assumed to interact. Transverse position of the participating nucleons is then known in each event and will fluctuate from event to event. If a particular event has $N_{\mathrm{part}}$ participants, participants positions in the transverse plane can be labeled as, $(x_1, y_1)$, $(x_1, y_1)$. . . $(x_{N_{\mathrm{part}}}, y_{N_{\mathrm{part}}})$. The energy density in the transverse plane can be approximated as,

$$\epsilon(x, y) \propto \sum_{i=1}^{N_{\mathrm{part}}} \delta(x - x_i, y - y_i). \tag{6.7}$$

However, fluid dynamical model require continuous density distribution and discrete distribution as in Eq. 6.7 cannot be evolved. To use in a hydrodynamic model, the discrete density distribution has to be converted into a smooth energy-density distribution. This can be done by smearing the discrete participant positions by some smoothening function, $\delta(x - x_i, y - y_i) \rightarrow g(x - x_i, y - y_i, .., \zeta_1, \zeta_2, ...)$, where $\zeta_i$ are the parameters of the smoothening function $g$. Incidentally, even though smoothening of the nucleon positions is a must if one uses Monte Carlo Glauber model, existing literature in general do not elaborate on the procedure. However, if the flow coefficients are to be used for diagnostic purpose, e.g., to constrain the viscosity over entropy ratio, it is important to know the effect of smoothening. In this work, we have studied the effect of smoothening of Monte Carlo Glauber model initial condition on the elliptic and triangular flow. It will be shown that the flow coefficients depend minimally on the smoothening function. We write the smoothed energy density in the transverse

plane as,

$$\epsilon(x, y) = \epsilon_o \sum_{i=1}^{N_{\text{part}}} g(x - x_i, y - y_i, \zeta_1, \zeta_2, ...), \qquad (6.8)$$

where $g(x - x_i, y - y_i, \zeta_1, \zeta_2, ...)$ is the smoothening function and $\zeta_i$ 's are the parameters of the smoothening function. $\epsilon_0$ is a parameter, which is fixed in such a way that the event averaged particle multiplicity reproduces the experimental value. In this work we considered two smoothening functions: (i) a Woods-Saxon distribution and (ii) a Gaussian distribution. The Woods-Saxon smoothening function is defined as,

$$g_{\text{WS}}(x - x_i, \ y - y_i, \ C, \ a) \propto \frac{1}{1 + \exp\left(\frac{\sqrt{(x-x_i)^2+(y-y_i)^2}-C}{a}\right)}. \qquad (6.9)$$

The half radius $C$ in Eq. 6.9 is kept fixed at $C = 1$ fm. Only the diffuseness parameter $a$ is varied to obtain different smoothening. In this study, we considered four different values, $a = 0.05, 0.1, 0.25,$ and $0.5$ fm. The effect of smoothening on the energy density distribution can be seen in Fig. 6.1. In panel (a), the transverse distribution of participating nucleons, in b = 7 fm Au+Au collisions, for a typical Monte Carlo event is shown. The discrete positions of the participants are smoothed with a Woods-Saxon distribution. In panels (b)−(d), the smoothed energy density distribution, for diffuseness parameter $a = 0.1, 0.25,$ and $0.5$ fm are shown. One notes that structures in the density profiles are diffused as the diffuseness increase. In the following, we study the effect of smoothening on elliptic and triangular flow. To show the dependence on the functional form, we have also smoothed the participant nucleons positions with a Gaussian function,

$$g_{\text{gauss}}(x - x_i, \ y - y_i, \ \sigma) \propto \exp[-\frac{(x - x_i)^2 + (y - y_i)^2}{2\sigma^2}]. \qquad (6.10)$$

Two values of the Gaussian width, $\sigma = 0.1$ and $0.5$ fm are considered. In the following sections, we will refer to the diffuseness parameter ($a$) of the Woods-Saxon function and the width ($\sigma$) of the Gaussian function as the smoothening parameter
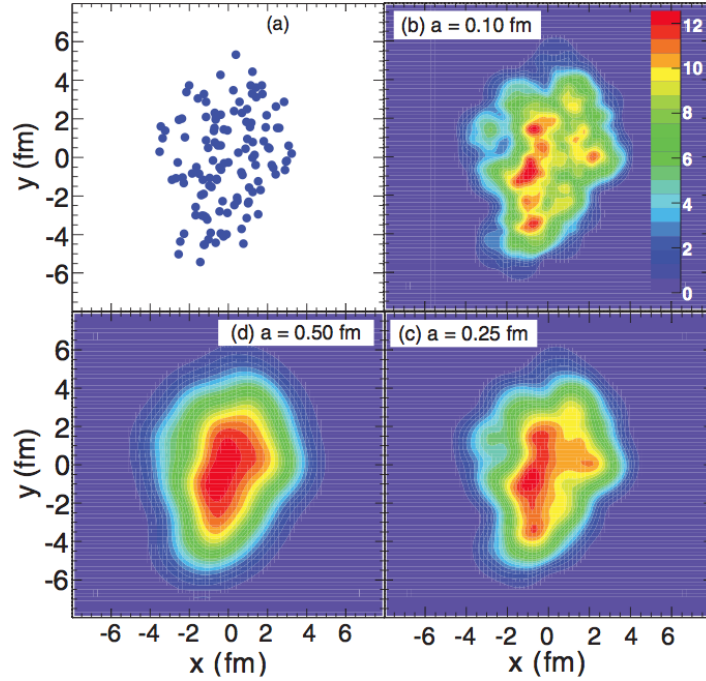
Figure 6.1: (a) discrete positions of participating nucleons in the transverse plane in a typical event from Monte Carlo Glauber model, in b = 7 fm Au + Au collision. (b)−(d) density distribution obtained by smoothening the discrete position by Woods-Saxon function, with diffuseness parameter, $a = 0.1, 0.25,$ and 0.5 fm. C = 1 fm for all panels.

($s$). With fluctuating initial conditions, in each event, space-time evolution of the fluid is obtained by solving the Eq. 6.1 using the code AZHYDRO-KOLKATA [1]. From the invariant distribution, harmonic flow coefficients are obtained from Eq. 6.3 and 6.4 and initial eccentricities are calculated using Eq. 6.5.

Results of hydrodynamic simulations for N = 100 Monte Carlo Glauber model events for 30−35% central collisions in Au+Au at $\sqrt{s_{NN}} = 200$ GeV are shown in Fig. 6.2, Fig. 6.3 and Fig. 6.4. The filled/open symbols are event averaged values and the bars represent the variance. The open symbols are obtained with smoothening with the Woods-Saxon function, the filled symbols are obtained with the Gaussian function. The top panel of Fig. 6.2 shows that the parameter $\epsilon_0$ in Eq. 6.8 is fixed in such a way that the average charged particle multiplicity dN/dy $\approx$ 210, irrespective of the smoothening function and the smoothening parameter. In the middle panel of Fig. 6.2, dependence of the integrated elliptic flow on the smoothening function and
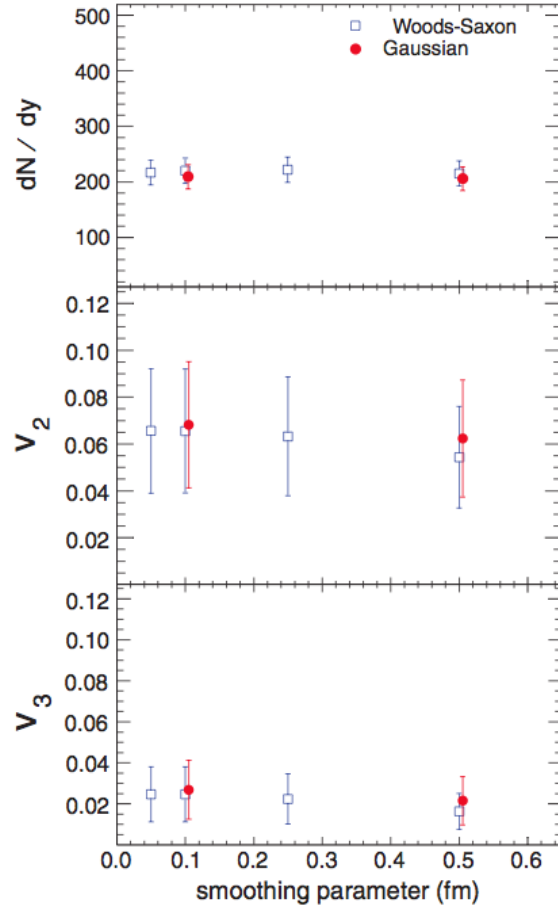
Figure 6.2: Charged particles multiplicity (top), integrated elliptic flow (middle), and integrated triangular flow (bottom), as a function of smoothening parameter ($s$). The open and solid symbols are for Woods-Saxon and Gaussian smoothening functions, respectively. Error bars corresponds to the RMS width of the corresponding observable.

smoothening parameter is shown. Both for Gaussian and Woods-Saxon smoothening function, elliptic flow do not show any dependence on the smoothening parameter. Note that for the Woods-Saxon function, the smoothening parameter is varied by a factor of 10 and for the Gaussian function, by a factor of 5. Even though the smoothening parameter is changed a factor of $5-10$, event averaged $v_2$ and their variances remain approximately unchanged. More interestingly, smoothening with Gaussian or Woods-Saxon function, both produces approximately same $v_2$. The bottom panel of Fig. 6.2 shows model result for the triangular flow ($v_3$). As it was observed for the elliptic flow, integrated triangular flow also does not show any dependence on

the functional form of the smoothening function or on the smoothening parameter. Both for Gaussian function and Woods-Saxon function, approximately similar value is obtained for the triangular flow. Event averaged triangular flow also show marginal dependence on the smoothening parameter. In event-by-event hydrodynamics, with Monte Carlo Glauber model initial conditions, the elliptic and triangular flow seems
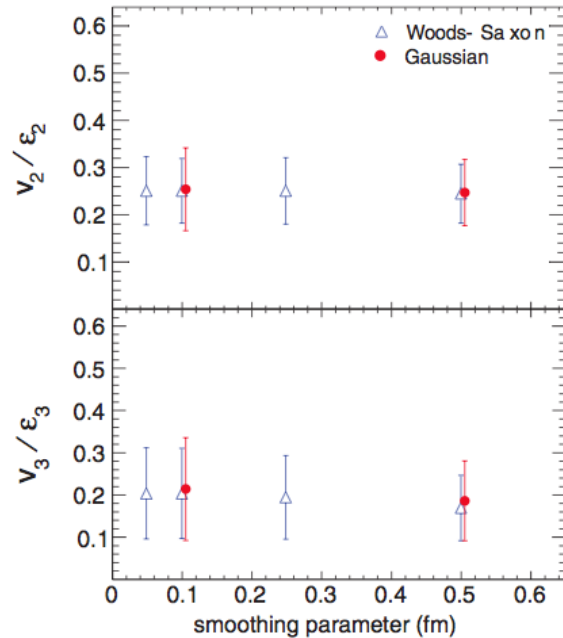


Figure 6.3: Top panel: integrated elliptic flow scaled by initial eccentricity as a function of smoothening parameter ($s$). The open and solid symbols are for Woods-Saxon and Gaussian smoothening functions, respectively. Bottom panel: same for the initial triangularity scaled integrated triangular flow. Error bars corresponds to the RMS width of the corresponding observable.

to be independent of the smoothening function as well as of the smoothening parameter. In ideal hydrodynamics, anisotropic flow is expected to scale with initial asymmetry of the collision, quantified in terms of initial eccentricity and initial triangularity, etc. In this study, we did not study the scaling behavior of flow coefficient. Rather, we have measured the effect of smoothening on the scaled observables, the initial eccentricity scaled elliptic flow ($v_2/\varepsilon_2$) and initial triangularity scaled triangular flow ($v_3/\varepsilon_3$). The simulation results are shown in Fig. 6.3. As it was for the elliptic and triangular flow, initial eccentricity scaled elliptic flow as well as initial

triangularity scaled triangular flow also remain unaltered for Gaussian and Woods-Saxon smoothening functions. It also shows little dependence on the smoothening parameter.
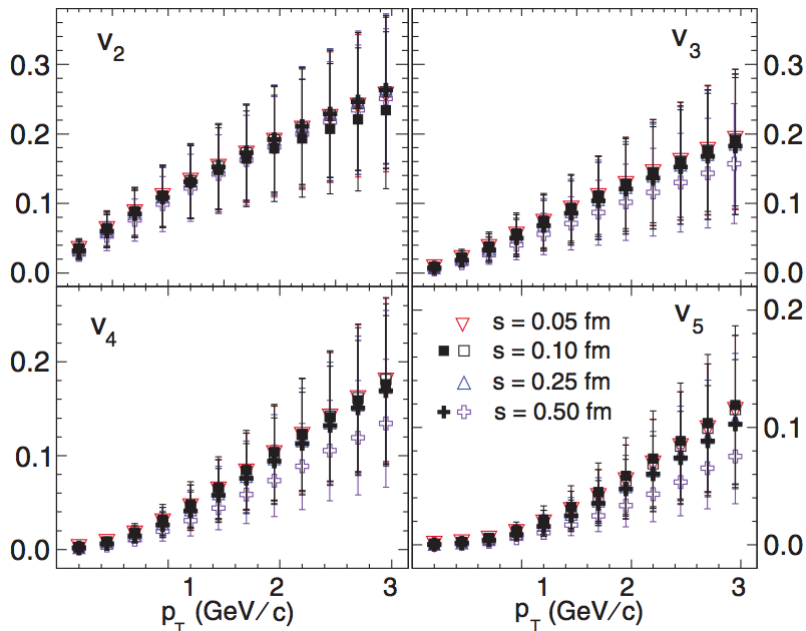


Figure 6.4: Top panel: dependence of differential elliptic (left) and differential triangular (right) flow, on the smoothening parameter ($s$) is shown. The open and filled symbols are, respectively, for Woods-Saxon and Gaussian smoothening functions. The bottom panels show the dependence of differential $v_4$ (left) and $v_5$ (right). Error bars corresponds to the RMS width of the corresponding observable.

In the top two panels of Fig. 6.4, effect of smoothening on the differential elliptic and triangular flow is shown. As before, the open/filled symbols are for Woods-Saxon/Gaussian smoothening functions. As it was for the integrated $v_2$, differential $v_2$ also depend marginally on the smoothening function or on the smoothening parameter. For Gaussian smoothening function, event averaged $v_2$ ( $p_T \approx 1.5$ GeV) changes by $\sim 3\%$ for a factor of 5 change in the smoothening parameter, from 0.1 to 0.5. The change is even less for the Woods-Saxon function. Indeed, within the uncertainties, the differential $v_2$ is approximately independent of the smoothening function and of smoothening parameter. The differential triangular flow is also remains approximately independent of the smoothening function and smoothening parameter.

However, absolute change is marginally more. For example, for Gaussian smoothening function, event averaged $v_3$ ($p_T \approx 1.5$ GeV) is reduced by $\sim 10\%$ for a factor of 5 increase in the smoothening parameter. The change is even less ($\sim 7\%$) for a factor of 10 change in the smoothening parameter of the Woods-Saxon function. In [17], effect of smoothening on $v_2$, $v_3$, $v_4$, and $v_5$ were studied. A Gaussian smoothening function was used. It was shown that smoothening effect is not strong on $v_2$ and $v_3$ which is also concluded in this study. However, smoothening has considerable influence on higher flow coefficients $v_4$ and $v_5$. $v_4$ and $v_5$ reduces with increased smoothening. We also obtain similar results. In the bottom two panels of Fig. 6.4, smoothening effect on higher flow coefficients $v_4(p_T)$ and $v_5(p_T)$ is shown. Compared to $v_2$ and $v_3$, smoothening effect is more in higher harmonics. For example, at $p_T \approx 2$ GeV, for Woods-Saxon smoothening function, for a factor of 10 increase in the smoothening parameter, mean values of higher harmonics $v_4(p_T)$ and $v_5(p_T)$ reduces by $\sim 28\%$ and $\sim 39\%$, respectively. Mean values of $v_2$ and $v_3$ on the other hand reduces by $\sim 4\%$ and $\sim 20\%$, respectively.

## 6.3   Event-by-event Hydrodynamical Simulations for Au + Au Collisions at $\sqrt{s_{NN}} = 200$ GeV and Correlation Between Flow Coefficients and Initial Spacial Anisotropy

Experimentally observed finite, nonzero $v_2$ is regarded as definite proof of QCD matter with collectivity created in Au+Au collisions. Qualitatively, elliptic flow is naturally explained in a hydrodynamical model in which, rescattering of secondaries generates pressure and drives the subsequent collective motion. In non-central collisions, the reaction zone is asymmetric (almond shaped). The pressure gradient is large in one direction and small in the other. The asymmetric pressure gradient generates the

222

elliptic flow. As the fluid evolves and expands, asymmetry in the reaction zone decreases and a stage arises when the reaction zone become symmetric and the system no longer generates elliptic flow. Elliptic flow is early time phenomena. It is a sensitive probe to, (i) degree of thermalization, (ii) transport coefficient, and (iii) equation of state of the early stage of the fluid.

Ideal and viscous hydrodynamic models have been extensively used to analyze the experimental data at RHIC and LHC energy collisions. Most of the analyses were performed with smooth initial matter distribution obtained from geometric overlap of density distributions of the colliding nuclei. For smooth matter distribution, the plane of symmetry of the collision zone coincides with the reaction plane ($\Psi_{RP}$). The odd Fourier coefficients are zero by symmetry. As, mentioned before, one of the important realization in recent years, is that the participating nucleons, rather than the reaction plane, determines the symmetry plane of the initial collision zone [2]. The realization is the results of analysis of various experimental data, e.g., the two-particle correlation in the $\Delta\Phi$ plane [24, 25, 26]. Importance of the higher order flow harmonics in explaining the peculiar structures in two-body correlation was argued by Sorensen [23]. The ridge structure in collisions [27, 28] also has a natural explanation if odd harmonic flows develop. In recent years, there is much interest in event-by-event hydrodynamics and several authors have simulated Au+Au and Pb+Pb collisions at RHIC/LHC, in event-by-event hydrodynamics [15, 32, 33, 34, 35, 36, 37, 38, 39, 40, 41, 42, 43]. In this work we have simulated $\sqrt{s_{NN}} = 200$ GeV Au + Au collisions in $0-10\%$, $10-20\%$, $20-30\%$, $30-40\%$ and $40-50\%$ collision centralities using event-by-event hydrodynamics with Monte Carlo Glauber model initial energy density distribution. Details of the Monte Carlo Glauber model can be found in [44]. In each collision centrality, we have simulated $N_{event} = 1000$ events for Au+Au collisions at $\sqrt{s_{NN}}$ = 200 GeV. The constant $\epsilon_0$ in Eq. 6.7 is fixed in such a way so that experimental charged particles multiplicity in $0-10\%$ collision is reproduced. It was then kept fixed for all the other collision centralities. Simulation results have been compared with the existing experimental data on charged particle multiplicity, transverse momen-

tum spectra, and integrated and differential elliptic flow. The centrality dependence of the correlation between the (integrated) flow coefficients with the initial spatial anisotropy is also studied.
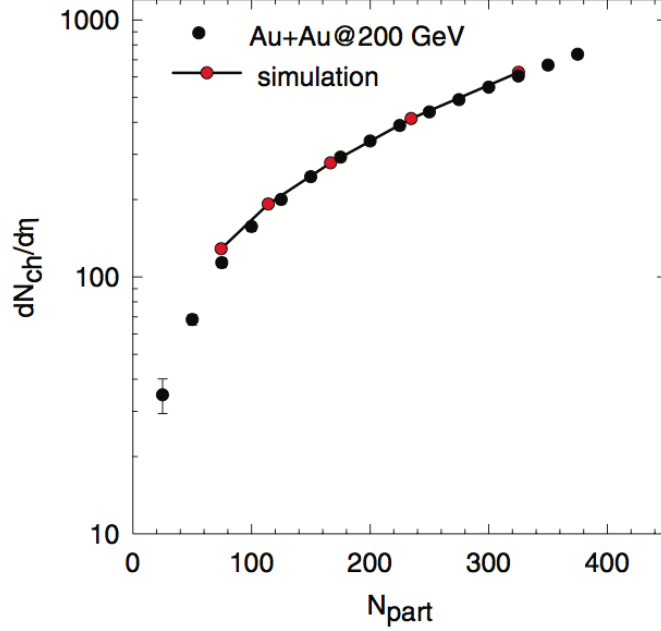


Figure 6.5: The black circles are the PHENIX data for the centrality dependence of charged particle multiplicity in $\sqrt{s_{NN}} = 200$ GeV Au + Au collisions. The red symbols are the multiplicity in simulated events. The lines are to guide the eye.

In Fig. 6.5, simulated charged particle multiplicities are compared with the PHENIX data [46]. The model parameters, namely, initial entropy density $S_{in}$, initial time $\tau_i$, freeze-out temperature $T_f$ and width ($\sigma$) of Gaussian distribution function used for

Table 6.1: The initial parameters for the hydrodynamic model.

| Parameters | $S_{in}$ (fm$^{-3}$) | $\tau_i$ (fm/c) | $T_f$ (MeV) | $\sigma$ (fm) |
|---|---|---|---|---|
| Values | 110 | 0.6 | 130 | 0.5 |

smoothening are listed in Table 6.1. Once the model parameters are fixed to reproduce experimental multiplicity in $0-10\%$ collision, event-by-event simulations well reproduces the experimental multiplicity in other collision centralities. We observed

that in peripheral collisions, simulated multiplicity overestimate the experimental multiplicity by $\sim 10-15\%$.
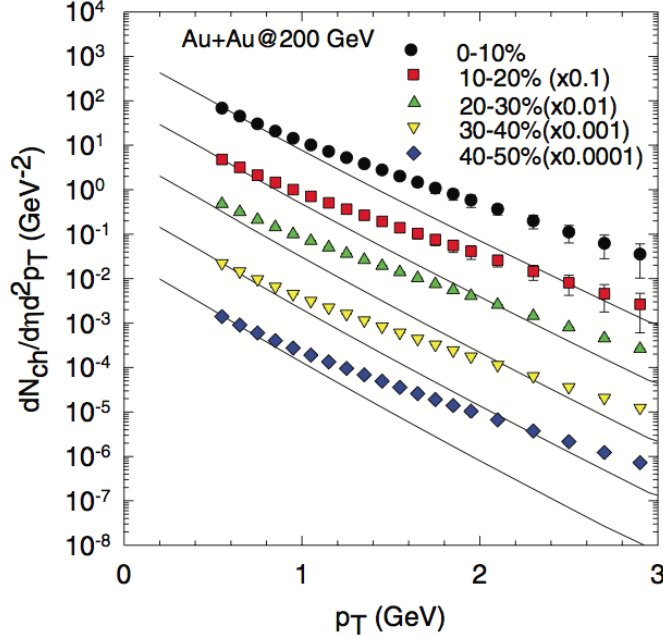


Figure 6.6: The colored symbols are PHENIX measurements for the charged particle transverse momentum spectra in $0\%-10\%$ to $40\%-50\%$ Au + Au collisions. The solid lines are the event-by-event hydrodynamic simulations for the spectra.

Even though charged particle multiplicities are well reproduced, the model simulations failed to reproduce charged particles $p_T$ spectra in the high $p_T$ region. In Fig. 6.6, model simulations for charged particles $p_T$ spectra, in $0-10\%$, $10-20\%$, $20-30\%$, $30-40\%$, and $40-50\%$ collision centralities are compared with the PHENIX measurements [47]. Simulated spectra explain the experimental data only up to $p_T \approx$ 1 GeV. In all the collision centralities, at higher $p_T$, the model produces fewer particles than in experiment. The results are interesting. It is well known that, compared to smooth hydrodynamics, in event-by-event hydrodynamics, $p_T$ spectrum is hardened [15]. Still the hardening is not enough to produce a requisite number of particles at large $p_T$. It is also well known that $p_T$ spectra are hardened in viscous fluid. A better fit to charged particles, $p_T$ spectra at large $p_T$ are expected if viscous rather than ideal fluid is formed in the collisions. We do note that in the present simulations,

we have not made any conscientious attempt to fit the $p_T$ spectra. Only the charged particle multiplicity in $0-10\%$ collision was fitted. Varying other parameters, e.g., initial time, initial fluid velocity, freeze-out temperature etc., fit to charged particle $p_T$ spectra may be improved.
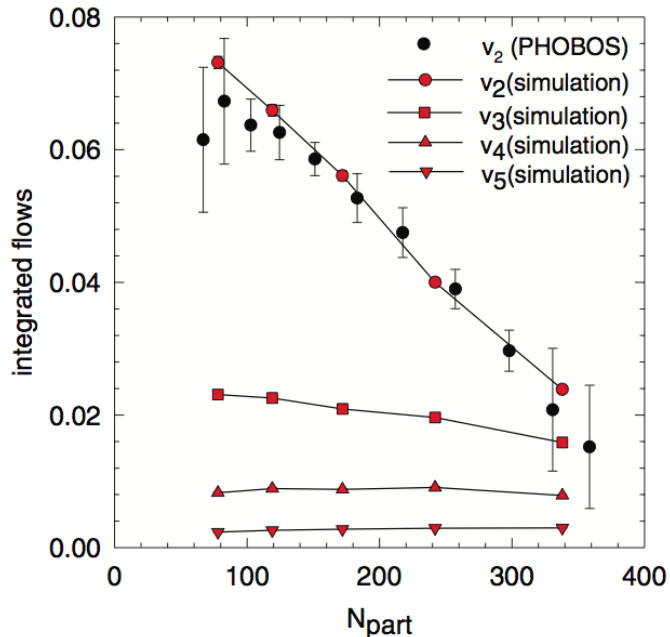


Figure 6.7: The colored symbols are PHENIX measurements for the charged particle transverse momentum spectra in $0-10\%$ to $40-50\%$ Au + Au collisions. The solid lines are the event-by-event hydrodynamic simulations for the spectra.

Integrated flows are one of the important observables in heavy ion collisions. As discussed earlier, initial spatial symmetry is converted into momentum asymmetry, which is quantified in terms of different flow coefficients. For example, elliptic flow ($v_2$) is a response of an initial eccentricity ($\varepsilon_2$) of the collision zone. Triangular flow ($v_3$) is a response of initial triangularity ($\varepsilon_3$) of the medium. Similarly, higher flow coefficients $v_4$ and $v_5$ are a response of initial rectangularity ($\varepsilon_4$) and pentangularity ($\varepsilon_5$) of the initial medium. In Fig. 6.7, the black circles are PHOBOS measurements [48] for centrality dependence of elliptic flow ($v_2$). $v_2$ increases rapidly as the collisions become more and more peripheral. Present simulations for $v_2$ in event-by-event hydrodynamics are shown as red circles. The simulation results agree well with the

experimental data. In Fig. 6.7, simulation results for (integrated) $v_3$, $v_4$ and $v_5$ are also shown. Triangular flow also increases as the collisions become more and more peripheral. However, the rate of increase is much slower than that for elliptic flow. $v_4$ and $v_5$ on the other hand appear to be approximately independent of the collision centrality. From central $0-10\%$ to peripheral $40-50\%$ collisions, they change by less than a few percent. In smooth hydrodynamics, elliptic flow in Au + Au collisions was investigated in detail. Approximately, elliptic flow is proportional to initial eccentricity $\varepsilon_2$.

The dependence of the event averaged flow coefficients ($\langle v_n \rangle$, $n = 2-5$) on the asymmetry measures ($\langle \varepsilon_n \rangle$) in event-by-event hydrodynamics is shown in Fig. 6.8. The symbols, from left to right, correspond to $0-10\%$, $10-20\%$, $20-30\%$, $30-40\%$, and $40-50\%$ Au+Au collisions. As expected, asymmetry measures increase with collision centralities. The increase is most in $\varepsilon_2$, by a factor of $\sim 3.5$ from $0-10\%$ collision centrality to $40-50\%$ centrality. In other asymmetry measures, $\varepsilon_n$, n = 3-5, the increase is more modest, a factor of $\sim 2-2.5$ only. As it is in smoothed hydrodynamics, in event-by-event hydrodynamics also, elliptic flow increase, approximately linearly, with the initial eccentricity, $\langle v_2 \rangle \propto \langle \varepsilon_2 \rangle$. Higher flow coefficients, $v_3$, also increase with initial triangularity, however, the increase evidently is not linear. Still higher flow coefficients, $v_4$ and $v_5$, approximately remain the same in all the collision centralities (as already shown in Fig. 6.7), and they appear to be independent of the asymmetry measures, $\varepsilon_4$ ($\varepsilon_5$). Approximate centrality independence of higher flow coefficients, $v_4$ and $v_5$, in event-by-event hydrodynamics indicate that unlike the elliptic or triangular flow, rectangular flow $v_4$ or pentangular flow $v_5$ may not be related to an initial asymmetry measure of the collision zone. Later, we will discuss the issue in more detail.

Differential flow coefficients are very sensitive observables and a model is well tested by comparing its predictions against experimental differential flow data. In Fig. 6.9, in five panels (a)−(e), event-by-event hydrodynamic simulations for the differential flow coefficients, in $0-10\%$, $10-20\%$, $20-30\%$, $30-40\%$, and $40-50\%$
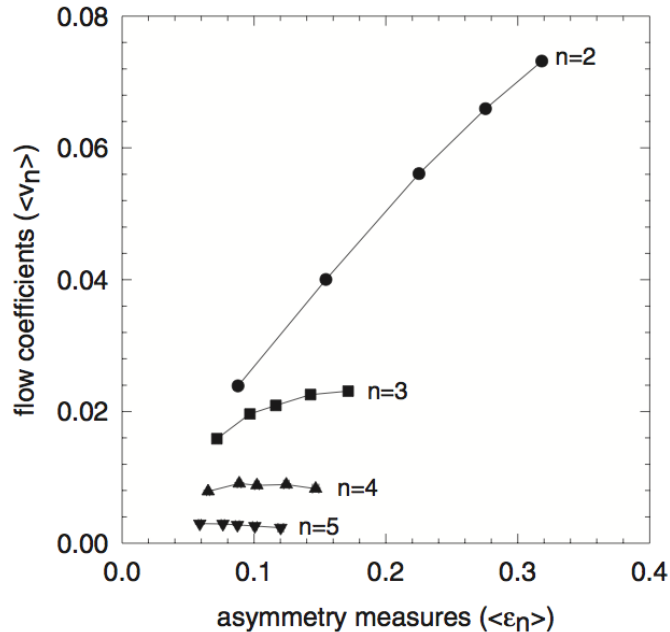
Figure 6.8: Event averaged flow coefficients ($\langle v_n \rangle$) against the asymmetry measures, ($\langle \varepsilon_n \rangle$) for n = 2−5.

Au+Au collisions are shown. In each panel, the black, red, green, and yellow lines are the simulation results for elliptic flow, triangular flow, rectangular flow, and pentangular flow, respectively. We have shown only the event averaged values. In each collision centrality, PHENIX measurements [29, 30, 31] for the elliptic, triangular, and rectangular flow are shown as the black circles, red squares, and green triangles. Simulations do reproduce the trend of the data, $v_2 > v_3 > v_4$, Event-by-event hydrodynamic simulations for the differential elliptic flow in Au+Au collisions agree well with the PHENIX data in all the collision centralities. In peripheral collisions, at $p_T > 2$ GeV, experimental data are marginally overpredicted. We have simulated Au+Au collisions in the ideal fluid approximation. If instead of ideal fluid, viscous fluid is produced, better agreement with data is expected. Indeed, explicit event-by-event hydrodynamic simulations [16, 49, 50] do indicate that the event averaged flow coefficients reduce with viscosity. In any case the agreement with data for elliptic flow measurements is much better for event-by-event ideal hydrodynamics compared to ideal hydrodynamic calculations with smooth CGC/Glauber model initial condi-
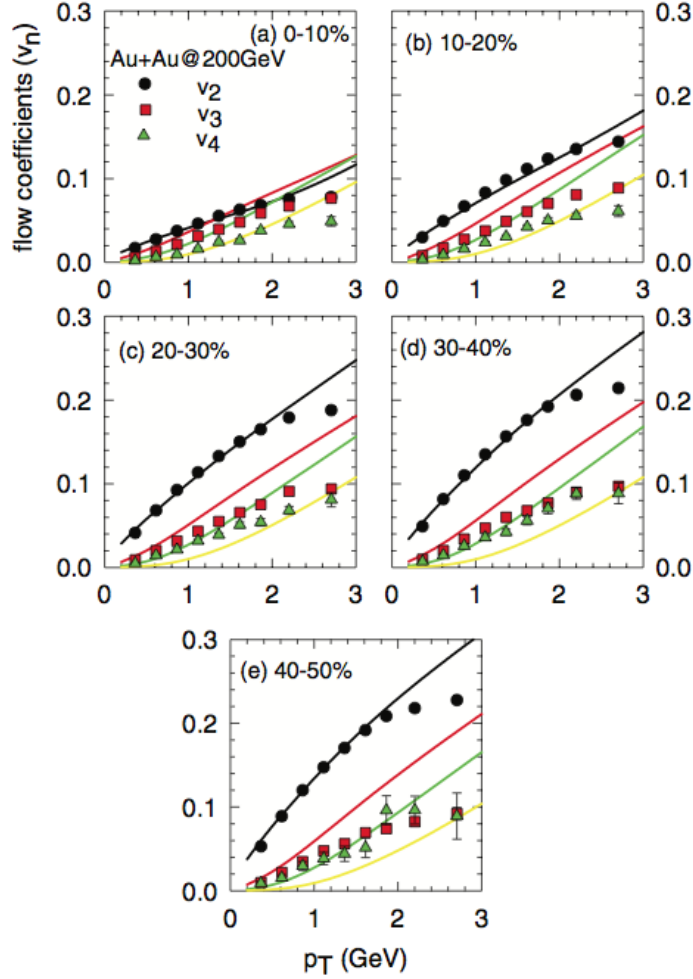
Figure 6.9: (color online) Event-by-event simulations for flow coefficients $v_n$, n = 2−5 in Au + Au collisions are shown. The black, red, green, and yellow lines are, respectively, for elliptic flow $v_2$, triangular flow $v_3$, rectangular flow $v_4$, and pentangular flow $v_5$. The solid circles, squares, and triangles are PHENIX measurements for elliptic, triangular, and rectangular flow in Au+Au collisions at RHIC.

tions [51, 52]. Even though simulation results for elliptic flow reasonably well agree with the PHENIX experiment, simulation results for triangular ($v_3$) and rectangular flow ($v_4$) appear to overpredict the PHENIX data for the same. Interestingly, triangular flow is more overpredicted than the rectangular flow. In addition, the discrepancy between simulations and experiment is more in peripheral collisions than in central collisions. For example, in 0−10% collision, simulated $v_3$, in the $p_T$ range 1-2 GeV, overpredict the PHENIX data by ∼30%. In 30−40% collision, the data are

overpredicted by $\sim 60\%$ or more. In $30-40\%$ collisions, rectangular flow, in the $p_T$ range 1-2 GeV, is overpredicted by $5-10\%$ only. Here again, better agreement with data is expected if instead of ideal fluid, viscous fluid is formed in Au+Au collisions.

We did not find any experimental data for the pentangular flow to compare with model results shown in Fig. 6.9. Following the trend of the simulation results for higher harmonic $v_3$, $v_4$, which are overpredicted in simulations, we do expect that the present simulation also overpredicts $v_5$. Present simulations then suggest that in experiments, in a peripheral $40-50\%$ Au + Au collisions, in the $p_T$ range 1-2 GeV,
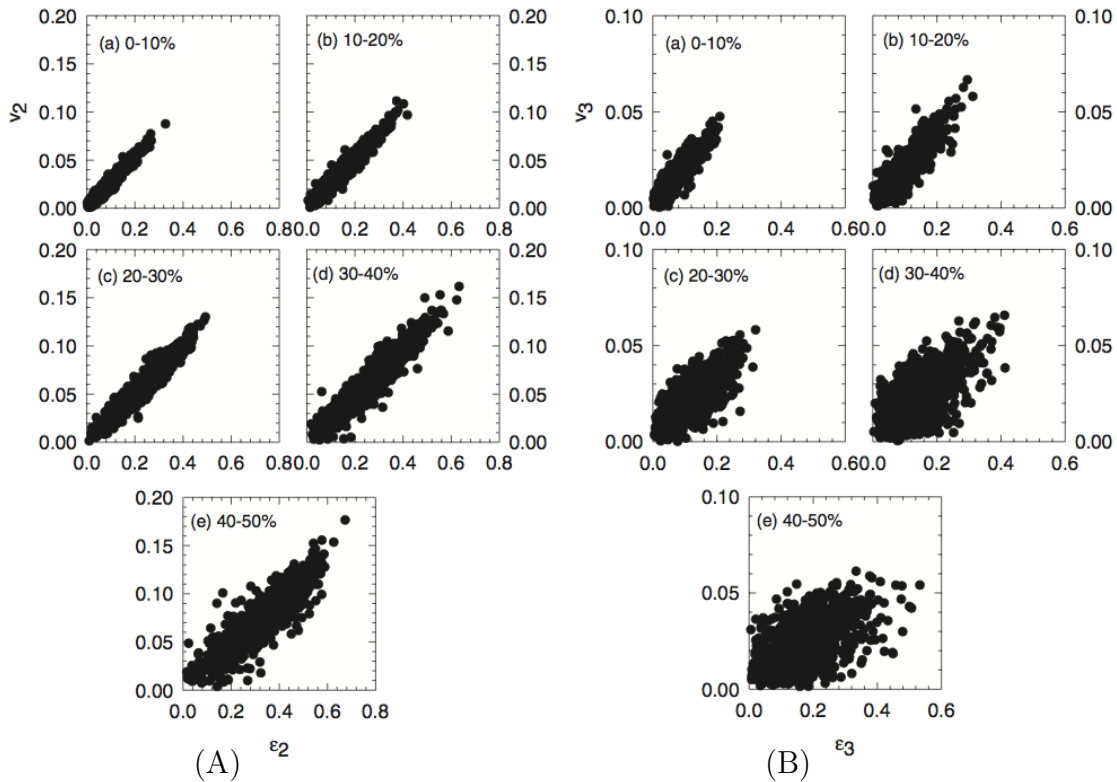


Figure 6.10: Correlation between (A) elliptic flow ($v_2$) and initial eccentricity ($\varepsilon_2$), (B) triangular flow ($v_3$) and initial triangularity ($\varepsilon_3$). Simulation results are for $N_{\text{event}} = 1000$ events. For a perfect correlation all the points should lie on a straight line.

$\sim 2-5\%$ or less pentangular flow may be expected. Recently, in [53, 54], correlation between integrated flow coefficients ($v_n$) and initial asymmetry measures ($\varepsilon_n$) of the collision zone was studied in event-by-event hydrodynamics. It was shown that while elliptic flow remains strongly correlated with initial eccentricity, correlations between

the higher flow coefficients $v_n$ and initial asymmetry measures $\varepsilon_n$, $n = 3, 4, 5$, are much more weak. In [53, 54] correlations between flow coefficients and asymmetry measures, in a single collision centrality, were studied. Correlation between the flow coefficients and asymmetry measures in event-by-event hydrodynamic have been studied also in several other publications [15, 38, 42, 43, 55]. Similar results are obtained, i.e., higher order flow coefficients show less correlation with the corresponding asymmetry
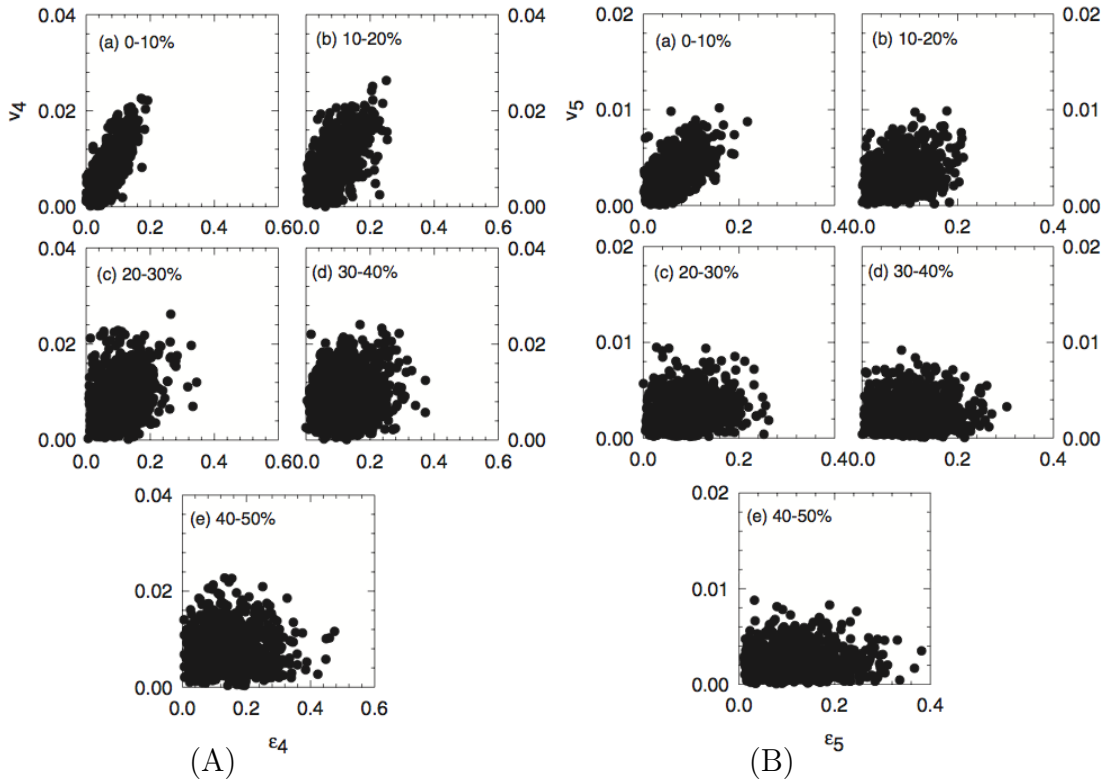


Figure 6.11: Correlation of (A) $v_4$ with $\varepsilon_4$ and (B) $v_5$ with $\varepsilon_5$. Simulation results are for $N_{\text{event}} = 1000$ events. For a perfect correlation all the points should lie on a straight line.

measures. In Fig. 6.10, we have plotted the simulated elliptic flow ($v_2$) against the initial eccentricity ($\varepsilon_2$) and triangular flow ($v_3$) against the initial triangularity ($\varepsilon_3$) for $N_{\text{event}} = 1000$ events. If $v_2$ ($v_3$) is perfectly correlated with $\varepsilon_2$ ($\varepsilon_3$) , all the points should lie on a straight line. One observes that in central collisions, elliptic flow is strongly correlated with eccentricity. The correlation is marginally reduced in more peripheral collisions. One can conclude that in event-by-event hydrodynamics also,

the correlation between elliptic flow and initial eccentricity is strong, irrespective of the collision centrality. In central collisions, correlation between triangular flow ($v_3$) and initial triangularity ($\varepsilon_3$) is strong, though degree of correlation appears to be less than that in elliptic flow. In more peripheral collisions, however, correlation between $v_3$ and $\varepsilon_3$ is significantly reduced. Figure 6.11 shows the correlations of $v_4$ and $v_5$ with $\varepsilon_4$ and $\varepsilon_5$ respectively. Correlation between higher flow harmonics, $v_4$ ($v_5$) and initial asymmetry measure $\varepsilon_4$ ($\varepsilon_5$) even in central collisions is visibly much weaker than the corresponding correlation between elliptic flow and initial eccentricity. The correlations deteriorate as the collisions become more and more peripheral. Indeed, from the scatter plot of $v_4$ and $v_5$ in peripheral collisions, it is difficult to claim that the flow coefficients are correlated with the asymmetry measures. In [53] a quantitative measure was defined to quantify the correlation between flow coefficients and initial spatial asymmetry measure. A modified form is used here to quantify the correlation.

For a perfect correlation, $v_n \propto \varepsilon_n$ and simulated flow coefficients will fall on a straight line. Dispersion of the flow coefficients around the best fitted straight line then gives a measure of the correlation. We thus define a correlation measure function,

$$C_{\text{measure}}(v_n) = 1 - \frac{\sum_i [v_n^i(\varepsilon_n) - v_{n,\text{st.line}}(\varepsilon_n)]^2}{\sum_i [v_{\text{random}}^i(\varepsilon_n) - v_{n,\text{st.line}}(\varepsilon_n)]^2}. \qquad (6.11)$$

$C_{\text{measure}}$ essentially measures the dispersion of the simulated flow coefficients from the best fitted straight line, relative to completely random flow coefficients. It varies between 0 and 1. If flow coefficients are perfectly correlated then $v_n \propto \varepsilon_n$ and $C_{\text{measure}}$ is identically unity. For completely random flow coefficients, $C_{\text{measure}} = 0$. To obtain an even ground for comparison of $C_{\text{measure}}$ for different flow coefficients, the flow coefficients ($v_n$) and the asymmetry parameters ($\varepsilon_n$) are scaled to vary between 0 and 1. Figure 6.12 shows the correlation measures for the flow coefficients as a function of collision centrality. The elliptic flow remains strongly correlated with initial eccentricity [$C_{\text{measure}}(v_2) \approx 0.95$-$0.99$] in $0-10\%$ to $40-50\%$ collisions. In central, $0-10\%$, $10-20\%$ collisions, triangular flow ($v_3$) is also strongly correlated with initial triangularity ($\varepsilon_3$), [$C_{\text{measure}}(v_3) \approx 0.95$]. Correlation is significantly reduced in

232
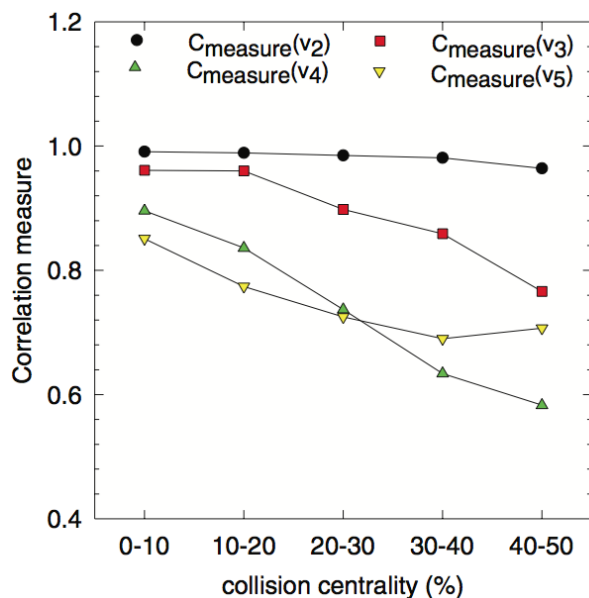
Figure 6.12: Collision centrality dependence of the correlation measure (see text) for $v_2$, $v_3$, $v_4$, and $v_5$.

more peripheral collisions and in $40-50\%$ collisions, $[C_{\mathrm{measure}}(v_3) \approx 0.75]$. In higher flow coefficients, correlation is even less in peripheral collisions. If departure of $C_{\mathrm{measure}}$ from unity is interpreted as a measure of flow uncorrelated with the initial asymmetry measure, for elliptic flow $v_2$, in $0-10\%$ to $40-50\%$ collisions, less than $\sim 5\%$ of the flow is uncorrelated with initial eccentricity. In higher flow coefficients, $v_n$, $n = 3$-$5$, uncorrelated flow grow with collision centrality. For example, in rectangular flow $v_4$, uncorrelated flow grows from $\sim 10\%$ in $0-10\%$ collisions to $\sim 40\%$ in $40-50\%$ collision. As was discussed previously, present analysis of Au + Au data also indicate that a better description of the data will be obtained if viscous fluid rather than ideal fluid is formed in the Au + Au collision. In [53] viscous effects on the correlation between elliptic flow and initial eccentricity and between triangular flow and initial triangularity were studied. It was shown that the correlations reduce significantly in viscous fluid. In more realistic event-by-event hydrodynamic simulation of Au+Au collisions, with viscous fluid, correlation between higher flow coefficients and asymmetry measures then expected to reduce even more than obtained presently. Comparatively low $C_{\mathrm{measure}}$ or equivalently, decorrelation of higher

flow harmonics could be understood as due to nonlinear mixing of modes [42]. For example, Gardim et al. [42] showed that to correctly predict $v_4$ and $v_5$, one must take into account nonlinear terms proportional $\varepsilon_2^2$ and $\varepsilon_2\varepsilon_3$, respectively.

## 6.4  Summary

The effect smoothening on elliptic and triangular flow is presented using event-by-event hydrodynamics. In each event, participating nucleons position from Monte Carlo Glauber model calculations are smoothed with either a Gaussian function or a Woods-Saxon function. Smoothening is controlled by a smoothening parameter, e.g., diffuseness for Woods-Saxon function and width for the Gaussian function. It was shown that integrated as well as differential elliptic and triangular flows remain largely unaltered, irrespective of functional form of the smoothening function, or the smoothening parameter. Higher harmonics $v_4$ and $v_5$ on the other hand are influenced by the smoothening effect.

Using the same event-by-event hydrodynamics simulations, the centrality dependence of charged particle multiplicity, $p_\mathrm{T}$ spectra, and flow coefficients (integrated and differential) are also presented for Au + Au collisions at $\sqrt{s_\mathrm{NN}} = 200$ GeV. The initial energy density distributions are obtained from the Monte Carlo Glauber model. The Monte Carlo Glauber model participant positions are smoothed with a Gaussian distribution of width $\sigma = 0.5$ fm and normalized to reproduce experimental charged particle multiplicity in $0-10\%$ collision. In this model work, $\sim$1000 events in each collision centrality was simulated which is sufficient for this study. Once the initial transverse energy density is fixed to reproduce multiplicity in the $0-10\%$ collision, the model reproduces the experimental multiplicity in other collision centralities within reasonable accuracy. Experimental charged particle transverse momentum spectra, however, are reproduced in the model, only in a limited $p_\mathrm{T}$ range ($p_\mathrm{T} \leq 1$ GeV). At $p_\mathrm{T} > 1$ GeV, simulated spectra under predict the experiment. In the simulations, dissipative effects are neglected. Dissipative effect like (shear) viscosity, will enhance

particle production, more at high $p_{\mathrm{T}}$ than at low $p_{\mathrm{T}}$. Better description of the $p_{\mathrm{T}}$ spectra is expected if instead of ideal fluid, viscous fluid is produced in Au + Au collisions. We have also compared the model simulations for integrated and differential flow coefficients with experimental data. Experimental (integrated) elliptic flow in Au + Au collisions is correctly reproduced in simulations. The model also reasonably well reproduces the experimental differential elliptic flow in $0-10\%$ to $40-50\%$ collisions. In peripheral collisions, elliptic flow data, however, is overpredicted at high $p_{\mathrm{T}}$. Higher flow coefficients $v_3$ and $v_4$, however, are overpredicted, more in peripheral than in central collisions. Here again, better description of the data is expected if instead of ideal fluid, viscous fluid is produced in Au + Au collisions.

We have also studied correlation between (integrated) flow coefficients and initial asymmetry measures of the collision zone. In all the collision centralities ($0-10\%$ to $40-50\%$) elliptic flow is strongly correlated with the initial asymmetry measure, the eccentricity of the collision zone. The higher flow coefficients, however, show much less correlation with the corresponding asymmetry measures. We have quantified the correlation and observe that with the exception for elliptic flow, which remains strongly correlated in all the collision centralities, for the higher flow coefficients, $v_3$, $v_4$, and $v_5$, correlation reduces significantly in more peripheral collisions. It appears that in higher flow coefficients, a significant part of the flow is not correlated to the initial asymmetry measures. The reason for this observation cannot be discerned presently. One can only conclude that apart from the initial density distribution of collision zone, other aspects, $e.g.$, higher moments or product of higher moments are also important for the development of higher harmonics.

# Bibliography

[1] A. K. Chaudhuri, arXiv:0801.3180 [nucl-th].

[2] S. Manly *et al.*, Nucl. Phys. A 774, 523 (2006).

[3] A. P. Mishra *et al.*, Phys. Rev. C 81, 034903 (2010).

[4] A. P. Mishra *et al.*, Phys. Rev. C 77, 064902 (2008).

[5] J. Takahashi *et al.*, Phys. Rev. Lett. 103, 242301 (2009).

[6] B. Alver and G. Roland, Phys. Rev. C 81, 054905 (2010).

[7] B. H. Alver *et al.*, Phys. Rev. C 82, 034913 (2010).

[8] D. Teaney and L. Yan, Phys. Rev. C 83, 064904 (2011).

[9] K. Aamodt *et al.*, Phys. Rev. Lett. 107, 032301 (2011).

[10] Y. Aoki *et al.*, Nature 443, 675 (2006).

[11] Y. Aoki *et al.*, J. High Energy Phys. 0906, 088 (2009).

[12] S. Borsányi *et al.*, J. High Energy Phys. 1011, 077 (2010).

[13] Z. Fodor, J. Phys.: Conf. Ser. 230, 012013 (2010).

[14] V. Roy and A. K. Chaudhuri, Phys. Lett. B 703, 313 (2011).

[15] Z. Qiu and U. W. Heinz, Phys. Rev. C 84, 024911 (2011).

[16]  A. K. Chaudhuri, Phys. Lett. B 710, 339 (2012).

[17]  B. Schenke, S. Jeon, and C. Gale, Phys. Rev. C 85, 024901 (2012).

[18]  H. Holopainen and P. Huovinen, J. Phys. Conf. Ser. 389, 012018 (2012).

[19]  K. Aamodt *et al.*, Phys. Rev. Lett. 105, 252301 (2010).

[20]  K. Aamodt *et al.*, Phys. Rev. Lett. 107, 032301 (2011).

[21]  K. Aamodt *et al.*, Phys. Lett. B 696, 30 (2011).

[22]  F. Cooper and G. Frye, Phys. Rev. D 10, 186 (1974).

[23]  P. Sorensen, J. Phys. G 37, 094011 (2010).

[24]  J. Adams *et al.*, Phys. Rev. Lett. 95, 152301 (2005).

[25]  J. Putschke, J. Phys. G 34, S679 (2007).

[26]  B. I. Abelev *et al.*, Phys. Rev. Lett. 102,052302 (2009).

[27]  V. Khachatryan *et al.*, J. High Energy Phys. 09, 091 (2010).

[28]  D. Velicanu (CMS Collaboration), arXiv:1107.2196.

[29]  A. Adare *et al.*, Phys. Rev. Lett. 105, 062301 (2010).

[30]  A. Adare *et al.*, Phys. Rev. Lett. 107, 252301 (2011).

[31]  R. Lacey *et al.*, J. Phys. G 38, 124048 (2011).

[32]  B. Schenke, S. Jeon, and C. Gale, Phys. Rev. Lett. 106, 042301 (2011).

[33]  B. Schenke, S. Jeon, and C. Gale, Phys. Rev. C 85, 024901 (2012).

[34]  B. Schenke, P. Tribedy, and R. Venugopalan, Phys. Rev. Lett. 108, 252301 (2012).

[35]  C. Gale *et al.*, Phys. Rev. Lett. 110, 012302 (2013).

[36] H. Petersen, G.-Y. Qin, S. A. Bass, and B. Muller, Phys. Rev. C 82, 041901 (2010).

[37] H. Holopainen, H. Niemi, and K. J. Eskola, Phys. Rev. C 83, 034901 (2011).

[38] H. Niemi, G. S. Denicol, H. Holopainen, and P. Huovinen, arXiv:1212.1008.

[39] K. Werner, I. Karpenko, T. Pierog, M. Bleicher, and K. Mikhailov, Phys. Rev. C 82, 044904 (2010).

[40] C. E. Aguiar, Y. Hama, T. Kodama, and T. Osada, Nucl. Phys. A 698, 639 (2002).

[41] P. Bozek and W. Broniowski, Phys. Rev. C 85, 044910 (2012).

[42] F. G. Gardim, F. Grassi, M. Luzum, and J.-Y. Ollitrault, Phys. Rev. C 85, 024908 (2012).

[43] F. G. Gardim, F. Grassi, M. Luzum, and J.-Y. Ollitrault, arXiv:1210.8422.

[44] B. Alver, M. Baker, C. Loizides, and P. Steinberg, arXiv:0805.4411.

[45] Md. R. Haque, V. Roy, and A. K. Chaudhuri, Phys. Rev. C 86, 037901 (2012).

[46] S. S. Adler *et al.*, Phys. Rev. C 71, 034908 (2005); 71, 049901(E) (2005).

[47] S. S. Adler *et al.*, Phys. Rev. C 69, 034910 (2004).

[48] B. B. Back *et al.*, Phys. Rev. C 72, 051901 (2005).

[49] Z. Qiu, C. Shen, and U. Heinz, Phys. Lett. B 707, 151 (2012).

[50] B. Schenke, S. Jeon, and C. Gale, J. Phys. G 38, 124169 (2011).

[51] V. Roy, A. K. Chaudhuri, and B. Mohanty, Phys. Rev. C 86, 014902 (2012).

[52] A. K. Chaudhuri, J. Phys. G 37, 075011 (2010).

[53] A. K. Chaudhuri, Phys. Lett. B 713, 91 (2012).

[54] A. K. Chaudhuri, arXiv:1210.2249.

[55] Z. Qiu and U. Heinz, Phys. Lett. B 717, 261 (2012).

# Chapter 7

# Summary and Conclusions

In this thesis, we present the results on energy and centrality dependence of $d$ and $\bar{d}$ production at $\sqrt{s_{\mathrm{NN}}}$ = 7.7, 11.5, 19.6, 27, 39 GeV and azimuthal anisotropy of $d$, $\bar{d}$, $t$, $^{3}He$ and $^{3}\overline{He}$ at $\sqrt{s_{\mathrm{NN}}}$ = 7.7, 11.5, 19.6, 27, 39, 62.4 and 200 GeV in Au+Au collisions at RHIC. The data in the aforementioned energy were recorded by the STAR experiment at RHIC in the years 2010 and 2011. Transverse momentum ($p_{\mathrm{T}}$) spectra of $d$ and $\bar{d}$ for different centralities at $\sqrt{s_{\mathrm{NN}}}$ = 7.7-39 GeV are presented. The shape of the $p_{\mathrm{T}}$-spectra is found to be less steeper in the central collisions compared to that in peripheral collisions which might be due the of large radial flow developed in central collisions compared to peripheral. The $p_{\mathrm{T}}$ integrated yields of $d$ and $\bar{d}$ per participant pair $((dN/dy)/(0.5N_{\mathrm{part}}))$ are found increase with centrality for peripheral events, then it becomes constant for mid-central to central collisions. This observation suggests that particle production does not scale with number of participating nucleons (estimated from Glauber model simulations at the respective beam energies) for the peripheral collisions. For a given centrality, $(dN/dy)/(0.5N_{\mathrm{part}})$ of $\bar{d}$ increases with increasing energy, which is expected due to the increase of energy available to produce the anti-particles. However, $(dN/dy)/(0.5N_{\mathrm{part}})$ of $d$ shows the opposite trend with respect to energy, when compared with the trend of $\bar{d}$. $(dN/dy)/(0.5N_{\mathrm{part}})$ of $d$ is found to increase with decreasing collision energy, which is expected due to large

baryon stopping expected at the lower beam energies. The coalescence parameter $B_2$ of $d$ and $\bar{d}$ have been measured and presented as a function of centrality and collision energy. $B_2$ of both $d$ and $\bar{d}$ decreases with increasing centrality for all center-of-mass energies studied in this thesis. Since the correlation volume ($V_f$) is inversely proportional to $B_2$, therefore the decrease in $B_2$ with increasing centrality implies that $V_f$ increases with increasing centrality. The energy dependence of $B_2$ of $d$ and $\bar{d}$ for central Au+Au collisions are presented and compared with corresponding published results. The measurements of $B_2$ in this thesis are consistent with the published results for the same center-of-mass energies. $B_2$ of both $d$ and $\bar{d}$ is found have almost no energy dependence for the energy range studied in this thesis. This indicates that the source volume does not change appreciably with center-of-mass energies studied in this thesis (with the caveat that $B_2$ varies as a function of centrality). This observation is consistent with what has been observed in Hanbury Brown Twiss analysis at RHIC for identified particles. The similar magnitude of $B_2$ of $d$ and $\bar{d}$ also indicate that nuclei and anti-nuclei might have similar temperature, flow, and freeze-out density distributions. We have also measured centrality and energy dependence of $\bar{d}/\bar{p}$ and $d/p$ ratios. Both $\bar{d}/\bar{p}$ and $d/p$ ratio increase with increasing centrality at first then reaches a plateau from midcentral to central collisions. We also observe, that both $\bar{d}/\bar{p}$ and $d/p$ show energy dependence for all collision centralities. The $d/p$ ratio increases with decreasing beam energy, indicating the formation of baryon rich system at low beam energies. However, the $\bar{d}/\bar{p}$ ratio, decreases with decreasing beam energy. Decreasing $\bar{d}/\bar{p}$ ratio at lower beam energy can be attributed to the lower production of anti-particles at low beam energies. The $\bar{d}/\bar{p}$ ratio as a function of $\sqrt{s_{\mathrm{NN}}}$ has been compared with other published results and found to be consistent within the same center-of-mass energy range. The $\bar{d}/\bar{p}$ ratio is found to increase monotonically with increasing beam energy and then reaches a plateau above ISR beam energy, regardless of the beam species ($pp$, $pA$, $AA$).

The measurement of light nuclei ($d$, $\bar{d}$, $^3He$, $^3\overline{He}$, $t$) $v_2$ as a function of $p_\mathrm{T}$ and collision centrality is presented. Light nuclei $v_2(p_\mathrm{T})$ is found to exhibit mass

ordering at low $p_\mathrm{T}$ indicating the presence of strong radial flow in the medium. We observed that $d$ and $\bar{d}$ show similar magnitude of $v_2$ as a function of $p_\mathrm{T}$ for $\sqrt{s_\mathrm{NN}} \geq$ 39 GeV. However, the difference in $v_2$ of $d$ and $\bar{d}$ is found to qualitatively follow the difference in $v_2$ of $p$ and $\bar{p}$ for $\sqrt{s_\mathrm{NN}} \leq 19.6$ GeV. The $v_2$ of $^3He$ and $t$ is found to have similar magnitude within error for $\sqrt{s_\mathrm{NN}} = 7.7$-200 GeV. This similarity in the magnitude of $v_2$ of $d$ and $\bar{d}$ ($A = 2$) and $^3He$ and $t$ ($A = 3$) indicate that the $v_2$ of light nuclei depends only on the mass of individual nuclei and not on their internal composition (neutrons and protons). The $v_2(p_\mathrm{T})$ of $d$ and $\bar{d}$ is found to have clear centrality dependence similar to that observed for identified hadrons. The atomic mass number ($A$) scaling of nuclei $v_2$ is observed for $p_\mathrm{T}/A \approx 1.5$ GeV/c for $\sqrt{s_\mathrm{NN}}$ = 7.7-200 GeV. This scaling behavior supports the physics idea that the light nuclei might have formed via coalescence of nucleons. A model based study is performed using transport+coalescence model to find theoretical prediction of nuclei $v_2$. The transport+coalescence model is found to reproduce the measurement of $v_2(p_\mathrm{T})$ of nuclei from the data. The model study therefore, supports the coalescence picture of light nuclei formation in heavy-ion collisions as indicated by the atomic mass scaling of nuclei $v_2$.

Transport model (AMPT) based study of $\varepsilon_2$, $v_2$, $\varepsilon_3$, $v_3$, fluctuations in $\varepsilon_2$, $\varepsilon_3$, and their centrality ($N_\mathrm{part}$) dependence is presented for various asymmetric colliding ion species (Ag+Au, Cu+Au, and Si+Au) as well as in various collision geometries of U+U. We find that $\varepsilon_2$ and its fluctuations, for a given collision centrality, are highly dependent on the colliding ion type. However, no such strong dependencies are observed for $\varepsilon_3$ and its fluctuations. $v_2(p_\mathrm{T})$ is found to decrease as the colliding system size decreases for a given collision centrality. However no such sensitivity to colliding ion type is observed for $v_3(p_\mathrm{T})$. The study thus indicates that asymmetric heavy-ion collisions can be used to constrain models dealing with flow fluctuations in heavy-ion collisions but with greater sensitivity for $v_2(p_\mathrm{T})$ related observables than for $v_3(p_\mathrm{T})$.

$\varepsilon_2$, $v_2$, $\varepsilon_3$, $v_3$, fluctuations in $\varepsilon_2$ and $\varepsilon_3$ have also been presented for three specific

configurations of U+U collisions along with minimum bias configuration for $\sqrt{s_{NN}}$ = 200 GeV. The results from these collisions have been compared to Au+Au collisions at the same beam energy. The results for both default and string-melting configurations of the AMPT model have been presented. The charged particle multiplicity and charged particle transverse energy is found to be about $15-35\%$ higher for the different U+U configurations relative to Au+Au collisions. The average transverse momentum ($\langle p_T \rangle$) for charged particles increases with number of participating nucleons for the default case, whereas they saturate for central collisions in the string-melting version. This is perhaps due to additional partonic interactions and the quark coalescence process in the string-melting model relative to the default case. Within the different configurations studied, the multiplicity, transverse energy, and $\langle p_T \rangle$ at midrapidity are found to be largest for the tip-to-tip configuration. The average $\varepsilon_2$ and fluctuations in $\varepsilon_2$ show a rich dependence on collision centrality. The side-on-side configuration possesses the maximum $\varepsilon_2$ and minimum fluctuations of $\varepsilon_2$ as a function of collision centrality. In contrast, the body-to-body configuration has the minimum $\varepsilon_2$ and maximum $\varepsilon_2$ fluctuations from peripheral to mid-central collisions. The tip-to-tip configuration has minimum $\varepsilon_2$ and maximum $\varepsilon_2$ fluctuations for central collisions. We did not observe large variation in $\varepsilon_3$ and its fluctuations for Au+Au collisions and different collisions configurations of U+U. The variation of eccentricities and their fluctuations get reflected in the dependence of $v_2$ and $v_3$ as a function of collision centrality. The side-on-side configuration has maximum $v_2$ compared to all other configurations of U+U for all collision centralities. $v_2$ is smallest for the body-to-body configuration in peripheral to mid-central collisions while it is minimum for the tip-to-tip configuration in central collisions. For peripheral collisions, $v_2$ in U+U can be about 40% larger than in Au+Au, whereas for central collisions, it can be a factor of 2 higher depending on the collision configuration. It seems the body-to-body and tip-to-tip configurations have higher $v_3$ values as a function of collision centrality compared to other cases studied. The side-on-side configuration is found to possess the largest $v_2$ while the U+U body-to-body configuration has the smallest $v_2$. The

tip-to-tip in U+U and Au+Au has similar $v_2$ values.

The azimuthal anisotropy and their fluctuations in heavy-ion collisions have also been studied using a event-by-event hydrodynamics model. The input to the hydrodynamic calculations were taken from a Monte Carlo Glauber model. It is found that integrated as well as differential $v_2$ and $v_3$ flows remain largely unaltered, irrespective of functional form of the smoothening function, used to smooth discrete participating nucleons position from Monte Carlo Glauber model. Higher harmonics ($v_4$ and $v_5$), on the other hand, are influenced by the smoothening effect.

Using the same event-by-event hydrodynamics simulations, the centrality dependence of charged particle multiplicity, $p_{\mathrm{T}}$ spectra, and flow coefficients (integrated and differential) are also presented for Au+Au collisions at $\sqrt{s_{\mathrm{NN}}} = 200$ GeV. The hydrodynamic simulation uses the initial energy density distributions from a Monte Carlo Glauber model, smoothed with a Gaussian distribution of width $\sigma = 0.5$ fm and normalized to reproduce charged particle multiplicity in data for $0-10\%$ centrality. In this hydrodynamic model study, dissipative effects (*e.g.* viscosity) are neglected. We have compared the model results for integrated and differential flow coefficients with published data. Experimental (integrated) elliptic flow in Au+Au collisions is correctly reproduced with the ideal hydrodynamic calculations. The model also reproduces the experimental differential elliptic flow ($v_2(p_{\mathrm{T}})$) for $0-10\%$ to $40-50\%$ collisions centralities with reasonable extent. The elliptic flow ($v_2$) is found to overpredicted the data at high $p_{\mathrm{T}}$ for peripheral collisions. Higher flow coefficients $v_3$ and $v_4$, are overpredicted, more in peripheral than central collisions. Better description of the data is expected if, instead of ideal fluid, viscous fluid is assumed in the hydrodynamic calculations. $v_2$ is found to be strongly correlated with the initial asymmetry $\varepsilon_2$ of the collision zone for the collision centralities studied (0-10% to 40-50%). The higher flow coefficients ($v_3$, $v_4$, $v_5$) is found to have much less correlation with the corresponding initial asymmetry ($\varepsilon_3$, $\varepsilon_4$, $\varepsilon_5$).